MACHINING TECHNOLOGY AND ENVIRONMENTAL DEGRADATION MECHANISM OF SURFACE MICROSTRUCTURE OF SPECIAL MATERIALS

EDITED BY: Guijian Xiao, Rdk Misra and Kun Li
PUBLISHED IN: Frontiers in Materials

frontiers Research Topics

About Frontiers

Frontiers is more than just an open-access publisher of scholarly articles: it is a pioneering approach to the world of academia, radically improving the way scholarly research is managed. The grand vision of Frontiers is a world where all people have an equal opportunity to seek, share and generate knowledge. Frontiers provides immediate and permanent online open access to all its publications, but this alone is not enough to realize our grand goals.

Frontiers Journal Series

The Frontiers Journal Series is a multi-tier and interdisciplinary set of open-access, online journals, promising a paradigm shift from the current review, selection and dissemination processes in academic publishing. All Frontiers journals are driven by researchers for researchers; therefore, they constitute a service to the scholarly community. At the same time, the Frontiers Journal Series operates on a revolutionary invention, the tiered publishing system, initially addressing specific communities of scholars, and gradually climbing up to broader public understanding, thus serving the interests of the lay society, too.

Dedication to Quality

Each Frontiers article is a landmark of the highest quality, thanks to genuinely collaborative interactions between authors and review editors, who include some of the world's best academicians. Research must be certified by peers before entering a stream of knowledge that may eventually reach the public - and shape society; therefore, Frontiers only applies the most rigorous and unbiased reviews.
Frontiers revolutionizes research publishing by freely delivering the most outstanding research, evaluated with no bias from both the academic and social point of view. By applying the most advanced information technologies, Frontiers is catapulting scholarly publishing into a new generation.

What are Frontiers Research Topics?

Frontiers Research Topics are very popular trademarks of the Frontiers Journals Series: they are collections of at least ten articles, all centered on a particular subject. With their unique mix of varied contributions from Original Research to Review Articles, Frontiers Research Topics unify the most influential researchers, the latest key findings and historical advances in a hot research area! Find out more on how to host your own Frontiers Research Topic or contribute to one as an author by contacting the Frontiers Editorial Office: frontiersin.org/about/contact

MACHINING TECHNOLOGY AND ENVIRONMENTAL DEGRADATION MECHANISM OF SURFACE MICROSTRUCTURE OF SPECIAL MATERIALS

Topic Editors:
Guijian Xiao, Chongqing University, China
Rdk Misra, The University of Texas at El Paso, United States
Kun Li, Chongqing University, China

Table of Contents

Research on Modeling Crystallographic Texture Evolution of Al Alloy 7075

Hao Liu, Man Zhao, Yufeng Zhou and Gang Liu *

School of Mechanical and Automotive Engineering, Shanghai University of Engineering Science, Shanghai, China

Crystallographic texture is related to the anisotropy or isotropy of material physical properties, including mechanical performance. The crystallographic effect in micromachining is more significant than that in macro-processing owing to that the depth of the cut and the grain size are in the same order. It is of great significance to model the crystallographic texture evolution induced by mechanical and thermal load during micro-machining to investigate the surface integrity and performance of the finished product. This study performed hot deformation experiments of Al alloy 7075 (AA7075) under various input parameters, including the temperature, temperature rate, stain rate, and strain, which was designed using the Taguchi method. Following that, crystallographic orientation of the samples before and after the deformation was tested using electron back-scattered diffraction (EBSD). Then, the crystallographic texture evolution was modeled with the parameters obtained by fitting a part of the experimental data. The crystallographic texture evolution of AA7075 under different levels of input parameters is studied and analyzed. Finally, the sensitivity of crystallographic orientation evolution to the process parameter is analyzed. The results indicate that these four input parameters have a significant impact on some crystallographic texture of the specimens. The proposed model is instructive in the future investigation of micromachining and microstructure evolution.

Keywords: hot deformation, crystallographic texture, mechanical load, thermal load, EBSD

INTRODUCTION

Aluminum is the most abundant metal material in the Earth's crust. It is easy to process and has high corrosion resistance, electrical conductivity, and thermal conductivity. Alloying aluminum with other elements can obtain better mechanical properties. Alloy aluminum 7075 (AA7075) is used as the main structural material for aviation applications and has been the first choice for the aircraft industry for decades (Yasakau et al., 2014). AA7075, which has high strength-to-density ratio, high ductility, light weight, corrosion resistance, and superior mechanical properties, is widely used in the automotive and aerospace industries (Puchicabrera et al., 2006).

The microstructure of the material includes grain orientation, grain size, dislocation density, and phase transition. During micromachining, the quality of the workpiece will be affected by the microstructure of the workpiece material (Wu et al., 2019). The machining surface quality has an important impact on the performance of the part, and many scholars have done some research around the machining surface quality (Ding et al., 2021). Guo et al. (2021) proposed a new surface roughness prediction system with good prediction performance, which has certain feasibility and

practicality. Li et al. (2021) found that grinding assisted by graphene oxide coolant could improve the surface quality of grinding. The influence mechanism of surface generation and the generation mechanism of residual stress in the grinding process have attracted the attention of many researchers (Li et al., 2019; Ding et al., 2020; Sun et al., 2021; Xiao et al., 2021). For the surface quality requirements of precision machining of complex parts, robotic grinding is also used as a method to control the surface integrity (Lv et al., 2020; Xie et al., 2020; Zhu et al., 2020). The grain orientation is a key parameter in the analysis of the microstructure effect. The study of the evolution of the grain orientation during processing is of great significance for obtaining better machining quality.

The importance of texture in materials science stems from "anisotropy". The properties of single crystals such as mechanical, thermal, magnetic, optical, and chemical can be very different in different crystallographic directions. For example, rotation of the axis of loading can result in a 15% increase in the Young's modulus of commercial pure aluminum from 63 to 72 GPa. Simoneau et al. (2007) through the orthogonal micromachining of normalized AISI 1045 steel and refined AISI 1045 steel found that the small grain size will reduce the maximum plastic strain during chip formation. If the orientation of the grain boundary is not parallel to the shear surface, it can reduce the size of the pits on the processed surface. Cho et al. (2004) studied the effect of initial crystallographic orientation on the microstructure evolution of Ni-30 Fe alloy and found that the development of the deformed microstructure will be affected to a certain extent by the initial grains. Wu et al. (2015) found through copper microcutting experiments that the grain orientation has a great influence on the cutting force and the formation of burrs. The movement direction of the dislocation is obliquely forward of the cutting direction, which is beneficial to reduce the cutting force and the formation of burrs. Lin and Shiu (2016) used molecular dynamics methods to study the nanogrooving of single-crystal copper, and the results showed that the grain orientation has a significant effect on the cutting force and groove morphology. As a typical micro-part processing technology, microgrinding will be significantly influenced by the microstructure effect of the workpiece material. Min et al. (2006) used the tool at different angles relative to the workpiece direction to micro grind face centered cubic (FCC) single crystal materials and found that due to different crystal grain orientations, the activated slip system is different, which will have a significant effect on the surface and edges. Zhao et al. (2021) found that the grain orientation has a significant effect on the residual stress of microgrinding. Aicheler (2010) found that [111] surface grains produced much greater damage and roughness than the oriented surface grains in [100] through surface thermal fatigue experiments of polycrystalline copper. This is because the grains of the two orientations of <111> and <100> had different evolution during the thermal fatigue test of polycrystalline copper, and the surface with a grain orientation of <111> was severely deformed, while the surface with a grain orientation of <100> remained almost unchanged (Aicheler et al., 2011).

The texture evolution of aluminum alloys is mainly caused by the rotation of the operating slip system towards the direction of the applied external force. Also, twinning is considered to contribute to the texture evolution of AA7075 (Tabei 2015). Zhang and Li (2008) studied the grain orientation evolution of extruded magnesium alloy AZ31B sheets under uniaxial stretching at room temperature and found that the twin behavior is also different due to different initial orientations of the grains. Fang et al. (2011) carried out tensile tests on high manganese TWIP steel at different temperatures and found that temperature has a certain effect on the grain orientation evolution and twinning. Chen et al. (2018) studied the effect of strain rate and temperature caused by friction during high-speed sliding on the evolution of copper microstructure, and the results showed that the deformation is dominated by dislocation movement and twinning at lower or higher strain rates. Peng et al. (2018) conducted a uniaxial tensile test on a pure copper sample. In the experiment, with the increase of strain, the crystal grains with orientation <110> gradually rotated to the <111> orientation, and finally found that there were three main grain orientations. The ratio of <111> oriented grains increased significantly, the ratio of <110> oriented grains decreased significantly, and the ratio of <100> oriented grains hardly changed. Sun et al. (2019) studied the Cu-Sn low-temperature TLP-bonding solder joints and observed the grain orientation of the samples at 235, 250, and 265°C reflow and found that Cu_6Zn_5 and Cu_3Zn grains showed the preferential orientations of [001] and [100]. Parajuli et al. (2018) found that after annealing the gold film along the <111> direction, the grain orientation changed significantly. The proportion of <111> oriented grains increased from 50 to 70% because <111> is the preferred orientation of the gold film under certain conditions.

Zhang et al. (2018) conducted stress fracture experiments on Waspaloy alloy and found that the grain orientation evolution behavior is related to the initial grain size of the sample. Zhang et al. (2021) conducted cold rolling experiments on ultra-thin grain-oriented silicon steel and found that changing the shear distribution during the rolling process would change the evolution of grain orientation. Wang et al. (2021) combined the VPSC model and the finite element cutting simulation model to study the texture changes during Ti-6Al-4V processing and found that the slip system plays an important role in the formation of shear texture. Gong et al. (2017) studied the effect of microgrinding parameters on the ground surface and microstructure through a nickel-based single-crystal superalloy microgrinding experiment. Riyad et al. (2021) established a simulation framework based on multilevel crystal plasticity to study the texture evolution of Ti-6Al-4V in tension and compression. Tang et al. (2019) considered thermo-mechanical effects and established a viscoplastic self-consistent model based on dislocation density and introduced it into the hot extrusion process of magnesium alloy bars to analyze the changes in the microstructure. Roatta et al. (2021) used a polycrystalline plastic viscoplastic self-consistent (VPSC) model based on an affine linearization procedure to analyze the crystallographic texture evolution of Zn–Cu–Ti alloy sheets under simple shear and uniaxial tension.

FIGURE 1 | Schematic illustration of Euler angles defined by Bunge's notation.
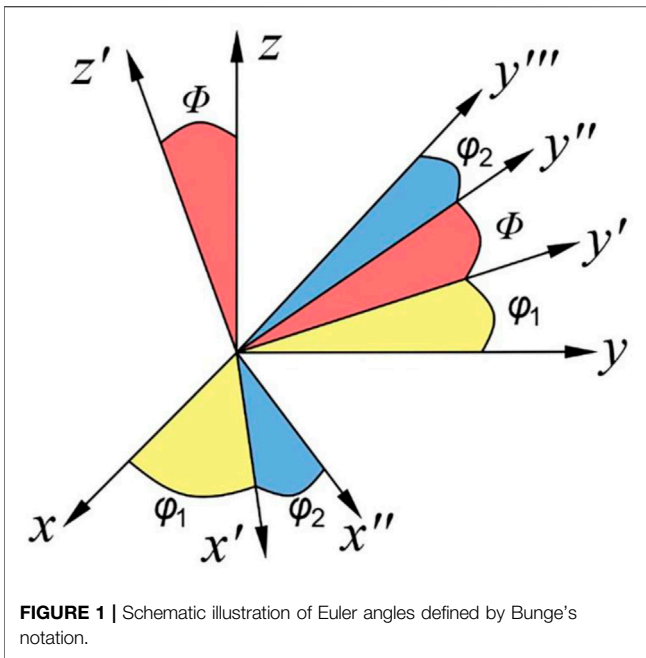
Researchers concur that crystallographic texture evolutions are important microstructural evolutions occurring in the processing of materials. The above literature mentioned several experimental observations of the abovementioned phenomena. To the best of my belief, the predictive model of crystallographic texture evolution is not presented, which takes the effect of strain rate, strain, temperature, and temperature rate induced by the thermal-mechanical load in machining of different types of metals and alloys. This work focused on analytically modeling the crystallographic texture evolution in microgrinding of AA7075 and developed an empirical model considering the effect of the strain rate, strain, temperature, and temperature rate with the parameters obtained by fitting the experimental data.

CRYSTALLOGRAPHIC TEXTURE EVOLUTION MODELING

Representation of Crystallographic Texture

AA7075 is a FCC metal, and there is no phase transformation in the microgrinding process. The texture research of materials is mainly focused on microtexture analysis. Electron backscatter diffraction (EBSD) is the main tool for microtexture analysis.

Euler angles are about Cartesian axes of the rotation required, and it can be obtained in the desired direction from a reference direction. The work follows Bunge's notation; the Euler angles are represented by φ_1, Φ, and φ_2. The definition of Bunge's notation is shown in **Figure 1**. In order to get to the desired orientation, φ_1 is rotated around the z axis. Φ is rotated around the x axis that has already been rotated, as shown by x' in **Figure 1**. φ_2 is the rotation about the z' axis (the z axis after the first two rotations).

Each crystallite's orientation coordinates are called the "crystal" frame. In Bunge's notation of Euler angles, the range of φ_1 and φ_2 is $[0, 2\pi]$ while the range of Φ is $[0, \pi]$.

Modeling of Crystallographic Texture Evolution

Experimental results show that twinning is mostly suppressed in FCC metals such as aluminum, and the major mechanism of inelastic deformation is slip (Barlat et al., 1997). The reason for the change of the crystallographic orientation in slip deformation is explained by Schmid's law (Schmid and Boas 1950). From the perspective of thermodynamics, the direction of the normal slip plane (n) of the crystal should be consistent with the direction of the externally applied load(s). The activation of any slip system requires that the shear stress acting on the slip system to reach a critical value, the so-called "critical resolved shear stress" or τ_{CRSS}. Eshelby proposed the strain and rotation fields in the ellipsoidal grain (Eshelby 1957). Therefore, the rotation of each grain can be determined. Following that, "self-consistent" approaches were introduced to solve the crystal plasticity problem (Hutchinson 1970). The spin (rotation rate) Ω_{ij}^c of the crystal explains that the crystallographic texture evolution can be found using the following formula:

$$\Omega_{ij}^c - \bar{\Omega}_{ij} = \prod : S^{-1} : \left(\dot{\varepsilon}_{ij}^c - \bar{\dot{\varepsilon}}_{ij} \right), \qquad (1)$$

where S is the fourth-order Eshelby tensor that is only a function of the shape of the ellipsoid particle, and $\prod$ is the skew-symmetric fourth-order Eshelby tensor (Eshelby 1957). $\dot{\varepsilon}_{ij}^c$ is the strain rate in the crystal; the overline denotes the value of the medium. The self-consistent approach leads to the following (Molinari et al., 1987):

$$\dot{\varepsilon}_{ij}^c - \bar{\dot{\varepsilon}}_{ij} = \bar{M}^c : (\sigma^c - \bar{\sigma}), \qquad (2)$$

where $\bar{M}^c$ is the secant modulus associated with the rate.

Feng et al. (2018) used the modified Johnson–Cook flow stress law to calculate the cutting and plowing forces considering the grain size and proposed an analytical model for predicting the milling temperature of Inconel 718 considering the effect of dynamic recrystallization. In this study, we consider only the effect of grain orientation. In this process, the hardening behavior of the material is taken into account and is used to update τ_{CRSS}. The Johnson–Cook model can be used to obtain the constitutive behavior of AA7075 at each temperature.

$$\sigma = (A + B\varepsilon^n)\left(1 + C\ln\frac{\dot{\varepsilon}}{\dot{\varepsilon}_0}\right)\left(1 - \left(\frac{T_0 - T_w}{T_m - T_w}\right)^m\right), \qquad (3)$$

where A, B, C, m, n, and $\dot{\varepsilon}_0$ are material constants, ε is the plastic strain, $\dot{\varepsilon}$ is the plastic strain rate, T_0 is the workpiece temperature, T_w is the ambient temperature, and T_m is the material melting

TABLE 1 | Johnson–Cook model parameters for Al Alloy 7075.

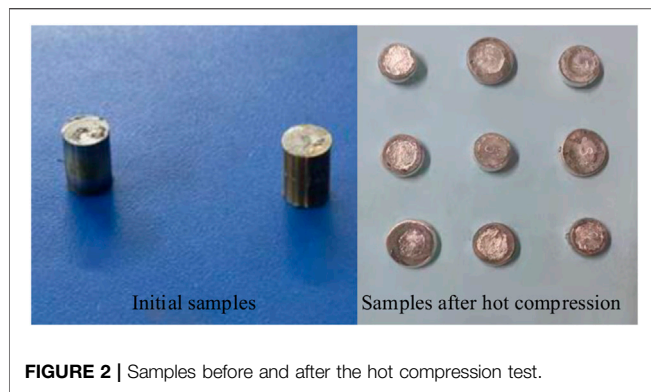| A (MPa)	B (MPa)	C	m	n	T_m(°C)	$\dot{\varepsilon}_0$ (s⁻¹)
520	477	0.001	1	0.52	619.85	5×10^{-4}

FIGURE 2 | Samples before and after the hot compression test.

temperature. The values of Johnson–Cook model parameters are from Flores-Johnson et al. (2014) in **Table1**.

From the theoretical analysis, it is captured that crystallographic texture evolution is related to the strain rate, strain, temperature, and temperature rate. Therefore, the empirical model can be expressed as follows:

$$\Omega_{ij}^C = f\left(T, \dot{T}, \dot{\varepsilon}, \varepsilon\right). \tag{4}$$

For polycrystalline material, crystallographic texture is represented by COs and the corresponding orientation distribution functions (ODFs). Crystallographic texture evolution can be represented by the ODF variation of main COs, as follows:

$$f_{\left(\varphi_1, \varnothing, \varphi_2\right)} = a_{k1} T^{a_{k2}} \dot{T}^{a_{k3}} \dot{\varepsilon}^{a_{k4}} \varepsilon^{a_{k5}}, \tag{5}$$

where a_{ij} is the constant and exponents.

To convert the nonlinear model to a linear model, logarithmic transformation is used.

$$\ln f_{\left(\varphi_1, \varnothing, \varphi_2\right)} = \ln a_{k1} + a_{k2}\ln T + a_{k3}\ln \dot{T} + a_{k4}\ln \dot{\varepsilon} + a_{k5}\ln \varepsilon. \tag{6}$$

For model simplification, Eq. (6) can be given as follows:

$$y = \beta_0 + \beta_1 A + \beta_2 B + \beta_3 C + \beta_4 D + \delta, \tag{7}$$

where y is logarithmic transformations of the measured surface roughness, and A, B, C, and D are temperature, temperature rate, strain rate, and strain on a logarithmic scale, respectively; β_0, β_1, β_2, β_3, etc., are coefficients to be estimated by the least squares method, and δ is the randomly distributed error terms.

EXPERIMENTS METHOD

Hot Compression Test

In the research process, AA7075 is used as the experimental material. The dimension of samples is a diameter of 8 mm and the height of 12 mm as shown in **Figure 2**.

In order to simulate the microgrinding process and study the flow behavior and crystallographic texture evolution of AA7075, the isothermal compression test was carried out on the G1eeble-3800 thermo-mechanical simulator as shown in

Figure 3, and each parameter was set to 3 levels, respectively; the temperature was 350, 400, and 450°C, and the temperature rate was 1, 10, and 100°C/s; the strain rate was 0.01, 0.1, and 1 s-1, and the strain was 0.5, 0.6, and 0.7. The hot compression tests were designed according to the Taguchi method, as shown in **Table 2**.

The G1eeble-3800 thermo-mechanical simulator is composed of a computer control system, mechanical control system, and thermal control system, which can simulate various thermal-mechanical processes, such as thermal tension, thermal compression, and plane deformation. For the hot compression test, each sample was heated to the target temperature according to the respective set temperature rate in **Table 1** and then held for 2 min, after which the specimens were compressed according to the respective corresponding strain rate and strain.

The details of the hot compression process are shown in **Figure 4**.

Microstructure Observation

To study the microstructure evolution during hot compression, the microstructure of the samples before and after the test was observed by EBSD. The surface of the compressed sample was polished before the EBSD examination. EBSD data were taken from the center of the polished surface. The samples were polished and tested as depicted in **Figure 5**.

RESULTS AND DISCUSSION

EBSD Measurement Result

Inverse pole diagrams (IPFs) of nine samples were obtained from EBSD, as shown in **Figure 6**, which can be used as a qualitative description of microtexture.

The COs and the corresponding distributions of the nine samples were analyzed by TSL OIM Data Collection 5 software and depicted by the OIM micrographs, as shown in **Figure 7**.
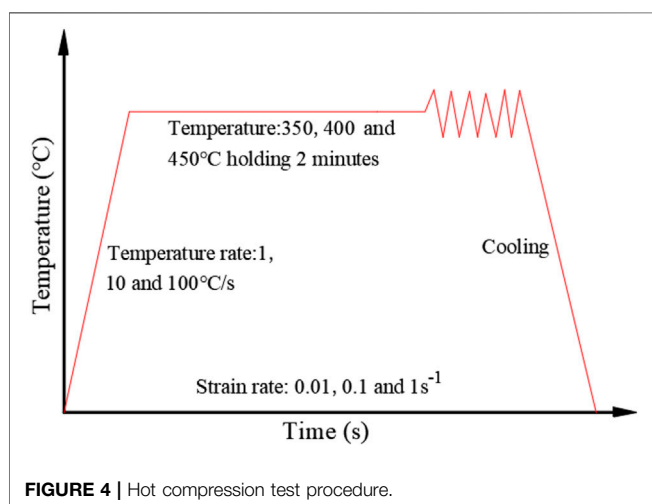
The ODF is a preferred orientation representation of the three-dimensional spatial distribution of a crystal and represents the

FIGURE 3 | G1eeble-3800 compression test setup.

TABLE 2 | Parameter details in the hot compression test.

Factors NO.	Temperature rate (°C/s)	Temperature (°C)	Strain rate (s^{-1})	Deformation (um)
1	1	350	0.01	50
2	1	400	0.1	60
3	1	450	1	70
4	10	350	0.1	70
5	10	400	1	50
6	10	450	0.01	60
7	100	350	1	60
8	100	400	0.01	70
9	100	450	0.1	50

FIGURE 4 | Hot compression test procedure.

odds of a particular crystal orientation defined by the Euler angles. The COs and the corresponding ODFs of the nine samples were obtained by EBSD tests. The top 11 ODFs and COs are listed in **Table 3**.

For comparing the variance of microtexture intuitively, the ODFs of nine specimens are described in **Figure 8**.

Form **Figure 8**, it is found that the ODFs of specimens are completely different, which indicates that crystallographic texture evolution is conspicuous.

The Linear Regression Analysis

In the research process, the crystallographic texture evolution is represented by the main COs evolution of specimens. To determine the main COs, the calculated method was developed. In the method, the ODF variation of each CO is obtained by calculating the difference value between the specimens before and after hot deformation. Then, the sum for ODF variation of each CO was calculated, and the top three variations represent COs evolution. The ODF variation of each specimen is listed in **Table 4**.

It is found that the top three COs are (270.0, 35.3, and 45.0), (35.3, 90.0, and 45.0), and (270.0, 25.2, and 45.0). To connect the crystallographic texture evolution to the process parameters of hot deformation intuitively, the process parameters and ODF variation of the top three COs are listed in **Table 5**.

The coefficients of the three CO evolutions are determined by fitting predictions with 9 groups of experimental data, with the R-squares of 0.8460, 0.9575, and 0.7064, respectively.

$$f_{(270.0,\ 35.3, 45.0)} = -4.1189 T^{0.0536} \dot{T}^{0.9495} \dot{\varepsilon}^{0.0202} \varepsilon^{0.6141},$$

$$f_{(35.3, 90, 45.0)} = -10.0246 T^{0.1197} \dot{T}^{-2.4915} \dot{\varepsilon}^{0.0619} \varepsilon^{1.6069},$$

$$f_{(270.0, 25.2, 45.0)} = 25.9283 T^{-0.0372} \dot{T}^{-7.1702} \dot{\varepsilon}^{0.2640} \varepsilon^{-4.7421}.$$

Sensitive Analysis

The sensitivity analysis of crystallographic orientation evolution to the parameters of the hot deformation process was carried out to investigate the significance of input parameters. Four input

FIGURE 5 | Initial microstructure of AA7075.
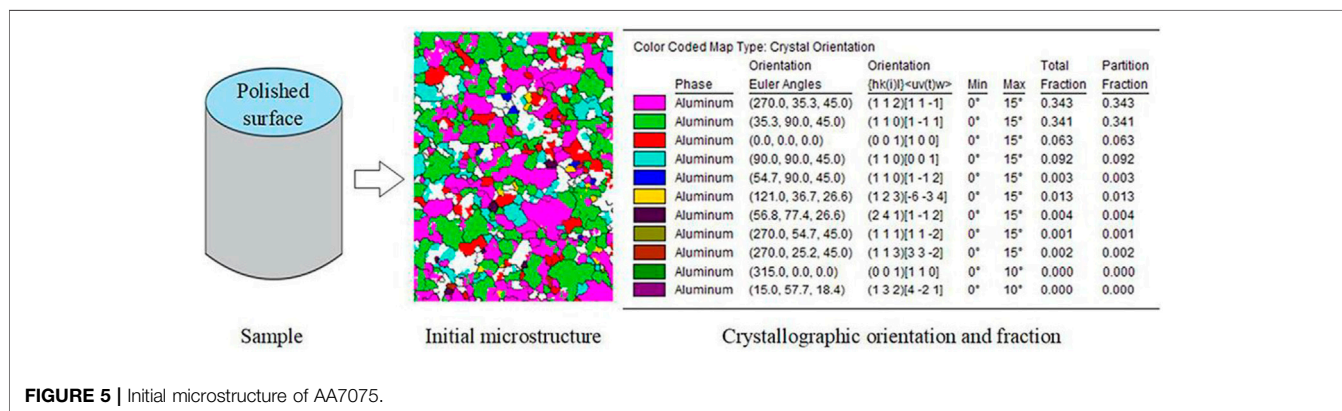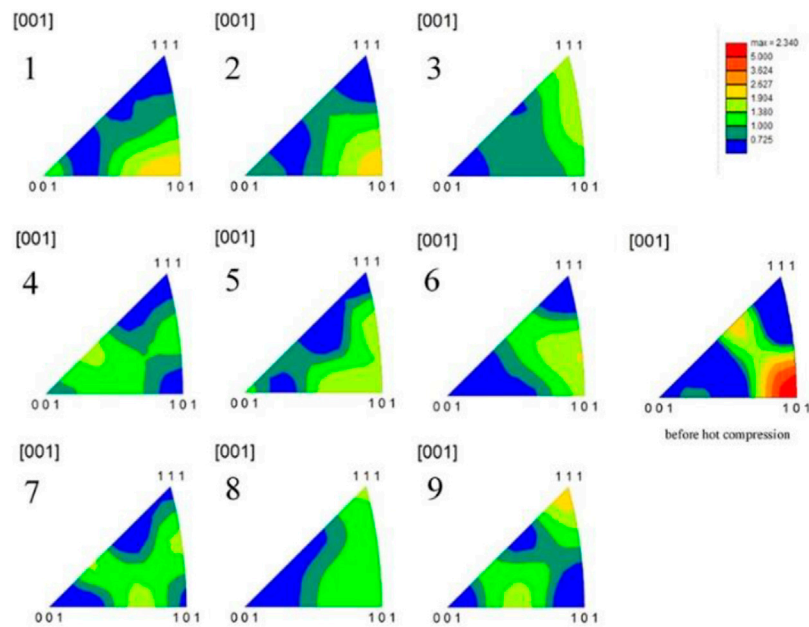
FIGURE 6 | Inverse pole figures of AA7075.
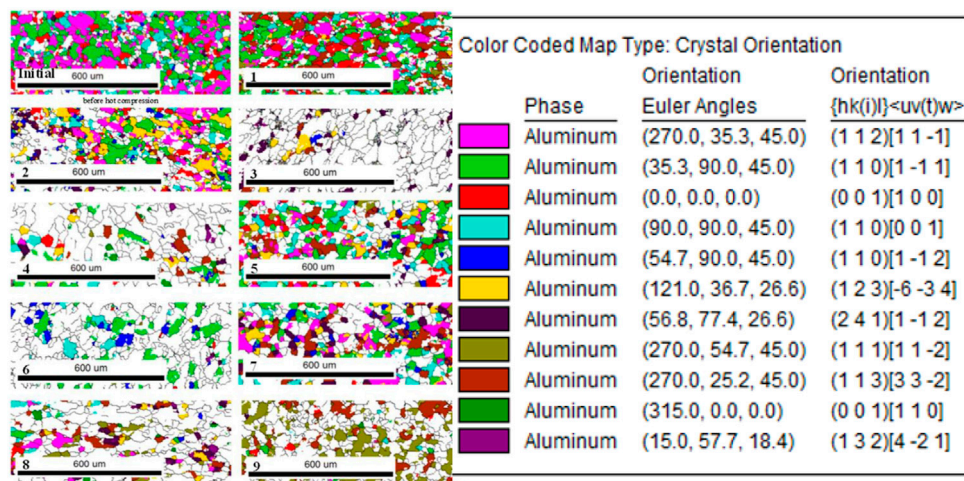
FIGURE 7 | The COs and the corresponding distributions.

parameters were selected for sensitivity analysis, including temperature, temperature rate, strain rate, and strain. The influence of each main input on the three crystallographic orientations (270.0, 35.3, 45.0), (35.3, 90.0, 45.0), and (270.0, 25.2, 45.0) was shown in **Figure 9**.

The results show that the process parameters have a greater impact on the crystallographic orientation evolution within the scope of the experimental exploration. The three crystallographic orientations (270.0, 35.3, 45.0), (35.3, 90.0, 45.0), and (270.0, 25.2, 45.0) have negative correlation with temperature, temperature rate, and strain. The grain orientations of (270.0, 35.3, 45.0) and (35.3,

90.0, 45.0) also show negative correlation with the strain rate, while grain orientations of (270.0, 25.2, and 45.0) are positively correlated with the strain rate. Therefore, to obtain the two crystallographic orientations (270.0, 35.3, 45.0) and (35.3, 90.0, 45.0), lower temperature, temperature rate, strain rate, and the strain are required. To obtain crystallographic orientation of (270.0, 25.2, 45.0), low temperature, small temperature rate, small strain, and large strain rate are required. At the same time, it can be seen that the effect of temperature on the evolution of grain orientation is almost linear, and as the strain rate increases, the rate of grain orientation evolution slows down.

TABLE 3 | The COs and the corresponding ODFs of specimens.

Bunge Euler angles	ODF								
$(\varphi_1, \varnothing, \varphi_2)$									
Specimen	Initial	NO.1	NO.2	NO.3	NO.4	NO.5	NO.6	NO.7	NO.8	NO.9
(270.0, 35.3, 45.0)	0.343	0.144	0.109	0.000	0.014	0.047	0.000	0.047	0.010	0.003
(35.3, 90.0, 45.0)	0.341	0.262	0.171	0.002	0.078	0.123	0.053	0.110	0.022	0.018
(0.0, 0.0, 0.0)	0.063	0.069	0.062	0.002	0.018	0.047	0.008	0.025	0.001	0.021
(90.0, 90.0, 45.0)	0.092	0.078	0.059	0.002	0.015	0.065	0.010	0.031	0.038	0.021
(54.7, 90.0, 45.0)	0.003	0.004	0.025	0.008	0.006	0.028	0.014	0.016	0.045	0.001
(121.0, 36.7, 26.6)	0.013	0.031	0.127	0.019	0.032	0.085	0.002	0.041	0.020	0.004
(56.8, 77.4, 26.6)	0.004	0.007	0.028	0.044	0.008	0.051	0.006	0.059	0.048	0.015
(270.0, 54.7, 45.0)	0.001	0.025	0.012	0.001	0.008	0.036	0.014	0.074	0.022	0.173
(270.0, 25.2, 45.0)	0.002	0.154	0.054	0.020	0.070	0.082	0.000	0.083	0.012	0.107
(315.0, 0.0, 0.0)	0.000	0.000	0.000	0.002	0.003	0.000	0.000	0.000	0.006	0.001
(15.0, 57.7, 18.4)	0.000	0.001	0.002	0.014	0.003	0.002	0.001	0.001	0.054	0.000
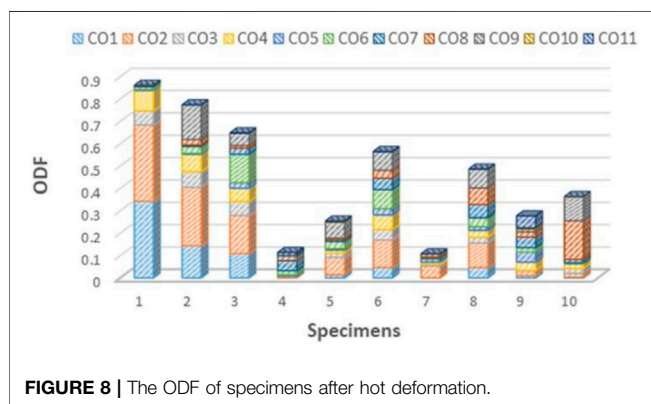
FIGURE 8 | The ODF of specimens after hot deformation.

CONCLUSION

This article mainly studies the crystallographic orientation evolution of Al alloy 7075 under mechanical and thermal loads. The Taguchi method was used to conduct hot compression tests on Al alloy 7075 samples at different temperatures, temperature rates, strains, and strain rates, and the COs and the corresponding ODFs are measured by the EBSD tests. The crystallographic texture evolution was modeled using the parameters obtained by the fitting part of the experimental data. The model linked the crystallographic texture evolution with the hot deformation process parameters to study the crystallographic texture evolution of Al Alloy 7075 under force-thermal loading. The following conclusions are drawn from this study:

1) The surface of Al Alloy 7075 sample had different crystallographic texture evolutions under the hot compression test with four different levels of parameter combination.

2) For the top three crystallographic orientations of the ODF variation, with the increase of temperature, temperature rate, strain rate, and strain, the grain orientations of (270.0, 35.3, 45.0) and (35.3, 90.0, 45.0) decrease, and oriented grains of (270.0, 25.2, 45.0) decrease with the increase of temperature, temperature rate, and strain, but there is a positive correlation with the strain rate.

3) The effect of temperature on the evolution of grain orientation is almost linear, and as the strain rate increases, the rate of grain orientation evolution slows down.

4) The thermo-mechanical load in micromachining is closely related to the process parameters. This study will be instructive for the crystallographic texture evolution in micromachining. This paper focuses on crystallographic orientation evolution under the thermo-mechanical load, and it is important to examine the

TABLE 4 | The ODF variation of each specimen.

Bunge Euler angles	ODF variation								
$(\varphi_1, \varnothing, \varphi_2)$									
Specimen	NO.1	NO.2	NO.3	NO.4	NO.5	NO.6	NO.7	NO.8	NO.9	Sum
(270.0, 35.3, 45.0)	0.199	0.234	0.343	0.329	0.296	0.343	0.296	0.333	0.34	2.713
(35.3, 90.0, 45.0)	0.079	0.17	0.339	0.263	0.218	0.288	0.231	0.319	0.323	2.23
(0.0, 0.0, 0.0)	0.006	0.001	0.061	0.045	0.016	0.055	0.038	0.062	0.042	0.326
(90.0, 90.0, 45.0)	0.014	0.033	0.09	0.077	0.027	0.082	0.061	0.054	0.071	0.509
(54.7, 90.0, 45.0)	0.001	0.022	0.005	0.003	0.025	0.011	0.013	0.042	0.002	0.124
(121.0, 36.7, 26.6)	0.018	0.114	0.006	0.019	0.072	0.011	0.028	0.007	0.009	0.284
(56.8, 77.4, 26.6)	0.003	0.024	0.04	0.004	0.047	0.002	0.055	0.044	0.011	0.23
(270.0, 54.7, 45.0)	0.024	0.011	0	0.007	0.035	0.013	0.073	0.021	0.172	0.356
(270.0, 25.2, 45.0)	0.152	0.052	0.018	0.068	0.08	0.002	0.081	0.01	0.105	0.568
(315.0, 0.0, 0.0)	0	0	0.002	0.003	0	0	0	0.006	0.001	0.012
(15.0, 57.7, 18.4)	0.001	0.002	0.014	0.003	0.002	0.001	0.001	0.054	0	0.078

TABLE 5 | The process parameters and ODF variation of the top three COs.

Factors NO.	Temperature rate (°C/s)	Temperature (°C)	Strain rate (s⁻¹)	Deformation (µm)	Bunge Euler angles $(\varphi_1, \phi, \varphi_2)$		
					(270.0, 35.3, 45.0)	(35.3, 90.0, 45.0)	(270.0, 25.2, 45.0)
1	1	350	0.01	50	0.199	0.079	0.152
2	1	400	0.1	60	0.234	0.17	0.052
3	1	450	1	70	0.343	0.339	0.018
4	10	350	0.1	70	0.329	0.263	0.068
5	10	400	1	50	0.296	0.218	0.08
6	10	450	0.01	60	0.343	0.288	0.002
7	100	350	1	60	0.296	0.231	0.081
8	100	400	0.01	70	0.333	0.319	0.01
9	100	450	0.1	50	0.34	0.323	0.105
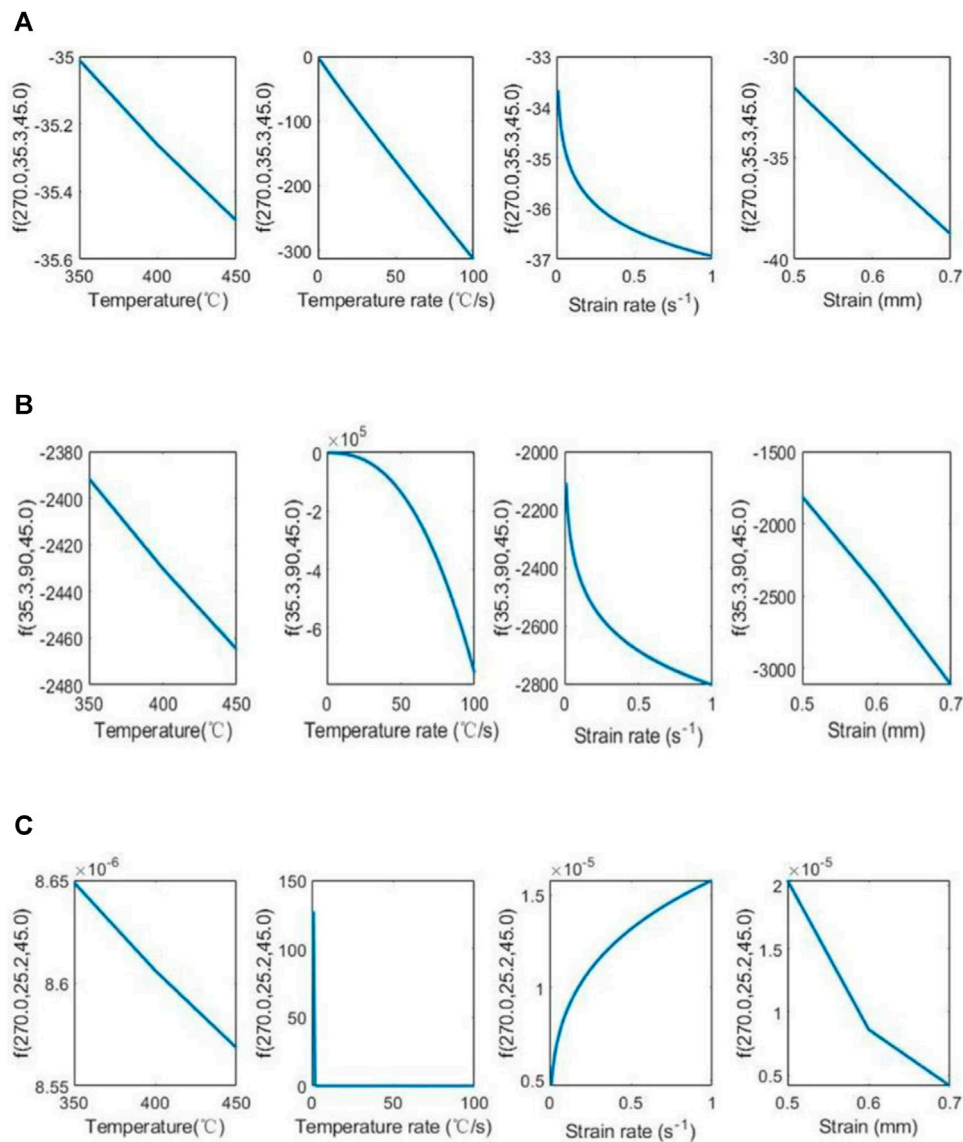
FIGURE 9 | Sensitivity analysis of the main effects on **(A)** (270.0, 35.3, 45.0), **(B)** (35.3, 90.0, 45.0), and **(C)** (270.0, 25.2, 45.0) orientations.

evolution of other material microstructures evolution such as grain size and recrystallization in future studies.

DATA AVAILABILITY STATEMENT

The raw data supporting the conclusion of this article will be made available by the authors, without undue reservation.

AUTHOR CONTRIBUTIONS

MZ, HL, and YZ contributed to conception and design of the study. MZ and HL participated in the experimental data acquisition and data analysis. HL wrote the first draft of the manuscript. MZ, GL, and YZ wrote sections of the manuscript. All authors contributed to manuscript revision, read, and approved the submitted version.

FUNDING

REFERENCES

Aicheler, M. (2010). Influence of Grain Orientation on Evolution of Surface Features in Fatigued Polycrystalline Copper: A Comparison of thermal and Uniaxial Mechanical Fatigue Results, *J. Phys. Conf. Ser.* 240, 012051. doi:10.1088/1742-6596/240/1/012051

Aicheler, M., Sgobba, S., Arnau-Izquierdo, G., Taborelli, M., Calatroni, S., Neupert, H., et al. (2011). Evolution of Surface Topography in Dependence on the Grain Orientation during Surface thermal Fatigue of Polycrystalline Copper. *Int. J. Fatigue* 33 (3), 396–402. doi:10.1016/j.ijfatigue.2010.09.015

Barlat, F., Becker, R. C., Hayashida, Y., Maeda, Y., Yanagawa, M., Chung, K., et al. (1997). Yielding Description for Solution Strengthened Aluminum Alloys. *Int. J. Plasticity* 13 (4), 385–401. doi:10.1016/S0749-6419(97)80005-8

Chen, X., Schneider, R., Gumbsch, P., and Greiner, C. (2018). Microstructure Evolution and Deformation Mechanisms during High Rate and Cryogenic Sliding of Copper. *Acta Materialia* 161, 138–149. doi:10.1016/j.actamat.2018.09.016

Cho, J.-Y., Inoue, T., Yin, F., and Nagai, K. (2004). Effect of Initial Grain Orientation on Evolution of Deformed Microstructure in Hot Compressed Ni-30Fe Alloy. *Mater. Trans.* 45 (10), 2960–2965. doi:10.2320/matertrans.45.2960

Ding, Z., Sun, G., Guo, M., Jiang, X., Li, B., and Liang, S. Y. (2020). Effect of Phase Transition on Micro-grinding-induced Residual Stress. *J. Mater. Process. Tech.* 281, 116647. doi:10.1016/j.jmatprotec.2020.116647

Ding, Z., Sun, J., Guo, W., Jiang, X., and Wu C, L. S. Y. (2021). Thermal Analysis of 3J33 Grinding under Minimum Quantity Lubrication Condition. *Int. J. Precision Eng. Manufacturing-Green Tech.* doi:10.1007/s40684-021-00391-y

Eshelby, J. D. (1957). The Determination of the Elastic Field of an Ellipsoidal Inclusion, and Related Problems. *Proc. R. Soc. Lond.* 241 (1226), 376–396. doi:10.1098/rspa.1957.0133

Fang, X.-H., Yang, P., Lu, F.-Y., and Meng, L. (2011). Dependence of Deformation Twinning on Grain Orientation and Texture Evolution of High Manganese TWIP Steels at Different Deformation Temperatures. *J. Iron Steel Res. Int.* 18 (11), 46–52. doi:10.1016/s1006-706x(11)60116-7

Feng, Y., Pan, Z., and Liang, S. Y. (2018). Temperature Prediction in Inconel 718 Milling with Microstructure Evolution. *Int. J. Adv. Manuf Technol.* 95 (9-12), 4607–4621. doi:10.1007/s00170-018-1581-1

Flores-Johnson, E. A., Shen, L., Guiamatsia, I., and Nguyen, G. D. (2014). Numerical Investigation of the Impact Behaviour of Bioinspired Nacre-like Aluminium Composite Plates. *Composites Sci. Tech.* 96, 13–22. doi:10.1016/j.compscitech.2014.03.001

Gong, Y., Zhou, Y., Wen, X., Cheng, J., Sun, Y., and Ma, L. (2017). Experimental Study on Micro-grinding Force and Subsurface Microstructure of Nickel-Based Single crystal Superalloy in Micro Grinding. *J. Mech. Sci. Technol.* 31 (7), 3397–3410. doi:10.1007/s12206-017-0629-8

Guo, W., Wu, C., Ding, Z., and Zhou, Q. (2021). Prediction of Surface Roughness Based on a Hybrid Feature Selection Method and Long Short-Term Memory Network in Grinding. *Int. J. Adv. Manuf Technol.* 112 (9-10), 2853–2871. doi:10.1007/s00170-020-06523-z

Hutchinson, J. W. (1970). Elastic-plastic Behaviour of Polycrystalline Metals and Composites. *Proc. R. Soc. Lond.* 319 (1537), 247–272. doi:10.1098/rspa.1970.0177

Li, C., Li, X., Huang, S., Li, L., and Zhang, F. (2021). Ultra-precision Grinding of Gd3Ga5O12 Crystals with Graphene Oxide Coolant: Material Deformation Mechanism and Performance Evaluation. *J. Manufacturing Process.* 61, 417–427. doi:10.1016/j.jmapro.2020.11.037

Li, C., Li, X., Wu, Y., Zhang, F., and Huang, H. (2019). Deformation Mechanism and Force Modelling of the Grinding of YAG Single Crystals. *Int. J. Machine Tools Manufacture* 143, 23–37. doi:10.1016/j.ijmachtools.2019.05.003

Lin, Y. C., and Shiu, Y. C. (2016). Effect of Crystallographic Orientation on Single crystal Copper Nanogrooving Behaviors by MD Method. *Int. J. Adv. Manuf Technol.* 89 (9-12), 3207–3215. doi:10.1007/s00170-016-9282-0

Lv, Y., Peng, Z., Qu, C., and Zhu, D. (2020). An Adaptive Trajectory Planning Algorithm for Robotic belt Grinding of Blade Leading and Trailing Edges Based on Material Removal Profile Model. *Robotics and Computer-Integrated Manufacturing* 66, 101987. doi:10.1016/j.rcim.2020.101987

Min, S., Dornfeld, D., Inasaki, I., Ohmori, H., Lee, D., Deichmueller, M., et al. (2006). Variation in Machinability of Single Crystal Materials in Micromachining. *CIRP Ann.* 55 (1), 103–106. doi:10.1016/s0007-8506(07)60376-x

Molinari, A., Canova, G. R., and Ahzi, S. (1987). A Self Consistent Approach of the Large Deformation Polycrystal Viscoplasticity. *Acta Metallurgica* 35 (12), 2983–2994. doi:10.1016/0001-6160(87)90297-5

Parajuli, P., Mendoza-Cruz, R., Santiago, U., Ponce, A., and Yacamán, M. J. (2018). The Evolution of Growth, Crystal Orientation, and Grain Boundaries Disorientation Distribution in Gold Thin Films. *Cryst. Res. Tech.* 53 (8), 1800038. doi:10.1002/crat.201800038

Peng, L., Xu, Z., Gao, Z., and Fu, M. W. (2018). A Constitutive Model for Metal Plastic Deformation at Micro/meso Scale with Consideration of Grain Orientation and its Evolution. *Int. J. Mech. Sci.* 138-139, 74–85. doi:10.1016/j.ijmecsci.2017.11.046

Puchicabrera, E., Villalobosgutierrez, C., Irausquin, I., Labarberasosa, J., and Mesmacque, G. (2006). Fatigue Behavior of a 7075-T6 Aluminum alloy Coated with an Electroless Ni-P deposit. *Int. J. Fatigue* 28 (12), 1854–1866. doi:10.1016/j.ijfatigue.2005.12.005

Riyad, I. A., Feather, W. G., Vasilev, E., Lebensohn, R. A., McWilliams, B. A., Pilchak, A. L., et al. (2021). Modeling the Role of Local Crystallographic Correlations in Microstructures of Ti-6Al-4V Using a Correlated Structure Visco-Plastic Self-Consistent Polycrystal Plasticity Formulation. *Acta Materialia* 203, 116502. doi:10.1016/j.actamat.2020.116502

Roatta, A., Leonard, M., Nicoletti, E., and Signorelli, J. W. (2021). Modeling Texture Evolution during Monotonic Loading of Zn-Cu-Ti alloy Sheet Using the Viscoplastic Self-Consistent Polycrystal Model. *J. Alloys Comp.* 860, 158425. doi:10.1016/j.jallcom.2020.158425

Schmid, E., and Boas, W. (1950). *Plasticity of Crystals*. Cambridge, UK: University of cambridge.

Simoneau, A., Ng, E., and Elbestawi, M. A. (2007). Grain Size and Orientation Effects when Microcutting AISI 1045 Steel. *CIRP Ann.* 56 (1), 57–60. doi:10.1016/j.cirp.2007.05.016

Sun, L., Chen, M.-h., and Zhang, L. (2019). Microstructure Evolution and Grain Orientation of IMC in Cu-Sn TLP Bonding Solder Joints. *J. Alloys Comp.* 786, 677–687. doi:10.1016/j.jallcom.2019.01.384

Sun, Y., Su, Z., Gong, Y., Ba, D., Yin, G., Zhang, H., et al. (2021). Analytical and Experimental Study on Micro-grinding Surface-Generated Mechanism of DD5 Single-crystal Superalloy Using Micro-diamond Pencil Grinding Tool. *Archiv. Civ. Mech. Eng.* 21 (1). doi:10.1007/s43452-020-00163-6

Tabei, S. B. (2015). Modeling of Microstructural Evolutions in Machining of Dual Phase Alloys. Dissertation. Atlanta, GA: Georgia Institute of Technology.

Tang, T., Zhou, G., Li, Z., Li, D., Peng, L., Peng, Y., et al. (2019). A Polycrystal Plasticity Based Thermo-Mechanical-Dynamic Recrystallization Coupled Modeling Method and its Application to Light Weight Alloys. *Int. J. Plasticity* 116, 159–191. doi:10.1016/j.ijplas.2019.01.001

Wang, Q., Shankar, R. M., and Liu, Z. (2021). Visco-plastic Self-Consistent Modeling of Crystallographic Texture Evolution Related to Slip Systems Activated during Machining Ti-6AL-4V. *J. Alloys Comp.* 853, 157336. doi:10.1016/j.jallcom.2020.157336

Wu, C., Pang, J., Li, B., and Liang, S. Y. (2019). High-speed Grinding of HIP-SiC Ceramics on Transformation of Microscopic Features. *Int. J. Adv. Manuf Technol.* 102 (5-8), 1913–1921. doi:10.1007/s00170-018-03226-4

Wu, X., Li, L., He, N., Zhao, M., and Zhan, Z. (2015). Investigation on the Influence of Material Microstructure on Cutting Force and Bur Formation in the Micro Cutting of Copper. *Int. J. Adv. Manuf Technol.* 79 (1-4), 321–327. doi:10.1007/s00170-015-6828-5

Xiao, G., Song, K., He, Y., Wang, W., Zhang, Y., and Dai, W. (2021). Prediction and Experimental Research of Abrasive belt Grinding Residual Stress for Titanium alloy Based on Analytical Method. *Int. J. Adv. Manuf Technol.* 115 (4), 1111–1125. doi:10.1007/s00170-021-07272-3

Xie, H., Li, W.-l., Zhu, D.-H., Yin, Z.-p., and Ding, H. (2020). A Systematic Model of Machining Error Reduction in Robotic Grinding. *Ieee/asme Trans. Mechatron.* 25 (6), 2961–2972. doi:10.1109/tmech.2020.2999928

Yasakau, K. A., Tedim, J., Zheludkevich, M. L., and Ferreira, M. G. S. (2014). "Smart Self-Healing Coatings for Corrosion protection of Aluminium Alloys," in *Handbook of Smart Coatings for Materials Protection*. Editor A. S. H. Makhlouf (United Kingdom: Woodhead Publishing), 224–274. doi:10.1533/9780857096883.2.224

Zhang, M.-c., Zhang, Q., and Wei, K. (2018). The Correlation between Grain Orientation Evolution and Stress Rupture Properties of Waspaloy. *Metall. Mat Trans. A.* 49 (12), 6063–6074. doi:10.1007/s11661-018-4923-6

Zhang, N., Meng, L., Zhang, B., Han, Y., Yang, F., Ma, G., et al. (2021). Experimental Investigation and Simulation of Crystallographic Orientations Evolution in a Cold-Rolled Ultra-thin Grain-Oriented Silicon Steel. *J. Magnetism Magn. Mater.* 517, 167385. doi:10.1016/j.jmmm.2020.167385

Zhang, S. H., and Li, Z. G. (2008). Experimental Research on Grain Orientation Evolution of Extruded Mg Alloy AZ31B Sheet during Uniaxial Tensile Deformation. *Amr* 32, 87–92. doi:10.4028/www.scientific.net/amr.32.87

Zhao, M., Mao, J., Ji, X., Feng, Y., and Liang, S. Y. (2021). Effect of Crystallographic Orientation on Residual Stress Induced in Micro-grinding. *Int. J. Adv. Manuf Technol.* 112 (5-6), 1271–1284. doi:10.1007/s00170-020-06329-z

Zhu, D., Feng, X., Xu, X., Yang, Z., Li, W., Yan, S., et al. (2020). Robotic Grinding of Complex Components: A Step towards Efficient and Intelligent Machining - Challenges, Solutions, and Applications. *Robotics and Computer-Integrated Manufacturing* 65, 101908. doi:10.1016/j.rcim.2019.101908

GLOSSARY

CO Crystallographic orientation

EBSD Electron back-scattered diffraction

FCC Face centered cubic

IPFs Inverse pole diagrams

ODF Orientation distribution function Notation

a_{ij} the constant and exponents

A the yield stress

B the coefficient of strain hardening

C the coefficient of strain rate hardening

m the thermal softening exponent

$\bar{M}^c$ the secant modulus

n the strain hardening exponent

S the fourth-order Eshelby tensor

T temperature

$\dot{T}$ temperature rate

T_0, T_m, T_w workpiece, melting and ambient temperature

δ the randomly distributed error terms

ε Plastic strain

$\dot{\varepsilon}$ Plastic strain rate

$\dot{\varepsilon}_0$ Material constant

$\dot{\varepsilon}_{ij}^c$ the strain rate in the crystal

$\prod$ the skew-symmetric fourth-order Eshelby tensor

τ_{CRSS} critical resolved shear stress

Ω_{ij}^c the rotation rate of the crystal

The Friction and Wear Behaviours of Inconel 718 Superalloys at Elevated Temperature

Zhibiao Xu[1], Zhijie Lu[1], Jun Zhang[2], Dexiang Li[1], Jihua Liu[1] and Chengxiong Lin[3]*

[1]School of Railway Tracks and Transportation, Wuyi University, Jiangmen, China, [2]AECC Aero Science and Technology Co.,Ltd., Metrology and Phys and Chem Testing Center, Chengdu, China, [3]Guangdong Key Lab of Medical Electronic Instruments and Polymer Material Products, National Engineering Research Center for Healthcare Devices, Guangdong Institute of Medical Instruments, Guangzhou, China

Machine parts made of nickel-based alloys usually work in high-temperature service environments such as aircraft turbines. The mechanical properties and antioxidant properties of materials tend to be reduced at high temperatures. Therefore, it is of great practical significance to reveal the wear mechanisms of materials at different temperatures. In the present investigation, the tribological behaviour of an Inconel 718 superalloy at different temperatures was investigated. First, the coefficient of friction curves obtained under different test conditions were analysed in detail to illustrate the dynamic change process of friction at high temperature. Next, the morphology of the wear surface, surface morphology of friction pairs and material transfer during friction were analysed via scanning electron microscopy 3D morphology and energy dispersive spectroscopy measurements to reveal the wear mechanisms of materials in a high-temperature environment. Finally, the microstructure of the cross section of the wear tracks was analysed by using optical microscopy electron back-scattered diffraction etc., to clarify the mechanisms of crack initiation and material removal. The results show that the friction properties of the Inconel 718 superalloy have differences at different test temperatures. Although increasing the test temperature does not necessarily aggravate the wear of the material, the oxidation of the wear surface during the friction process significantly increases. In addition, when the contact load increases, the thickness of the oxide layer and wear of the material simultaneously increase.

Keywords: Inconel 718 superalloy, friction behaviours, wear mechanism, elevated temperature, EBSD

INTRODUCTION

High-temperature alloys are materials with excellent strength, creep resistance and fatigue resistance at working temperatures above 600°C (Reed, 2008). A nickel-based superalloy is a preferred material with excellent mechanical capability and mechanical performance when it needs long service in harsh environments such as high-temperature and high-pressure situations (Pollock and Tin, 2006; González-Fernández et al., 2012; Zheng et al., 2012). However, because the material has long been serving under high temperature and harsh conditions, the actual service life of components is much lower than the design life in practical engineering applications (Mazur et al., 2005; Vardar and Ekerim, 2007). In addition, the material surface damage caused by friction, especially the wear damage under high temperature conditions, causes the early failure of

TABLE 1 | The primary chemical compositions of Inconel 718 (wt%).

C	Cr	Ni	Mo	Al	Ti	(Nb + Ta)	Fe
0.02–0.08	17.00–21.00	50.00–55.00	2.80–3.30	0.40–0.60	0.9–1.15	5.00–5.50	Balance

FIGURE 1 | Metallurgical structure of Inconel718: **(A)** 100X; **(B)** 500X.
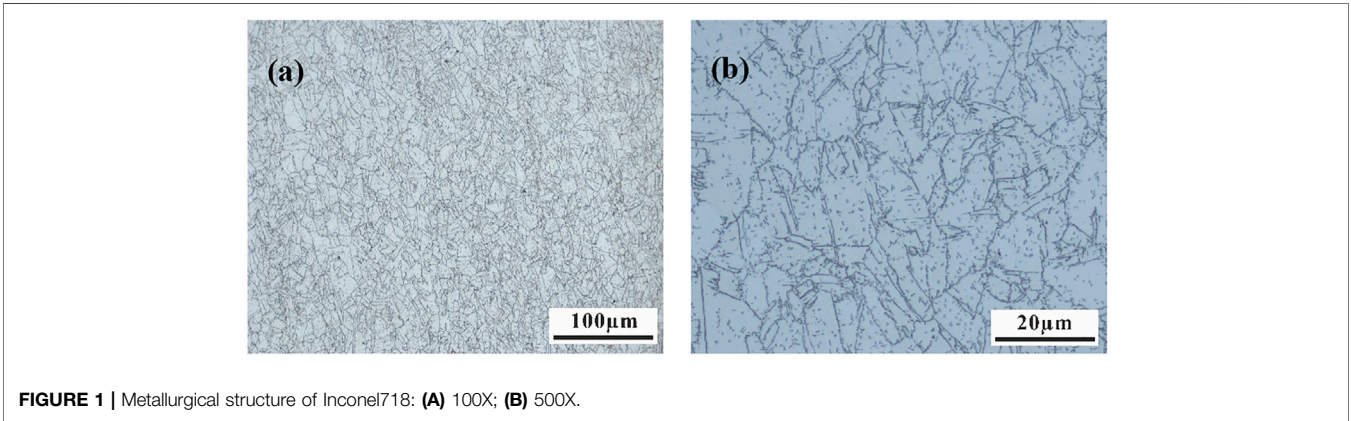
components (Laguna-Camacho et al., 2016). The early fracture and failure of these components seriously restrict the service safety of the equipment. For example, when an aero engine serves in a high-temperature environment for a long time, the turbine and blades of the engine are prone to damage due to fretting wear and fretting fatigue (Lavella and Botto, 2019). Thus, accidents and exposed hidden dangers can hinder passenger safety and the development of the national economy. Therefore, it has great practical significance to reveal the wear mechanisms of materials at different temperatures. In previous studies, many researchers have investigated the mechanical properties of nickel-based superalloys, e.g., the influence of high temperature on the

microstructure of materials (Lu et al., 2013; Deng et al., 2015; An et al., 2019; Gao et al., 2019). Liu (Lu et al., 2013) studied the microstructure, tension and stress rupture properties of GH4169 superalloys after long-term thermal exposure. These authors found that the tensile strength at room temperature and 650°C slowly decreased and the stress rupture life remarkably decreased with increasing thermal exposure time. An (An et al., 2019) investigated the evolution of the microstructures and properties of a GH4169 superalloy during high-temperature processing. These researchers found that superalloys decreased the tensile strength and yield strength and increased the ductility with increasing temperature and time. Due to strengthening, precipitates such as the γ' and γ'' phases in

FIGURE 2 | Testing device: **(A)** UMT-TriboLab; **(B)** schematic diagram.
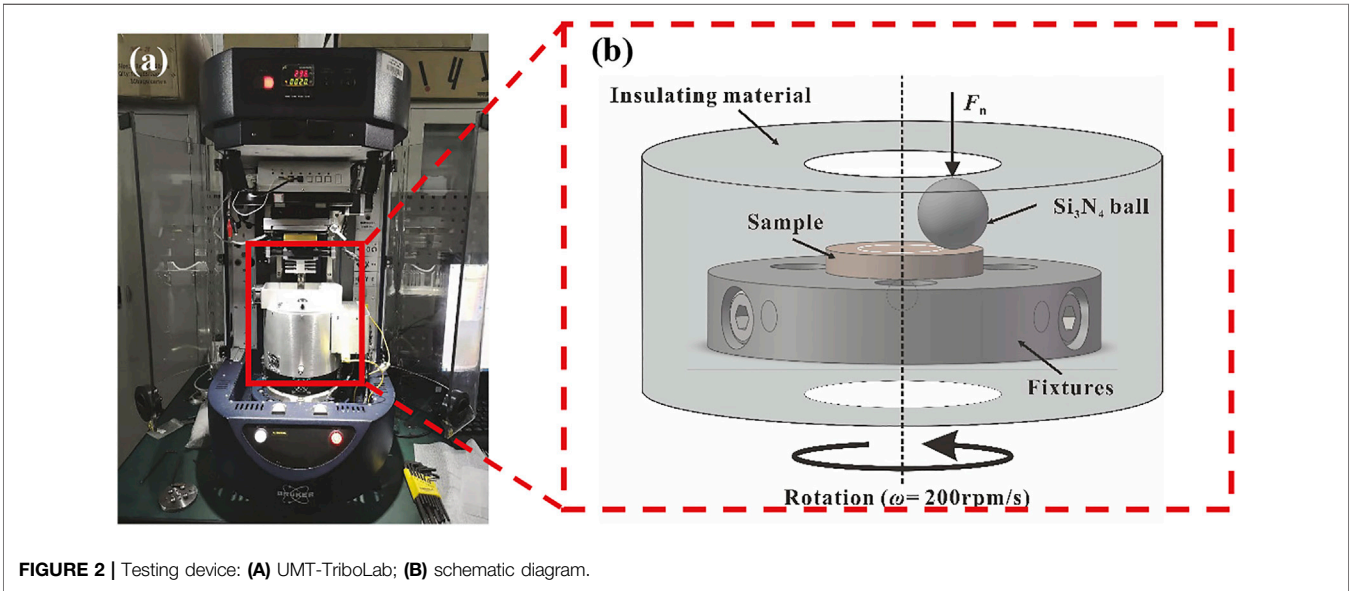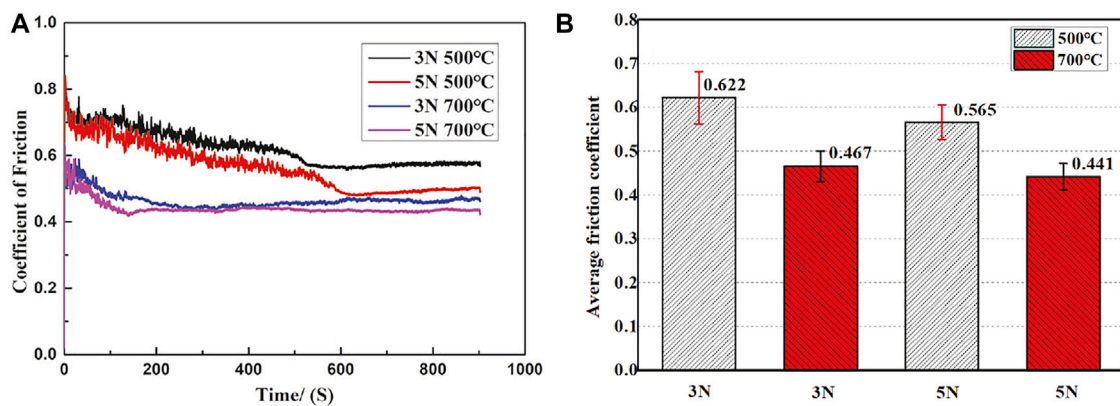
FIGURE 3 | The coefficient of frictional curves and average friction coefficient under different conditions during the tribological tests: **(A)** coefficient of friction curves; **(B)** average friction coefficient.
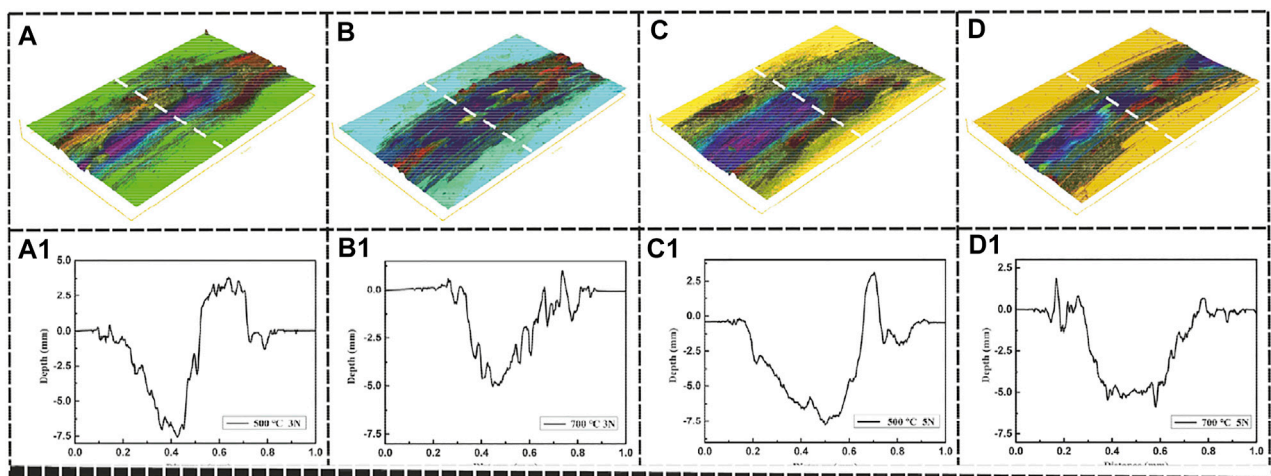

FIGURE 4 | 3D morphology and 2D profile of worm surface: **(A)**, (a1):F_n = 3N, T = 500°C; **(B)**, (b1): F_n = 3N, T = 700°C; **(C)**, (c1): F_n = 5N, T = 500°C; **(D)**, (d1): F_n = 5N, T = 700°C.

the grains and carbides in the grain boundaries gradually dissolve in the matrix. Other researchers have studied the fatigue and mechanical properties of superalloys from the viewpoint of high-temperature creep (Lund and Nix, 1976; Yeh et al., 2011; Chen et al., 2016; Long et al., 2019). Chen et al. (2016) studied the low cycle fatigue and creep-fatigue interaction behaviour of the nickel-base superalloy GH4169 at an elevated temperature of 650°C. They concluded that creep and oxidation at high temperatures greatly affected the fatigue life, especially for long holding periods. The effect of temperature on the wear mechanism of materials is also a focus of researchers (Günen, 2020; Li et al., 2020; Döleker et al., 2021). Zhen (Döleker et al., 2021) studied the influence of the test temperature on the tribological properties of nickel-based alloys. Through observation and analysis, the mechanism of friction wear was discussed. These scholars found that the composite had a good lubrication effect in a wide temperature

range of 25–800°C. Ali Günen (2020) used a ball-on-disk tribometer under dry sliding conditions at temperatures of 25°C, 400°C, and 750°C, and the high-temperature dry sliding wear mechanism of Inconel 718 was investigated. These investigators thought that two-body abrasion was the effective wear mechanism in the superalloy, and the wear increased when the temperature increased. However, fewer researchers have investigated the effects of temperature on its wear mechanism from the viewpoint of microstructural evolution.

Inconel 718 is a precipitation-reinforced superalloy (Li et al., 2019) that is widely used in aerospace applications, the nuclear power industry and national defence technology due to its good high-temperature structural stability, oxidation resistance, and excellent fatigue and creep resistance (Chen et al., 2015; Lin et al., 2015). Therefore, the microstructure evolution was examined to explore the
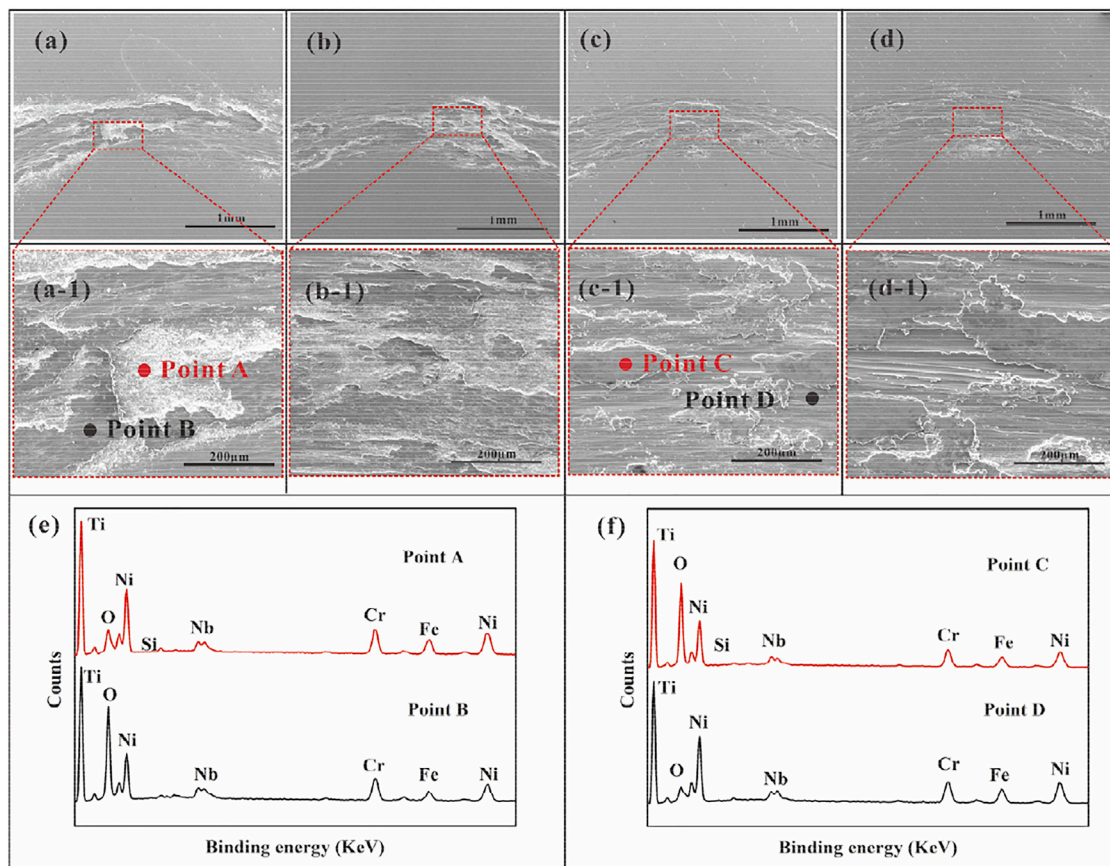
FIGURE 5 | 2D profile of worn surface.
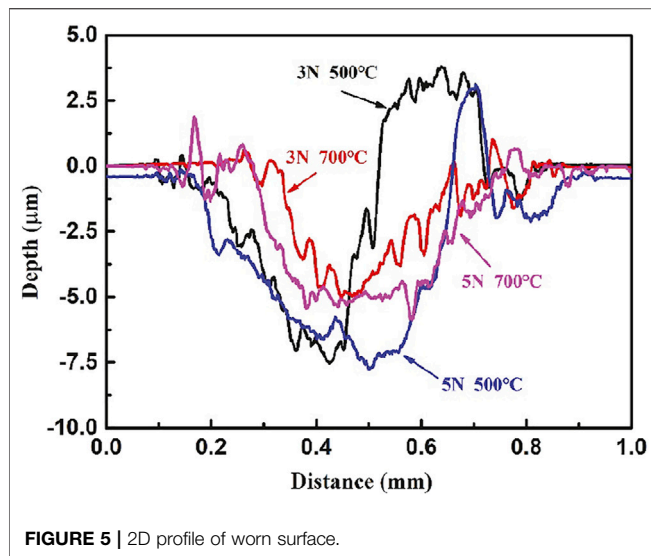
effect of temperature on the wear properties of the Inconel 718 superalloy. This approach can effectively reveal the wear mechanism of materials in different temperature

environments and ultimately provide scientific guidance to improve their service life at high temperatures.

MATERIAL AND METHODS

In the present study, the blades of assembled turbines are often coated with ceramic coatings. The primary chemical compositions of the Inconel 718 superalloy are listed in **Table 1**. The chemical compositions of the material are within the standard. The metallurgical structure of the material is shown in **Figure 1**. The preparation of test materials and the test methods are described in Ref. (Xu et al., 2021). Namely, the high-temperature friction tests were examined on a rotating tribo-tester system (Bruker, UMT-TriboLab, United States) via a ball-to-plate contact mode. The testing device are shown in **Figure 2A**. By rotating the disk, motion between friction pairs can be realized. Friction tests were conducted for 15 min at test temperatures of 500°C and 700°C. A high-temperature friction test schematic diagram is shown in **Figure 2B**. The Inconel 718 superalloy specimen included a round plate with a diameter and height of $\Phi 20$ and 5 mm, respectively. A Si_3N_4 ball with a diameter of
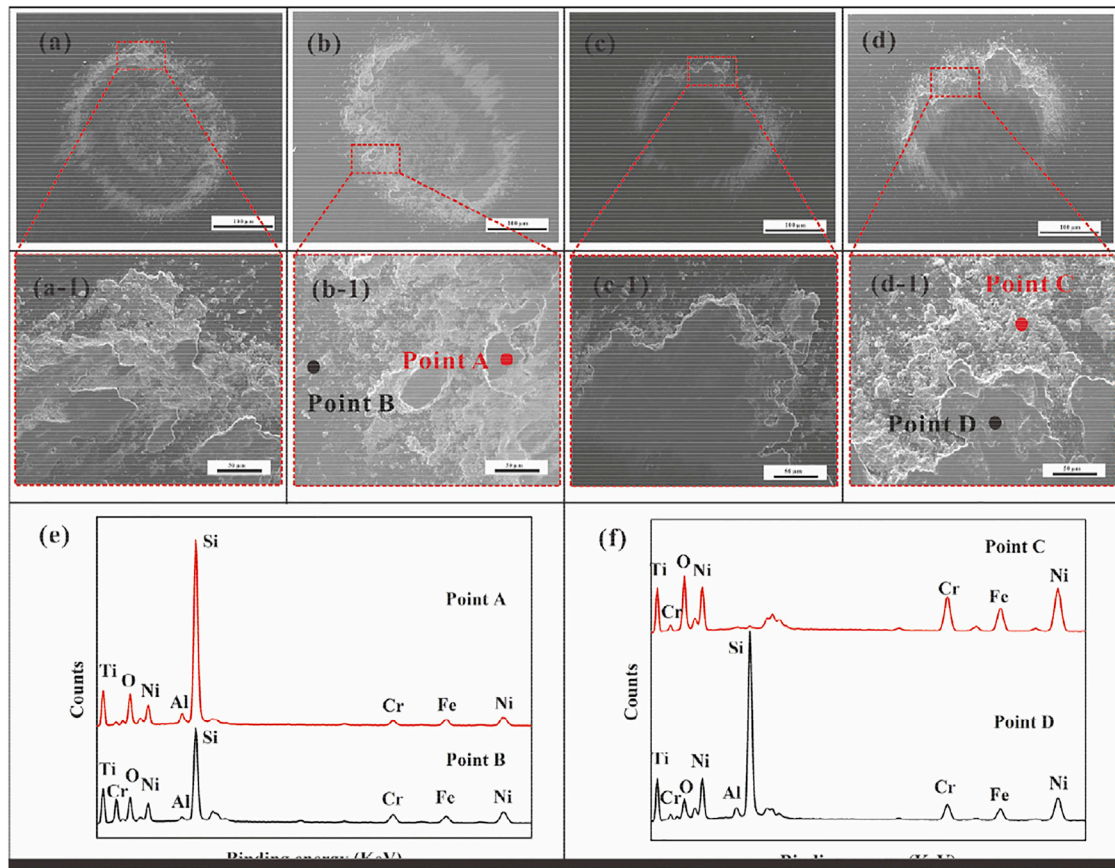

FIGURE 6 | SEM picture of worn surface: **(A)**: F_n = 3N, T = 500°C; **(B)**: F_n = 5N, T = 500°C; **(C)**: F_n = 3N, T = 700°C; **(D)**: F_n = 5N, T = 700°C.

FIGURE 7 | SEM images and EDS analysis of the wear scars on the counterpart Si_3N_4 ball under different conditions: **(A)**: 3N, 500°C; **(B)**: 5N, 500°C; **(C)**: 3N, 700°C; **(D)**: 5N, 700°C; **(E) (F)**: the element content map of EDS.

9 mm was selected. In the tests, the wear track diameter is Φ10 mm. The rate of rotation (ω) was selected to be 200 rpm. The normal loads were selected to be 3 and 5 N, which corresponded to maximum contact stresses of 801 and 950 MPa, respectively.

RESULTS AND DISCUSSION

Tribological Behaviours

In the high-temperature friction test, the coefficient of friction (COF) curve during the test was recorded in real time. An analysis of the value and change in COF can reveal the mechanism of friction and wear. The COF curves under different test conditions are shown in **Figure 3**. From **Figure 3A**, the COF curve progresses through three typical stages: 1) In the initial stage, the COF curve sharply rises. With the beginning of the high-temperature friction test, the contact pair is in direct contact with the matrix, and the typical two-body contact causes a sharp increase in friction coefficient. 2) In the decreasing stage, when the test continues, the oxidized debris produced by friction and wear enters the contact zone. The two-body

contact model becomes a typical three-body contact model. The oxidized debris plays the role of lubrication and effectively improves the state of dry friction. Thus, the COF slowly decreases. 3) In the stabilization stage, the COF value is stable, and the friction experiment enters a stable period. **Figure 3A** also shows that the COF curve requires a shorter time to enter the stabilization stage at 700°C. A possible reason is that compared with those at 500°C, the mechanical properties of the material were reduced, and it was easier to yield at 700°C. In other words, it was easier to produce oxidized debris in the process of friction and wear when the material became soft. Therefore, the friction experiment can more quickly transition from the second stage to the third stage. Combined with **Figures 3(A,B)**, the average COF in the friction process is lower when the temperature is higher. This phenomenon occurred in the friction tests regardless of the normal load at 3 and 5 N. In addition, at the same temperature, a high normal load, which corresponded to a lower average COF, was observed. These phenomena will be discussed in the analysis of surface wear tracks. Further analysis will be combined with the COF and evolution of surface wear to reveal the wear mechanism of the 718 alloy at different temperatures.
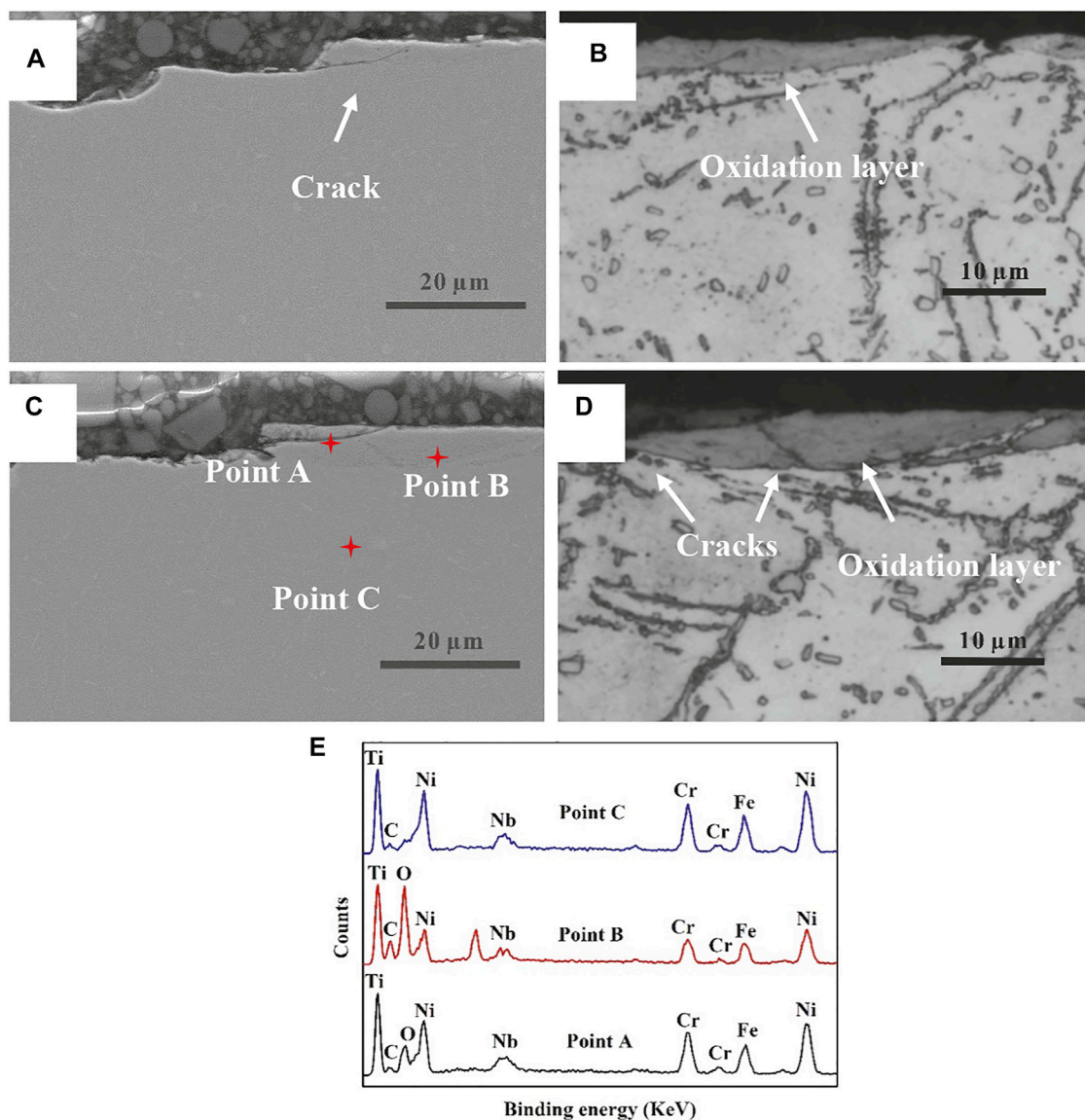
FIGURE 8 | SEM picture of the cross-section (T = 500°C): **(A)**,**(B)** F_n = 3N; **(C)**,**(D)** F_n = 5N; **(E)** eds-point.

Analysis of Worn Surfaces

After the high-temperature friction experiments, the morphology and 3D profile of the wear surface are shown in **Figure 4**. The wear surface of the Inconel 718 alloy at 500°C was more irregular than that at 700°C. However, under identical test temperature conditions, the wear of the material increased with increasing normal load. By more intuitively comparing the wear tracks under different conditions, **Figure 5** shows the 2D profile of the wear surface. As shown in **Figure 5**, both depth and width of the wear tracks were larger at 500°C than at 700°C under identical normal load conditions. Thus, the wear of the material is more serious at 500°C. Combined with the results of **Figure 4** and **Figure 5**, the damage states of the wear surface at the two temperatures were not identical. At 500°C, the main worn

mechanisms were abrasive wear, stripping and oxidative wear. At 700°C, there was mainly adhesive wear, oxidative wear and thermal creep of the materials. Therefore, the wear was more serious, and the wear tracks were more irregular when the temperature was 500°C.

To reveal the wear mechanisms, after the friction test, the worn surface was observed by scanning electron microscopy (SEM), as shown in **Figure 6**. In **Figures 6A,B**, the wear surface of the specimens was irregular at 500°C. The wear damage of tracks was also uneven. As shown in **Figure 6(A-1)** and **Figure 6(B-1)**, some areas have severe spalling, and other areas show the characteristics of abrasive wear. **Figure 6(A-1)** also presents the characteristics of adhesive wear. Therefore, with an increase in normal load from 3 to 5 N, the adhesive wear in the wear mechanism is more obvious.
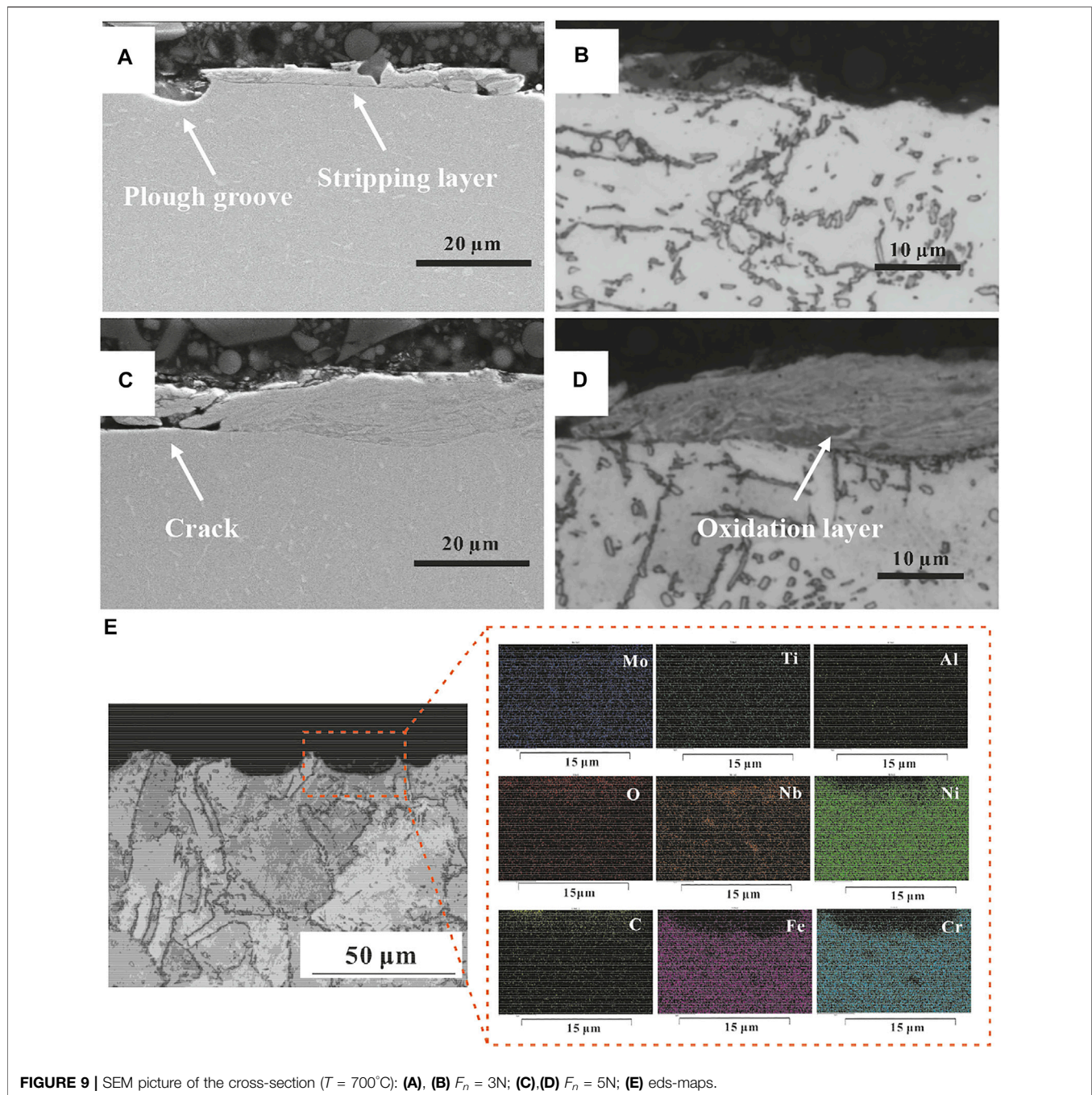
FIGURE 9 | SEM picture of the cross-section (T = 700°C): **(A)**, **(B)** F_n = 3N; **(C)**,**(D)** F_n = 5N; **(E)** eds-maps.

The energy dispersive spectroscopy (EDS) testing results in **Figure 6A** show that O was present on the surface, as shown in **Figure 6E**. This result indicates that oxidation wear occurred during friction, and the peeling debris was oxidized. However, the width of the wear tracks decreased but was more well distributed at 700°C. The wear surface also exhibited abrasive wear, but the main wear mechanism was adhesive wear. The EDS testing results showed that the oxidation reaction also occurred on the worn surface, as shown in **Figure 6F**. Moreover, the surface of the material shows high-temperature creep under the action of a contact load. Comparing the two-dimensional depth in **Figure 5**, the depth of the wear marks is deeper at 500°C than that under identical conditions at 700°C. The main reason for this difference may be temperature. The hardness of the material decreases at 700°C compared to that at 500°C. The softer material has better plastic deformation, and it is more difficult to produce cracks and surface peeling during friction. Moreover, the abrasive wear of the material is more serious at 500°C, which leads to an increase in wear. As a result, when the friction test was conducted at 700°C, the wear of the material
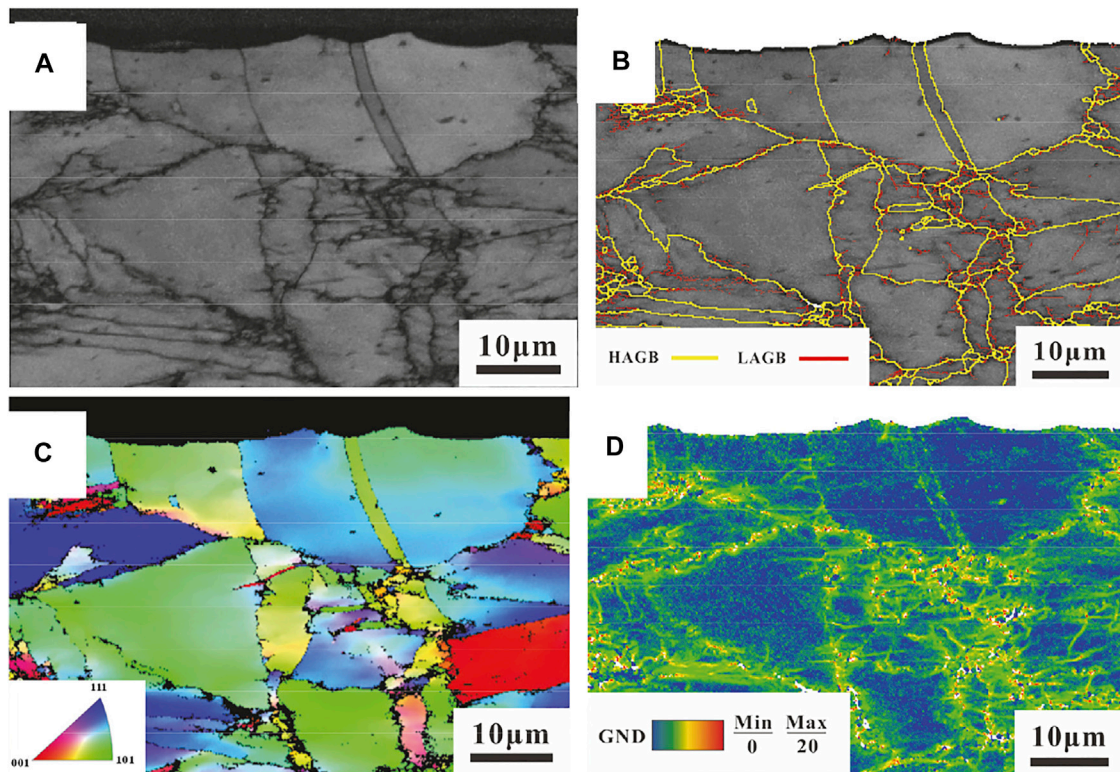
FIGURE 10 | The EBSD results of cross section of worn surface at 500°C: (F_n = 5N: **(A) (B)** EBSD band contrast and phase map; **(C)** Inverse pole figure (IPF) map; **(D)** Geometrically necessary dislocation (GND) map).

slowed compared to that at 500°C. The EDS test results show that Si was found at the wear surface at both temperatures, which indicates material transfer between the sample and the friction pairs. A further analysis of the material transfer will be presented in the next section.

Figure 7 shows the wear morphology of the friction pairs under different test conditions. Due to the point contact mode between the friction pairs and the test sample, the wear spot of the friction ball presents an irregular ellipse. As shown in **Figure 7**, the morphology of the wear spot is typical of dry friction. Thus, there is an obvious phenomenon of material transfer on the surface. Accordingly, the EDS results also demonstrate that the alloy material was transferred to the surface of the friction pairs during the friction process. In addition, the results show that the normal load has no obvious effect on the size of the wear spot. However, the temperature directly affects the wear spot size of the friction ball. At 500°C, there is a larger area of wear spot for the friction pairs. However, the material transfer in the wear spot is more dispersed. This is not like a phenomenon of bulk accumulation at 700°C. The main reason is that the hardness of the matrix material at 500°C is high. The main wear mechanism is abrasive wear. Abrasive wear leads to the dispersion of minute wear debris. At 700°C, the matrix material becomes soft. The abrasion wear decreases with increasing adhesion wear. Therefore, the morphology of wear spots mainly shows characteristics of adhesion wear.

Analysis of the Cross Section

The analysis of the cross section of wear tracks mainly clarifies the microstructure evolution and crack initiation mechanism during friction. At 500°C, the morphology of the cross section under different contact loads is shown in **Figure 8**. In **Figures 8(A–D)**, the groove formed by wear can be found on the surface layer of the sample. Some cracks can also be found in the surface layer. The cracks were distributed at different depths on the surface layer of the sample, as shown in **Figure 8C**. The EDS tests were performed on different depth surface layers of the sample in **Figure 8(C)**, which shows that the presence of O elements was detected in the surface layer that formed the crack. Thus, it can be speculated that the crack layer is an oxide layer that formed on the sample surface during high-temperature friction. The metallurgical structure of the cross section was prepared using a corrosion solution (copper sulfate pentahydrate + hydrochloric acid + alcohol), as shown in **Figures 8B,D**. The metallurgical image results verified the previous calculation that the sample surface contained an oxide layer. The surface of the material was subjected to the combined action of the normal stress and friction shear stress, which initiated and propagated microcracks. Simultaneously, oxidation of the sample surface occurred due to the high temperature and dry friction action. When the cracks propagated and connected with one another, the oxidation layer stripped the sample surface and eventually formed oxidation debris. The oxidation layer thickened with increasing normal
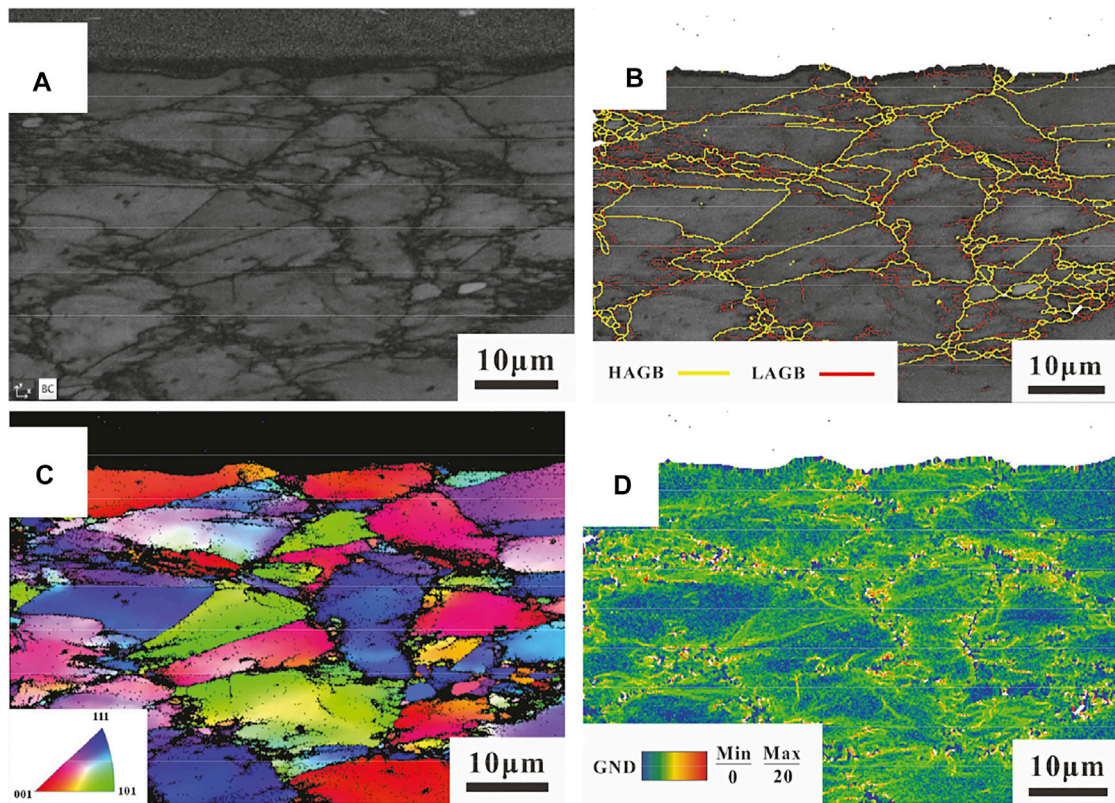
FIGURE 11 | The EBSD results of cross section of worn surface at 700°C.

loads. Thus, the thickness of the oxidation layer is affected by the normal loads. The high normal load acts on the sample surface and produces a higher contact stress and a deeper influence depth. The sample surface has a thicker oxidation layer.

These phenomena can also be found at 700°C. The difference is that the thickness of the oxidation layer significantly increases at higher temperatures, as shown in **Figure 9**, possibly because the rate of oxidation is faster on the material surface. Therefore, the material surface oxidation increases during the same friction time. Another reason is that the material becomes softer at 700°C than at 500°C, and the depth affected by the contact stress increases, which thickens the oxidation layer of the sample surface. The EDS map analysis results of the cross section are shown in **Figure 9**(E). The Ni, Fe, and Cr contents are higher in the matrix material. There is hardly any O present. However, a large amount of O can be found on the surface of the sample. This result validates the previous inference that oxide layers appeared on the surface.

EBSD Analyses
The EBSD results of the cross section at different temperatures are shown in **Figure 10** and **Figure 11**. **Figure 10** shows the cross section of the wear track when the contact load $F_n = 5$ N and the test temperature is 500°C. Many grains are observed in **Figure 10(A)** with dislocation accumulation at the grain boundaries. Additionally, some twins were found in the grain.

The appearance of twins indicates the stress concentration in the contact area. This result was mainly caused by the stress deformation of the material. **Figure 10(B)** shows that in the region of the cross section, high-angle grain boundaries (HAGBs) and angles greater than 10° (the yellow lines) dominate. Low-angle grain boundaries (LAGBs, with angles of 0–10°) form the subgrain boundaries by dislocation pile-up near the HAGBs. Geometrically necessary dislocations (GNDs) also confirm that dislocations accumulate near the grain boundaries. In **Figure 10D**, the GND value at the grain boundary is higher, especially at the location where the LAGB was formed. When the test temperature increases to 700°C, the EBSD result of the cross section is shown in **Figure 11**. Many dislocation cell structures were formed due to the generation and accumulation of dislocations, as seen in the subgrains in **Figure 11A**. The LAGB significantly increases at 500 °C, as shown in **Figure 11B**. Significant recrystallization occurs in the microstructure of the material at higher temperatures. The phenomena correspond to the previous results of wear analysis. Although the test temperature increases, the wear of the material does not increase. The main reason is that the material is softer at higher temperatures, so the material deforms more at identical contact loads. Finally, severe recrystallization occurs at 700°C. Thus, the recrystallization of the material is mainly affected by the temperature. The action of contact stress mainly produces twin crystals and dislocations. The

dislocations accumulate near the HAGBs, forming LAGBs (subgrain boundaries). The properties change due to the formation of cell structures in the microstructures of the material. Finally, the material effectively reduces wear damage through deformation.

(F_n = 5N:(a) (b) EBSD band contrast and phase map; (c) Inverse pole figure (IPF) map; 4) Geometrically necessary dislocation (GND) map;

CONCLUSION

In this study, the wear mechanisms and tribological behaviours of Inconel 718 against Si_3N_4 balls at different temperatures were investigated in detail. The conclusions are summarized as follows:

1. The wear mechanisms of the Inconel 718 superalloy materials are different at elevated temperatures. The wear mechanisms mainly include abrasive wear, oxidation wear and delamination wear at 500°C. However, the adhesive wear and oxidation wear became dominant in the wear mechanisms at 700°C. An oxide layer with a lubricating function appeared on the surface of the material under high-temperature conditions. Therefore, when the test temperature increases, the wear of the material decreases.
2. With increasing test temperature, the oxide layer significantly thickened. With increasing normal load, the oxide layer at identical test temperatures also thickened.

3. The microstructure of the material presents different changes under identical contact stress at different temperatures. At 500°C, the microstructure consists mainly of a twin structure and HAGBs. At 700°C, it mainly consists of the dislocation structure of LAGBs and dislocation cells.

DATA AVAILABILITY STATEMENT

The original contributions presented in the study are included in the article/Supplementary Material, further inquiries can be directed to the corresponding author.

AUTHOR CONTRIBUTIONS

ZX: Experiment, Investigation, Method, Writing—original draft, Writing—review and editing, Funding acquisition. ZL: Experiment, Data handing, Formal analysis, Investigation. JZ: Formal analysis, Method. DL: Formal analysis, Investigation. JL: Investigation, Supervision. CL: Revision manuscript, Guidance, Funding acquisition.

FUNDING

REFERENCES

An, X. L., Zhang, B., Chu, C. L., Zhou, L., and Chu, P. K. (2019). Evolution of Microstructures and Properties of the GH4169 Superalloy during Short-Term and High-Temperature Processing. *Mater. Sci. Eng. A* 744, 255–266. doi:10.1016/j.msea.2018.12.019

Chen, F., Liu, J., Ou, H., Lu, B., Cui, Z., and Long, H. (2015). Flow Characteristics and Intrinsic Workability of IN718 Superalloy. *Mater. Sci. Eng. A* 642, 279–287. doi:10.1016/j.msea.2015.06.093

Chen, G., Zhang, Y., Xu, D. K., Lin, Y. C., and Chen, X. (2016). Low Cycle Fatigue and Creep-Fatigue Interaction Behavior of Nickel-Base Superalloy GH4169 at Elevated Temperature of 650 °C. *Mater. Sci. Eng. A* 655, 175–182. doi:10.1016/j.msea.2015.12.096

Deng, D.-W., Wang, C.-G., Liu, Q.-Q., and Niu, T.-T. (2015). Effect of Standard Heat Treatment on Microstructure and Properties of Borided Inconel 718. *Trans. Nonferrous Met. Soc. China* 25 (2), 437–443. doi:10.1016/s1003-6326(15)63621-4

Döleker, K. M., Erdogan, A., Yener, T., Karaoglanlı, A. C., Uzun, O., Gök, M. S., et al. (2021). Enhancing the Wear and Oxidation Behaviors of the Inconel 718 by Low Temperature Aluminizing. *Surf. Coat. Technol.* 412, 127069. doi:10.1016/j.surfcoat.2021.127069

Gao, Y., Zhang, D., Cao, M., Chen, R., Feng, Z., Poprawe, R., et al. (2019). Effect of δ Phase on High Temperature Mechanical Performances of Inconel 718 Fabricated with SLM Process. *Mater. Sci. Eng. A* 767, 138327. doi:10.1016/j.msea.2019.138327

González-Fernández, L., Del Campo, L., Pérez-Sáez, R. B., and Tello, M. J. (2012). Normal Spectral Emittance of Inconel 718 Aeronautical alloy Coated with Yttria Stabilized Zirconia Films. *J. alloys Compd.* 513, 101–106. doi:10.1016/j.jallcom.2011.09.097

Günen, A. (2020). Properties and High Temperature Dry Sliding Wear Behavior of Boronized Inconel 718. *Metallurgical Mater. Trans. A* 51 (2), 927–939. doi:10.1007/s11661-019-05577-3

Laguna-Camacho, J. R., Villagrán-Villegas, L. Y., Martínez-García, H., Juárez-Morales, G., Cruz-Orduña, M. I., Vite-Torres, M., et al. (2016). A Study of the Wear Damage on Gas Turbine Blades. *Eng. Fail. Anal.* 61, 88–99. doi:10.1016/j.engfailanal.2015.10.002

Lavella, M., and Botto, D. (2019). Fretting Wear of alloy Steels at the Blade Tip of Steam Turbines. *Wear* 426-427, 735–740. doi:10.1016/j.wear.2019.01.039

Li, L., He, K., Sun, S., Yang, W., Yue, Z., and Wan, H. (2020). High-Temperature Friction and Wear Features of Nickel-Based Single Crystal Superalloy. *Tribology Lett.* 68 (1), 1–12. doi:10.1007/s11249-020-1266-4

Li, X., Shi, J. J., Cao, G. H., Russell, A. M., Zhou, Z. J., Li, C. P., et al. (2019). Improved Plasticity of Inconel 718 Superalloy Fabricated by Selective Laser Melting through a Novel Heat Treatment Process. *Mater. Des.* 180, 107915. doi:10.1016/j.matdes.2019.107915

Lin, Y. C., Li, K.-K., Li, H.-B., Chen, J., Chen, X.-M., and Wen, D.-X. (2015). New Constitutive Model for High-Temperature Deformation Behavior of Inconel 718 Superalloy. *Mater. Des.* 74, 108–118. doi:10.1016/j.matdes.2015.03.001

Long, H., Mao, S., Liu, Y., Wei, H., Deng, Q., Chen, Y., et al. (2019). Effect of Pre-Straining Treatment on High Temperature Creep Behavior of Ni-Based Single crystal Superalloys. *Mater. Des.* 167, 107633. doi:10.1016/j.matdes.2019.107633

Lu, X. D., Du, J. H., and Deng, Q. (2013). High Temperature Structure Stability of GH4169 Superalloy. *Mater. Sci. Eng. A* 559, 623–628. doi:10.1016/j.msea.2012.09.001

Lund, R. W., and Nix, W. D. (1976). High Temperature Creep of Ni-20Cr-2ThO2 Single Crystals. *Acta Metallurgica* 245, 469–481. doi:10.1016/0001-6160(76)90068-7

Mazur, Z., Luna-Ramírez, A., Juárez-Islas, J. A., and Campos-Amezcua, A. (2005). Failure Analysis of a Gas Turbine Blade Made of Inconel 738LC Alloy. *Eng. Fail. Anal.* 12 (3), 474–486. doi:10.1016/j.engfailanal.2004.10.002

Pollock, T. M., and Tin, S. (2006). Nickel-Based Superalloys for Advanced Turbine Engines: Chemistry, Microstructure and Properties. *J. propulsion Power* 22 (2), 361–374. doi:10.2514/1.18239

Reed, R. C. (2008). *The Superalloys: Fundamentals and Applications.* Cambridge: Cambridge University Press.

Vardar, N., and Ekerim, A. (2007). Failure Analysis of Gas Turbine Blades in a Thermal Power Plant. *Eng. Fail. Anal.* 14 (4), 743–749. doi:10.1016/j.engfailanal.2006.06.001

Xu, Z., Huang, Z., Zhang, J., Xu, X., Li, P., Su, F., et al. (2021). Tribological Behaviors and Microstructure Evolution of Inconel 718 Superalloy at Mid-High Temperature. *J. Mater. Res. Technol.* 14, 2174–2184. doi:10.1016/j.jmrt.2021.07.102

Yeh, A.-C., Lu, K.-W., Kuo, C.-M., Bor, H.-Y., and Wei, C.-N. (2011). Effect of Serrated Grain Boundaries on the Creep Property of Inconel 718 Superalloy. *Mater. Sci. Eng. A* 530, 525–529. doi:10.1016/j.msea.2011.10.014

Zheng, L., Schmitz, G., Meng, Y., Chellali, R., and Schlesiger, R. (2012). Mechanism of Intermediate Temperature Embrittlement of Ni and Ni-Based Superalloys. *Crit. Rev. Solid State. Mater. Sci.* 37 (3), 181–214. doi:10.1080/10408436.2011.613492

Check for
updates

Effect of Age on Mechanical Properties of Human Tooth Enamel

Xia Jing[1]*, Yang Zhipeng[1], Liu Kaiyong[1], Lu Junjie[1], He Xinyuan[1], Zhang Juan[2]* and Fan Yujie[1]*

[1]School of Mechanical Engineering, Jiangsu University of Science and Technology, Zhenjiang, China, [2]Zhenjiang Stomatological Hospital, Zhenjiang, China

Dental health is closely related with people's quality of life. Teeth are subject to different problems and risks over time. Therefore, studying the influence of age on mechanical properties of tooth enamel is of considerable importance. In this study, the collected human teeth were divided into four groups: deciduous (aged 6–12 years), juvenile permanent (aged 14–20 years), young adult permanent (aged 25–45 years), and older adult permanent (aged over 60 years) teeth. The mechanical properties of tooth enamel of all age groups were evaluated using a microhardness tester and laser confocal microscope. The results revealed that hardness of the deciduous teeth was much lower than that of permanent teeth. Hardness of young adult permanent teeth was the highest, followed by that of the older adult and juvenile permanent teeth. Deciduous teeth enamel had the highest fracture toughness, followed by that of young adult, juvenile, and older adult permanent teeth. The different chemical compositions and microstructures of enamel at different age groups resulted in the significant differences in mechanical properties. This research accords with the strategic requirement of improving peoples' dental health, and its results are noteworthy in developing specific protocols for dental hygiene and clinical prevention.

Keywords: age, dental enamel, fracture toughness, mechanical propertie, biomaterials

INTRODUCTION

Teeth are among the most critical oral organs in the human body. In addition to cutting, biting, and chewing food to provide energy, they also ensure correct enunciation and good appearance. If the teeth do not develop or are not maintained properly, tooth loss due to decay occurs, which affects food intake and causes the lips and cheeks to lose support and sag, deforming the face. Thus, dental health is closely related to people's quality of life.

The teeth are mainly constituted of dentine, with the outer layer comprising enamel (in the crown part) and cementum (in the root part). The enamel covers the outer layer of the crown and protects the inner dentine and pulp against damage from external loads. However, as an individual advances in age, the mechanical properties of enamel can change due to long-term exposure to the complex oral environment. Therefore, studying the influence of ageing on the mechanical properties of enamel for clinical treatment is of great importance.

Tooth enamel is the hardest mineralized substance in the human body. It has excellent mechanical properties and plays a key long-term role in the complex oral environment. Enamel is composed of 96–97% inorganic minerals and a small proportion of organic matter and water. The inorganic materials are mainly hydroxyapatite crystals but also contain a small amount of calcium fluoride and calcium phosphate (Robinson et al., 2000; Simmer and Hu, 2001; Beniash et al., 2009). Nanoscale

hexagonal hydroxyapatite crystals are the basic constituent units of enamel. These long strips of hydroxyapatite particles are bonded with proteins to form the glaze column and interstitial glaze by employing numerous arrangements and orientations (He and Swain, 2008; Pan et al., 2008; Moradian-Oldak, 2012). The column is shaped like a keychain, and the hydroxyapatite particles that constitute the enamel pillar are arranged longitudinally, perpendicular to the enamel occlusal surface. The hydroxyapatite particles in the enamel interstitial region are deflected in orientation, which leads to a discontinuity of the enamel pillar and interstitium, thus forming a gap. This gap is called as enamel sheath and is rich in sheathlin known as ameloblastin and amelogenin (Zeichner-David et al., 1997). Moreover, the orientation of hydroxyapatite crystals on the occlusal surface and tooth enamel section differs as does the arrangement of inner and outer enamel, which results in a complex microscopic structure of tooth enamel and differences in the mechanical properties of tooth enamel at distinct positions (Cui and Ge, 2007; Shieh et al., 2011; Niu et al., 2017; Shen et al., 2020).

The mechanical properties and biological functions of enamel are not only attributed to its excellent structure but also to the effective combination of inorganic minerals and organic proteins. General materials will produce plastic damage close to atomic scale when impacted, thus showing very low fracture toughness (Li et al.,2022). According to the pull-shear chain model of proteins, under tensile stress, hard inorganic mineral crystals mainly bear tensile stress along the long axis, whereas soft organic protein layers mainly bear shear force (Ji and Gao, 2004). Tooth enamel wear entails the destruction of the interfacial protein bonds between hydroxyapatite crystals in nanofibers, which consumes considerable energy (Lei et al., 2020). Protein removal results in a reduction in fracture toughness of approximately 40% compared with a complete protein control. The loss of organic content reduces protein contribution to total fracture energy by more than 80%. This degradation manifests in the embrittlement of the unfractured bridging ligament and a subsequent reduction in fracture closure stress. Although the organic content of enamel is low, it is essential to enhance strength by promoting the formation of unbroken ligaments and enhancing enamel resilience (Yahyazadehfar and Dwayne, 2015). Concentrations of Mg and other minor ions on the surface of the microcrystalline layer (and adjacent media) also change systematically during the formation of human tooth enamel. This may affect the mineral phases and interactions of enamel matrix proteins and their degradation products with each other (Derocher et al., 2020). The water content in enamel can improve its fracture toughness and protect the surface from impact wear (Zheng et al., 2016). Compared with dehydrated enamel, hydrated enamel demonstrates superior wear resistance despite its lower hardness and higher coefficient of friction and sliding (Hua et al., 2019).
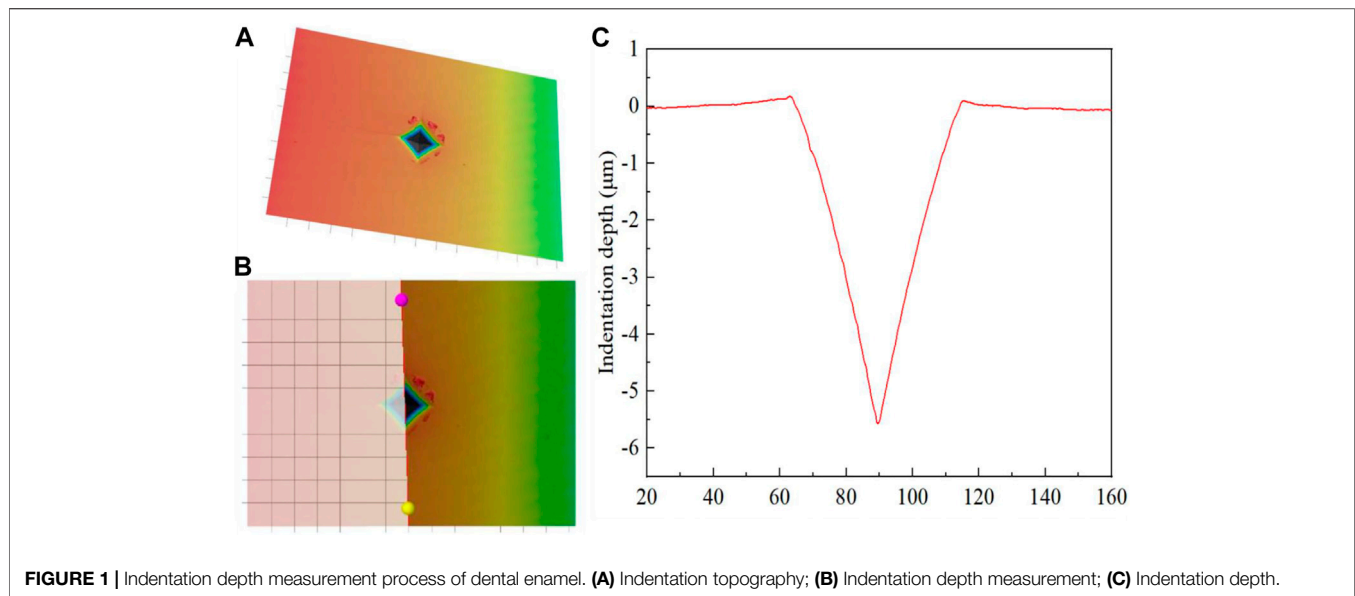
The mechanical properties of enamel, in addition to its microstructure and chemical composition, are also influenced by oral environmental factors such as pH and salivary lubrication (Galbany et al., 2014; Adhani, 2015; Antoine and Hillson, 2015).

After 1 min of adsorption in saliva, tooth enamel forms a dense protein membrane, which is the initial membrane of the tooth enamel surface and can effectively reduce tooth enamel wear (Zhang et al., 2013; Steiger-Ronay et al., 2020). The enamel wears more rapidly in citrate media than in artificial saliva. In conditions of citric acid erosion, the enamel surface forms a softened layer, and the enamel surface wear mechanism mainly manifests as adhesion peeling. The enamel surface is mainly ploughed and accompanied by peeling in the artificial saliva medium (Zheng et al., 2011). The hardness and elastic modulus of the enamel also decrease with pH (Barbour et al., 2010).

The oral environment as well as the microstructure and chemical components of the enamel change with age, which may lead to changes in their mechanical properties. However, most studies on the teeth of individuals from distinct age groups have focused on the correlation between age and dentine. Montoya et al., 2015 investigated the effects of age on dentine microstructure, hardness, and chemical composition, observing no significant difference in the tooth tube density or diameter, with the major difference exhibited in the occlusion rate of the dental tubule. Older dentine has a higher rate of dental tubule occlusion, thus leading to a higher mineral–collagen ratio. Thus, older dentine has higher hardness than younger dentine because of its higher mineral–collagen ratio. Mandra et al., 2020 discovered that the strength of the microshear bond between the dentine surface and composite resin adhesive decreased with age under different bonding systems, indicating a significant negative effect of ageing on the bonding strength of the dentine surface. Ryou et al. (2015) studied the effect of ageing on the mechanical properties of dentine, noting that the maximum bending stress and fracture energy of dentine decreased with age. The fracture toughness and fatigue strength of dentine in older adults was nearly 70% lower than in younger adults.

To date, few studies have investigated the age-related properties and the effects of age on enamel materials. Tooth and enamel rod sheath colours vary with age, and studies have revealed that the crystal gap and enamel rod sheath inhibit the reflection of lower dentin colour, with a tendency to scatter light from the surface to the deep layer. Young dental enamel rods are clear, but the number of crystal gaps and enamel rods decrease rapidly with age. The colour of the dentine is thus strongly reflected, resulting in a darker appearance (Miake et al., 2016). The thickness of enamel also begins to decrease from age 50 years onwards, and after 65 years, the amount of enamel is approximately one third less than that in younger people's teeth (Carvalho and Lussi, 2017). These reports have not discussed the effect of age on the mechanical properties of enamel or fully analysed the changes in the mechanical properties of human enamel throughout its life cycle.

In the present study, the mechanical properties of human enamel throughout its life cycle were examined. In accordance with human enamel's growth characteristics, its life cycle was divided into four parts: 1) the deciduous teeth group (aged 6–12 years), 2) juvenile permanent teeth group (aged 14–20 years), 3) young adult permanent teeth group (aged

FIGURE 1 | Indentation depth measurement process of dental enamel. **(A)** Indentation topography; **(B)** Indentation depth measurement; **(C)** Indentation depth.

25–45 years), and 4) older permanent teeth group (aged over 60 years). We investigated the mechanical properties of dental enamel at distinct ages. By using a microhardness tester and laser confocal scanning microscope and examining the Vickers hardness of the enamel surfaces at different ages, we studied the influence of age on enamel mechanical properties, providing strong support for further analysis of the connection between enamel microstructures and material performance.

MATERIAL AND METHODS

Sixteen molar teeth extracted from patients at Zhenjiang Stomatological Hospital were divided into deciduous teeth (aged 9–12 years), juvenile permanent teeth (aged 14–20 years), young adult permanent teeth (aged 25–45 years), and older adult permanent teeth (aged over 60 years) groups, with four teeth in each group. The collected teeth were soaked in deionised water and stored in a refrigerator at 4°C.

The dental inclusion criteria were as follows: 1) the teeth were third molars extracted due to orthodontics, periodontal disease, or trauma, or retained second deciduous molars and 2) crown was normal without caries. Written informed consent was obtained from all of the patients and their guardians.

For sample preparation, plaque and stones were first removed by sonication, and then the roots were partially removed (with the crown portion retained) using a handheld saw blade. Then, each sample was embedded in a soft plastic mould (25 mm × 18 mm) with resin, with the teeth occlusal surface faced downward. After solidification, the samples were polished successively with 400-, 800-, 1,500-, and 2,000-grit sandpapers in water cooling conditions and then polished successively with 5, 2.5, 1, and 0.5 μm water-soluble diamond polishing paste in water cooling conditions until the average surface roughness (R_a) was ≤0.1 μm. In order to reduce the

FIGURE 2 | Indentation topography diagram.
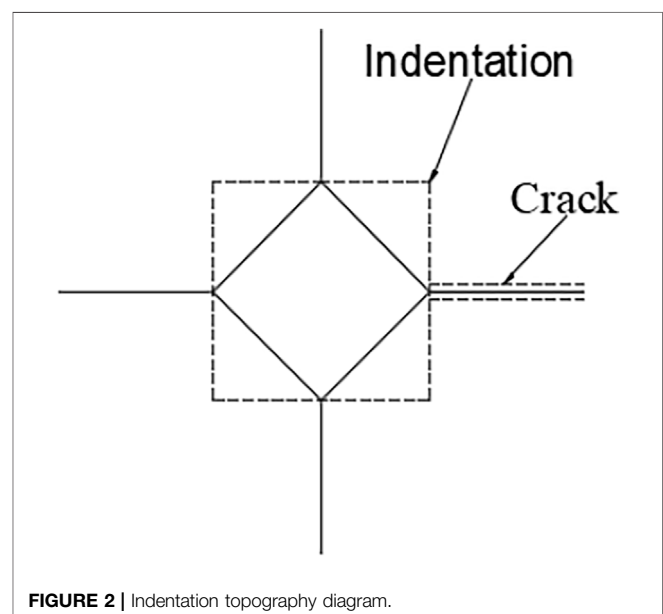
influence of enamel thickness on the experimental results, the thickness of enamel polishing was controlled between 0.2 and 0.3 mm.

First, a microhardness tester (HVS-1000AT/EOS100B, China) was used to load each sample surface with different loads (0.1, 0.5, 1, 2, 5, and 10 N). The loading time for each load was 15 s and the ambient temperature was 25°C. Next, their Vickers hardness was measured based on the indentation morphology. At each load, 2 values were measured for each of the 16 samples, yielding a total of 192 values. Data relating to the same age group and load were averaged.

After the Vickers hardness measurement was completed, the indentation morphology of each sample was observed using a

FIGURE 3 | Detection of hardness–load curves of tooth enamel at different age.

FIGURE 4 | Comparisons of mean indentation depth of tooth enamel at different age at a load of 5 N.
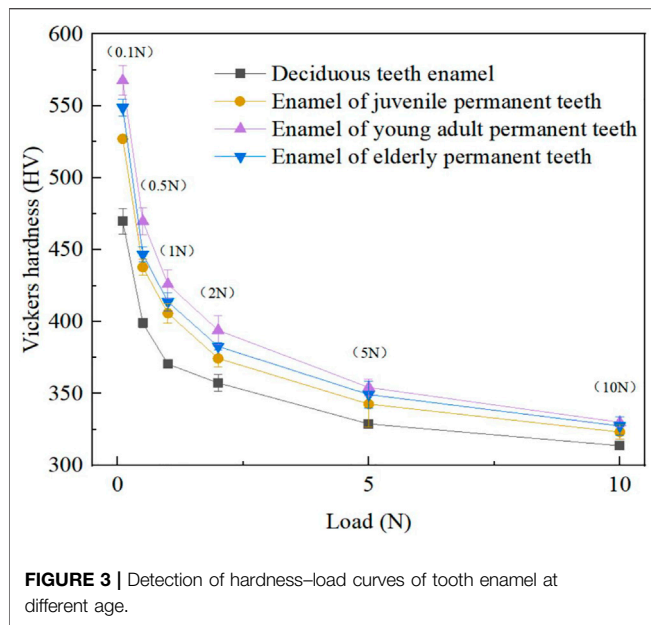
laser confocal scanning microscope (LCSM, XK-X1000, KEYENCE, Japan), and the indentation depth was measured. The process of measuring enamel indentation depth were depicted (see **Figure 1**).

The crack length of each indentation was then measured (see **Figure 2**). The fracture toughness of the enamel was calculated using **Eq. 1** (Rivera et al., 2013):

$$K_{c\,(app)} = 0.0084 \left(\frac{E}{H_v}\right)^{0.4} \left(\frac{2F}{L}\right) \frac{1}{c^{0.5}} \; (MPa \cdot m^{0.5}) \qquad (1)$$

Where E is the elastic modulus of the enamel (with $E = 7.27 \times 1{,}010$ Pa), HV is the Vickers hardness of the enamel, c is the average length of four cracks, F is the normal load, and L is the average length of the indentation diagonal. The Chinese units are all the basic units of the international unit system.

Finally, the Ca and P elements in enamel of all ages were analyzed using X-ray energy spectrometer (Zeiss Crossbeam 540).

RESULTS

Vickers Hardness

As illustrated by **Figure 3**, the relationship curve of the enamel surface Vickers hardness varied with normal loading among the age groups. The results suggest that at the same load, the young adult permanent teeth group exhibited the highest Vickers hardness of tooth enamel, followed successively by the older adult permanent, juvenile permanent, and deciduous teeth groups. Although the vickers hardness of enamel in different age groups decreased with the increase of loading. But under the same load, the size relationship between them is still quite obvious. The results of microhardness test revealed that when the normal load was

FIGURE 5 | Detection of indentation depth of tooth enamel at different age at a load of 5 N.
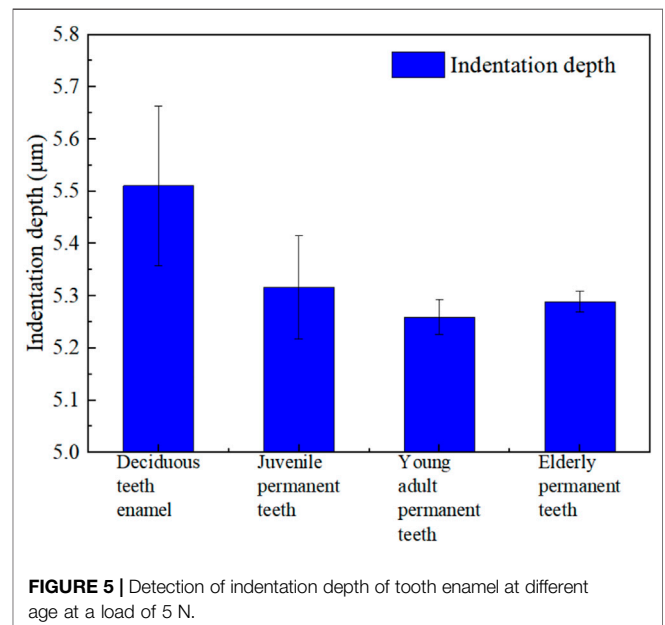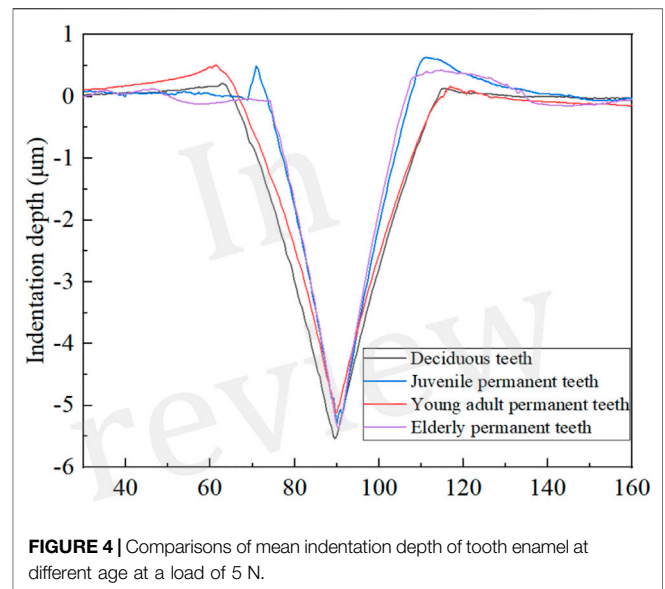
0.1 N, the enamel hardness values (HV's) of the young adult permanent, older permanent, juvenile permanent, and deciduous teeth were approximately 567, 548, 527, and 469, respectively. With an increase in the normal load, the Vickers hardness of the enamel of all four groups decreased. When the normal load was increased to 10 N, the Vickers HV's of the young adult permanent, older permanent, juvenile permanent, and deciduous tooth enamel decreased to approximately 330, 327, 323, and 313, respectively, (see **Figure 3**). In addition, as depicted in **Figure 3**, Nonetheless, the Vickers hardness of enamel of the permanent teeth of all ages did not differ markedly, whereas that of the deciduous tooth enamel was
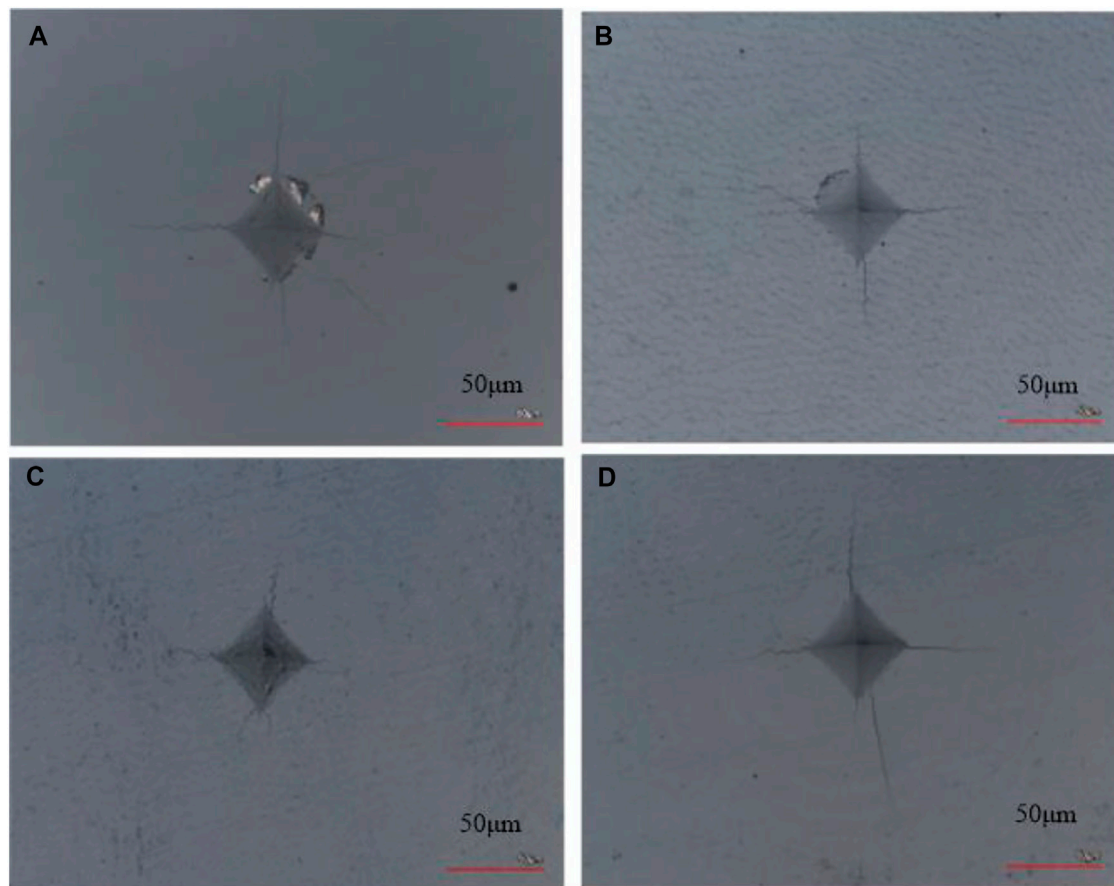
FIGURE 6 | Topography of the enamel surface of different age groups at a load of 5 N. **(A)** Deciduous teeth group. **(B)** Juvenile permanent teeth group. **(C)** Young adult permanent teeth group. **(D)** Older adult permanent teeth group.

TABLE 1 | The mean crack propagation length of enamel indentation at different ages.

Age Group	The Mean Crack Propagation Length c (µm)
Deciduous teeth group	36.8314 ± 0.8711
Juvenile permanent teeth group	34.6203 ± 0.6766
Young adult permanent teeth group	33.0615 ± 1.0848
Older adult permanent teeth group	38.6293 ± 0.9607

substantially lower than that of the permanent tooth enamel (of all ages). Therefore, from the perspective of Vickers hardness, the mechanical properties of the tooth enamel materials of different age groups differ considerably.

Depth of the Indentation

Figures 4, **5** present and compare the tooth enamel indentation depth for each age group at a load of 5 N. The depth of enamel indentation was the highest in the

FIGURE 7 | Detection of fracture toughness–load curves of different age groups' tooth enamel.
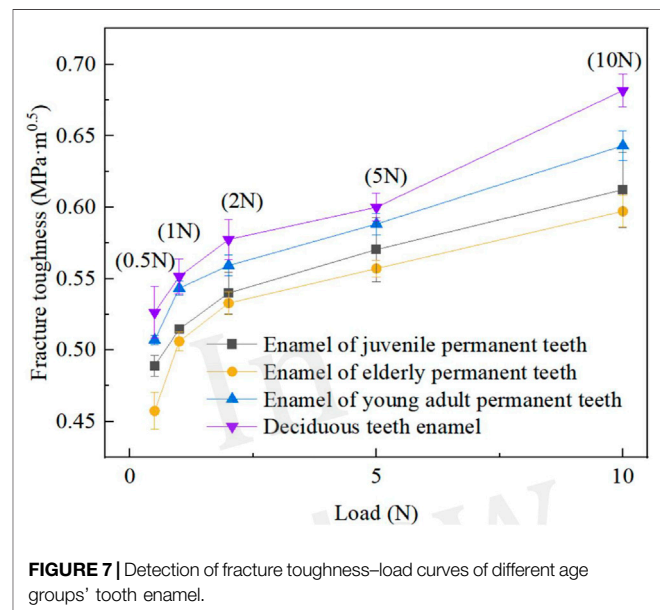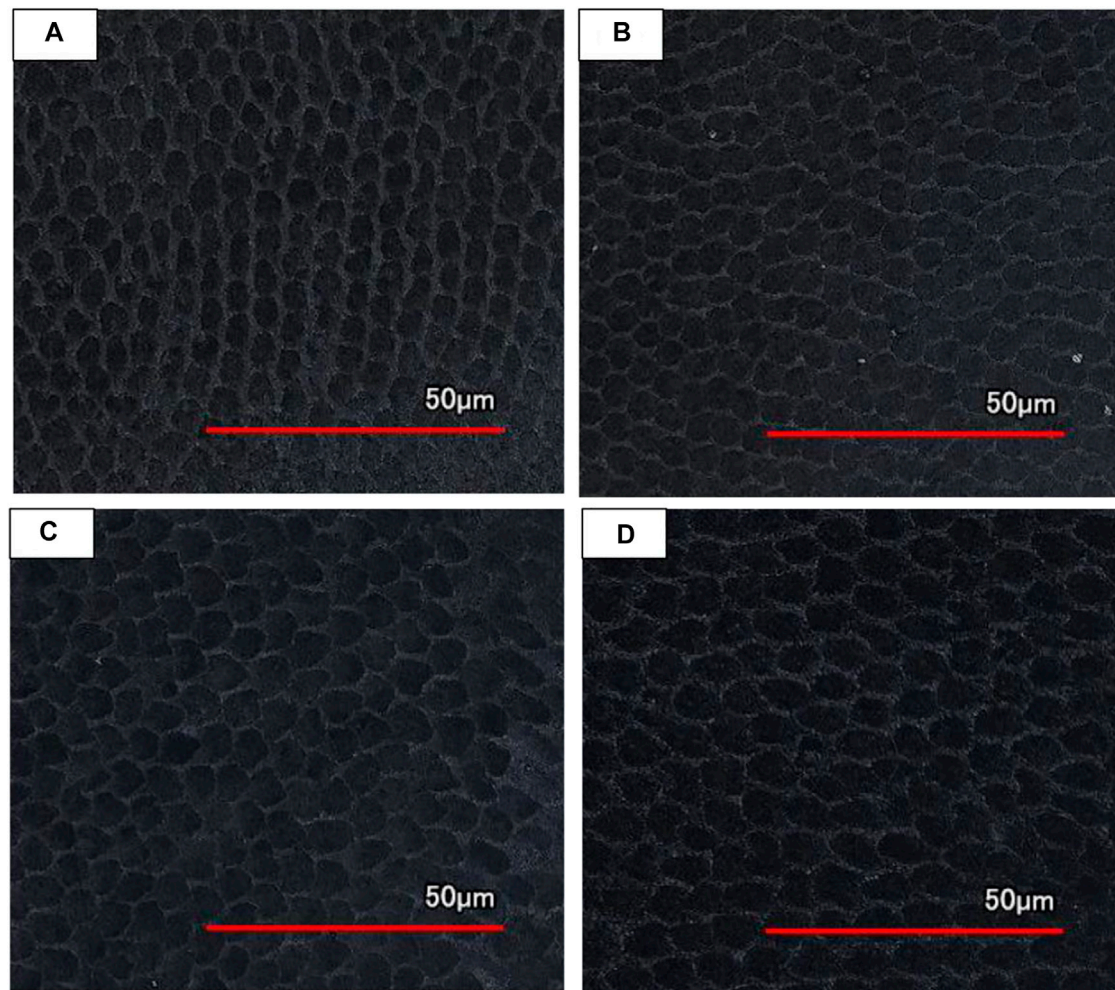
FIGURE 8 | LCSM topography of enamel surface of different age groups after slight acid etching. **(A)** Deciduous teeth group. **(B)** Juvenile permanent teeth group. **(C)** Young adult permanent teeth group. **(D)** Older adult permanent teeth group.

deciduous teeth group, followed by the juvenile, older adult, and young adult permanent teeth groups (in that order). From the Angle of indentation depth, there are significant differences in the compressive ability of enamel materials in different ages.

Fracture Toughness

As illustrated in **Figure 6**, the enamel surface indentation topography with a load of 5 N varies by age group, with the shortest crack propagation observed in the enamel of the young adult permanent teeth, followed successively by that of the juvenile permanent, deciduous, and older adult permanent teeth. **Table 1** shows the mean crack propagation length of enamel indentation at different ages.

Figure 7 displays the relationship curves of enamel fracture toughness and normal load, which varied among the age groups. Within the test range (0.1–10 N), the fracture toughness of the enamel in all age groups presented a trend

TABLE 2 | Ca/P values of enamel surface at different ages.

Age group	Ca/P
Deciduous teeth group	1.27
Juvenile permanent teeth group	1.62
Young adult permanent teeth group	1.70
Older adult permanent teeth group	1.68

of increase with an increase in load. The fracture toughness values for the enamel in the older adult permanent, juvenile permanent, young adult permanent, and deciduous teeth were 0.457–0.597, 0.489–0.612, 0.507–0.643, and 0.526–0.682 MPa m$^{0.5}$ (see **Figure 7**), respectively. Thus, the enamel surface fracture toughness values were the lowest in the older adult permanent teeth group, followed by the juvenile permanent, young adult permanent, and deciduous teeth groups.

Surface Topography

As illustrated in **Figure 8**, the surface topography of enamel changes with age. Compared with permanent teeth, the diameter of enamel rod of deciduous teeth is smaller and the arrangement is relatively scattered. The inter rod enamel of deciduous teeth is much wider. Water and protein are mainly stored in the inter rod enamel, so deciduous teeth have a lower hardness. The diameter of enamel rod of Juvenile permanent teeth is a litter smaller than young adult permanent teeth, they showed a more regular round shape. As the number of chewing increases, the enamel rod of older adult permanent teeth is flattened into an oval shape.

EDS Results

Table 2 shows the Ca/P values of enamel surfaces at different ages. And what we can see is, we can see that the young adult group has the highest Ca/P, followed by the older adult permanent, juvenile permanent, and deciduous teeth groups. This is consistent with the law of Vickers hardness in different age groups.

DISCUSSION

Studying the mechanical properties of tooth enamel is a crucial scientific venture. Due to the complex microstructure of tooth enamel and substantial limitations of quasistatic and dynamic testing methods, the use of the traditional indentation method is feasible (Xu et al., 2017). Microhardness testing indicated that at the same load, the Vickers hardness of the deciduous teeth was much lower than that of the permanent teeth. Although differences in Vickers hardness among the three age-based permanent teeth groups was not as obvious as that between the deciduous and permanent teeth, increasing age also altered the Vickers hardness in permanent teeth. This was possibly because of the lower enamel thickness, lower mineralisation, and higher organic content of deciduous teeth than of permanent teeth, which leads to the lower Vickers hardness in deciduous tooth enamel than in permanent tooth enamel. After an individual initially develops permanent teeth, the degree of mineralisation of the teeth increases as they grow. Zaichick and Zaichick, 2016 observed that the content of Ca, Cl, K, Mg and P in the teeth of people aged 25–35 years were the highest, and the content decreased with increasing age. In addition, the content of the minerals Ca and P in enamel determined changes in enamel hardness (Qiu et al., 2003; Zajcev et al., 2003). We noted that the changes in the Vickers hardness of enamel across ages coincide with the changes in Ca/P.

Fracture toughness is a measure of a material's ability to resist crack propagation. For many ceramics, it depends on the phase composition as well as microstructure (e.g., crystal size and shape, distribution of glass and secondary crystal phases, closed porosity) (Medvedovski, 2001). The distinct chemical compositions and microstructures of tooth enamel at different ages also contribute to the differences in fracture toughness. Studies have revealed that when tooth enamel is subjected to an external load, the protein undergoes shear deformation (Li and Swain, 2007), and the enamel dissipates energy during chewing through this protein microdamage behaviour, thus increasing the toughness of the tooth enamel. Proteins are essential for the development of nanobridged

ligaments, and their mechanisms include crack deflection, branching, and mineralised crack bridges. Removal of protein reduces the fracture toughness of the longitudinal and transverse directions of crack growth by approximately 40% (Yahyazadehfar and Dwayne, 2015). The protein content of the enamel in mature deciduous teeth was also noted to be nearly twice that in permanent teeth (Chen et al., 1988). The fracture toughness of deciduous tooth enamel is much higher than that of permanent tooth enamel, which may be related to the substantial difference in protein content between deciduous and permanent tooth enamel. At the same time, the protein content of permanent teeth of different ages is not different, but with the increase of age, the mineralization degree of enamel of permanent teeth is deepening, and the enamel column keeps growing, the enamel glaze column is arranged more closely. The microporous structure of the enamel is greatly reduced in young adults, it could promote the constant fang enamel fracture toughness increases in young adults. The enamel of older adult permanent teeth is exposed to the complex oral environment for a long time. Over time, a large amount of fluoride ions in the oral cavity erodes the hydroxyapatite crystals on the surface of the enamel, transforming those crystals and the microscopic structure of the tooth enamel (Brudevold et al., 1982; Leventouri et al., 2009). Furthermore, the thickness of older adult permanent tooth enamel is also one third less than that of young permanent tooth enamel because of the complex oral environment (Carvalho and Lussi, 2017). All of these factors potentially reduce the fracture toughness in older adults' permanent tooth enamel.

The mechanical properties of deciduous and permanent teeth differ considerably, as do those of young and older adult permanent teeth and those of young adult and juvenile permanent teeth. However, Vickers hardness and fracture toughness can, notably, only indicate the mechanical properties of human tooth enamel in distinct ages from certain dimensions. The two are not directly related to one another and cannot completely represent the mechanical properties of human tooth enamel in different age groups.

CONCLUSION

In this paper, the surface mechanical properties of human tooth enamel of different age groups were characterised using a microhardness instrument and a laser confocal microscope to study the Vickers hardness, indentation depth, and fracture toughness. The results suggest the following conclusions.

(1) At the same load, the young adult permanent teeth group exhibited the highest Vickers hardness of enamel, followed successively by the older age permanent, juvenile permanent, and deciduous teeth groups. Nevertheless, the Vickers hardness of the enamel of the permanent teeth (of all ages) did not markedly differ, whereas the Vickers hardness of the deciduous tooth enamel was far less than that of the permanent tooth enamel.

(2) At the same load, the enamel indentation depth of the deciduous teeth was the highest, followed by that of the juvenile, older adult, and young adult permanent teeth.

(3) At the same load, the fracture toughness of the deciduous tooth enamel was the highest, followed by that of the

young adult, juvenile, and older adult permanent tooth enamel.

(4) The different chemical compositions and microstructures of enamel at different age groups resulted in the significant differences in mechanical properties.

DATA AVAILABILITY STATEMENT

The datasets presented in this study can be found in online repositories. The names of the repository/repositories and accession number(s) can be found below: https://figshare.com/s/d314f1285f989af449a9.

ETHICS STATEMENT

Ethical review and approval was not required for the study on human participants in accordance with the local legislation and institutional requirements. Written informed consent to participate in this study was provided by the participants' legal guardian/next of kin.

AUTHOR CONTRIBUTIONS

XJ, YZ, LK, HX and FY conceived the study and designed the experiments, XJ, YZ and LJ conducted the experiments, and XJ, YZ and FY analyzed the results and wrote the paper, ZJ collected the teeth samples.

FUNDING

REFERENCES

Antoine, D., and Hillson, S. (2015). *Enamel Structure and Properties*, 29. John Wiley & Sons, 223–243. doi:10.1002/9781118845486.ch16

Barbour, M. E., Parker, D. M., Allen, G. C., and Jandt, K. D. (2003). Human Enamel Dissolution in Citric Acid as a Function of pH in the Range 2.30≤pH≤6.30 - a Nanoindentation Study. *Eur. J. Oral Sci.* 111 (3), 258–262. doi:10.1034/j.1600-0722.2003.00039.x

Beniash, E., Metzler, R. A., Lam, R. S. K., and Gilbert, P. U. P. A. (2009). Transient Amorphous Calcium Phosphate in Forming Enamel. *J. Struct. Biol.* 166 (2), 133–143. doi:10.1016/j.jsb.2009.02.001

Brudevold, F., Aasenden, R., and Bakhos, Y. (1982). A Preliminary Study of Posteruptive Maturation of Teeth *In Situ*. *Caries Res.* 16, 243–248. doi:10.1159/000260604

Carvalho, T. S., and Lussi, A. (2017). Age-related Morphological, Histological and Functional Changes in Teeth. *J. Oral Rehabil.* 44 (4), 291–298. doi:10.1111/joor.12474

Chen, W. Y., Wu, A. J., Shao, J. J., and Li, L. Q. (1988). Analysis of Enamel Protein in Different Age Groups. *Chin. J. Stomatology* 05, 287–290.

Cui, F.-Z., and Ge, J. (2007). New Observations of the Hierarchical Structure of Human Enamel, from Nanoscale to Microscale. *J. Tissue Eng. Regen. Med.* 1 (3), 185–191. doi:10.1002/term.21

Derocher, K. A., Smeets, P. J. M., Goodge, B. H., Zachman, M. J., Balachandran, P. V., Stegbauer, L., et al. (2020). Chemical Gradients in Human Enamel crystallitesImpact Wear Behavior of Human Tooth Enamel under Simulated Chewing Conditions. *NatureJournal Mech. Behav. Biomed. Mater.* 583 (7814), 66119–71127. doi:10.1038/s41586-020-2433-3

Galbany, J., Romero, A., Mayo-Alesón, M., Itsoma, F., Gamarra, B., Pérez-Pérez, A., et al. (2014). Age-related Tooth Wear Differs between forest and savanna Primates. *PLoS ONE* 9 (4), e94938. doi:10.1371/journal.pone.0094938

He, L. H., and Swain, M. V. (2007). Contact Induced Deformation of Enamel. *Appl. Phys. Lett.* 90 (17), 171916. doi:10.1063/1.2450649

He, L. H., and Swain, M. V. (2008). Understanding the Mechanical Behaviour of Human Enamel from its Structural and Compositional Characteristics. *J. Mech. Behav. Biomed. Mater.* 1 (1), 18–29. doi:10.1016/j.jmbbm.2007.05.001

Hua, L. C., Wang, W. Y., Swain, M. V., Zhu, C. L., Huang, H. B., Du, J. K., et al. (2019). The Dehydration Effect on Mechanical Properties of Tooth Enamel. *J. Mech. Behav. Biomed. Mater.* 95, 210–214. doi:10.1016/j.jmbbm.2019.04.013

Jeng, Y.-R., Lin, T.-T., Hsu, H.-M., Chang, H.-J., and Shieh, D.-B. (2011). Human Enamel Rod Presents Anisotropic Nanotribological Properties. *J. Mech. Behav. Biomed. Mater.* 4, 515–522. doi:10.1016/j.jmbbm.2010.12.002

Ji, B., and Gao, H. (2004). Mechanical Properties of Nanostructure of Biological Materials. *J. Mech. Phys. Sol.* 52 (9), 1963–1990. doi:10.1016/j.jmps.2004.03.006

Lei, L., Zheng, L., Xiao, H., Zheng, J., and Zhou, Z. (2020). Wear Mechanism of Human Tooth Enamel: the Role of Interfacial Protein Bonding between HA Crystals. *J. Mech. Behav. Biomed. Mater.* 110, 103845. doi:10.1016/J.JMBBM.2020.103845

Leventouri, T., Antonakos, A., Kyriacou, A., Venturelli, R., Liarokapis, E., and Perdikatsis, V. (2009). Crystal Structure Studies of Human Dental Apatite as a Function of Age. *Int. J. Biomater.* 2009 (1), 1–6. doi:10.1155/2009/698547

Li, C., Piao, Y., Meng, B., Hu, Y., Li, L., and Zhang, F. (2022). Phase Transition and Plastic Deformation Mechanisms Induced by Self-Rotating Grinding of GaN Single Crystals. *Int. J. Mach. Tools Manuf.* 172, 103827. doi:10.1016/j.ijmachtools.2021.103827

Mandra, J. V., Votyakov, S. L., Smirnova, M. E., Zholudev, S. E., and Grigorjev, S. S. (2020). Comparative Evaluation of Adhesive Performance to Dentin: Study in Patients of Different Ages. *BIO Web Conf.* 22 (1), 01026. doi:10.1051/bioconf/20202201026

Medvedovski, E. (2001). Wear-resistant Engineering Ceramics. *Wear* 249 (9), 821–828. doi:10.1016/S0043-1648(01)00820-1

Miake, Y., Tsutsui, S., and Eshita, Y. (2016). Variation in the Color of Japanese Teeth and Structural Changes in Enamel Rod Sheath Associated with Age. *J. Hard Tissue Biol.* 25 (2), 131–136. doi:10.2485/jhtb.25.131

Montoya, C., Arango-Santander, S., Peláez-Vargas, A., Arola, D., and Ossa, E. A. (2015). Effect of Aging on the Microstructure, Hardness and Chemical Composition of Dentin. *Arch. Oral Biol.* 60 (12), 1811–1820. doi:10.1016/j.archoralbio.2015.10.002

Moradian-Oldak, J. (2012). Protein-mediated Enamel Mineralization. *Front. Biosci.* 17 (6), 1996–2023. doi:10.2741/4034

Niu, L., Zhang, H., Dong, S., Wang, Y., and Zou, R. (2017). The Microstructure Properties of Human Enamel on the Multi-Scale. *J. Shanxi Med. Univ.* 48, 1075–1078. doi:10.13753/j.issn.1007-6611.2017.10.022

Pan, H., Tao, J., Yu, X., Fu, L., Zhang, J., Zeng, X., et al. (2008). Anisotropic Demineralization and Oriented Assembly of Hydroxyapatite Crystals in Enamel: Smart Structures of Biominerals. *J. Phys. Chem. B* 112 (24), 7162–7165. doi:10.1021/jp802739f

Qiu, Y. N., Liu, W. M., Li, T. S., and Liu, L. Z. (2003). Comparative Study of Friction and Wear Behavior of Different Human Enamel *In Vitro*. *Zhonghua Kou Qiang Yi Xue Za Zhi* 38 (3), 213–216. doi:10.1007/BF02974893

R, A. (2015). Effect pH on Demineralization Dental Erosion. *Ijcea* 6 (2), 138–141. doi:10.7763/IJCEA.2015.V6.468

Rivera, C., Arola, D., and Ossa, A. (2013). Indentation Damage and Crack Repair in Human Enamel. *J. Mech. Behav. Biomed. Mater.* 21 (Complete), 178–184. doi:10.1016/j.jmbbm.2013.02.020

Robinson, C., Shore, R. C., Brookes, S. J., Strafford, S., Wood, S. R., and Kirkham, J. (2000). The Chemistry of Enamel Caries. *Crit. Rev. Oral Biol. Med.* 11 (4), 481–495. doi:10.1177/10454411000110040601

Ryou, H., Romberg, E., Pashley, D. H., Tay, F. R., and Arola, D. (2015). Importance of Age on the Dynamic Mechanical Behavior of Intertubular and Peritubular Dentin. *J. Mech. Behav. Biomed. Mater.* 42, 229–242. doi:10.1016/j.jmbbm.2014.11.021

Shen, L., Barbosa de Sousa, F., Tay, N., Lang, T. S., Kaixin, V. L., Han, J., et al. (2020). Deformation Behavior of normal Human Enamel: a Study by Nanoindentation. *J. Mech. Behav. Biomed. Mater.* 108, 103799. doi:10.1016/J.JMBBM.2020.103799

Simmer, J. P., and Hu, J. C.-C. (2001). Dental Enamel Formation and its Impact on Clinical Dentistry. *J. Dental Education* 65 (9), 896–905. doi:10.1002/j.0022-0337.2001.65.9.tb03438.x

Steiger-Ronay, V., Kuster, I. M., Wiedemeier, D. B., Attin, T., and Wegehaupt, F. J. (2020). Erosive Loss of Tooth Substance Is Dependent on Enamel Surface Structure and Presence of Pellicle - an *In Vitro* Study. *Arch. Oral Biol.* 112, 104686. doi:10.1016/j.archoralbio.2020.104686

Xu, Y. Z., Yang, Q. X., Wang, R. R., and Zhang, D. S. (2017). Effects of Aging and Location on Mechanical Properties of Human Dentin. *Yiyong Shengwu Lixue/Journal Med. Biomech.* 32 (6), 519–523. doi:10.16156/j.1004-7220.2017.06.006

Yahyazadehfar, M., and Arola, D. (2015). The Role of Organic Proteins on the Crack Growth Resistance of Human Enamel. *Acta Biomater.* 19, 33–45. doi:10.1016/j.actbio.2015.03.011

Zaichick, V., and Zaichick, S. (2016). The Effect of Age on Ca, Cl, K, Mg, Mn, Na, P and Sr Contents in Roots of Human Female Permanent Teeth. *J. Radioanal. Nucl. Chem.* 309, 295–301. doi:10.1007/s10967-016-4803-8

Zajcev, V. M., Lifljandskij, V. G., and Mirinkin, V. I. (2003). *Applied Medical Statistics (Tutorial)*. St. Petersburg: Foliantpress.

Zeichner-David, M., Vo, H., Tan, H., Diekwisch, T., Berman, B., Thiemann, F., et al. (1997). Timing of the Expression of Enamel Gene Products during Mouse Tooth Development. *Int. J. Dev. Biol.* 41 (1), 27–38. doi:10.1007/s11626-997-0027-0

Zhang, Y. F., Zheng, J., Zheng, L., Shi, X. Y., Qian, L. M., and Zhou, Z. R. (2013). Effect of Adsorption Time on the Lubricating Properties of the Salivary Pellicle on Human Tooth Enamel. *Wear* 301 (1-2), 300–307. doi:10.1016/j.wear.2012.11.037

Zheng, J., Huang, H., Shi, M. Y., Zheng, L., Qian, L. M., and Zhou, Z. R. (2011). *In Vitro* study on the Wear Behaviour of Human Tooth Enamel in Citric Acid Solution. *Wear* 271 (9-10), 2313–2321. doi:10.1016/j.wear.2010.11.027

Zheng, J., Zeng, Y., Wen, J., Zheng, L., and Zhou, Z. (2016). Impact Wear Behavior of Human Tooth Enamel Under Simulated Chewing Conditions. *J. Mech. Behav. Biomed. Mater.* 62, 119–127. doi:10.1016/j.jmbbm.2016.04.039

Numerical Modeling and Experimental Study on the Material Removal Process Using Ultrasonic Vibration-Assisted Abrasive Water Jet

Zhichao Cheng[1,2], Shikang Qin[1,2] and Zhufang Fang[1,2]*

[1]College of Mechanical Engineering, Zhejiang University of Technology, Hangzhou, China, [2]Key Laboratory of Special Purpose Equipment and Advanced Processing Technology, Ministry of Education and Zhejiang Province, Zhejiang University of Technology, Hangzhou, China

Currently, micro-abrasive water jet machining has the problem of insufficient processing capacity in the central area. To assist with improving the processing efficiency, ultrasonic vibration is introduced. First, based on the computational fluid dynamics method, the mathematical model of the three-dimensional shape prediction of micro-holes is established using a mixed model, standard k-ε model, discrete phase model, and dynamic mesh model. The effects of the ultrasonic vibration on the static pressure, jet velocity field, abrasive particle motion state, and material erosion rate in the stagnation zone are studied. Then the accuracy of the prediction model is verified by comparing the two-dimensional section of the experimental data and the simulated data and calculating the three-dimensional mean square deviation. The established prediction model is used to further analyze the optimal frequency of the ultrasonic vibration and the specific influence of the optimal amplitude on the machining effect in micro-abrasive water jet machining. The above research results have profound guiding significance for determining how to use ultrasonic vibration in micro-abrasive water jet machining.

Keywords: abrasive water jet, ultrasonic vibration, jet velocity field, root mean square, static pressure distribution

INTRODUCTION

In recent years, with the rapid development of high-tech fields such as electrical and electronic engineering, optics, and biomedicine, the demand for microfluidic chips has continued to increase (Yeo et al., 2011; Espulgar et al., 2015; Chen et al., 2021; Ji et al., 2022). Currently, the main substrate materials used in microfluidic chips are hard and brittle materials such as silicon, glass, and ceramics. Hard and brittle materials have the characteristics of high hardness, high brittleness, wear resistance, and oxidation resistance. At the same time, these materials are easily affected by heat, so processing is difficult. K9 glass is a type of typical hard and brittle material. It has the advantages of high transparency, good optical uniformity, and stable chemical and physical properties. Hence, it is widely used in electronics, electrical engineering, and other fields (Hu et al., 2022; Qi et al., 2022).
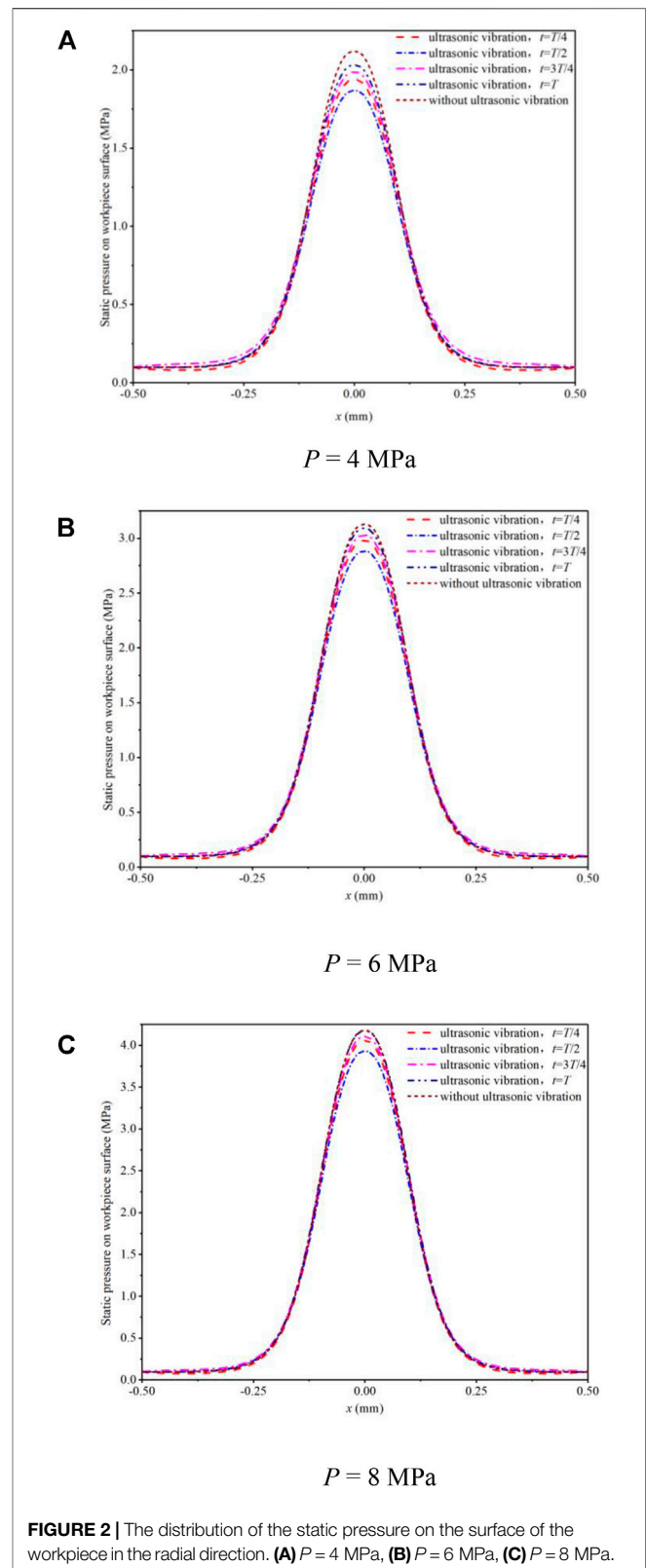
Compared with laser beam machining, electric discharge machining, and chemical machining, the micro-abrasive water jet technology has the advantages of no thermal damage, high flexibility, and a fast cutting speed (Nguyen et al., 2018; Zhu et al., 2019; Li
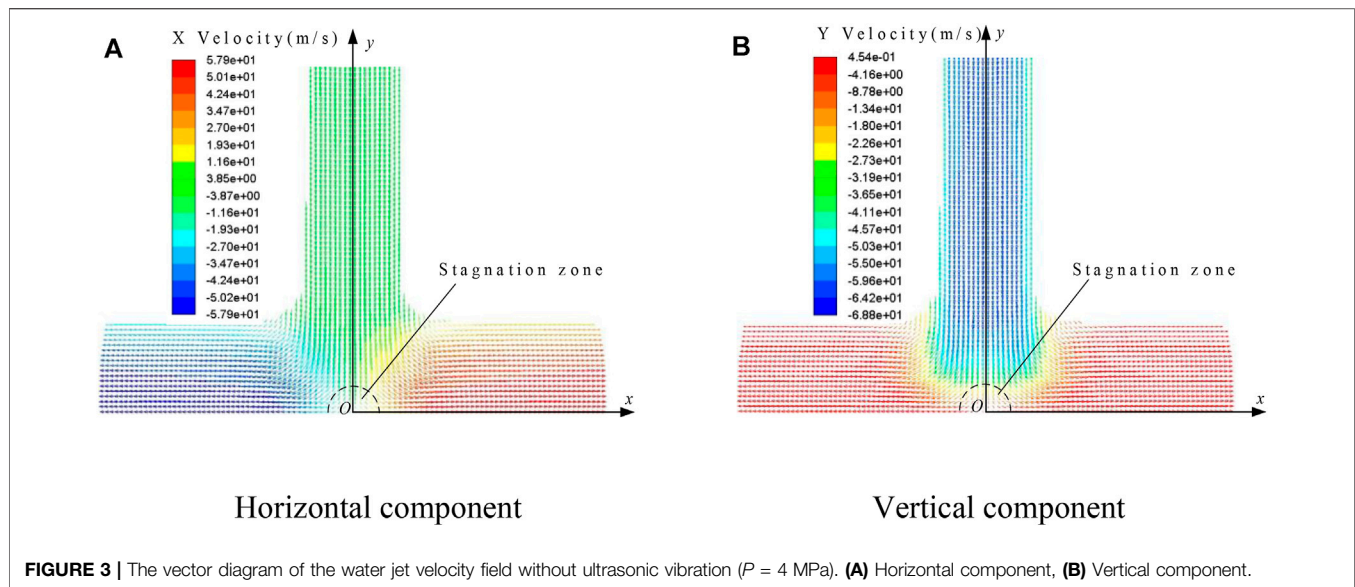
FIGURE 1 | Geometry model of the flow field.
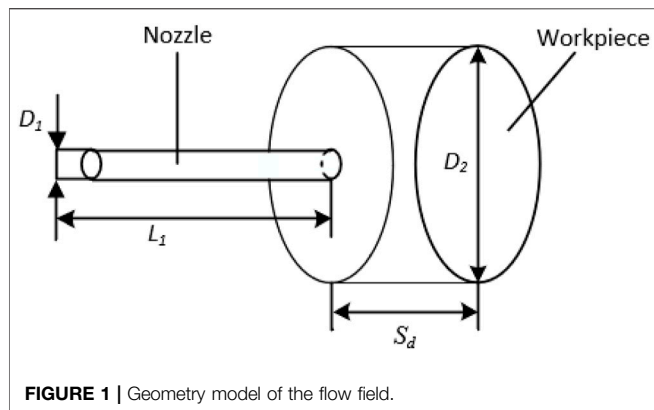
et al., 2021). It provides an efficient means of processing tiny geometric shapes. Although water jet processing is not selective in terms of materials, it can be used to machine tiny structures of almost any material, including ductile materials and brittle materials, and it is often used in processing hard and brittle materials and other difficult-to-process materials. In the process of micro-abrasive water jet machining, the grinding material is sprayed from the nozzle and then hits the workpiece, forming plastic deformation or a brittle fracture to achieve the purpose of material removal. When processing micro-channels, a high-pressure water jet is likely to cause a chip break. It has been found that when using a low-pressure abrasive water jet to process hard and brittle materials, high flexibility, easy control, and good surface processing quality can be obtained. However, the bottom surface of the micro-holes processed by a micro-abrasive water jet usually presents a "W" shape. The material at the center of the hole is difficult to remove, which affects the processing efficiency.

Due to the insufficient pressure and the characteristics of a stagnant zone, in the processing of micro-abrasive water jet technology, there has always been a phenomenon of insufficient processing capacity in the center area. To improve the processing effect of the micro-abrasive water jet technology, some auxiliary methods have been used. Researchers are continuously attempting to use different methods such as electrochemical-assisted micro-abrasive water jet machining (Liu et al., 2015), magnetorheological field-assisted micro-abrasive water jet machining (Lee et al., 2015), cavitation-assisted micro-abrasive water jet machining (Beaucamp et al., 2018), and ultrasonic vibration-assisted abrasive water jet processing. Among these methods, ultrasonic-assisted micro-abrasive water jet processing technology has been proven to improve the material removal rate of a workpiece, but its mechanism of action needs to be further studied.

Narayanan analyzed the formation mechanism of an abrasive water jet, analyzed the coupling mechanism between the liquid-gas-solid phase, and established a detailed mathematical model that could predict the energy of abrasive particles when they left the outlet of a polymer tube (Narayanan et al., 2013). The actual experimental results

$P = 4$ MPa

$P = 6$ MPa

$P = 8$ MPa

FIGURE 2 | The distribution of the static pressure on the surface of the workpiece in the radial direction. (A) $P = 4$ MPa, (B) $P = 6$ MPa, (C) $P = 8$ MPa.

were consistent to a certain extent, but the establishment of the mathematical model was slightly too complicated. Li et al. simulated the multiple particle impact process based on FEM

FIGURE 3 | The vector diagram of the water jet velocity field without ultrasonic vibration (P = 4 MPa). **(A)** Horizontal component, **(B)** Vertical component.

and used the Monte Carlo method to generate a random flow of impact particles, and they considered the heat exchange during the entire impact process (Li et al., 2014). The study found that the fracture caused by inertia was the vertical impact of the jet. The main material removal mechanism at the time and the destruction driven by thermal instability caused a higher material removal rate when the jet was tilted and impacted. Qi et al. used computational fluid dynamics (CFD) software to simulate the process of a micro-abrasive water jet eroding a workpiece with a two-dimensional model, and they analyzed the static pressure distribution in the jet field, the fluid velocity and the motion state of the abrasive particles, and the simulation results The experimental results could be successfully explained (Qi et al., 2016). Anwar et al. used an FE model to simulate the abrasive water jet milling process of titanium alloys in which the impact particles involved in the abrasive flow were modeled in layers to reduce the calculation time. These layers were very close to each other, making the particles impact. The interval was close to that of the actual abrasive water jet cutting process, and the results showed that the model could accurately predict the jet trajectory and material erosion rate (Anwar et al., 2013). Huang et al. used computational fluid dynamics software with the three-dimensional model of an abrasive water jet nozzle to numerically simulate the internal flow field of the liquid-solid two-phase flow and obtained the velocity distribution in the nozzle and the mixing chamber in all directions, as well as the relationship between the water flow velocity and the abrasive velocity (Huang et al., 2007).

In recent years, researchers have gradually discovered that the application of ultrasonic vibration can effectively increase processing efficiency and improve the processing effect. However, few people have effectively combined a model with an experiment to obtain a better prediction model of

abrasive water-jet machining assisted by ultrasonic vibration, let alone further analyzed the optimal frequency of ultrasonic-assisted machining and the influence of the amplitude on the machining effect. The effectiveness of ultrasonic-assisted processing has always been a vague concept. A mathematical model that can effectively predict ultrasonic vibration-assisted abrasive water jet processing is of great significance for improving processing efficiency and guiding future abrasive water jet processing.

In this study, a mathematical model based on the CFD method is established to predict the three-dimensional shape of micro-holes. The effects of the ultrasonic vibration on the static pressure, jet velocity field, abrasive particle motion state, and material erosion rate in the stagnation zone are studied. After an experiment, the accuracy of the prediction model is verified by a two-dimensional section comparison and a three-dimensional mean square difference calculation. Using the established prediction model, we further analyze the optimal frequency of ultrasonic-assisted machining and the influence of the amplitude on the machining effect. Guidance for the vibration assistance used in the subsequent micro-abrasive water jet machining is also proposed.

Numerical Modeling

Fluent has rich physical models. Fluent can be used to solve anything that involves a fluid. When using Fluent for the numerical simulation of the ultrasonic-assisted micro-abrasive water jet erosion process, the multiphase flow model, turbulence model, discrete phase model, and dynamic mesh are mainly used. For this research, the mesh model is established with ICEM and imported into Fluent. The water flow uses the standard k-ε model, and the DPM model is used to track the movement state and the trajectory of the particles. Since the air, water, and particles enter the

FIGURE 4 | The horizontal component of the jet velocity near the surface of the workpiece. **(A)** $y = 20$ μm, $P = 4$ MPa, **(B)** $y = 60$ μm, $P = 4$ MPa, **(C)** $y = 100$ μm, $P = 4$ MPa, **(D)** $y = 20$ μm, $P = 6$ MPa, **(E)** $y = 60$ μm, $P = 6$ MPa, **(F)** $y = 100$ μm, $P = 6$ MPa, **(G)** $y = 20$ μm, $P = 8$ MPa, **(H)** $y = 60$ μm, $P = 8$ MPa, and **(I)** $y = 100$ μm, $P = 8$ MPa.

y = 20 μm, P = 8 MPa

y = 60 μm, P = 8 MPa

y = 100 μm, P = 8 MPa

FIGURE 4 | *(Continued).*

nozzle at the same time, the mixture model can be used as the multiphase flow model in the ultrasonic-assisted micro-abrasive water jet simulation model. Considering the influence of ultrasonic vibration on the abrasive water jet machining process, a dynamic mesh is introduced into the model to make the workpiece move periodically during the simulation process. The workpiece is K9 glass, and the abrasive is composed of alumina particles. The geometric model of the micro-abrasive water jet flow field is shown in the figure below. The diameter of the nozzle is 0.125 mm (D_1) and the length is 10.5 mm (L_1). According to nozzle design, this nozzle aspect (length to diameter) ratio allowed the contraction coefficient of the jet to be considered as unity (Mccarthy and Molloy, 1974). Considering the external flow field distribution, simulation calculation time, and small jet impact area, the outer flow field area of the nozzle uses a cylinder with a diameter of 1 mm (D_2) and a height of 2 mm (S_d), The distance of the nozzle outlet to the surface of the

workpiece is S_d = 2 mm, as shown in **Figure 1**. For the other parameters used in the simulation, please refer to our previously published studies (Qi et al., 2016; Qi et al., 2017).

Influence of Ultrasonic Vibration on Static Pressure in Stagnation Zone of Workpiece Surface

In the process of micro-abrasive water jet erosion, a stagnation zone with large static pressure forms on the surface of a workpiece, which hinders the abrasive particles from impacting the workpiece vertically, results in the decrease of the abrasive particle velocity and the deflection of the direction. Therefore, ultrasonic vibration is introduced. **Figures 2A–C** show the distribution of the static pressure on the workpiece surface along the radial direction before and after the introduction of ultrasonic vibration when the nozzle inlet pressures are 4 MPa, 6 MPa, and 8 MPa.
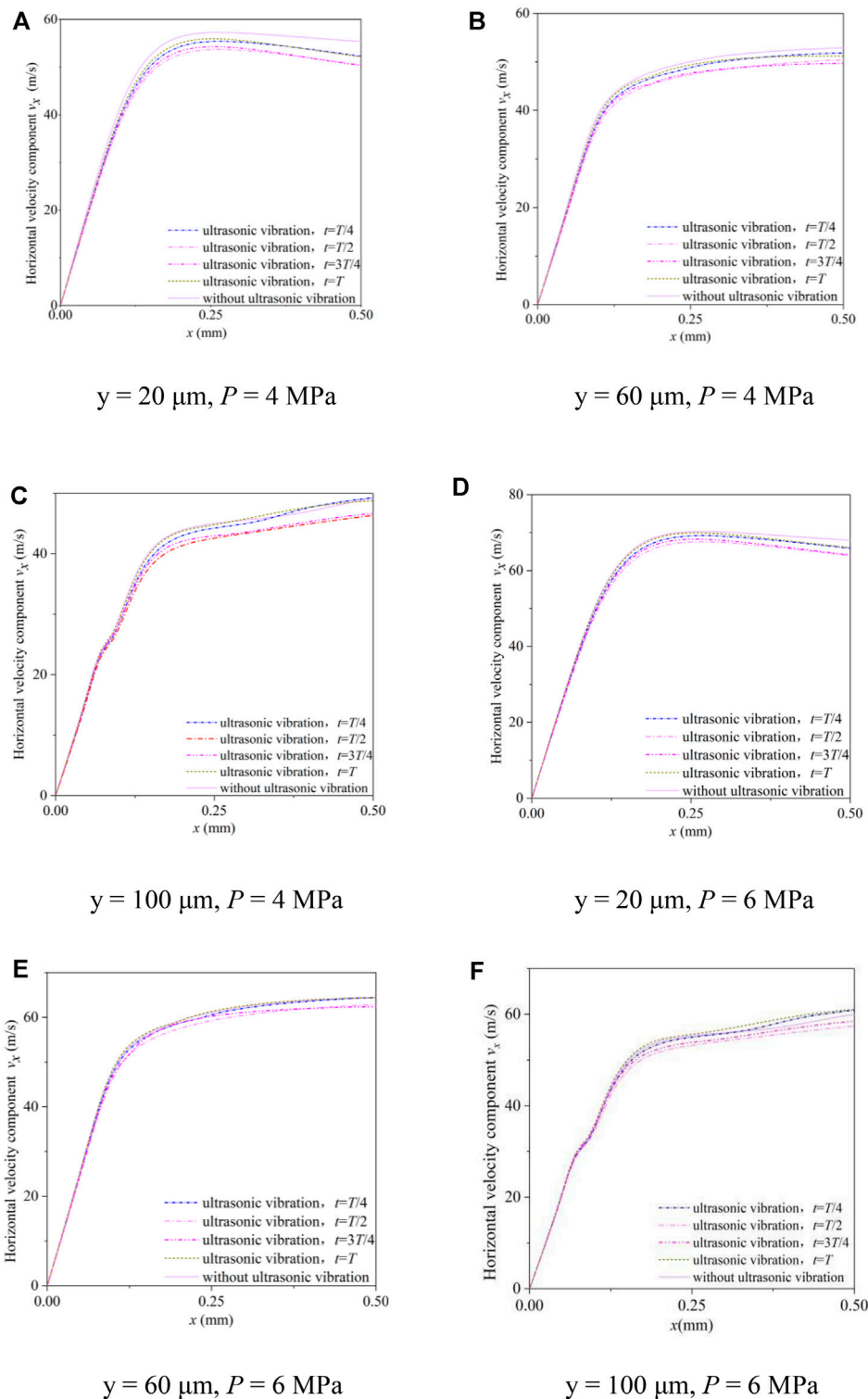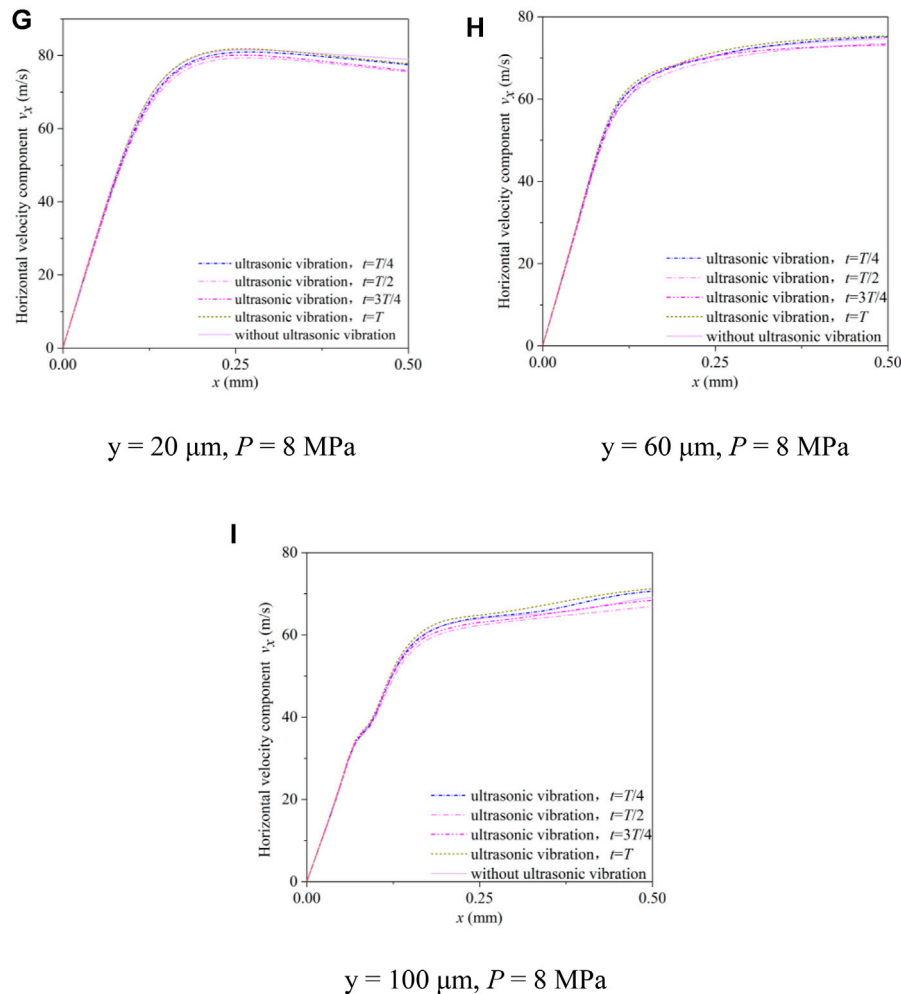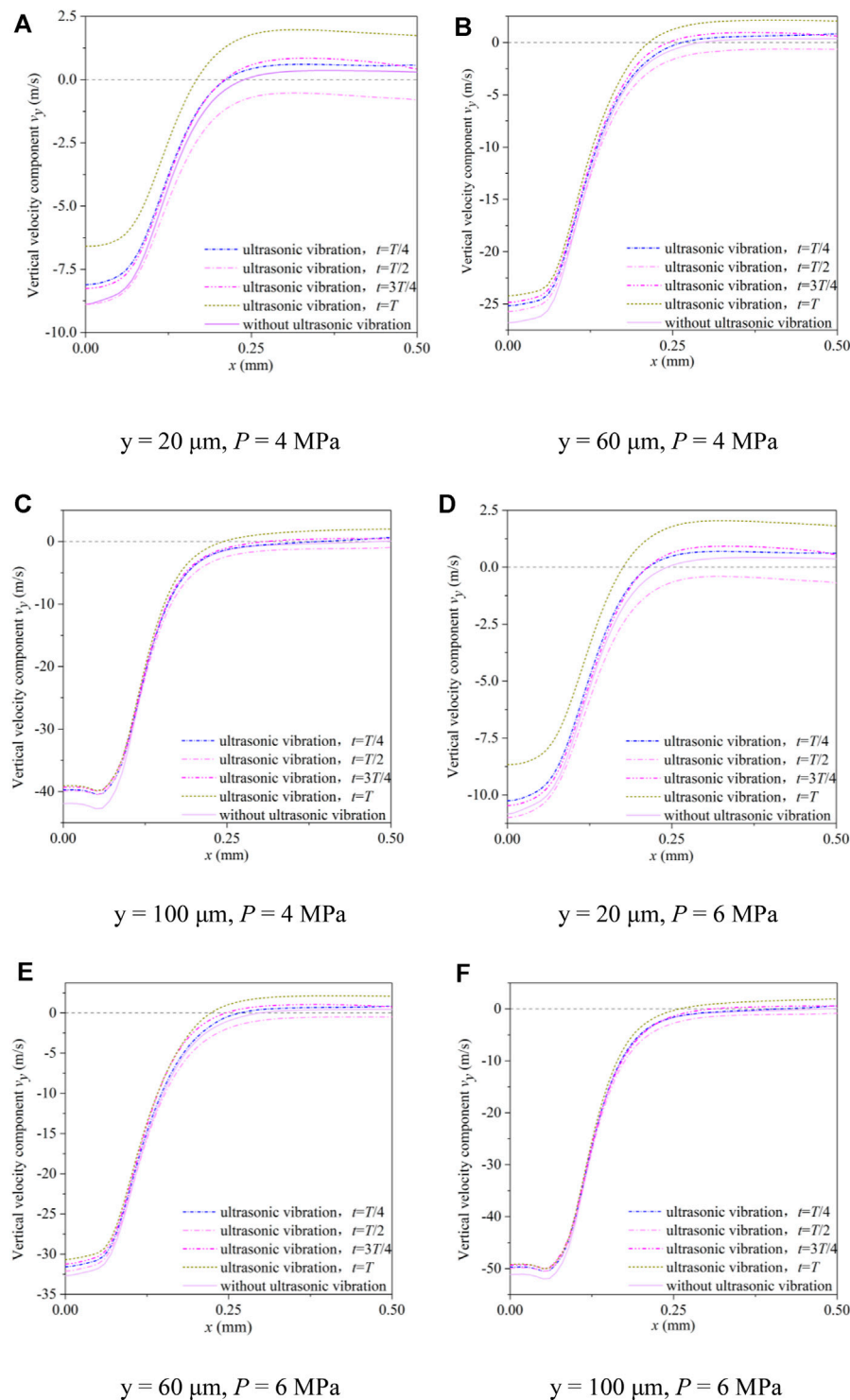
FIGURE 5 | The vertical component of the jet velocity near the surface of the workpiece. **(A)** y = 20 μm, P = 4 MPa, **(B)** y = 60 μm, P = 4 MPa, **(C)** y = 100 μm, P = 4 MPa, **(D)** y = 20 μm, P = 6 MPa, **(E)** y = 60 μm, P = 6 MPa, **(F)** y = 100 μm, P = 6 MPa, **(G)** y = 20 μm, P = 8 MPa, **(H)** y = 60 μm, P = 8 MPa, **(I)** y = 100 μm, P = 8 MPa.

Figure 2 shows four representative moments in a vibration cycle: $t = T$, $t = 3T/4$, $t = T/2$, and $t = T/4$. It can be seen from the figure that before and after the introduction of ultrasonic vibration, the static pressure changes on both sides of the workpiece surface are not obvious. After the ultrasonic vibration is introduced into the center of the workpiece,

y = 20 μm, *P* = 8 MPa

y = 60 μm, *P* = 8 MPa

y = 100 μm, *P* = 8 MPa
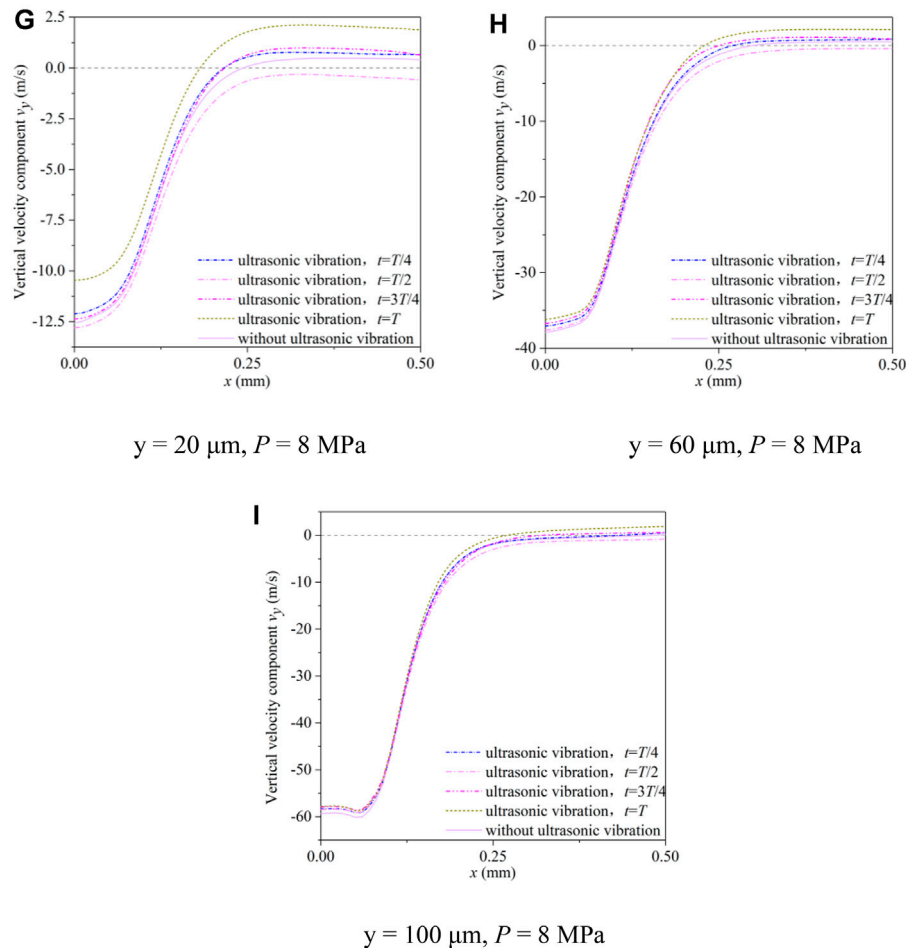
FIGURE 5 | *(Continued.)*

the static pressure on the surface of the workpiece in the four stagnation zones is on the order of $T > 3T/4 > T/4 > T/2$. In time T, the workpiece moves towards the direction close to the nozzle at the maximum speed in the middle position, and at time $T/2$, the workpiece moves away from the nozzle at the maximum speed in the middle position. The velocity of the workpiece at $T/4$ and $3T/4$ is 0. At $T/4$, the acceleration of the workpiece in the y-direction is negative and reaches the maximum. The acceleration of the workpiece in the y-direction at $3T/4$ time is positive and reaches the maximum value. The analysis shows that the static pressure on the surface of the workpiece in the stagnation zone may be related to the velocity and acceleration of the workpiece vibration, and the influence of the velocity is greater than that of the acceleration. After the introduction of ultrasonic vibration, the static pressure in the stagnation zone of the jet is generally smaller than that without ultrasonic vibration. This may be due to the oscillation of the flow field near the workpiece during the vibration process, and the external energy is applied to the stagnation zone to break the

original balance, thereby reducing the static pressure value and facilitating the removal of materials.

Effect of Ultrasonic Vibration on the Jet Velocity Field

Based on results of previous studies (Qi et al., 2016; Qi et al., 2017), we analyze the change of the water jet velocity after adding an ultrasonic vibration field. **Figure 3** shows the vector diagram of the velocity field of the water jet without ultrasonic vibration. It can be seen that when the vertical water jet reaches the vicinity of the workpiece surface, the velocity V_y in the vertical direction decreases sharply, and the velocity V_x in the horizontal direction increases rapidly from the center to the surrounding. At the same time, due to the existence of the stagnation zone, the streamline in the central region of the water jet is not perpendicular to the workpiece surface, but rather deflects a certain angle.

Taking the surface of the workpiece as the reference system, the water flow velocities at 20 μm, 60 μm, and 100 μm from the surface of the workpiece are selected as the research object. When
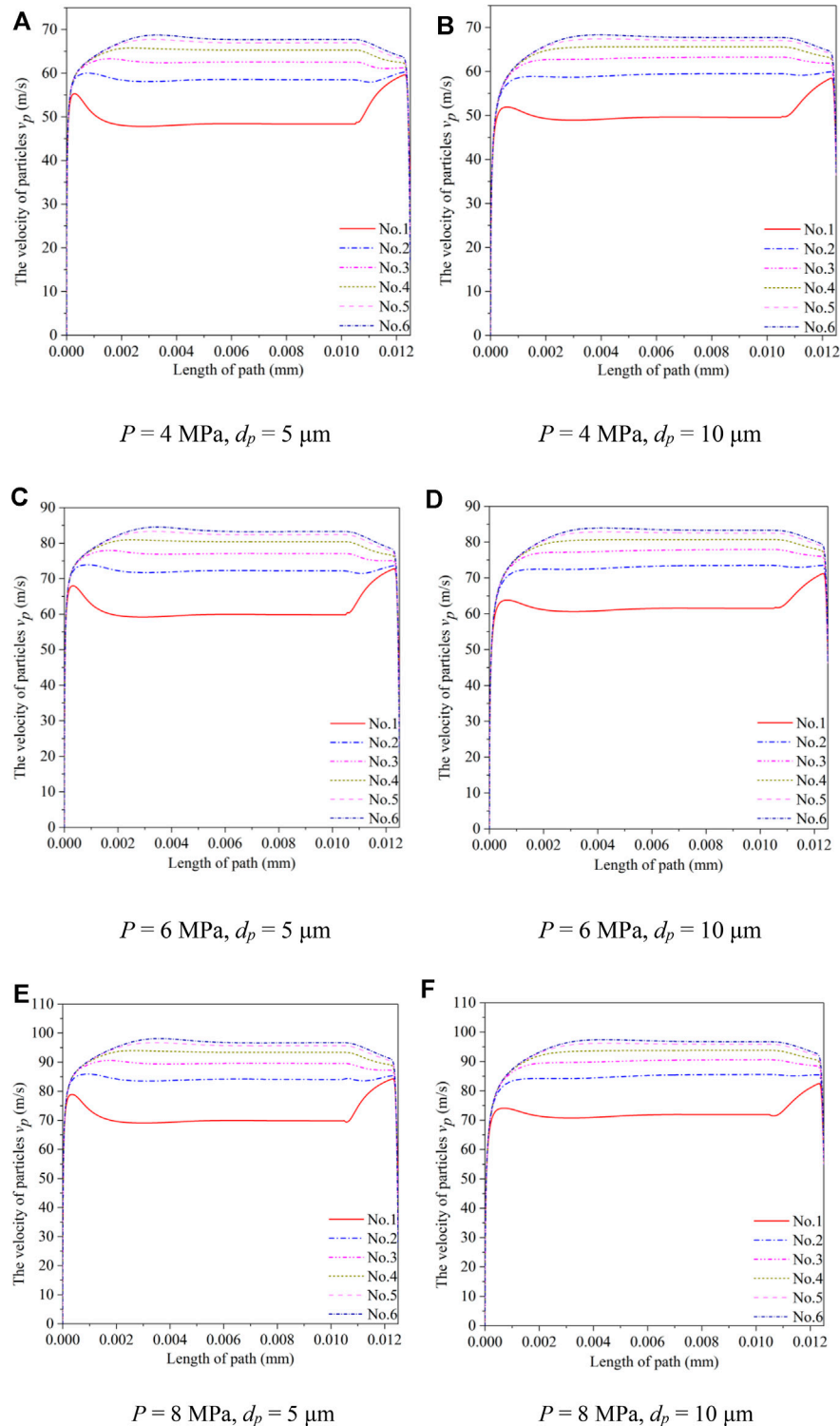
FIGURE 6 | Velocity changes of abrasive particles of different sizes in the flow field along the movement path. **(A)** P = 4 MPa, d_p = 5 μm, **(B)** P = 4 MPa, d_p = 10 μm, **(C)** P = 6 MPa, d_p = 5 μm, **(D)** P = 6 MPa, d_p = 10 μm, **(E)** P = 8 MPa, d_p = 5 μm, **(F)** P = 8 MPa, d_p = 10 μm.
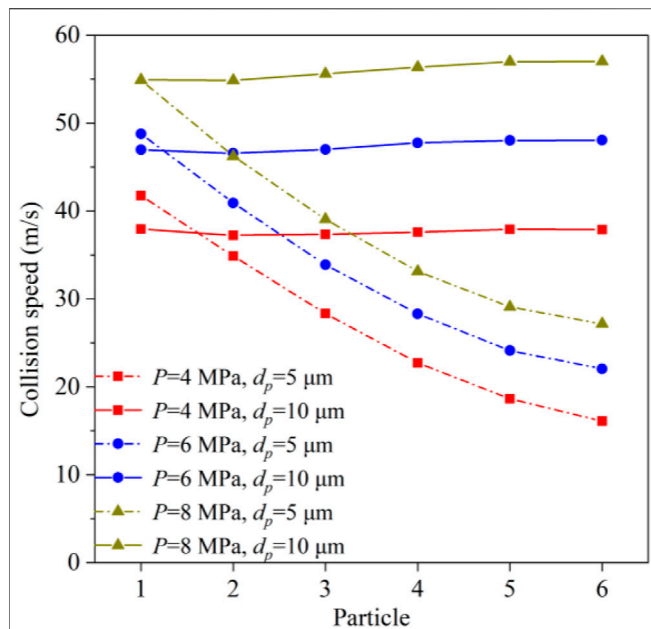
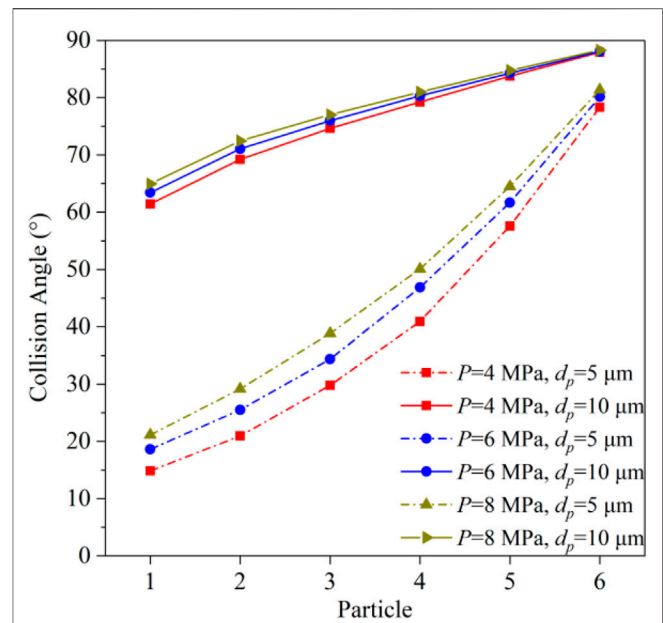FIGURE 7 | Collision speed of abrasive particles of two sizes.

FIGURE 8 | Collision angle of abrasive particles of two sizes.

the nozzle inlet pressures are 4 MPa, 6 MPa, and 8 MPa, the changes of the velocity components V_x and V_y at four moments in a cycle without ultrasonic vibration and after ultrasonic vibration is introduced are analyzed, as shown in **Figures 4A–I** and **Figures 5A–I**.

As displayed in **Figure 4**, after the introduction of the ultrasonic vibration, the horizontal component of the flow velocity shows a periodic change, which is slightly lower than that without ultrasonic vibration. The velocity components at time T and time $T/4$ are relatively close, and the velocity components at time $T/2$ and time $3T/4$ are relatively close. In the region near the jet center, the horizontal component of the flow velocity changes linearly with the position, and the magnitude is almost independent of the ultrasonic vibration.

Figure 5 shows that when $y = 20 \, \mu m$, near the center of the jet, the vertical component of the flow velocity at $T/4$, $3T/4$, and T in one period of ultrasonic vibration is smaller than that without ultrasonic vibration, and the vertical component of velocity at T is the smallest, while that at $T/2$ it is slightly larger than that without ultrasonic vibration. In the external flow field area far from the jet center, for the times $T/4$, $3T/4$, and T without ultrasonic vibration, the direction of the vertical component of the velocity reverses. After the reverse, the velocity component at time T is the largest, and the velocity component is the smallest without ultrasonic vibration, close to 0. From **Figure 5**, it can also be found that in terms of the influence of the jet pressure on the vertical component of the flow velocity near the workpiece surface, the flow velocity in the central area of jet erosion increases obviously with the increase of the jet pressure, while the vertical component of the flow velocity at the periphery does not change obviously.

Motion of Abrasive Particles in the Jet Flow Field
Effect of Particle Size on Particle Motion

In the simulation, we study the variation of the velocities of 5 and 10 μm Al_2O_3 abrasive particles with the length of the moving path in the flow field, as shown in **Figures 6A–F**. We extract six of the particles as the research objects, of which the No. One abrasive particle is at the edge and the No. Six abrasive particle is in the middle. The abrasive particles with two sizes reach a stable velocity in the nozzle, and the velocity is independent of the particle size. When approaching the workpiece, the abrasive particle velocity decreases rapidly, but the abrasive particle velocity with a large particle size decreases more slowly.

Figures 7, 8 show the velocities and angles of the No. one to six abrasive particles when they first collide with the workpiece in the jet field when the particle sizes are 5 and 10 μm. It can be seen from **Figures 7, 8**, that the initial impact velocity of the abrasive particles with a particle size of 5 μm gradually decreases from the edge of the jet to the center of the jet. When the abrasive particles first exit the nozzle, the velocity of the abrasive particles at the center of the jet is larger than that at the edge, indicating that the 5 μm abrasive particles lose a large amount of energy when passing through the stagnation zone of the jet, and the closer it is to the center, the greater the loss is. The collision angle increases gradually from the edge to the center, which is caused by the following effect of the abrasive particles on the fluid motion. When the particle size is 10 μm, the initial collision velocity of the abrasive particles is almost the same from the edge to the center, indicating that when the 10 μm abrasive particles pass through the stagnation zone, the velocity loss is not as large as that when the particle size is 5 μm. The collision angle also increases
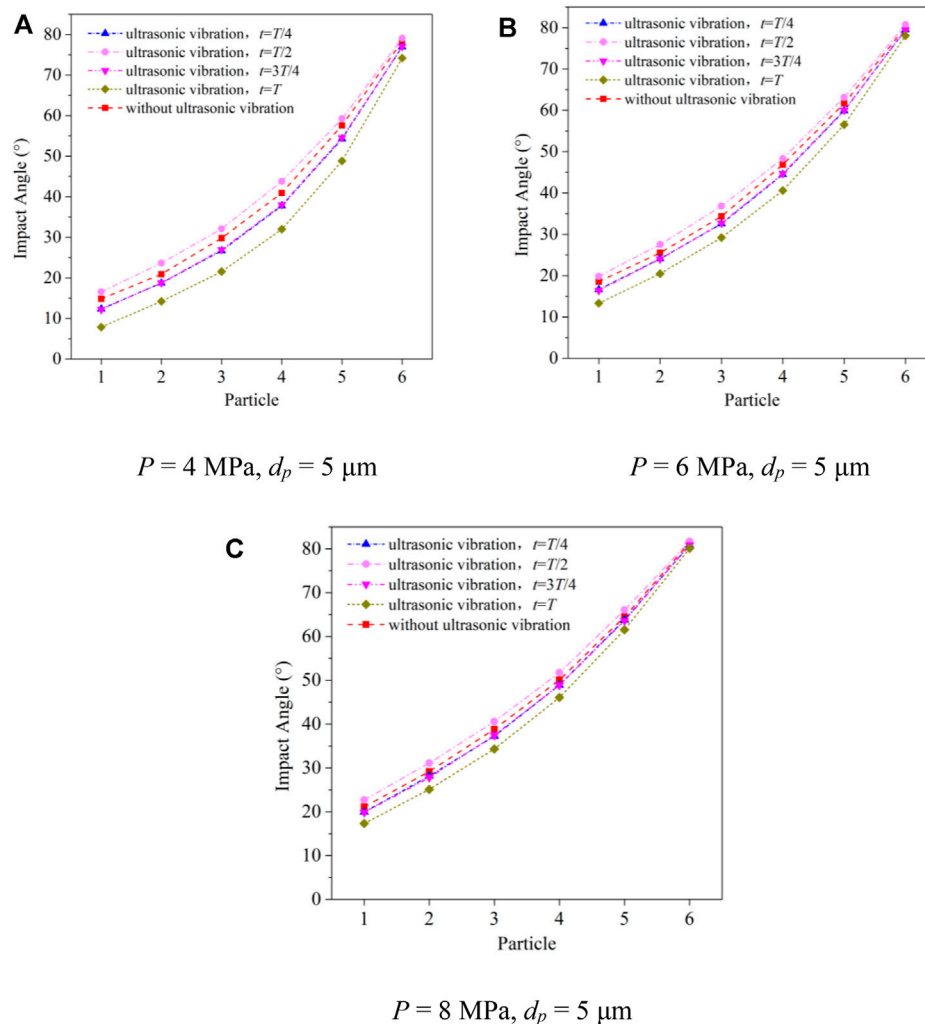
FIGURE 9 | Effect of ultrasonic vibration on the collision angle of the abrasive particles in the jet field. **(A)** $P = 4$ MPa, $d_p = 5$ μm, **(B)** $P = 6$ MPa, $d_p = 5$ μm, **(C)** $P = 8$ MPa, $d_p = 5$ μm.

gradually from the edge to the center, but the change is relatively small. Comparing the impact velocities and angles of the 5 and 10 μm abrasive particles, it can be found that the impact velocity of the 10 μm abrasive particles is significantly greater than that of 5 μm abrasive particles for the same conditions, which is also consistent with the calculation results of the kinetic energy formula. It can be seen from **Figure 8** that the maximum collision angle of the 10 μm abrasive particles reaches 88.31°, which is close to the vertical collision. Therefore, the 10 μm abrasive particles are more likely to cause the removal of brittle mode materials on the workpiece surface than the 5 μm abrasive particles.

Effect of Ultrasonic Vibration on Impact Angle Change of Abrasive Particles
Figures 9A–C reflect the changes of the angle of 5 μm abrasive particles before and after the introduction of ultrasonic

vibration in the jet field with inlet pressures of 4 MPa, 6 MPa, and 8 MPa.

From **Figures 9A–C**, it can be found that the initial impact angle of the abrasive particles is the smallest at time T and the largest at time $T/2$. At the same time, the initial impact angle of each abrasive particle at $T/2$ is larger than that without ultrasonic vibration, which has a positive effect on improving the "W" bottom morphology formed by micro-abrasive water jet erosion.

Effect of Ultrasonic Vibration on Erosion Rate of Workpiece Surface Materials
Comparing **Figures 10A–C,D–F**, it can be found that when the 10 μm abrasive particles are used, the material erosion rate in the stagnation zone is not much different from that around. When 5 μm abrasive particles are used, the material erosion
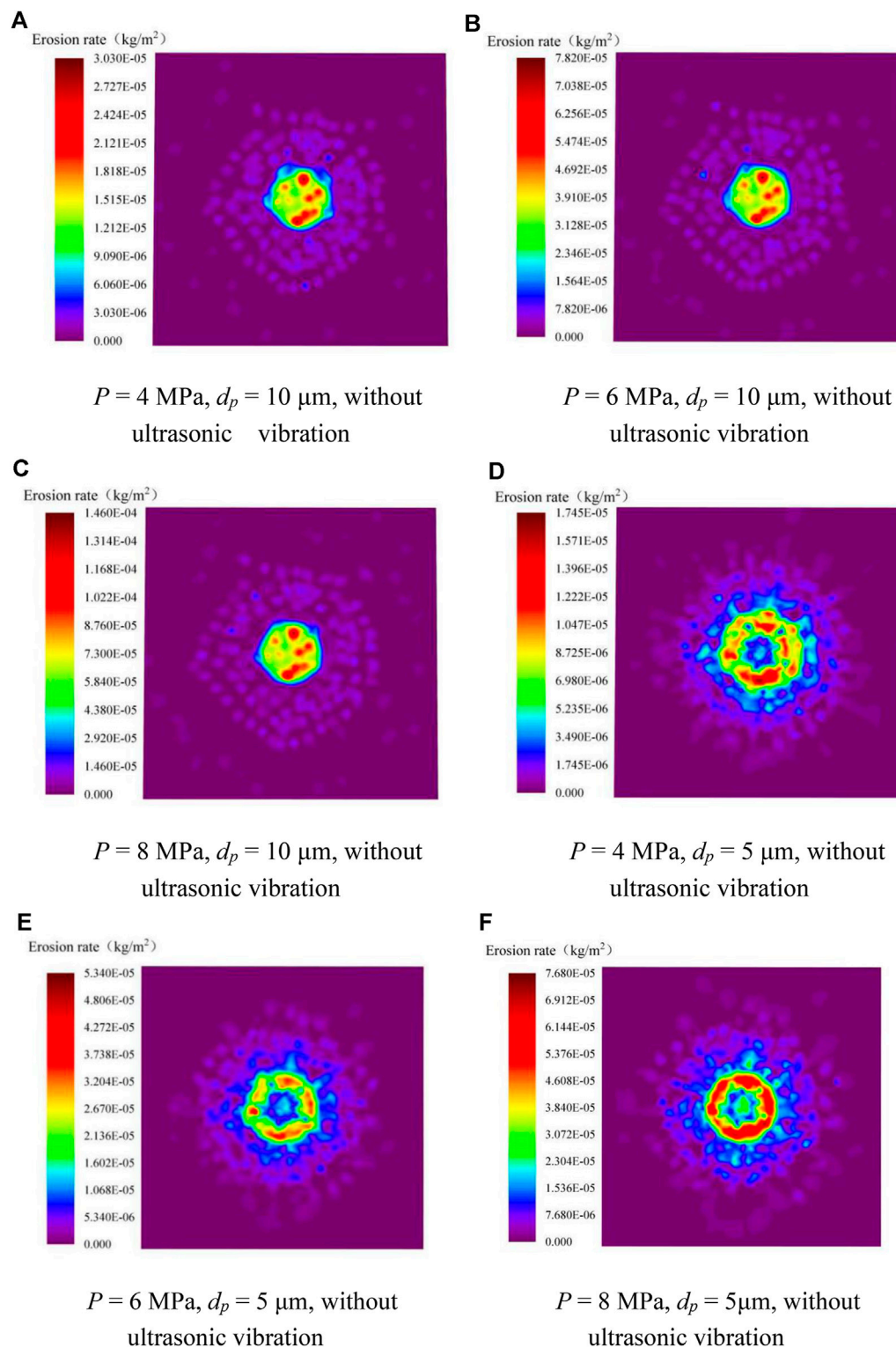
FIGURE 10 | Cloud map of material erosion rate on the workpiece surface. **(A)** P = 4 MPa, d_p = 10 μm, without ultrasonic vibration, **(B)** P = 6 MPa, d_p = 10 μm, without ultrasonic vibration, **(C)** P = 8 MPa, d_p = 10 μm, without ultrasonic vibration, **(D)** P = 4 MPa, d_p = 5 μm, without ultrasonic vibration, **(E)** P = 6 MPa, d_p = 5 μm, without ultrasonic vibration, **(F)** P = 8 MPa, d_p = 5 μm, without ultrasonic vibration, **(G)** P = 4 MPa, d_p = 5 μm, with ultrasonic vibration, **(H)** P = 6 MPa, d_p = 5 μm, with ultrasonic vibration, **(I)** P = 8 MPa, d_p = 5 μm, with ultrasonic vibration.

G

Erosion rate（kg/m²）

2.290E-05
2.061E-05
1.832E-05
1.603E-05
1.374E-05
1.145E-05
9.160E-06
6.870E-06
4.580E-06
2.290E-06
0.000

P = 4 MPa, d_p = 5 μm, with ultrasonic vibration

H

Erosion rate（kg/m²）

6.740E-05
6.066E-05
5.392E-05
4.718E-05
4.044E-05
3.370E-05
2.696E-05
2.022E-05
1.348E-05
6.740E-06
0.000

P = 6 MPa, d_p = 5μm, with ultrasonic vibration

I

Erosion rate（kg/m²）

1.055E-04
9.495E-05
8.440E-05
7.385E-05
6.330E-05
5.275E-05
4.220E-05
3.165E-05
2.110E-05
1.055E-05
0.000

P = 8 MPa, d_p = 5 μm, with ultrasonic vibration

FIGURE 10 | *(Continued).*

rate in the central region is significantly lower than that in the surrounding area. It can also be found from the figure that the maximum material erosion rate of the workpiece surface caused by 10 μm abrasive particles is significantly greater than that caused by 5 μm abrasive particles, but the erosion area is smaller than that caused by 5 μm abrasive particles. This is because, in the jet field, the 10 μm abrasive particles can maintain a large impact angle and velocity, and the distribution of the abrasive particle angles and velocities at different radial positions of the jet is more uniform, so it is more prone to material removal 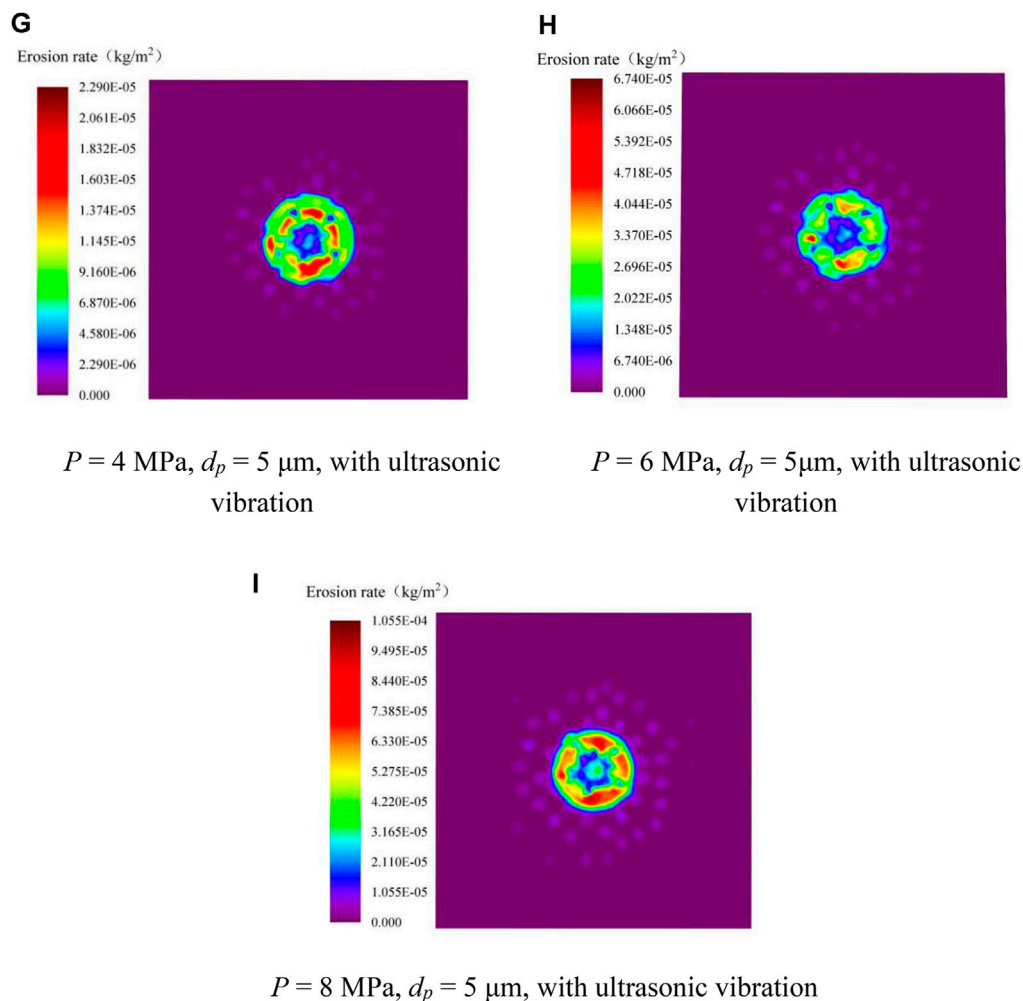in the brittle mode. Through the calculation of momentum equilibration numbers, we find that the small abrasive particles with the average diameter of 5 μm are more likely to follow the fluid flow streamlines and these particles deflect larger angle when impacting workpiece surface. While the average diameter of 10 μm under same experimental conditions are more likely to keep the original state of motion and impact the workpiece in a vertical direction. It is theoretically explained that the holes

processed by abrasives with smaller sizes have larger diameters.

Figures 10 D–F,G–I illustrate the fact that when 5 μm abrasive particles are applied to the workpiece, the material erosion rate in the direct impact area of the jet is significantly increased compared with that without ultrasonic vibration. The maximum erosion rate increases most obviously when the inlet pressure is 8 MPa. After calculation, it is determined that the increase is up to 37%, and the distribution of erosion is more uniform. However, the diameter of the erosion area caused by the abrasive particles on the surface of the workpiece is significantly reduced, which also indicates that the erosion of the workpiece by the jet is more concentrated after the ultrasonic vibration is applied.

Experimental Work

To achieve higher precision for the abrasive water jet processing of micro-holes, the corresponding processing device is designed and built independently, as shown in **Figure 11**. The device is
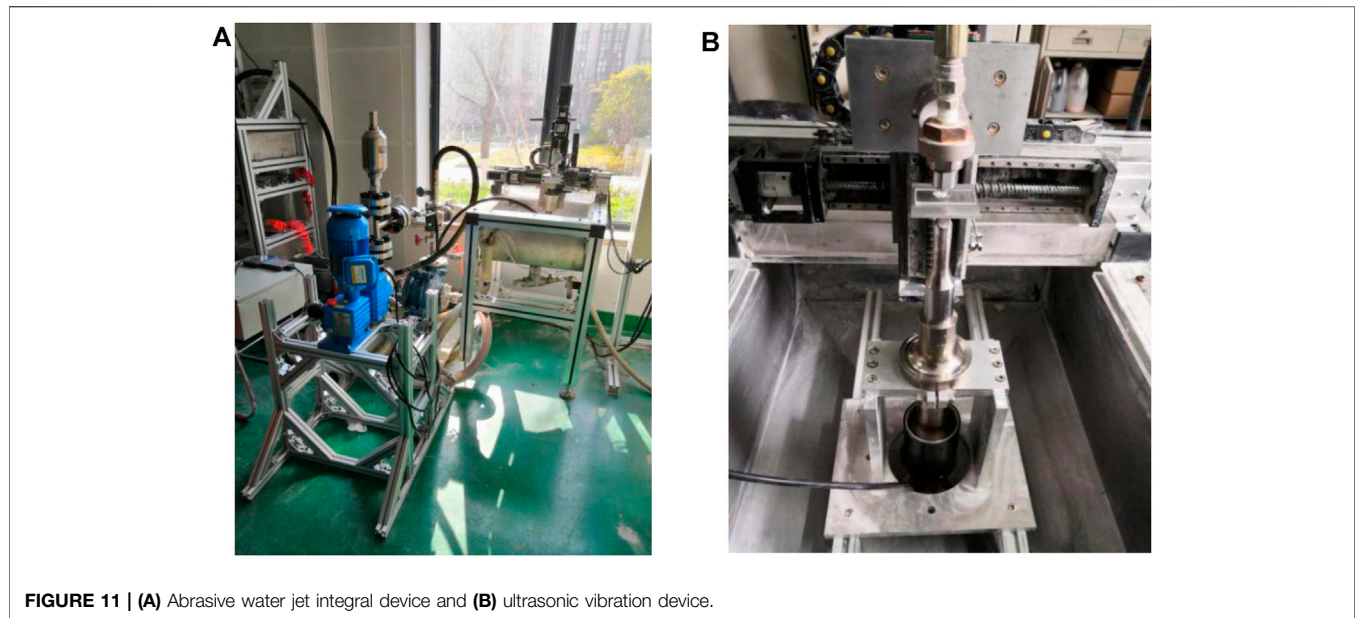
FIGURE 11 | (A) Abrasive water jet integral device and **(B)** ultrasonic vibration device.

TABLE 1 | Material properties of K9 glass for experiment.

Material	Density (kg/m^3)	Young's modulus (GPa)	Hardness (GPa)	Fracture Toughness (MPa·m$^{1/2}$)
K9 glass	2,520	82	7.7	0.82

TABLE 2 | Experimental process parameters and values.

Variables	Value
Abrasive mass concentration (%)	2
Standoff distance (mm)	2
Ultrasonic vibration frequency (kHz)	20
Amplitude of ultrasonic vibration (μm)	10
Average size of particle (μm)	5
Pressure (MPa)	4, 6, 8
Processing time (s)	20, 40, 60

composed of an abrasive water jet generating device, an ultrasonic vibration platform, and a three-dimensional motion platform. The pressurized equipment of this device is a diaphragm metering pump (LDB1/M910S) purchased from Germany. To carry out long-term stable processing and correct the pressure pulse fluctuation state of the metering pump at the same time, we install a pulse damper at the outlet of the pump. The nozzle connected with the hose is loaded on a three-dimensional motion platform with a fixture. The platform can achieve 0.001 mm precision control in the three directions of x, y, and z, which is convenient for adjusting the target distance between the nozzle and the workpiece. The workpiece is clamped on the ultrasonic vibration platform below the nozzle. The ultrasonic vibration platform has a vibration frequency of 20 kHz and the amplitude can be adjusted by itself. In all experiments, the ultrasonic vibration platform maintains an amplitude of 20 μm, and the distance

between the workpiece and the nozzle is 2 mm. The remaining experimental parameters, including the jet pressure, and processing time are attached in **Tables 1**, **2**.

The experimental design is explained as follows. Using alumina abrasive with an average particle size of five microns, the experimental processing time is divided into 20, 40, and 60 s. The water jet pressures are 4 MPa, 6 MPa, and 8 MPa. There are nine combinations. Then these nine combinations are tested independently with and without ultrasonic vibration. For the tests with these 18 conditions, each experiment needs to be repeated at least five times. The data obtained in each experiment is tested with a KEYENCE three-dimensional laser measuring microscope and the average value is taken, including the cross-section and bottom morphologies of the micropores, for further comparison and analysis.

RESULTS AND DISCUSSION

Based on the selected three sets of experimental photographs shown in **Figure 12** (images taken with a KEYENCE VHX-600E ultra-depth-of-field 3D microscope), it can be seen that the depth of the micro-hole increases significantly after the ultrasonic vibration is added, especially when the jet pressure is 8 MPa and the processing time is 60 s, and the depth increases by 52.4%. It can be seen from **Figure 13** that for the selected case of 8 MPa and 60 s with vibration, there is a good agreement between the simulation data and the
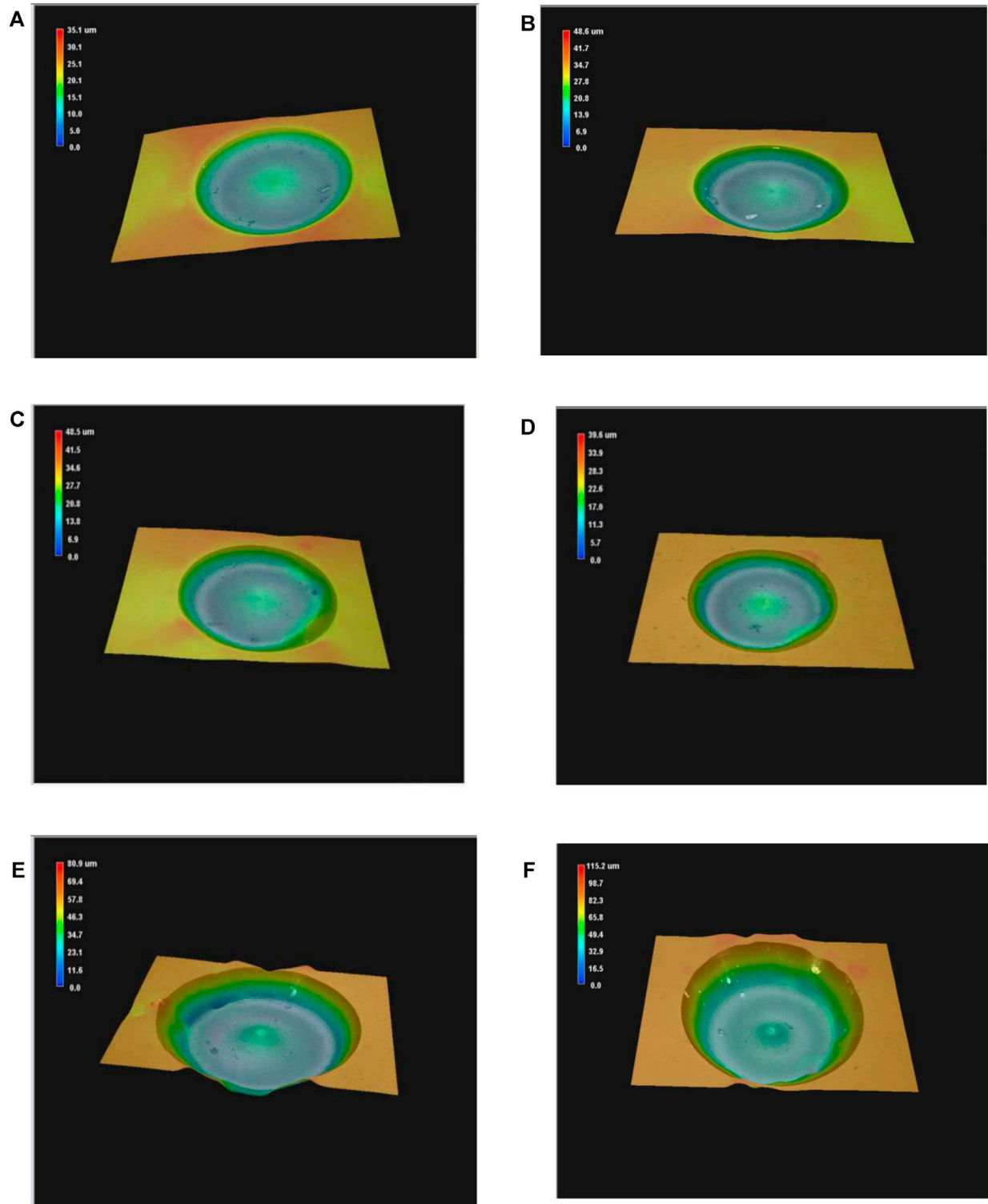
FIGURE 12 | Machining performance of micro-holes under experimental conditions: **(A)** P = 4 MPa; t = 60 s and without ultrasonic vibration; **(B)** P = 4 MPa; t = 60 s and with ultrasonic vibration; **(C)** P = 6 MPa; t = 40 s and without ultrasonic vibration; **(D)** P = 6 MPa; t = 40 s and with ultrasonic vibration; **(E)** P = 8 MPa; t = 60 s and without ultrasonic vibration; **(F)** P = 8 MPa; t = 60 s and with ultrasonic vibration.
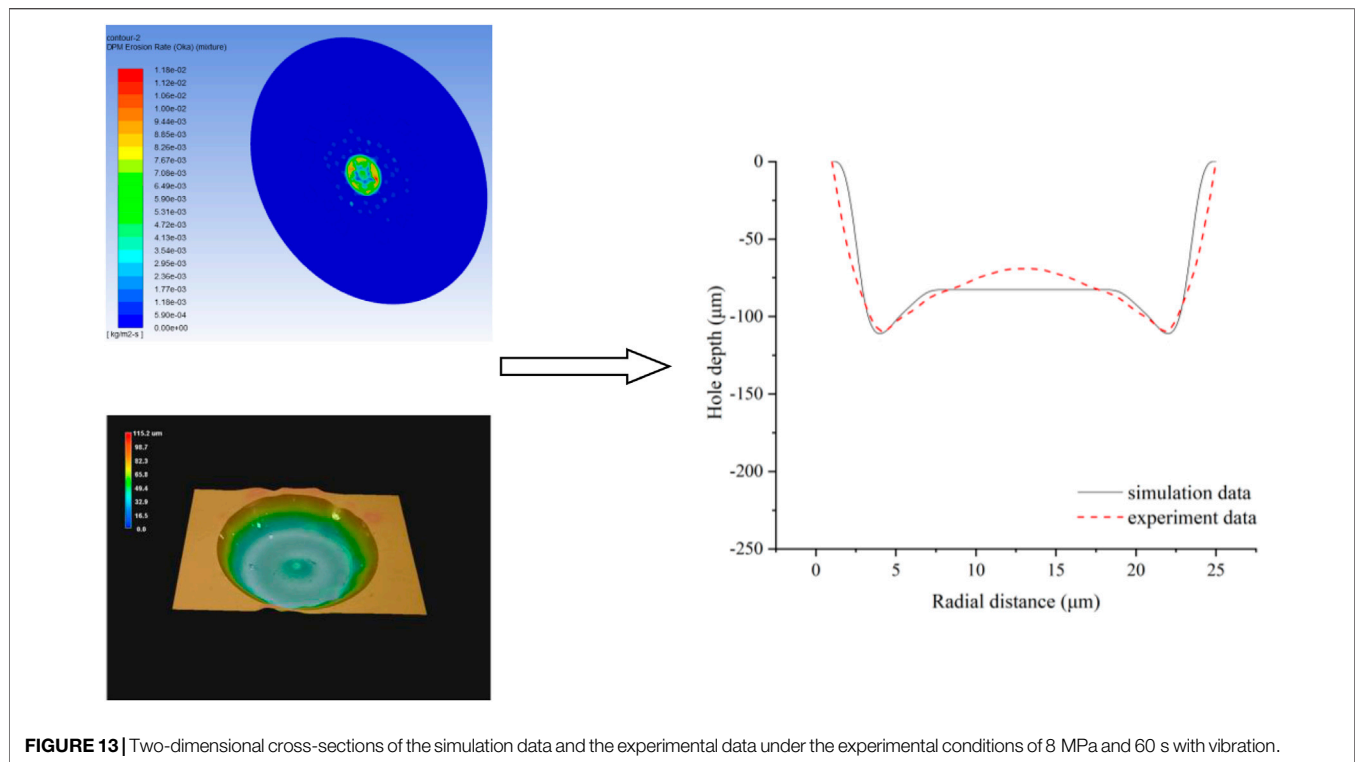
FIGURE 13 | Two-dimensional cross-sections of the simulation data and the experimental data under the experimental conditions of 8 MPa and 60 s with vibration.

experimental data in the two-dimensional section. In addition, to more intuitively analyze the proximity of the prediction model, a three-dimensional diagram of the deviation between the prediction model and the experimental data is created, and the mean square deviation is marked in the figure. After completing the experiment of an ultrasonic-assisted micro-abrasive water jet impacting K9 glass, we determine whether non-ultrasonic vibration and the changing of the amplitude have a better effect on the machining process, and a series of simulation calculations are carried out with our proposed prediction model.

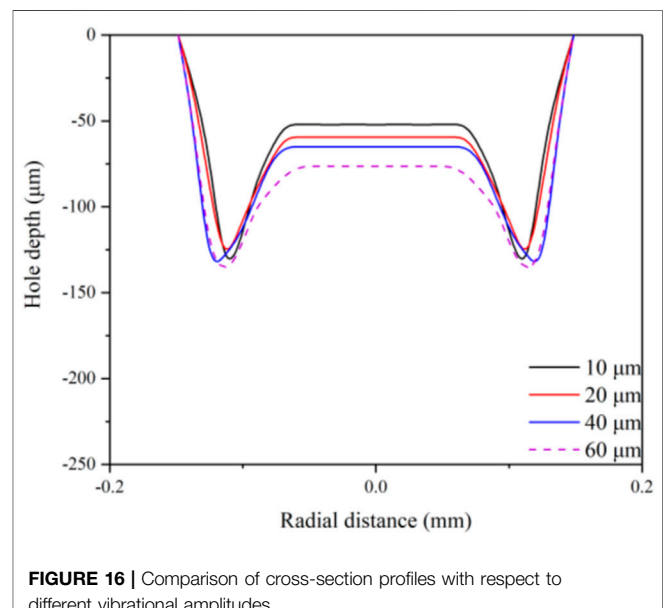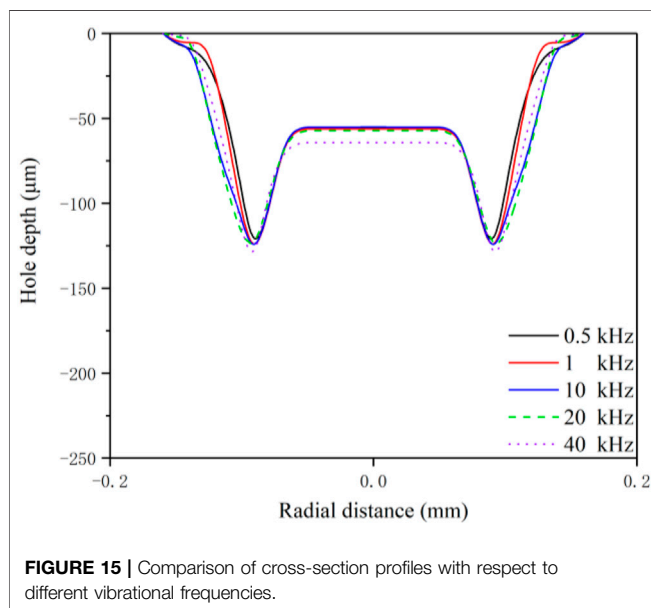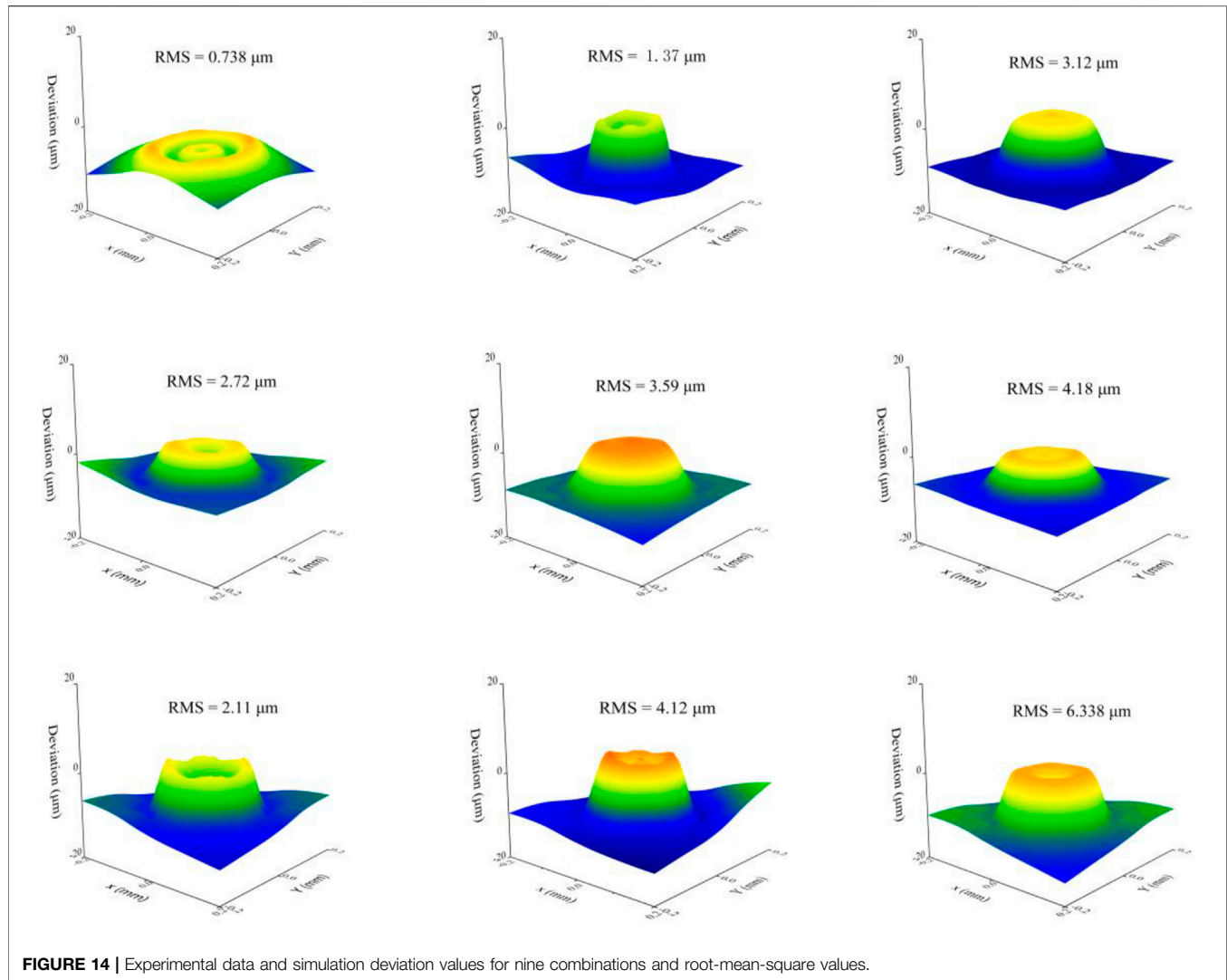In **Figure 12**, it can be seen that when 5 μm abrasive is used to impact the workpiece, the cross-sections of the micro-holes at 4 MPa, 6 MPa, and 8 MPa all show a "W" shape. However, it can also be found that for the same experimental conditions, the addition of ultrasonic vibration to the workpiece not only increases the depth of the micro-holes but also improves the quality and morphology of the bottom surface. More of the material at the center of the micro-holes is removed to form a flatter "W"-shaped profile. In the experiment, we calculate the energy threshold to judge the material removal mechanism. With the change of pressure, the change of abrasive particle size and the introduction of ultrasonic vibration, the material removal mechanism also changed correspondingly. According to our research, the ultrasonic vibration velocity is far less than the abrasive impact velocity, so it has little effect on the kinetic energy. Ultrasonic vibration has more influence on particle trajectory (Qi et al., 2021). In the experiment, due to

inevitable factors such as the particle-to-particle collision and particle size, the prediction model often has large deviations. After our further improvement of the various conditions, in **Figure 14**, as shown for the nine groups experimental data, the deviation value from the simulation data, the variance value relative to the depth and diameter of the micro-holes, the deviation value, and the root-mean-square value of each group of experiments are kept within a good range. Therefore, the prediction model can predict the experiment well.

After obtaining a high-quality prediction model, we change the dynamic mesh motion frequency of the prediction model while keeping the processing conditions such as the amplitude, pressure, and incident angle unchanged. Through the cross-sectional section shown in **Figure 15**, the vibration frequency can be found. For the cases of the low frequencies of 0.5, 1, and 10 kHz, the depth and the morphology of the workpiece are consistent with the results of the ultrasonic vibrations at 20 and 40 kHz.

As shown in **Figure 16**, we adjust the amplitude of the moving mesh while keeping the other conditions unchanged. It can be seen from the figure that the removal rate of the W-shaped middle convex part at the bottom of the workpiece is increased, and the bottom processing efficiency has an amplitude of 60 μm. The processing efficiency of the bottom bump with an amplitude of 10 μm is increased by about 41%. In micro-abrasive water jet processing, Qi et al. introduced a vivid term in the w-shaped middle protrusion, called a hump peak (Qi et al., 2021). The ratio of the hump peak to the depth of the micro-holes decreased,

FIGURE 14 | Experimental data and simulation deviation values for nine combinations and root-mean-square values.

FIGURE 15 | Comparison of cross-section profiles with respect to different vibrational frequencies.

FIGURE 16 | Comparison of cross-section profiles with respect to different vibrational amplitudes.

which meant that the material removal rate increased, and the bottom surface of the micro-holes became flatter. This factor plays an important role in obtaining better-processed micro-holes.

Based on the above analysis, it is obvious that the prediction model we designed has extremely high accuracy. It can be used to guide future experiments. The impact of the vibration frequency and amplitude changes obtained with the prediction model on the processing effect could allow researchers to have a more effective and reliable plan for the selection of the vibration frequency and amplitude of auxiliary processing for the same type of micro-abrasive water jet processing in the future.

CONCLUSION

To effectively predict the machining of hard and brittle materials with an ultrasonic vibration-assisted micro-abrasive water jet, a mixture model, standard k-ε model, discrete phase model, and dynamic mesh model are used to analyze the effects of the ultrasonic vibration on the static pressure, jet velocity field, abrasive particle motion state, and material erosion rate in the stagnation zone. Through the mathematical model established, we find ultrasonic vibration has a significant influence on the jet velocity field, abrasive particle motion state, and the static pressure in the stagnation zone of the jet is generally smaller than that without ultrasonic vibration. At the same time, the erosion rate increased significantly. By comparing the experimental data

with the simulation data, the mean square difference is calculated to confirm the accuracy of the model. Next, the model was used to further analyze the optimal frequency of ultrasonic-assisted machining and the influence of the amplitude on the machining effect. The simulation results showed that in the experiment, the increase in amplitude could effectively increase the machining efficiency and improve the bottom flatness. However, the results were favorable when the vibration frequency was lower. These conclusions could provide effective guidance for future similar ultrasonic vibration-assisted machining experiments.

DATA AVAILABILITY STATEMENT

The raw data supporting the conclusion of this article will be made available by the authors, without undue reservation.

AUTHOR CONTRIBUTIONS

Conceptualization, ZF; Data curation, ZC; Formal analysis, ZC; Investigation, ZC; Software, SQ; Writing—original draft, ZC; Writing—review and editing, ZF.

FUNDING

REFERENCES:

Anwar, S., Axinte, D. A., and Becker, A. A. (2013). Finite Element Modelling of Overlapping Abrasive Waterjet Milled Footprints. *Wear* 303, 426–436. doi:10.1016/j.wear.2013.03.018

Beaucamp, A., Katsuura, T., and Takata, K. (2018). Process Mechanism in Ultrasonic Cavitation Assisted Fluid Jet Polishing. *CIRP Ann.* 67, 361–364. doi:10.1016/j.cirp.2018.04.075

Chen, H., Xu, Q., Wang, J., Li, P., Yuan, J., Lyu, B., et al. (2021). Effect of Surface Quality on Hydrogen/helium Irradiation Behavior in Tungsten. *Nucl. Eng. Tech.* In Press. doi:10.1016/j.net.2021.12.006

Espulgar, W., Aoki, W., Ikeuchi, T., Mita, D., Saito, M., Lee, J.-K., et al. (2015). Centrifugal Microfluidic Platform for Single-Cell Level Cardiomyocyte-Based Drug Profiling and Screening. *Lab. Chip* 15, 3572–3580. doi:10.1039/c5lc00652j

Hu, W., Teng, Q., Hong, T., Saetang, V., and Qi, H. (2022). Stress Field Modeling of Single-Abrasive Scratching of BK7 Glass for Surface Integrity Evaluation. *Ceramics Int.* 48, 12819–12828. doi:10.1016/j.ceramint.2022.01.153

Huang, C. Z., Hou, R. G., Wang, J., Lu, X. Y., and Zhu, H. T. (2007). Three-dimensional Simulation of Liquid-Solid Two-phase Flow inside the Abrasive Water Jet Nozzle. *Key Eng. Mater.* 329, 329–334. doi:10.4028/www.scientific.net/kem.329.329

Ji, R., Zhang, L., Zhang, L., Li, Y., Lu, S., and Fu, Y. (2022). Processing Method for Metallic Substrate of Liquid Metal Lapping-Polishing Plates. *Front. Mater.* 9, 896346. doi:10.3389/fmats.2022.896346

Lee, J.-W., Ha, S.-J., Cho, Y.-K., Kim, K.-B., and Cho, M.-W. (2015). Investigation of the Polishing Characteristics of Metal Materials and Development of Micro MR Fluid Jet Polishing System for the Ultra Precision Polishing of Micro Mold Pattern. *J. Mech. Sci. Technol.* 29, 2205–2211. doi:10.1007/s12206-015-0136-8

Li, T., Takahata, K., and Gianchandani, Y. (2021). "Chapter 4 - Batch Mode Microelectro-Discharge Machining," in *Micro Electro-Fabrication*. Editors

T. Saleh, M. S. Mohamed Ali, and K. Takahata (Elsevier), 89–114. doi:10.1016/b978-0-12-820049-0.00003-7

Li, W., Wang, J., Zhu, H., and Huang, C. (2014). On Ultrahigh Velocity Micro-particle Impact on Steels - A Multiple Impact Study. *Wear* 309, 52–64. doi:10.1016/j.wear.2013.10.011

Liu, Z., Nouraei, H., Spelt, J. K., and Papini, M. (2015). Electrochemical Slurry Jet Micro-machining of Tungsten Carbide with a Sodium Chloride Solution. *Precision Eng.* 40, 189–198. doi:10.1016/j.precisioneng.2014.11.009

Mccarthy, M. J., and Molloy, N. A. (1974). Review of Stability of Liquid Jets and the Influence of Nozzle Design. *Chem. Eng. J.* 7, 1–20. doi:10.1016/0300-9467(74)80021-3

Narayanan, C., Balz, R., Weiss, D. A., and Heiniger, K. C. (2013). Modelling of Abrasive Particle Energy in Water Jet Machining. *J. Mater. Process. Tech.* 213, 2201–2210. doi:10.1016/j.jmatprotec.2013.06.020

Nguyen, T., Liu, D., Thongkaew, K., Li, H., Qi, H., and Wang, J. (2018). The Wear Mechanisms of Reaction Bonded Silicon Carbide under Abrasive Polishing and Slurry Jet Impact Conditions. *Wear* 410-411, 156–164. doi:10.1016/j.wear.2018.06.001

Qi, H., Qin, S., Cheng, Z., Teng, Q., Hong, T., and Xie, Y. (2021). Towards Understanding Performance Enhancing Mechanism of Micro-holes on K9 Glasses Using Ultrasonic Vibration-Assisted Abrasive Slurry Jet. *J. Manufacturing Process.* 64, 585–593. doi:10.1016/j.jmapro.2021.01.048

Qi, H., Shi, L., Teng, Q., Hong, T., Tangwarodomnukun, V., Liu, G., et al. (2022). Subsurface Damage Evaluation in the Single Abrasive Scratching of BK7 Glass by Considering Coupling Effect of Strain Rate and Temperature. *Ceramics Int.* 48, 8661–8670. doi:10.1016/j.ceramint.2021.12.077

Qi, H., Wen, D., Lu, C., and Li, G. (2016). Numerical and Experimental Study on Ultrasonic Vibration-Assisted Micro-channelling of Glasses Using an Abrasive Slurry Jet. *Int. J. Mech. Sci.* 110, 94–107. doi:10.1016/j.ijmecsci.2016.03.013

Qi, H., Wen, D., Yuan, Q., Zhang, L., and Chen, Z. (2017). Numerical Investigation on Particle Impact Erosion in Ultrasonic-Assisted Abrasive Slurry Jet Micro-machining of Glasses. *Powder Tech.* 314, 627–634. doi:10.1016/j.powtec.2016.08.057

Yeo, L. Y., Chang, H.-C., Chan, P. P. Y., and Friend, J. R. (2011). Microfluidic Devices for Bioapplications. *Small* 7, 12–48. doi:10.1002/smll.201000946

Zhu, H., Zhang, Z., Xu, K., Xu, J., Zhu, S., Wang, A., et al. (2019). Performance Evaluation and Comparison between Direct and Chemical-Assisted Picosecond Laser Micro-trepanning of Single Crystalline Silicon. *Materials (Basel)* 12, 41. doi:10.3390/ma12010041

Control Mechanism of Particle Flow in the Weak Liquid Metal Flow Field on Non-Uniform Curvature Surface Based on Lippmann Model

Li Zhang[1,2], Bingjun Zheng[1,2], Yi Xie[3,4]*, Renquan Ji[1,2], Yanbiao Li[1,2] and Wenbing Mao[1,2]

[1]College of Mechanical Engineering, Zhejiang University of Technology, Hangzhou, China, [2]Key Laboratory of Special Purpose Equipment and Advanced Processing Technology at Zhejiang University of Technology, Ministry of Education, Hangzhou, China, [3]School of Management Engineering and E-Business, Zhejiang Gongshang University, Hangzhou, China, [4]Contemporary Business and Trade Research Center of Zhejiang Gongshang University, Hangzhou, China

In order to realize the uniform distribution in the abrasive flow polishing of the titanium alloy workpiece with curved surface, a novel method based on the liquid metal-abrasive flow machining technology is proposed in this study. Based on the SST k-ω model, Preston model and fluid flow particle tracking model, the COMSOL software is employed to study the dynamic characteristics of liquid metal-abrasive flow under different AC electric field conditions, and the two-phase flow field is used to simulate the liquid state, the movement of liquid metal particles on the surface of the workpiece and the varitation of the Pv value in the near-wall region. It is found from numerical simulation results that the average Pv value in the strong flow field is 23,718.8 W/m^2, and that in the weak flow field is 5,427.3 W/m^2. By the assistance of the electric filed with the voltage of AC 36 V, the average Pv value of the liquid metal particles in the weak flow field is found to be 10,948.6 W/m^2 with an increase of 101.7%. Therefore, to properly control the electric field strength, the movement of liquid metal in the flow field can be found to be controlled, and hence improving the uniformity of the turbulent kinetic energy on the workpiece surface and improving the processing quality.

Keywords: curved surface, abrasive flow polishing, gallium-based liquid metal, weak flow field, polishing uniformity

INTRODUCTION

With the development of aerospace science and technology, the performance requirements of aero-engine has been greatly improved. As one of the core components in aero-engine, aviation blades play an important role in improving the overall performance of the engine (Huang et al., 2021). The profile accuracy of the blade has an important impact on its aerodynamic performance, and the aero-engine blade with poor profile accuracy would result in its fatigue failure, deformation or fracture under high-temperature and high-pressure environments (Huai et al., 2017; Yao et al., 2020).

To ensure the stability of the airflow field and reduce the energy loss of airflow, the aero-engine blade has a gradually increasing twist angle from the blade root to the blade tip, which makes the curvature of blade surface and is a typical non-uniform curvature surface part. The workpiece with non-uniform curvature surface mainly has special characteristics, such as a certain curvature with the concavity and convexity. At present, the workpiece with non-uniform curvature surfaces is mainly processed by manual polishing, grinding wheel polishing, and belt polishing. Manual polishing has

disadvantages of low efficiency, high labor intensity and unstable machining quality (Zhu et al., 2021). However, the processing accessibility of the grinding wheel for the complex inner surface is not suitable, and in the grinding wheel polishing process, the grinding heat will be generated in the contact area and the thermal damage will often occur on the target surface (He et al., 2018; Huai et al., 2019; Xian et al., 2020). Moreover, due to the elastic contact between the belt grinding and workpiece, there are many factors affecting the material removal process, and hence leading to the difficulty in controlling the material removal rate by belt grinding (Luo et al., 2020).

Abrasive flow polishing is an effective surface processing method, which has the good profiling properties and is suitable for processing the non-uniform curvature surface. However, under the strong action of the abrasive flow, the machined surface will leave processing stripes with obvious directionality, and it will also cause the workpiece to be deformed (Hu et al., 2022; Qi et al., 2022). In addition, the non-uniform curvature of the workpiece makes the flow field to be uneven on the target surface, which would result in the insufficient-polishing at the weak flow field surface while the over-polishing at the strong flow field, and hence affecting the quality of the machined surface (Wang et al., 2018).

To improve the uniformity of the abrasive flow polishing process, Zhai et al. combined the vibration with the chemical mechanical polishing for improving the polishing uniformity of silicon wafer during the chemical mechanical polishing process (Zhai et al., 2017). By adding the ultrasonic vibration into the abrasive flow, Beaucamp et al. increased the turbulence intensity of the flow field for improving the surface polishing quality (Beaucamp et al., 2018). Moreover, Liu proposed the electrochemical assisted abrasive flow polishing method, which used electrochemical dissolution to improve the polishing efficiency and uniformity (Liu, 2018). Zhu proposed a novel abrasive flow polishing method by using the magnetic particles, and it could use the effective magnetic field control to determine the movement of magnetic particles and then improving the polishing uniformity (Zhu, 2020).

In this paper, a novel liquid metal-abrasive flow polishing method which consists of the gallium-based liquid metal, weak viscous fluid and abrasive particles is proposed to overcome the difficulties in polishing non-uniform curvature surfaces of titanium alloy. A liquid metal-abrasive flow model is first developed, and then the dynamic characteristics of liquid metal under the action of the flow field and electric field are tracked and analyzed numerically, by which the mechanism of liquid metal-abrasive flow polishing process can be further investigated. Gallium-based liquid metal has been widely used due to its good fluidity, high chemical stability, excellent electrical conductivity and non-toxicity (Daeneke et al., 2018). Gallium-based liquid metal is a liquid at room temperature, which has a small cutting effect on the target surface, and its driving characteristics under the action of the electric field can be used to realize the controlled flow of liquid metal particles, so as to increase the kinetic energy of abrasive particles and improve the uniformity of the overall polishing.

FIGURE 1 | Principle of liquid metal-abrasive flow polishing: 1-Abrasive particle, 2-Electrode, 3-Liquid metal particle, 4-Workpiece, a-Inactive area, b-Buffer area, c-Active area.
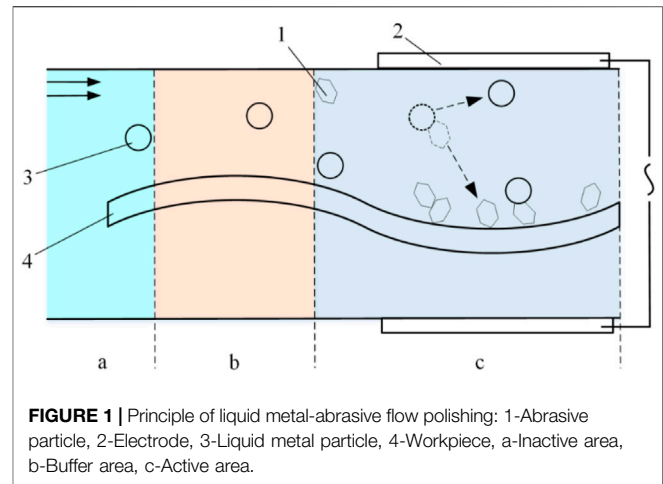
PRINCIPLE OF LIQUID METAL-ABRASIVE FLOW POLISHING

In the abrasive flow polishing process, due to the characteristics of the curved surface, the flow field on the target surface is not uniform, which could result in a certain difference in terms of the turbulent kinetic energy at different regions of the workpiece, and the average of turbulent kinetic energy $\overline{I_T}$ can be defined as follows:

$$\overline{I_T} = \frac{\sum_1^N I_{T_i}}{N} \tag{1}$$

where N is the number of workpiece surface elements and I_{T_i} is the turbulent kinetic energy at the unit surface of the workpiece. When the average turbulent kinetic energy of a certain area on the target surface is less than the average turbulent kinetic energy on the entire target surface, this certain area is defined as a weak flow field. Due to the turbulent kinetic energy difference between the weak flow field and the strong flow field, the cutting performance of the abrasive particles in these two regions is different as well, and hence affecting the overall surface polishing uniformity.

Liquid metal-abrasive flow machining combines the gallium-based liquid metal particles with the abrasive flow. By applying an electric field at the weak flow field, it would enhance the movement of abrasive particles in the weak flow field and improve their cutting performance. The abrasive particles could move randomly under the action of the liquid carrier in the turbulent flow channel, and perform the random cutting actions on the target surface, thereby realizing the polishing of the target surface. The principle of liquid metal-abrasive flow polishing is shown in **Figure 1**.

According to the influence of electric field on liquid metal particles, three areas can be divided as shown in **Figure 1**, i.e., inactive area, buffer area and active area. In the inactive area, the effect of the electric field on liquid metal particles is weak, which can be considered as particles only affected by the flow field. When the liquid metal particles are close to the electric field, that is, entering the buffer area these particles begin to be

FIGURE 2 | Schematic of the electric field force of liquid metal particles.
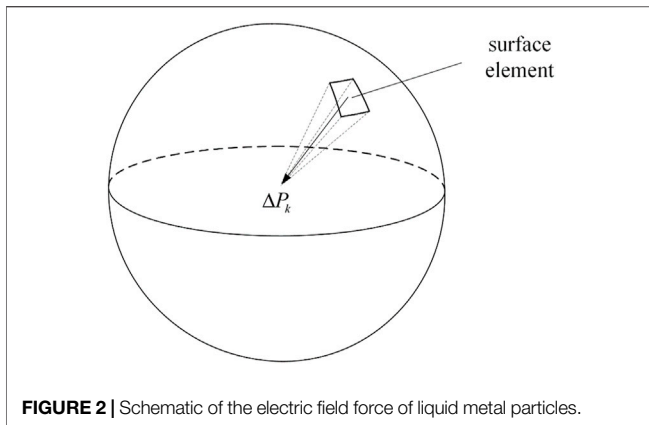
affected by the electric field, and the interactions between the liquid metal particles and the abrasive particles become frequently, which can increase the kinetic energy of the abrasive particles. The, when the liquid metal particles enter the active area, the effect of the electric field on these particles is significantly enhanced, and a large number of collisions occur between the liquid metal particles and abrasive particles, which makes the impacts of abrasive particles on the target surface more frequently, thereby further improving their cutting performance.

MATERIAL REMOVAL MODEL OF LIQUID METAL-ABRASIVE FLOW POLISHING
Modelling of Force Caused by the Liquid Metal Under the Electric Field

The gallium-based liquid metal reacts slowly with NaOH to produce $[Ga(OH)_4]^-$ ions, which carries a large amount of negative charge on the surface of liquid metal droplets. These charges will form an electric double layer corresponding to the free ions. When there is no voltage applied externally, these negative ions are uniformly distributed on the surface of the liquid metal droplet, where the surface tension of the liquid metal droplet is symmetric. When the external electric field is applied, the surface charge of the liquid metal is redistributed due to the good conductivity of the liquid metal, and the electric equilibrium state can be reached according to the Lippmann equation:

$$\gamma = \gamma_0 - \frac{cV^2}{2} \tag{2}$$

Where γ, c, and V are, respectively, the surface tension, the capacitance and the potential difference across the electrical double layer. γ_0 is the maximum surface tension when $V = 0$. Thus, it can be found that the driving force of liquid metal particles is the resultant force of the driving force on the unit surface, as shown in **Figure 2**.

The electric field driving force F_E can be expressed as:

$$F_E = \sum_{k=1}^{n} \Delta P_k \frac{S}{n} \tag{3}$$

where n is the number of surface units with the same area and capacitance divided by the surface of liquid metal particles, S is the surface area of liquid metal particles, ΔP_k is the surface pressure difference of surface element k, and the direction points to the curvature center of the surface element. According to the Young–Laplace equation it can obtain that:

$$\Delta P_k = \frac{2\gamma_k}{R} = \frac{2\left[\gamma_0 - \frac{c}{2}(V_0 + \Delta u_k)^2\right]}{R} \tag{4}$$

where R is the radius of curvature, Δu_k is the change of the potential difference between the two ends of the electric double layer on the surface element k under the action of an external electric field, δV_0 is the initial potential of the electric double layer Its value is the ratio of charge to capacitance in the electric double layer (Yang et al., 2016; Li et al., 2019). Since an AC electric field is applied externally, the surface of the liquid metal is an induced electric double layer, and its potential difference changes can be taken from:

$$\Delta u_k = \frac{1}{1 + \delta} Re\left(\left(\tilde{\varnothing}_{AC} - \tilde{\varnothing}_{AC}^O\right)e^{j\omega t}\right) \tag{5}$$

where δ is the surface capacitance ratio, $\tilde{\phi}_{AC}$ is the AC potential outside the electric double layer, $\tilde{\phi}_{AC}^o$ is the liquid metal body potential, and ω is the AC signal frequency.

Material Removal Modelling of the Liquid Metal-Abrasive Flow Polishing Process

The Preston equation is an empirical formula widely used in developing the material removal model in the abrasive machining technology, which can be taken from:

$$\Delta z = \int_0^t k_p pv dt \tag{6}$$

where Δz is the amount of material removal, k_p includes some factors related to the properties of the abrasive, p is the contact pressure of abrasive particles in the near-wall region and v is the relative velocity of abrasive particles in the near-wall region (Ji et al., 2011).

In the liquid metal-abrasive flow polishing process, both the liquid metal particle size and the abrasive particle size will have a certain influence on k_p. When the liquid metal particles are too large, they will be deposited at the bottom of the flow field, and the driving effect of the abrasive particles in the weak flow field decrease, thereby reducing the material removal amount. If the diameter of the liquid metal particles is too small, the driving force for the abrasive particles is small and the control effect seems not good. The liquid metal-abrasive flow polishing method mainly uses the solid-liquid two-phase flow in a turbulent state to produce abrasive cutting actions on the target surface. During this process, when the diameter of the abrasive particles is large, the force on the target surface is large, but it is not conducive to the formation of turbulent flow with large abrasive particles, so that the abrasive particles should be of appropriate size.
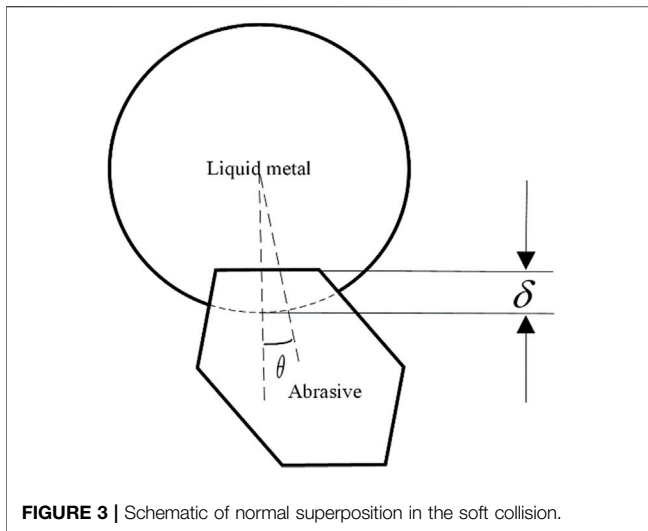
FIGURE 3 | Schematic of normal superposition in the soft collision.

When the abrasive particles contact with the target surface, the abrasive particles will squeeze the contact point and generate the contact pressure, which can be expressed as:

$$p = \sqrt{\frac{4E^*F_N}{\sqrt{3}}} \tag{7}$$

where E^* is the elastic contact modulus between the target surface and the abrasive particles, F_N is the normal force acting on the abrasive particles (Dong, 2012). In the weak flow field, the force between the liquid metal particles and the abrasive particles is weak, so that the force of liquid metal particles on the abrasive particles is mainly considered.

Since the hardness of liquid metal particles is much less than the hardness of abrasive particles, so that when these two particles
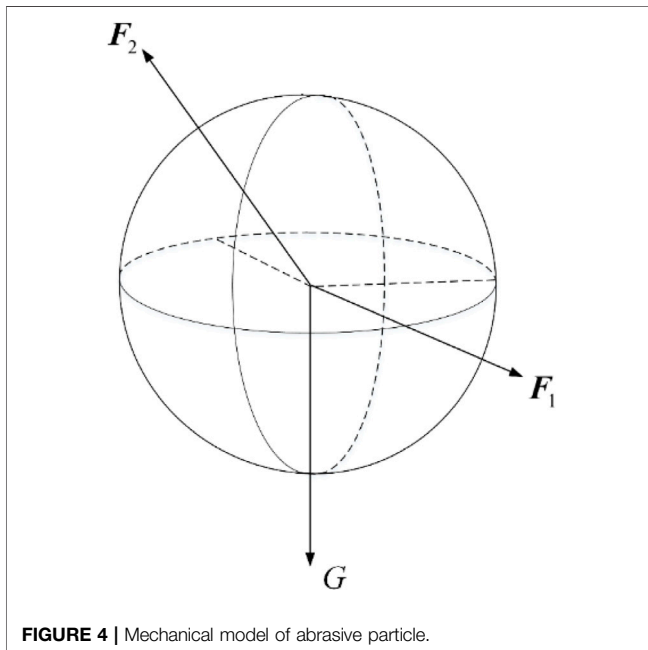

FIGURE 4 | Mechanical model of abrasive particle.
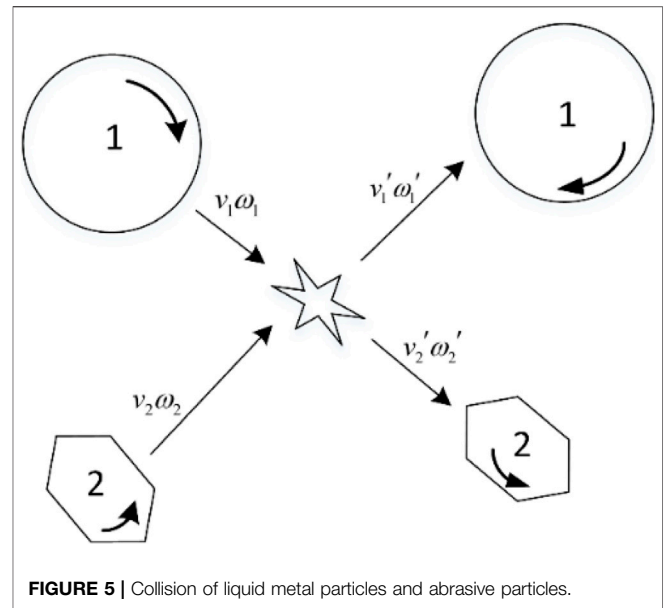

FIGURE 5 | Collision of liquid metal particles and abrasive particles.

collide with each other, the liquid metal particles will be deformed. The physical model of soft collision is equivalent to a set of spring-damper-slider, which considers the elastic effect, buffering effect, friction slip, rolling and locking of solid particles during the collision. In the soft collision model, it is assumed that the shape of particles remains unchanged during the collision, but overlaps with each other, as shown in **Figure 3**, in which δ is the superimposed amount of particles and abrasive particles.

In the soft collision process, the normal force received by the abrasive particle consists of two parts which are spring force and damping force. Combined with Hertzian contact theory, the normal force received by the abrasive particle is expressed as:

$$\overrightarrow{F_n} = \left(-k_n\delta_n^{1.5} - \eta_n\vec{G} \cdot \vec{n} \right)\vec{n} \approx F_E \cos\theta \tag{8}$$

Where k_n is the normal elasticity coefficient, δ_n is the normal superposition between particles, $\vec{G}$ is the relative velocities of the two particles, η_n is the normal damping coefficient, and θ is the collision angle.

During the liquid metal-abrasive flow polishing process, the velocity of abrasive particle is affected by multiple forces, as shown in **Figure 4**, and it can be expressed as:

$$m_i\frac{d\mathbf{v}_i}{dt} = \sum \mathbf{F} = \mathbf{F}_1 + \mathbf{F}_2 + \mathbf{G} \tag{9}$$

Where $\mathbf{G}$ is gravity, F_1 is the force of liquid metal particles on abrasive particles, F_2 is fluid force, and m_2 is the mass of a single particle.

In the liquid metal-abrasive flow polishing process, the collision between the liquid metal particles and abrasive particles can change the relative velocity of the abrasive particles in the near-wall area. The schematic of the collision between the liquid metal particles and the abrasive particles is shown in **Figure 5**, where v_1 and v_2 are the motion velocities of
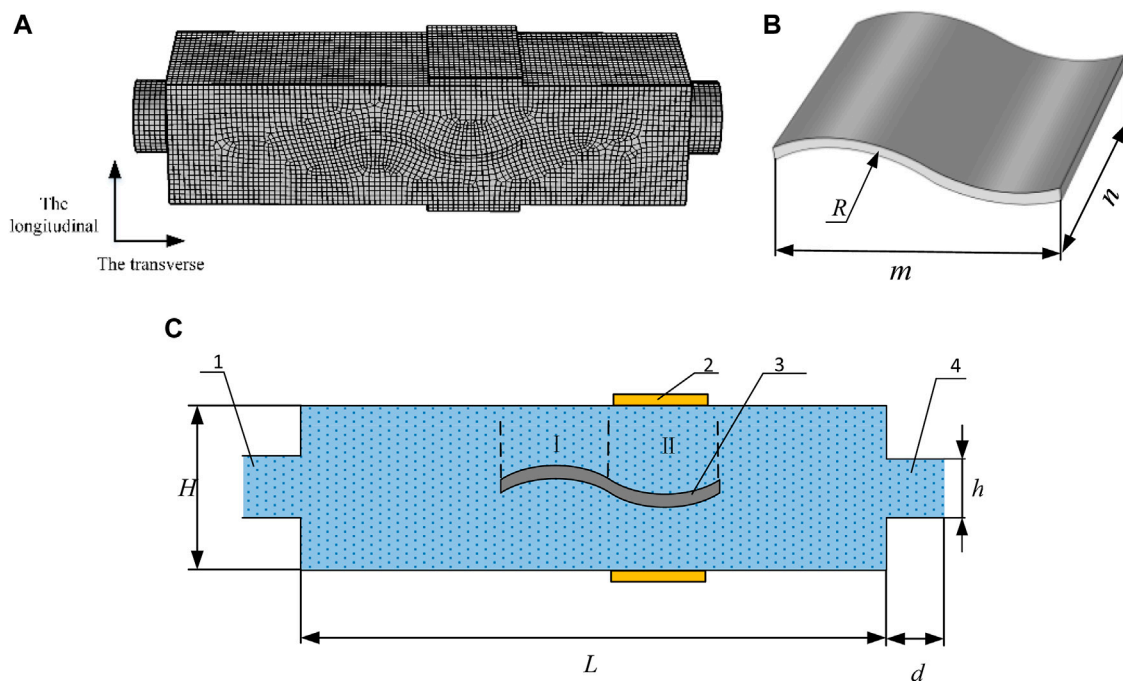
FIGURE 6 | (A) Flow channel meshing in simulation, **(B)** Titanium alloy workpiece, **(C)** Schematic representation of inside flow channel: 1-Flow field entrance, 2-Electrode, 3- Titanium alloy thin-walled curved parts, and 4- Flow field exit.

TABLE 1 | Parameters of model geometry.

Parameters	Length, m	Width, n	Curvature, R	Total height, H	Total length, L	Inflow length, d	Inflow width, h
Value (mm)	50	40	20	30	140	10	18

liquid metal particles and abrasive particles, respectively, and ω_1 and ω_2 are the rotation speed of liquid metal particles and abrasive particles, respectively.

The velocity S of the liquid metal particles relative to the abrasive particles is:

$$S = v_1 - v_2 \qquad (10)$$

The normal unit vector n when the liquid metal particle collides with the abrasive particle is:

$$\mathbf{n} = \frac{\mathbf{r}_1 - \mathbf{r}_2}{|\mathbf{r}_1 - \mathbf{r}_2|} \qquad (11)$$

Where r_1 and r_2 are the centroid position vector of the liquid metal particle and the abrasive particle respectively. The normal vector S^n and tangential vector S^t of the relative velocity are:

TABLE 2 | Simulation parameters.

| Simulation parameters	Value
Thin-walled curved workpiece material	Ti-6Al-4V titanium alloy
fluid density $\rho_1/kg \cdot m^{-3}$	1000
conductivity S/m	9.7
Abrasive particle density $\rho_2/kg \cdot m^{-3}$	3200
The average diameter of abrasive particles $d/\mu m$	50
Abrasive particle volume fraction $V_1/\%$	10
The volume fraction of liquid metal particles $V_2/\%$	5
Liquid metal particle density	6400
Flow channel voltage V_3/V	36 V alternating current with frequency of 50 Hz
The average diameter of liquid metal particles D/mm	1
Fluid inflow conditions	1, 3 and 5 m/s
Fluid outlet conditions	$p = 0$
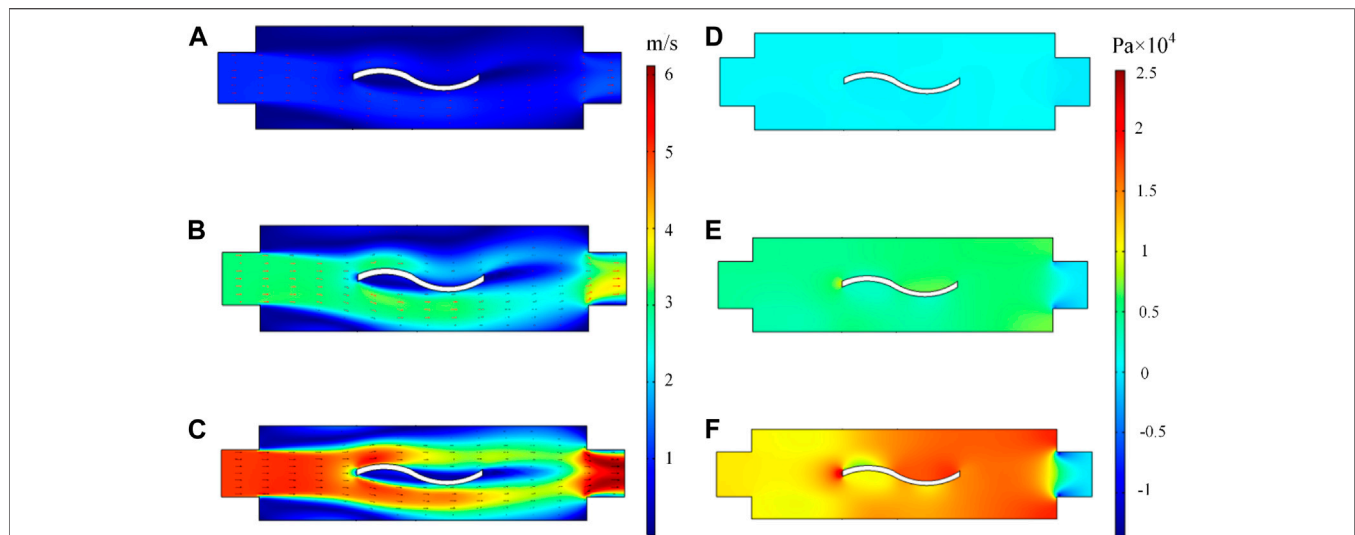
FIGURE 7 | Flow field characteristics: **(A)** Velocity distribution at inlet 1 m/s, **(B)** Velocity distribution at inlet 3 m/s, **(C)** Velocity distribution at inlet 5 m/s, **(D)** Pressure distribution at inlet 1 m/s, **(E)** Pressure distribution at inlet 3 m/s, **(F)** Pressure distribution at inlet 5 m/s.

$$S^n = (S \cdot n)n \tag{12}$$

$$S^t = S - S^n \tag{13}$$

Assuming that the liquid metal particles and abrasive particles do not rotate during the collision, and the tangential vector before and after the collision remains unchanged, then there is:

$$S^t = S^n \tag{14}$$

The velocity after the normal collision is:

$$v' = -ev \tag{15}$$

Thus, it can be concluded that the velocity of the abrasive particles after the collision is:

$$v_2' = v_2 - \frac{m^*}{m_2}(1+e)(S \cdot n)n \tag{16}$$

Where m^* is the effective mass, e is the coefficient of restitution and m_2 is the mass of abrasive particles.

In summary, the material removal model of the liquid metal-abrasive flow polishing process under the electric field is taken from:

$$\Delta z = \int_0^t k_p \sqrt{4E^* \cdot 3^{\frac{1}{2}} \left(\sum_{k=1}^n 2\left[\gamma_0 - \frac{C}{2}\frac{\left(V_0 + \frac{1}{1+\delta}\mathbf{Re}\left(\left(\tilde{\varnothing}_{AC} - \tilde{\varnothing}_{AC}^O\right)e^{j\omega t}\right)\right)^2}{R}\right]\frac{S}{n}\right)\cos\theta\left(v_2 - \frac{m^*}{m_2}(1+e)(S \cdot n)n\right)}dt \tag{17}$$

Where k_p is the abrasive factor, E^* is the elastic contact modulus between the machined surface and the abrasive particles, n is the number of surface units with the same area and capacitance divided by the surface of liquid metal particles, γ_0 is the maximum surface tension when V = 0, C is the capacitance per unit area, R is the radius of curvature, δ is the surface capacitance ratio, $\tilde{\phi}_{AC}$ is the AC potential outside the electric double layer, $\tilde{\phi}_{AC}^o$ is the liquid metal body potential, ω is the AC signal frequency., V_0 is the
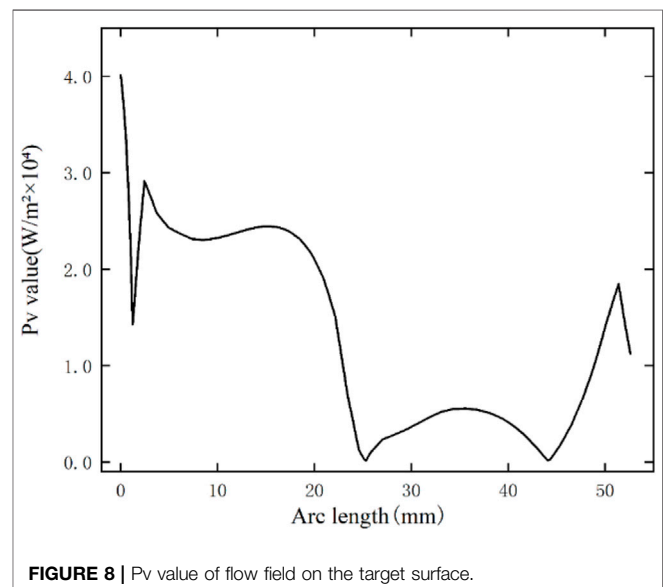
FIGURE 8 | Pv value of flow field on the target surface.

initial potential of the electric double layer, S is the surface area of liquid metal particles, θ is the collision angle, v_2 is the velocity of abrasive particles before impact, m^* is the effective mass; e is the coefficient of restitution; m_2 is the mass of abrasive grains, S is the relative velocities of the two particles, **n** is the normal unit vector when the liquid metal particle collides with the abrasive particle.

NUMERICAL SIMULATION AND ANALYSIS

Model Development and Boundary Conditions

In the liquid metal-abrasive flow polishing process, the fluid is considered as the carrier to take the abrasive particles and the

FIGURE 9 | Trajectories of liquid metal particles under different voltages. (A) 0 V, (B) 6 V, (C) 12 V, (D) 24 V, (E) 36 V.

FIGURE 10 | Comparison of Pv values under different conditions.

Flow Field Analysis

The workpiece to be polished is with a non-uniform curvature surface, when the abrasive flow contacts with the target surface the relative velocity and pressure of the abrasive particles on the surface are different. As shown in **Figure 7**, the arrow direction indicates the direction of the flow field, and it can be seen from the figure that due to the structural characteristics of the workpiece, the turbulent flow energy in region II is less than that in region I. According to Preston equation, the amount of material removal is positively proportional to the relative velocity, v, and pressure, P, thus, in order to present the surface characteristics of the workpiece more clearly, the Pv value curve is calculated b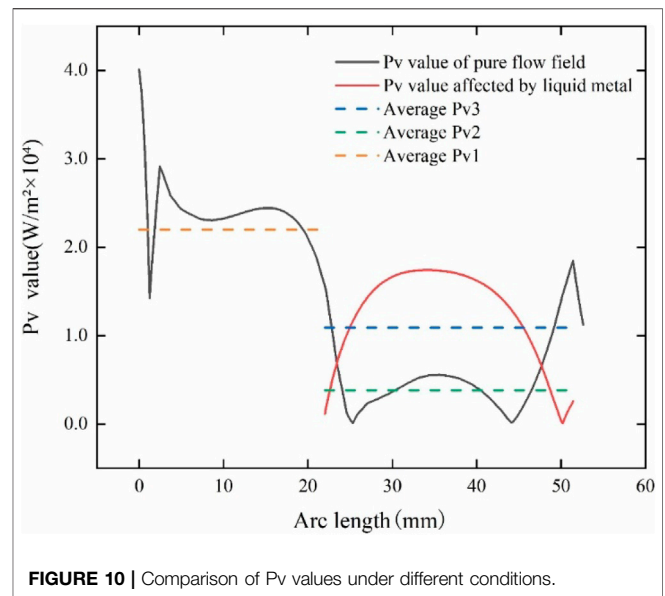y considering the velocity and pressure values on the target surface, as shown in **Figure 8**, which is used to evaluate the polishing performance of surface in simulation.

Particle Trajectory Induced by Liquid Metal

In the liquid metal-abrasive flow polishing process, the electric field is mainly used to affect the liquid metal, thereby driving the abrasive particles to impact the target surface. The electric field has a gradual effect on the liquid metal particles, and its trajectory is affected by the flow field and the AC electric field as well. **Figure 9** shows the trajectories of liquid metal particles under different voltages.

When there is no electric field applied, the liquid metal particles are not affected by the force induced by the electric field, and the trajectories of the liquid metal particles are only affected by the turbulence of flow field, as shown in **Figure 9A**. When the AC electric field is applied, the liquid metal particles are significantly affected, and it is found from **Figure 9** that with an increase of the voltage the liquid metal particles would diverge in more directions when passing through the electric field.

Then, a quantitative analysis on the Pv values under different conditions has been conducted, as shown in **Figure 10**, where Pv1, Pv2, Pv3 are the average Pv values of pure flow field region I, pure flow field region II and region II under the with the liquid

liquid metal particles. Based on the characteristics of liquid metal-abrasive flow, the SST k-ω turbulence model is selected in COMSOL software to simulate the flow field in this study. Further, the simulation in this paper is composed of upper and lower electrodes, thin-walled curved parts and abrasive flow channels. In order to study the processing of non-uniform curvature surfaces by liquid metal-abrasive flow polishing, the minimum structural unit of non-uniform curvature surface with the same curvature and concave-convex properties is selected, and the thickness of the surface structure is 2 mm. The upper surface of the workpiece is divided into region I and region II, as shown in **Figure 6**, and the parameters of model geometry are given in **Table 1**. According to previous simulation and calculated algorithm related to the abrasive flow machining process (Zhang et al., 2019; Xie et al., 2021; Ji et al., 2022), in this simulation the simulation parameters are given in **Table 2**.

metal. It can be found from **Figure 10** that Pv1 value is 23,718.8 W/m^2, Pv2 value is 5,427.3 W/m^2 and Pv3 value is 10,948.6 W/m^2, which indicates that with the assistance of the liquid metal the average Pv value at the weak flow field increases by about 101.7%, and thus, according to the simulation results that the effect of liquid metal particles can significantly improve the polishing uniformity of the entire workpiece surface.

CONCLUSION

A novel liquid metal-abrasive flow polishing method was proposed in this study, and the material removal model of the liquid metal-abrasive flow polishing process has been theoretically developed. Then, according to the SST *k-ω* model, Preston model and fluid flow particle tracking model, the numerical investigation has been carried out in COMSOL to study the dynamic characteristics of liquid metal-abrasive flow under different AC electric field conditions, and the two-phase flow field has been used to simulate the liquid state, the movement of metal particles on the surface of the workpiece and the change of the Pv value in the near-wall area during the movement. It is found from numerical simulation results that the average Pv value in the strong flow field is 23,718.8 W/m^2, and that in the weak flow field is 5,427.3 W/m^2. By the assistance of the electric filed with the voltage of AC 36 V, the average Pv value of the liquid metal particles in the weak flow field is found to be 10,948.6 W/m^2 with an increase of 101.7%. By adjusting the magnitude of the

electric field strength, the movement of liquid metal in the flow field can be found to be controlled, and hence improving the uniformity of the turbulent kinetic energy on the workpiece surface and improving the processing quality. The related research work in this study could provide a good reference for the abrasive flow polishing of curved surface.

DATA AVAILABILITY STATEMENT

The raw data supporting the conclusion of this article will be made available by the authors, without undue reservation.

AUTHOR CONTRIBUTIONS

Conceptualization, LZ; Data curation, BZ; Formal analysis, BZ; Investigation, RJ; Software, WM; Paper Revision, YL; Writing-original draft, LZ; Writing-review and editing, YX.

FUNDING

REFERENCES

Beaucamp, A., Katsuura, T., and Takata, K. (2018). Process Mechanism in Ultrasonic Cavitation Assisted Fluid Jet Polishing. *CIRP Ann.* 67, 361–364. doi:10.1016/j.cirp.2018.04.075

Daeneke, T., Khoshmanesh, K., Mahmood, N., De Castro, I. A., Esrafilzadeh, D., Barrow, S. J., et al. (2018). Liquid Metals: Fundamentals and Applications in Chemistry. *Chem. Soc. Rev.* 47, 4073–4111. doi:10.1039/c7cs00043j

Dong, Z. G. (2012). *Research on Cutting Mechanism and Processing Technology of Abrasive Flow Machining*. Taiyuan, China: Taiyuan University of Technology.

He, Q., Fu, Y., Chen, J., Zhang, W., and Cui, Z. (2018). Experimental Investigation of Cooling Characteristics in Wet Grinding Using Heat Pipe Grinding Wheel. *Int. J. Adv. Manuf Technol.* 97, 621–627. doi:10.1007/s00170-018-1881-5

Hu, W., Teng, Q., Hong, T., Saetang, V., and Qi, H. (2022). Stress Field Modeling of Single-Abrasive Scratching of BK7 Glass for Surface Integrity Evaluation. *Ceramics Int.* 48, 12819–12828. doi:10.1016/j.ceramint.2022.01.153

Huai, W., Tang, H., Shi, Y., and Lin, X. (2017). Prediction of Surface Roughness Ratio of Polishing Blade of Abrasive Cloth Wheel and Optimization of Processing Parameters. *Int. J. Adv. Manuf Technol.* 90, 699–708. doi:10.1007/s00170-016-9397-3

Huai, W., Shi, Y., Tang, H., and Lin, X. (2019). An Adaptive Flexible Polishing Path Programming Method of the Blisk Blade Using Elastic Grinding Tools. *J. Mech. Sci. Technol.* 33, 3487–3495. doi:10.1007/s12206-019-0643-0

Huang, Y., Li, S., Xiao, G., Chen, B., Zhang, Y., He, Y., et al. (2021). Research Progress of Aero-Engine Blade Materials and Anti-fatigue Grinding Technology. *J. Aeronaut. Mater.* 41, 17. doi:10.11868/j.issn.1005-5053.2021.000058

Ji, S., Li, C., Tan, D. P., Yuan, Q. L., Chi, Y. W., and Zhao, L. H. (2011). Study on Machinability of Softness Abrasive Flow Based on preston Equation. *J. Mech. Eng.* 47, 156–163. doi:10.3901/jme.2011.17.156

Ji, R., Zhang, L., Zhang, L., Li, Y., Lu, S., and Fu, Y. (2022). Processing Method for Metallic Substrate of Liquid Metal Lapping-Polishing Plates. *Front. Mater.* 9, 896346. doi:10.3389/fmats.2022.896346 Submitted for publication.

Li, X., Xie, J., Tang, S.-Y., Xu, R., Li, X., Li, W., et al. (2019). A Controllable Untethered Vehicle Driven by Electrically Actuated Liquid Metal Droplets. *IEEE Trans. Ind. Inf.* 15, 2535–2543. doi:10.1109/tii.2018.2870857

Liu, S. Y. (2018). *Research on Hybrid Finishing Method of Electrochemical Machining Assisted by Freely Flowing Abrasive Particles*. Nanjing, China: Nanjing University of Aeronautics and Astronautics.

Luo, G., Zou, L., Huang, Y., and Gong, M. (2020). Study on Material Removal and Surface Quality in Titanium Alloy Grinding with Alumina Hollow-Sphere Abrasive Belt. *China Mech. Eng.* 31, 2363–2370. doi:10.3969/j.issn.1004-132X.2020.19.013

Qi, H., Shi, L., Teng, Q., Hong, T., Tangwarodomnukun, V., Liu, G., et al. (2022). Subsurface Damage Evaluation in the Single Abrasive Scratching of BK7 Glass by Considering Coupling Effect of Strain Rate and Temperature. *Ceramics Int.* 48, 8661–8670. doi:10.1016/j.ceramint.2021.12.077

Wang, A.-C., Cheng, K.-C., Chen, K.-Y., and Lin, Y.-C. (2018). A Study on the Abrasive Gels and the Application of Abrasive Flow Machining in Complex-Hole Polishing. *Proced. CIRP* 68, 523–528. doi:10.1016/j.procir.2017.12.107

Xian, C., Shi, Y., Lin, X., and Liu, D. (2020). Experimental Study on Energy Partition of Polishing Aero-Engine Blades with Abrasive Cloth Wheel. *Int. J. Adv. Manuf Technol.* 106, 1839–1853. doi:10.1007/s00170-019-04690-2

Xie, Y., Gui, F.-X., Wang, W.-J., and Chien, C.-F. (2021). A Two-Stage Multi-Population Genetic Algorithm with Heuristics for Workflow Scheduling in Heterogeneous Distributed Computing Environments. *IEEE Trans. Cloud Comput.*, 1. doi:10.1109/tcc.2021.3137881

Yang, X., Tan, S., Yuan, B., and Liu, J. (2016). Alternating Electric Field Actuated Oscillating Behavior of Liquid Metal and its Application. *Sci. China Technol. Sci.* 59, 597–603. doi:10.1007/s11431-016-6026-1

Yao, S., Cao, X., Liu, S., Gong, C., Zhang, K., Zhang, C., et al. (2020). Two-sided Ultrasonic Surface Rolling Process of Aeroengine Blades Based on On-Machine Noncontact Measurement. *Front. Mech. Eng.* 15, 240–255. doi:10.1007/s11465-019-0581-7

Zhai, K., Ren, Y., Li, L., and He, Q. (2017). Realization of Polishing Uniformity in Megasonic Vibration Assisted Chemical Mechanical Polishing. *Nanotechnology Precision Eng.* 15, 538–544. doi:10.13494/j.npe.20160015

Zhang, L., Huang, Y., Chen, G., Xu, M., Xia, W., and Fu, Y. (2019). Experimental Study of Coverage Constraint Abrasive Flow Machining of Titanium alloy Artificial Joint Surface. *Proc. Inst. Mech. Eng. B: J. Eng. Manufacture* 233, 2399–2409. doi:10.1177/0954405419840553

Zhu, X. (2020). *Research on Precision Machining Technology of Solid-Liquid Two-phase Abrasive Flow Containing Magnetic Particles*. Changchun, China: Changchun University of Science and Technology.

Zhu, Z.-Q., Chen, Z.-T., and Zhang, Y. (2021). A Novel Polishing Technology for Leading and Trailing Edges of Aero-Engine Blade. *Int. J. Adv. Manuf Technol.* 116, 1871–1880. doi:10.1007/s00170-021-07574-6

Surface Form Accuracy Evaluation in Abrasive Lapping of Single-Crystal Silicon Wafers

Zhengwei Wang[1], Yang Lei[1]* and Xiaofeng Wu[2]

[1]Hangzhou Vocational & Technical College, Hangzhou, China, [2]Zhejiang Zhongjing Technology Co., Ltd., Changxing, China

Silicon-based materials still dominate the current semiconductor industry for the foreseeable years such that it is needed in continuously developing the related advanced manufacturing technologies. For the abrasive precision lapping of single-crystal silicon wafers, the surface form accuracy is very important which can significantly improve its efficiency and reduce the cost in the following ultra-precision polishing process. In this study, a novel driving system is proposed in the single-side planetary lapping process that could realize the irrational rotation speed ratio of the lapping plate to the workpiece, and it is found from the numerical qualitative and quantitative analysis that the uniformity of the particle trajectories moving on the target surface has been significantly improved using the irrational rotation speed ratio and hence resulting in the higher surface form accuracy than that driven by the rational rotation speed ratio. Moreover, an in-house developed irrational rotation speed ratio driving system has been designed for the experimental study, and it is found that the effect of the rational and irrational rotation speed ratios on surface roughness is not significant, while all the five essential values related to the surface form accuracy are better under the rotation speed ratio of $i = 1.0772\ldots$ than that under the rotation speed ratio of $i = 1$, which demonstrates that the irrational rotation speed ratio driving system has the advantage of being able to obtain a good surface form accuracy and agrees well with the numerical simulation results.

Keywords: surface form accuracy, single-side planetary lapping, irrational rotation speed ratio, particle trajectories, uniform distribution

1 INTRODUCTION

Silicon carbide, gallium nitride, and aluminum nitride with excellent properties are considered as the third-generation semiconductor materials which will be the future of the semiconductor industry (Burk et al., 1999), but silicon-based materials, such as single-crystal silicon, still dominate the current semiconductor industry for the foreseeable years such that it is needed in continuously developing the advanced manufacturing technologies for these silicon-based materials (Niitsu and Yan, 2020; Bu et al., 2022).

Currently, the single-crystal silicon wafer is one of the commonly used materials in fabricating substrates of chips, and the surface quality of these substrates plays an important role in affecting their performance and service life (Zhao et al., 2020). Abrasive machining technologies are often used for the precision machining of high-performance parts in the information technology, aerospace engineering, and civil engineering (Hu et al., 2022; Li et al., 2022; Qi et al., 2022). For example, the abrasive flow machining technology is usually employed to fabricate and polish the micro-structures

on different kinds of materials with high quality and efficiency (Cheng et al., 2022; Ji et al., 2022; Zhang et al., 2022), while the abrasive lapping technology can be used to machine the hard-brittle substrates with a good surface finish (Belkhir et al., 2009; Wen et al., 2016; Li et al., 2019). However, the distribution of the particle trajectories moving on the target surface in the abrasive lapping process could affect the surface form accuracy and hence decreasing its efficiency and increasing the cost in the following ultra-precision polishing process (Yuan et al., 2015; Fang et al., 2018).

The particle trajectories moving on the target surface in the abrasive lapping process have a great influence on the uniformity of the material removal rate and the surface form accuracy (Sanchez et al., 2011; Yang et al., 2019). Tam et al. numerically investigated the effects of four different fractal particle trajectories on the lapping uniformity, and they found that the material removal rate and the distribution of the surface texture were significantly different (Tam and Cheng, 2010). Lu et al. established a model between the material removal rate and the random distribution of abrasive particles in the lapping process and found that selecting reasonable geometric and kinematic parameters can improve the machining efficiency and surface form accuracy (Lu et al., 2014). Zhang et al. carried out the kinematic simulation of the double-side planetary lapping process, and the curves of relative displacement, velocity, and acceleration were obtained with respect to the time that can be used to optimize the rotation speed ratio of gear ring and sun gear (Zhang et al., 2015). Wen et al. proposed a method to evaluate the uniformity of particle trajectories moving on the target surface by using the number and standard deviation of trajectory points per unit area in the single-side planetary lapping process, and it was found that the influence of the processing parameters, that is, the rotation speed ratio and eccentricity, on the uniformity of the particle trajectories was essential (Wen et al., 2016). According to the aforementioned analysis, it is found that most of the research practices on the particle trajectories in the abrasive lapping process are based on the kinematic mechanisms and associated numerical simulations, but limited research has been conducted to explore the novel driving system to realize the uniformity of particle trajectories with the effective and convenient way.

In this study, a novel driving system will be proposed in the single-side planetary lapping process to realize the irrational rotation speed ratio of the lapping plate to the workpiece, and its working mechanism is then theoretically analyzed. The numerical study is also conducted to evaluate the lapping uniformity by employing this novel driving system, and finally, the experimental study is carried out to explore the surface form accuracy and verify the numerical simulation results.

2 FUNDAMENTALS OF THE IRRATIONAL DRIVING SYSTEM

2.1 Mechanism of the Driving System to Realize the Irrational Rotation Speed Ratio

The planetary moving structure is a conventional and widely used design in driving the abrasive lapping process with advantages of

stability and convenience (Uhlmann et al., 2018). In this study, a planetary gear train using a pair of bevel gears with oblique engagement and planetary motion is designed to achieve the irrational ratio of output to input. The novel driving system to realize the irrational rotation speed ratio is the in-house developed driving system in **Figure 1**, which includes two bevel gears with a tooth number of 30 and planetary carrier with $\Sigma = 60°$, as shown in **Figures 1Bi,ii**. Because the shaft of the two bevel gears is not parallel to each other, it is necessary to calculate the rotation speed of the bevel gear 2, ω_2, by analyzing the angular velocity polygon given in **Figure 1Bii**, where δ can be taken from the following equation:

$$\delta = arc \cot \frac{i_{12} + \cos \Sigma}{\sin \Sigma} = arc \cot \frac{1 + \cos 60°}{\sin 60°} = 30°. \qquad (1)$$

It can also be seen from **Figure 1Bii** that in Δabc there are $ba//OO_H$, $ac//OO_2$, and $bc//OP$; thus, the relation between the input rotation speed, ω_H, and the rotation speed of the bevel gear 2, ω_2, can be obtained from the following equation:

$$\frac{\omega_2}{\sin{(180° - \Sigma)}} = \frac{\omega_H}{\sin{(\Sigma - \delta)}}. \qquad (2)$$

By substituting Σ and δ into **Eq. 2**, the ratio of ω_2 to ω_H can be calculated as follows:

$$\frac{\omega_2}{\omega_H} = \sqrt{3}. \qquad (3)$$

Therefore, the novel driving system designed in this study can be used to realize the irrational rotation speed ratio output, ω_2, with respect to the input rotation speed, ω_H.

2.2 Uniformity Evaluation of Particle Trajectories on Target

In order to evaluate the lapping uniformity of the irrational rotation speed ratio driving system, the trajectory of any point P (r_p, θ_p) fixed on the lapping plate moving along the target surface can be calculated according to the kinematics in **Figure 1Cii** which is given as follows:

$$\begin{cases} x = r_p \cos{(\theta + \omega_w t - \omega_p t)} - e \cos \omega_w t, \\ y = r_p \sin{(\theta + \omega_w t - \omega_p t)} - e \sin \omega_w t. \end{cases} \qquad (4)$$

Eq. 4 indicates that particle trajectories on the target surface are related to the rotation speed of the lapping plate, w_p and the workpiece, w_w, and the eccentric distance between O_1 and O_2, e. Thus, considering the experiment later in this study, the processing parameters in MATLAB are given in **Table 1** to numerically investigate the distribution of particle trajectories on the target surface.

As shown in **Figure 2**, 100 abrasive particles are randomly distributed on the lapping plate with a diameter of 610 mm, and their trajectories moving on the target surface have been numerically analyzed by considering the rational and irrational rotation speed ratios of the lapping plate to the workpiece, i, of 1:2 and 1: $\sqrt{2}$, respectively, and the simulation results are shown in **Figures 3**, **4**.
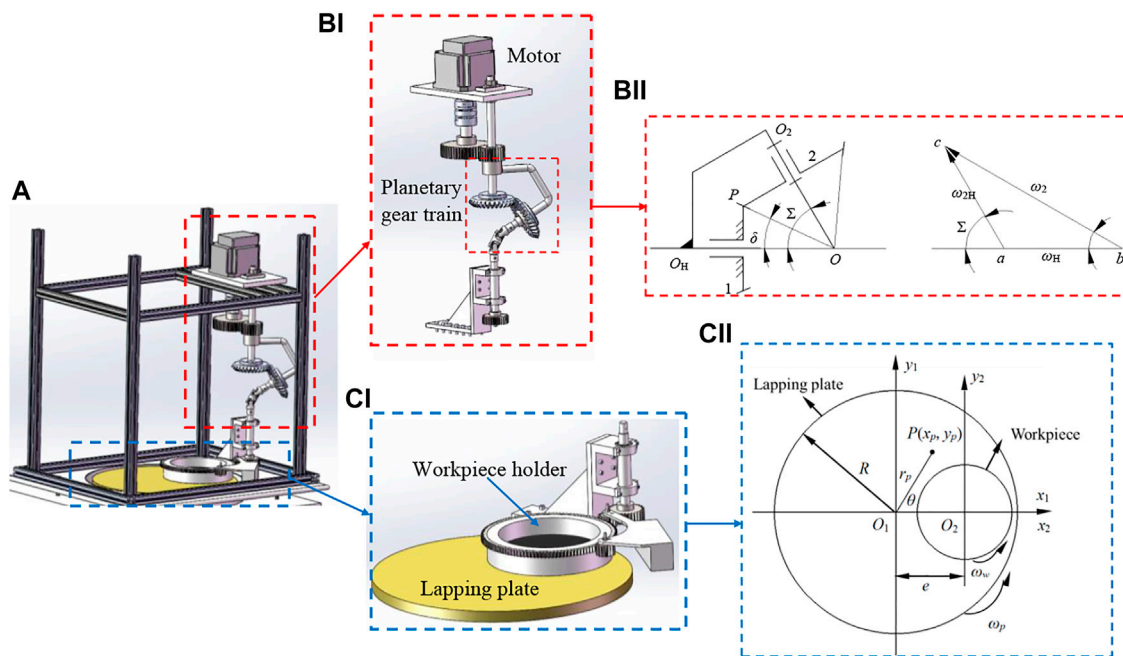
FIGURE 1 | (A) Single-side planetary lapping machine with an irrational rotation speed ratio of the lapping plate to workpiece, **(Bi)** novel driving system design with planetary gear train and **(Bii)** its working mechanism; **(Ci)** single-side planetary lapping device and **(Cii)** its working mechanism.

TABLE 1 | Processing parameters in simulation.

Processing parameter	Value
Rotation speed of the lapping plate	10 r/min
Diameter of the lapping plate	610 mm
Diameter of the workpiece	180 mm
Eccentric distance	180 mm

It can be found from **Figure 3** that there is almost no variation in the distribution of particle trajectories on the target surface when the lapping time is from 6 to 24 s, which indicates that the particle trajectories generated by the rational rotation speed ratio, $i = 1{:}2$, should be periodically superposed with the increase in the lapping time. In contrast, it is noted from **Figure 4** that with an increase in the lapping time, the coverage of particle trajectories on the target surface increases as well by employing the irrational rotation ratio, $i = 1{:}\sqrt{2}$, which demonstrates that the particle trajectories would cover the whole target surface by further increasing the lapping time because of the non-periodic characteristics. Thus, by comparing **Figures 3**, **4**, it can be found that the uniformity of the particle trajectories on the target surface has been significantly improved using the irrational rotation speed ratio and hence resulting in the higher surface form accuracy than that driven by the rational rotation speed ratio.

Furthermore, the uniformity of particle trajectories on the target surface has also been quantitatively evaluated by
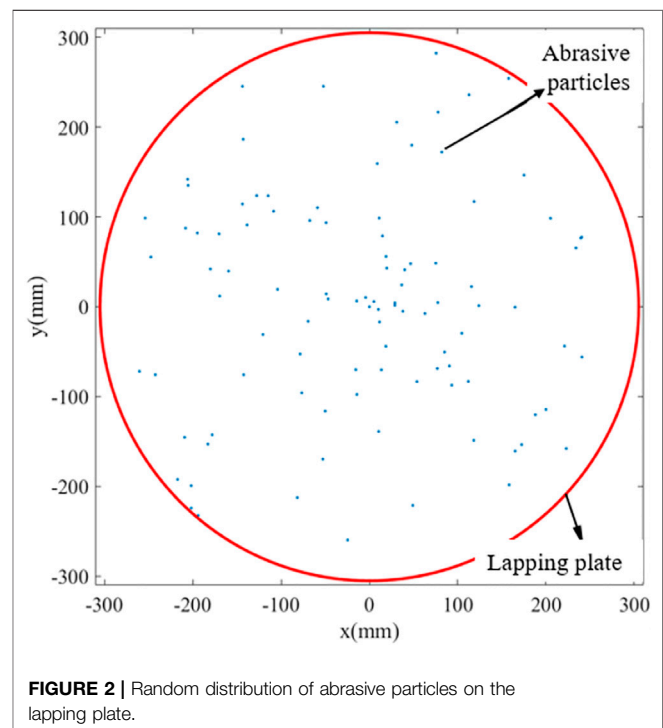
FIGURE 2 | Random distribution of abrasive particles on the lapping plate.

considering the additional i of 1:1, 1:3, 2:3, 2:1, 3:1, 1: $\sqrt{3}$, 1: $\sqrt{5}$, $\sqrt{2}$: 1, $\sqrt{3}$: 1, and $\sqrt{5}$: 1, respectively, according to the following steps. First, all the positions of the trajectories on the target surface as similar to **Figure 4** can be numerically

FIGURE 3 | Distribution of particle trajectories on the target surface under i = 1:2. **(A)** i = 1: 2, t = 3s. **(B)** i = 1: 2, t = 6s. **(C)** i = 1: 2, t = 12s. **(D)** i = 1: 2, t = 24s

FIGURE 4 | Distribution of particle trajectories on the target surface under i = 1: $\sqrt{2}$ **(A)** i = 1: $\sqrt{2}$, t = 3s. **(B)** i = 1: $\sqrt{2}$, t = 6s. **(C)** i = 1: $\sqrt{2}$, t = 12s. **(D)** i = 1: $\sqrt{2}$, t = 24s

FIGURE 5 | Comparison of CV under different values of i.

obtained. Then, the target surface is divided into Cartesian grids with small and same squares, and the number of trajectories passing over each square can be calculated with the standard

deviation. Thus, by comparing the values of the coefficient of variance (CV) obtained according to the aforementioned analysis and calculation under different values of i, the quantitative evaluation on the uniformity of particle trajectories on the target surface can be concluded from **Figure 5**. It is found that under the rational rotation speed ratios, the values of CV converge quickly and tend to be constant after the certain lapping time, and the overall values of CV are large and different from each other under the rational rotation speed ratios. It indicates that within a certain range of the lapping time, the uniformity of the particle tra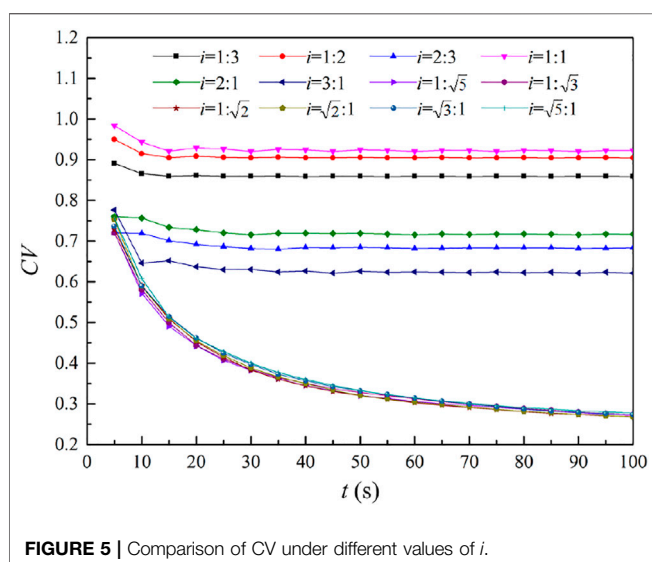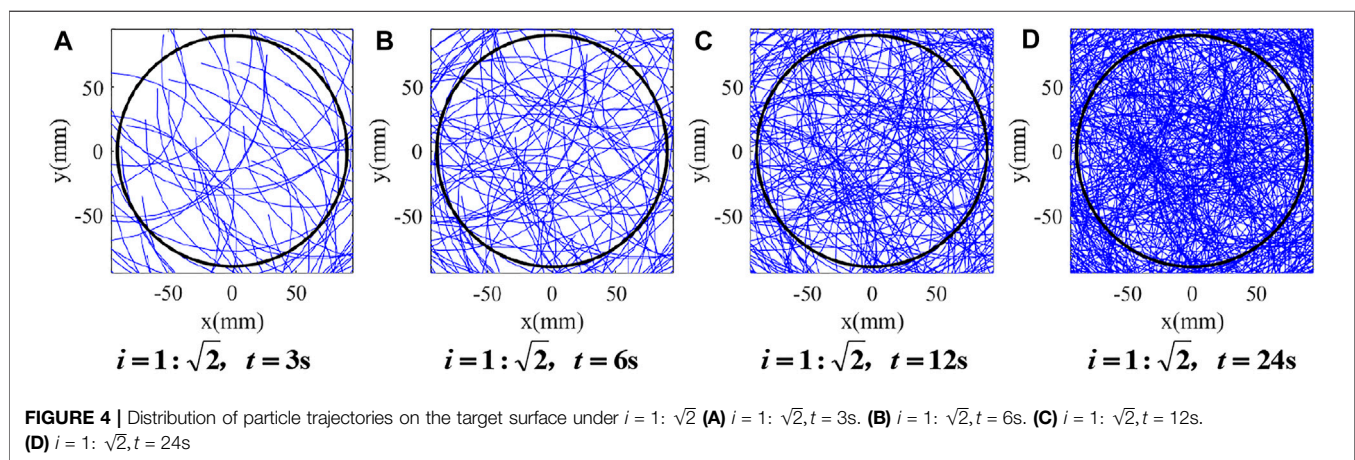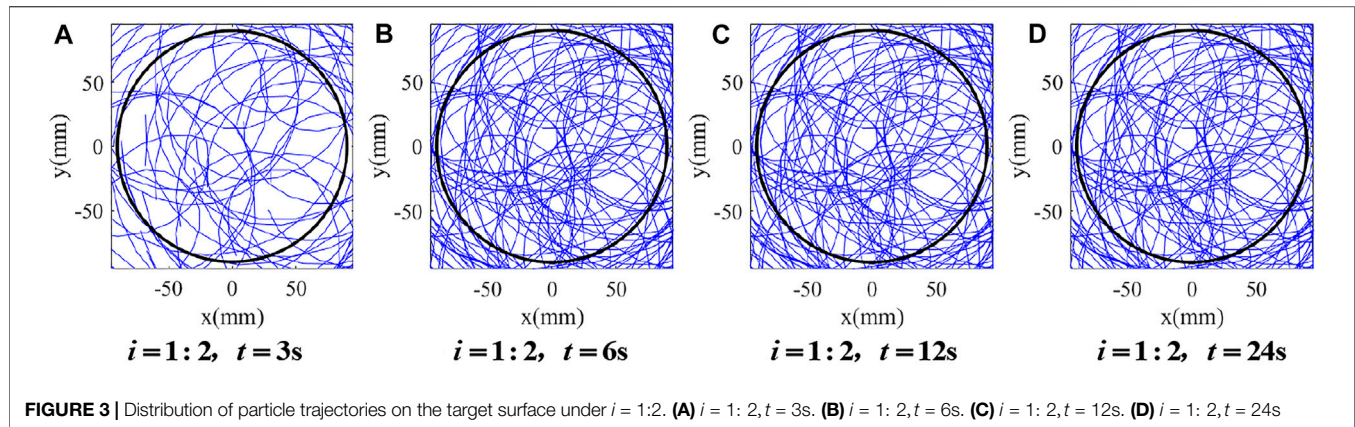jectories on the target surface can be improved, but with the further increase in the lapping time, the variation of the uniformity seems to be insignificant. In contrast, it is interesting to note that under the irrational rotation speed ratios, all the values of CV present the decreasing function of the lapping time, and the values of CV under different rational rotation speed ratios are close to each other. It demonstrates that with an increase of the lapping time, the uniformity of particle trajectories on the target surface is increasingly improved, and hence, the advantage of realizing the uniform particle trajectories on the target surface using the irrational rotation speed ratio in the lapping process can be quantitatively analyzed.

FIGURE 6 | Experimental setup.
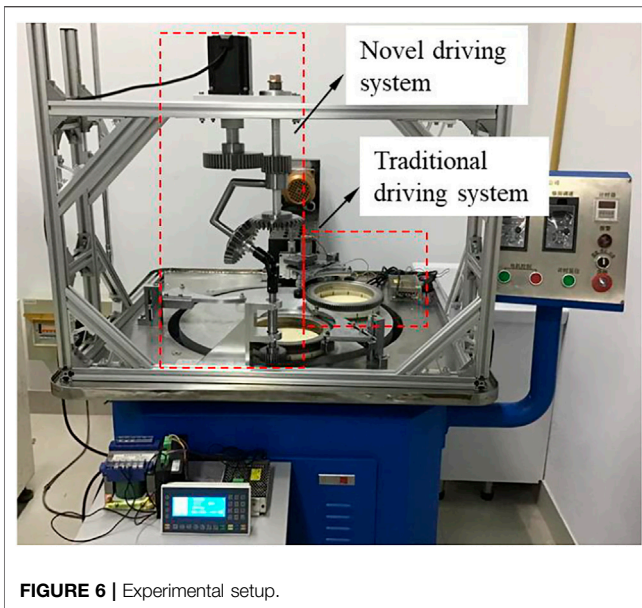
3 EXPERIMENTS

3.1 Experimental Work

An in-house developed driving system based on the design in **Section 2.1** has been designed to realize the irrational rotation speed ratio, and it is fixed in the YR610X single-side planetary lapping machine with the lapping plate diameter of 610 mm and the maximum lapping rotation speed of 300 r/min, as shown in **Figure 6**, where the traditional driving system to realize the rational rotation speed is also fixed in this machine to have a comparison in terms of surface form accuracy under the same processing parameters except the rotation speed ratio. Moreover, the single-crystal silicon wafer was selected as the workpiece with a diameter of 100 mm and thickness of 0.55 mm, and the processing parameters used in the experiment are given in **Table 2**. The workpiece was first roughly lapped using a P600 sandpaper (average diameter of 26 μm) for 10 min, and then, Al_2O_3 slurries with a concentration of 20% by mass and sizes of W14 (10–14 μm), W7 (5–7 μm), W3.5 (3–3.5 μm), W1.5 (1–1.5 μm), and W1 (0.5–1 μm) were used to conduct the precise lapping of the workpiece for 20, 20, 20, 10, and 10 min, respectively. After each test, the workpiece was measured with the assistance of the surface roughness measuring instrument Form Talysurf i60 and the wafer surface flatness measuring instrument ADE7200, and the values of total

thickness variation (TTV), total indicated reading (TIR), site total indicated reading (STIR), curvature of the wafer (BOW), and warping deformation of the wafer (WARP) were obtained to evaluate the surface form accuracy.

3.2 Evaluation on the Surface Form Accuracy

The overall surface morphology of the single-crystal silicon wafer after the abrasive lapping process is shown in **Figure 7**. By the qualitative comparison of surface morphology under the rotation speed ratios of $i = 1$ and $i = 1.0772...$, it is found from the resolution of the reflecting words on the target surface that there is no evident difference between $i = 1$ and $i = 1.0772...$, and a quantitative analysis on the average surface roughness by measuring 10 different positions on the target surface with respect to $i = 1$ and $i = 1.0772...$ can be obtained using the surface roughness measuring instrument Form Talysurf i60, which are 11.2 and 7.62 nm, respectively. Thus, it can be deduced that the effect of the rational and irrational rotation speed ratios on the surface roughness is not significant, but its effect on the surface form accuracy that is related to the distribution of particle trajectories on the target surface still needs to be explored.

Figure 8 shows the values of partial surface flatness, STIR, in the area of 15 mm × 15 mm under the rotation speed ratios of $i = 1$ and $i = 1.0772...$, respectively. It can be seen from **Figure 7A** that the maximum value of STIR is 9.02 μm under the rotation speed ratio of $i = 1$, while under the rotation speed ratio of $i = 1.0772...$ the maximum value of STIR significantly reduces to be about 2.49 μm (**Figure 8B**), and its distribution on the target surface is more uniform than that with the rotation speed ratio of $i = 1$, which is well agreed with the simulation results, as discussed in **Section 2.2**.

Furthermore, five essential values of TTV, TIR, STIR, BOW, and WARP, which are usually employed to evaluate the surface form accuracy (Satake et al., 2020) on the whole target surface are given in **Table 3** under different conditions. In general, all the five essential values are better under the rotation speed ratio of $i = 1.0772...$ than those under the rotation speed ratio of $i = 1$, which demonstrates that the irrational rotation speed of the ratio driving system has the advantage of being able to obtain a good surface form accuracy. It is also noticed that the variations of BOW and WARP are limited as compared between the original target surface and the lapping target surface, but the other values of TTV, TIR, and STIR present the significant change after the lapping process. Therefore, the surface form

TABLE 2 | Processing parameters in the experiment.

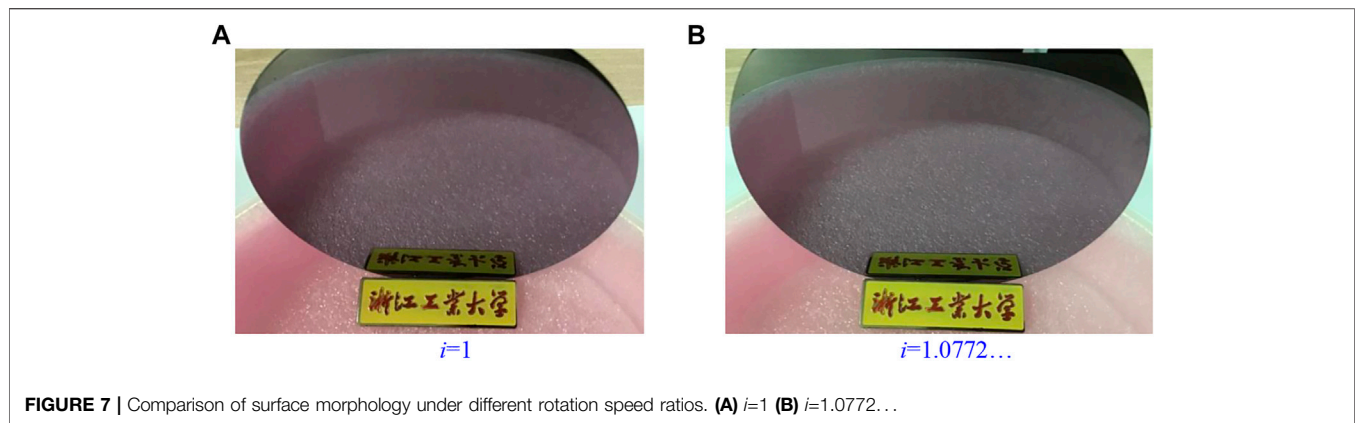| Processing parameter	Value	
Driving system	Novel driving system	Traditional driving system
Rotation speed ratio	1.0772...	1:1
Loading force	0.01 N/mm^2	0.01 N/mm^2
Rotation speed of the lapping plate	20 r/min	20 r/min
Lapping time	90 min	90 min

FIGURE 7 | Comparison of surface morphology under different rotation speed ratios. **(A)** i=1 **(B)** i=1.0772...
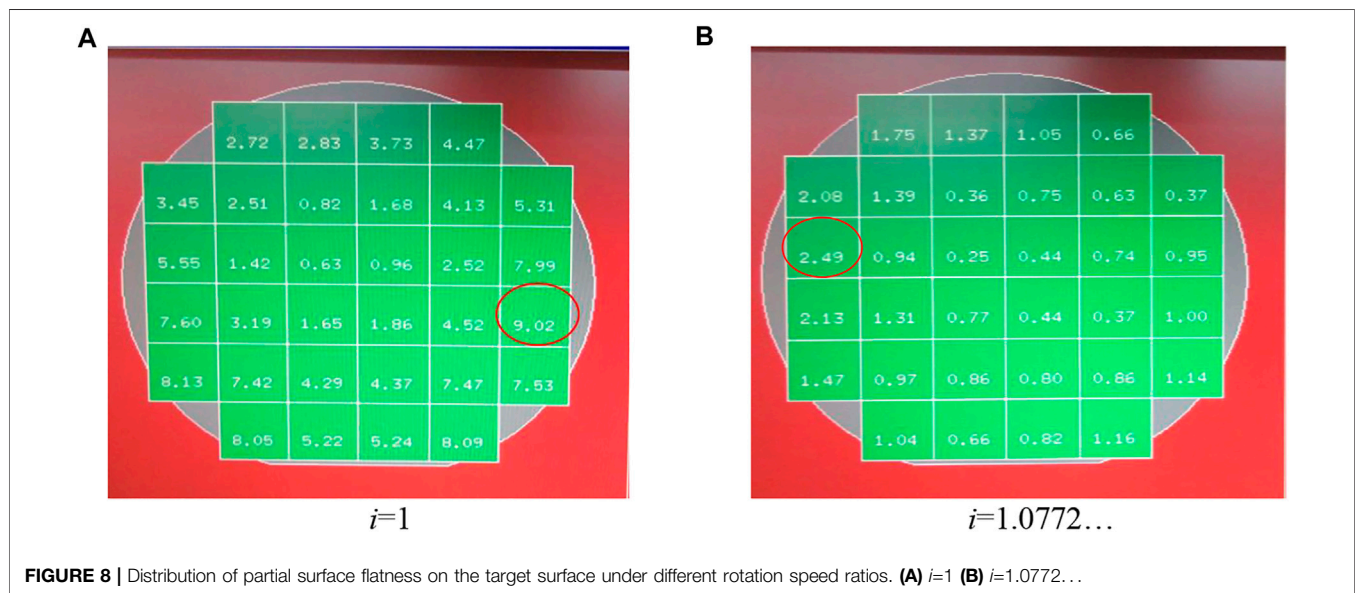
FIGURE 8 | Distribution of partial surface flatness on the target surface under different rotation speed ratios. **(A)** i=1 **(B)** i=1.0772...

TABLE 3 | Comparisons of surface form accuracy under different conditions.

No.	Processing parameter and value	TTV	TIR	STIR	BOW	WARP
1	Original workpiece	0.43	0.39	0.35	−6.10	15.58
2	Workpiece lapped by i = 1 in 90 min	15.50	12.89	9.02	−8.68	19.02
3	Workpiece lapped by i = 1.0772... in 90 min	4.24	2.99	2.49	−7.21	18.25

accuracy has been significantly improved by using the irrational rotation speed ratio realized by the novel driving system design in this study.

4 CONCLUSION

Single-crystal silicon wafer is one of the commonly used materials in fabricating substrates of chips, and the surface quality of these substrates plays an important role in affecting their performance

and service life. Thus, in this study, a novel driving system has been proposed to improve the uniformity of the particle trajectories moving on the target surface in the single-side planetary lapping process, and the main contributions are concluded as follows:

1) A novel driving system that consists of two bevel gears and a planetary carrier has been designed to realize the irrational rotation speed ratio, and its working mechanism has also been theoretically analyzed in detail.

2) It is found from numerically qualitative and quantitative studies that the particle trajectories generated by the rational rotation speed ratio are periodically superposed with the increase in the lapping time. In contrast, by employing the irrational rotation speed ratio, the particle trajectories would cover the whole target surface with the further increase in the lapping time because of the non-periodic characteristics. It indicates that the uniformity of the particle trajectories on the target surface can be significantly improved using the irrational rotation speed ratio and hence resulting in the higher surface form accuracy as well.

3) An in-house developed irrational rotation speed ratio driving system has been designed for the experimental study. It is found that the effect of the rational and irrational rotation speed ratios on the surface roughness is not significant, but all the five essential values related to the surface form accuracy are better under the rotation speed ratio than those under the rotation speed ratio, which demonstrates that the irrational rotation speed ratio driving system has the advantage of being able to obtain a good surface form accuracy and agrees well with the numerical simulation results.

Therefore, the novel driving system designed in this study to realize the irrational rotation speed ratio would provide good reference for the development of the abrasive lapping technology.

DATA AVAILABILITY STATEMENT

The raw data supporting the conclusion of this article will be made available by the authors, without undue reservation.

AUTHOR CONTRIBUTIONS

ZW and XW carried forward the design of the novel driving system. ZW conducted the numerical work, and XW carried out the experimental work. YL supervised this manuscript, prepared the original draft, and charged the review and editing of the manuscript.

FUNDING

ACKNOWLEDGMENTS

REFERENCES

Belkhir, N., Bouzid, D., and Herold, V. (2009). Surface Behavior during Abrasive Grain Action in the Glass Lapping Process. *Appl. Surf. Sci.* 255, 7951–7958. doi:10.1016/j.apsusc.2009.04.178

Bu, Z., Niu, F., Chen, J., Jiang, Z., Wang, W., Wang, X., et al. (2022). Single crystal Silicon Wafer Polishing by Pretreating Pad Adsorbing SiO2 Grains and Abrasive-free Slurries. *Mater. Sci. Semiconductor Process.* 141, 106418. doi:10.1016/j.mssp.2021.106418

Burk, A. A., O'loughlin, M. J., Siergiej, R. R., Agarwal, A. K., Sriram, S., Clarke, R. C., et al. (1999). SiC and GaN Wide Bandgap Semiconductor Materials and Devices. *Solid-State Electronics* 43, 1459–1464. doi:10.1016/s0038-1101(99)00089-1

Cheng, Z., Qin, S., and Fang, Z. (2022). Numerical Modeling and Experimental Study on the Material Removal Process Using Ultrasonic Vibration-Assisted Abrasive Water Jet. *Front. Mater. Accepted Publ.* 9, 895271. doi:10.3389/fmats.2022.895271

Fang, C., Liu, C., Zhao, Z., Lin, Y., Hu, Z., and Xu, X. (2018). Study on Geometrical Patterns of Textured Fixed-Abrasive Pads in Sapphire Lapping Based on Trajectory Analysis. *Precision Eng.* 53, 169–178. doi:10.1016/j.precisioneng.2018.03.008

Hu, W., Teng, Q., Hong, T., Saetang, V., and Qi, H. (2022). Stress Field Modeling of Single-Abrasive Scratching of BK7 Glass for Surface Integrity Evaluation. *Ceramics Int.* 48, 12819–12828. doi:10.1016/j.ceramint.2022.01.153

Ji, R., Zhang, L., Zhang, L., Li, Y., Lu, S., and Fu, Y. (2022). Processing Method for Metallic Substrate Using the Liquid Metal Lapping-Polishing Plate. *Front. Mater. Submitted for publication* 9, 896346. doi:10.3389/fmats.2022.896346

Li, C., Piao, Y., Meng, B., Hu, Y., Li, L., and Zhang, F. (2022). Phase Transition and Plastic Deformation Mechanisms Induced by Self-Rotating Grinding of GaN Single Crystals. *Int. J. Machine Tools Manufacture* 172, 103827. doi:10.1016/j.ijmachtools.2021.103827

Li, H. N., Yang, Y., Zhao, Y. J., Zhang, Z., Zhu, W., Wang, W., et al. (2019). On the Periodicity of Fixed-Abrasive Planetary Lapping Based on a Generic Model. *J. Manufacturing Process.* 44, 271–287. doi:10.1016/j.jmapro.2019.05.036

Lu, Y., Shu, Q., Wang, J., and Liu, Y. (2014). A Kinematical Analysis of the Polishing Processes of Hard Magnetic Disk Substrate. *Proc. Inst. Mech. Eng. B: J. Eng. Manufacture* 228, 215–222. doi:10.1177/0954405413498073

Niitsu, K., and Yan, J. (2020). Effects of Deep Subsurface Damages on Surface Nanostructure Formation in Laser Recovery of Grinded Single-crystal Silicon Wafers. *Precision Eng.* 62, 213–222. doi:10.1016/j.precisioneng.2019.12.005

Qi, H., Shi, L., Teng, Q., Hong, T., Tangwarodomnukun, V., Liu, G., et al. (2022). Subsurface Damage Evaluation in the Single Abrasive Scratching of BK7 Glass by Considering Coupling Effect of Strain Rate and Temperature. *Ceramics Int.* 48, 8661–8670. doi:10.1016/j.ceramint.2021.12.077

Sanchez, L. E. A., Jun, N. Z. X., and Fiocchi, A. A. (2011). Surface Finishing of Flat Pieces when Submitted to Lapping Kinematics on Abrasive Disc Dressed under Several Overlap Factors. *Precision Eng.* 35, 355–363. doi:10.1016/j.precisioneng.2010.09.012

Satake, U., Matsui, S., and Enomoto, T. (2020). Polishing Pad for Reducing Edge Roll-Off while Maintaining Good Global Flatness of Silicon Wafer. *Precision Eng.* 66, 577–592. doi:10.1016/j.precisioneng.2020.09.010

Tam, H.-y., and Cheng, H. (2010). An Investigation of the Effects of the Tool Path on the Removal of Material in Polishing. *J. Mater. Process. Technology* 210, 807–818. doi:10.1016/j.jmatprotec.2010.01.012

Uhlmann, E., List, M., Patraschkov, M., and Trachta, G. (2018). A New Process Design for Manufacturing Sapphire Wafers. *Precision Eng.* 53, 146–150. doi:10.1016/j.precisioneng.2018.03.011

Wen, D., Qi, H., Ma, L., Lu, C., and Li, G. (2016). Kinematics and Trajectory Analysis of the Fixed Abrasive Lapping Process in Machining of Interdigitated Micro-channels on Bipolar Plates. *Precision Eng.* 44, 192–202. doi:10.1016/j.precisioneng.2015.12.005

Yang, Y., Li, H., Liao, Z., and Axinte, D. (2019). A Curious Observation of Phenomena Occurring during Lapping/polishing Processes. *Proc. Math. Phys. Eng. Sci.* 475, 20190304. doi:10.1098/rspa.2019.0304

Yuan, J., Yao, W., Zhao, P., Lyu, B., Chen, Z., and Zhong, M. (2015). Kinematics and Trajectory of Both-sides Cylindrical Lapping Process in Planetary Motion Type. *Int. J. Machine Tools Manufacture* 92, 60–71. doi:10.1016/j.ijmachtools.2015.02.004

Zhang, L., Zheng, B., Xie, Y., Ji, R., Li, Y., and Mao, W. (2022). Control Mechanism of Particle Flow in the Weak Liquid Metal Flow Field on Non-uniform Curvature Surface Based on Lippmann Model. *Front. Mater. Accepted Publ.* 9, 895263. doi:10.3389/fmats.2022.895263

Zhang, P., Feng, X., and Yang, J. (2015). Kinematics Analysis on the Double-Sided Polishing without Planet Carrier of 3 Inch SiC Substrate. *J. Funct. Mater.*, 18105–18111.

Zhao, J., Jiang, E., Qi, H., Ji, S., and Chen, Z. (2020). A Novel Polishing Method for Single-crystal Silicon Using the Cavitation Rotary Abrasive Flow. *Precision Eng.* 61, 72–81. doi:10.1016/j.precisioneng.2019.10.002

Conflict of Interest: XW was employed by the company Zhejiang Zhongjing Technology Co., Ltd.

The remaining authors declare that the research was conducted in the absence of any commercial or financial relationships that could be construed as a potential conflict of interest.

Publisher's Note: All claims expressed in this article are solely those of the authors and do not necessarily represent those of their affiliated organizations, or those of the publisher, the editors, and the reviewers. Any product that may be evaluated in this article, or claim that may be made by its manufacturer, is not guaranteed or endorsed by the publisher.

Check for updates

Processing Method for Metallic Substrate Using the Liquid Metal Lapping-Polishing Plate

Renquan Ji[1,2], Liyang Zhang[1,2], Li Zhang[1,2], Yanbiao Li[1,2]*, Shasha Lu[1,2] and Yufei Fu[1,2]

[1]College of Mechanical Engineering, Zhejiang University of Technology, Hangzhou, China, [2]Key Laboratory of Special Purpose Equipment and Advanced Processing Technology at Zhejiang University of Technology, Ministry of Education, Hangzhou, China

Metal is the primary substrate for fabricating flexible sensors, and its surface quality has a significant effect on the performance of these sensors. The traditional lapping-polishing technology has the disadvantages of being time-consuming and presenting difficulty in controlling the uniformity. In this paper, a liquid metal lapping-polishing plate with a self-shaping function is proposed and developed, which can realize high quality and low surface damage in the processing of the metallic substrate. It is found from the fundaments of the liquid metal lapping-polishing plate that the temperature generated by the friction between the workpiece and plate plays an important role in affecting the processing performance, and then a numerical study of the temperature field on the liquid metal lapping-polishing plate surface has been carried out, and it is found that the temperature increase with the increment of the pressure and rotation speed of the lapping-polishing plate on the target surface. Finally, it is found from experiments that the experimental results have shown to be in good agreement with the corresponding experimental data for the highest temperature under specific conditions and the processing performance has been significantly improved as well.

Keywords: liquid metal lapping-polishing plate, metallic substrate, temperature field, bismuth-based alloy, processing performance

1 INTRODUCTION

With the increasing demand for sensors in some extreme environments, the requirements for range, accuracy, and stability are increasingly strict, such that sensors with the desirable characteristics of being flexible, freely bending, foldable, and wearable have attracted many researchers to investigate this field (Elashery et al., 2022; Maciel et al., 2022). Currently, there are a large number of materials being considered as the substrates of flexible sensors, such as metal, ultra-thin glass, and organic polymer substrates (Ren et al., 2020; Sayginer et al., 2021). The ultra-thin glass and organic polymer substrates have disadvantages of poor resistance to high temperatures, and poor water and oxygen barrier ability (Garner et al., 2019; Guan et al., 2022), while the metal substrates possess advantages of good high-temperature resistance, low coefficient of thermal expansion, and exemplary performance in heat resistance (Li et al., 2020; Liu et al., 2021; Goswami and Gupta, 2022).

However, the surface quality of the metal substrate has an essential effect on the performance of flexible sensors (Khalid and Chang, 2022). Abrasive machining technology has been extensively used in the precision and ultra-precision machining of almost any materials with high efficiency and quality (Qi et al., 2021; Cheng et al., 2022; Hu et al., 2022; Qi et al., 2022). Efforts have been contributed by many scholars to improve the abrasive lapping-polishing performance (Li et al., 2019;
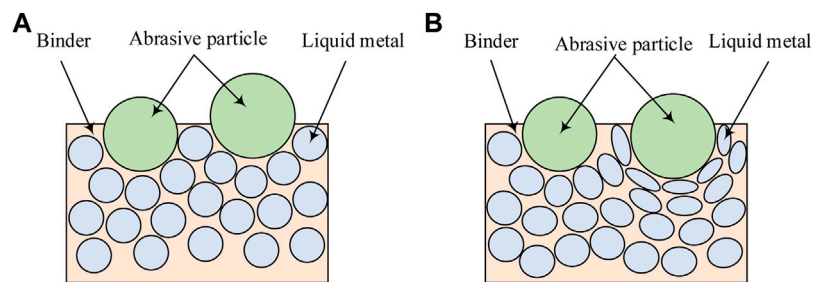
FIGURE 1 | Schematic of the liquid metal lapping-polishing plate. **(A)** Original plate, **(B)** Temperature increased plate.
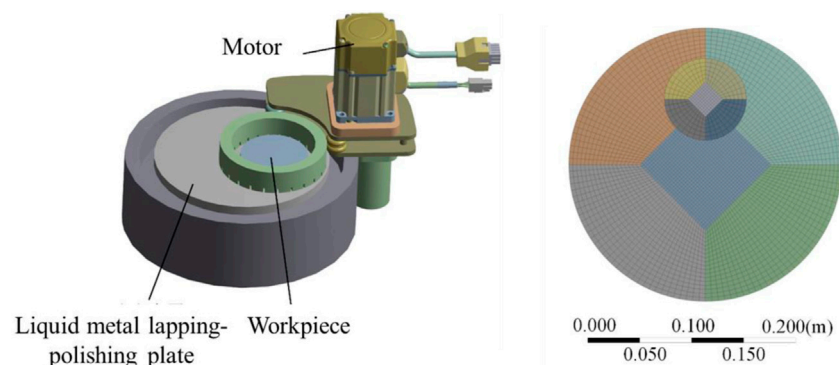

FIGURE 2 | Model geometry and meshing generation.

TABLE 1 | Material properties in simulation.

	Elastic Modulus (GPa)	Poisson's Ratio	Heat Capacity (J/kg·°C)	Thermal Conductivity (W/m/K)
Target (Stainless steel)	194	0.3	480	16.2
Lapping-polishing plate (Bismuth-based alloy)	0.132	0.45	1,200	3.3

Jin et al., 2020). Kim et al. prepared self-corrected polishing pads, which were mainly composed of a mixture of alumina abrasive particles and hydrophilic polymers, and compared with the traditional polishing pads, possesses good viscoelasticity and can extend the processing time, thus improving the processing quality (Kim et al., 2004). Zhao et al. proposed a semi-solid abrasive polishing method, which mainly employed the trap effect to reduce the defects caused by the large abrasive particles impacting the target surface during the polishing process and improve the processing quality (Zhao et al., 2011). Choi and Jeong used UV light to treat the hydrophilic polymers, by which they developed a polishing pad with self-healing and hydrophilic functions, and three types of the diamond abrasive polishing pads were fabricated to polish the die steel, which eventually reduced the surface roughness to be about 15.1 nm (Choi and Jeong, 2004). The above abrasive machining methods could realize the precision polishing of substrates with good surface quality, but the efficiency should be considered as well. In general, the abrasive lapping process is used to realize the fast thinning of the substrate, and the abrasive polishing process is employed to realize the high surface finishing of the substrate (Jin et al., 2020; Zhao et al., 2020). The liquid metal with characteristics of high electrical conductivity, low viscosity, and large tension has shown good performance in jet printing or carrying the abrasive particles to realize the machining of complicated structures (Wang et al., 2018; Zhang et al., 2022).

Thus, in this paper, the processing method of the metallic substrate using a liquid metal lapping-polishing plate is proposed to realize the combination of the abrasive lapping and polishing processes. The fundaments of the liquid metal lapping-polishing process are first analyzed, and the numerical study of the temperature field on the liquid metal lapping-polishing plate surface is then conducted to explore the effect of processing parameters on the distribution of the temperature. Finally, the corresponding experiments have been carried out to verify the numerical model and explore the processing performance.
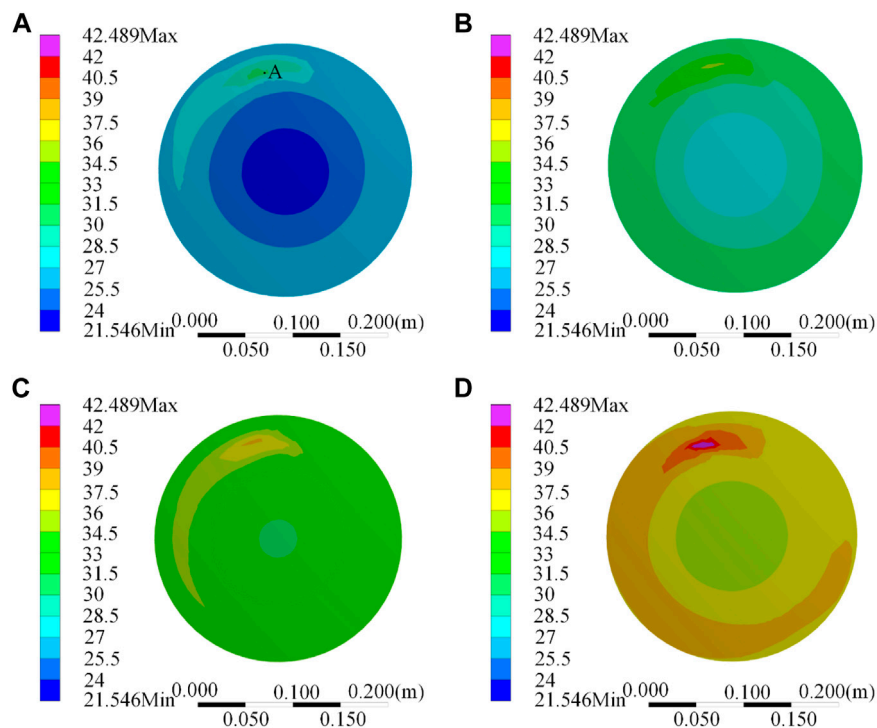
FIGURE 3 | Distribution of the temperature field on the liquid metal lapping-polishing plate with respect to the different processing time. **(A)** t=5 s, **(B)** t=10 s, **(C)** t=15 s, **(D)** t=20 s.

2 FUNDAMENTALS OF THE LIQUID METAL LAPPING-POLISHING PROCESS

A liquid metal lapping-polishing plate with the self-shaping function is first proposed and analyzed, as shown in **Figure 1**, where the liquid metal lapping-polishing plate consists of the binder, abrasive particles, and liquid metal whose hardness varies with respect to the temperature. During the lapping-polishing process, heat can be generated due to the mechanical friction between the lapping-polishing plate and the target surface, and this heat could result in
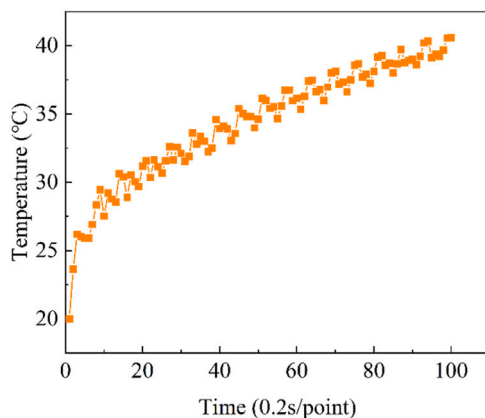
FIGURE 4 | The relationship between the temperature and processing time.

the increase of temperature in the lapping-polishing plate which in turn decreases the harness of liquid metal, such that the surface shape of the liquid metal lapping-polishing plate would be changed.

To be specific, the liquid metal lapping-polishing plate possesses originally high hardness due to the addition of liquid metal where the large abrasive particle is higher than the small abrasive particle that may cause the large surface damage on the target surface, as shown in **Figure 1A**, but during the lapping-polishing process, the hardness of liquid metal reduces with the increase of temperature, so that the large abrasive particle could recede to a certain depth under the pressure of workpiece (Li et al., 2016; Shrivastava et al., 2021). When the height of the large abrasive particle is equal to other small abrasive particles, the pressure of the workpiece is uniformly distributed by the abrasive particles on the surface of the lapping-polishing plate, as shown in **Figure 1B**, so that in this way the liquid metal lapping-polishing plate could realize the combination of the abrasive lapping and polishing processes due to its self-shaping function, and hence, significantly reducing the surface damage caused by the large abrasive particle, enhancing the surface form accuracy and improving the processing efficiency.

3 NUMERICAL STUDY OF TEMPERATURE FIELD ON THE LIQUID METAL LAPPING-POLISHING PLATE SURFACE

3.1 Model development

In the lapping-polishing process, the variation of temperature on the surface of the lapping-polishing plate would have an essential effect

FIGURE 5 | Distribution of the temperature field on the liquid metal lapping-polishing plate with respect to the different pressures in simulation. (A) P=6 KPa, (B) P=9 KPa, (C) P=12 KPa, (D) P=15 KPa.
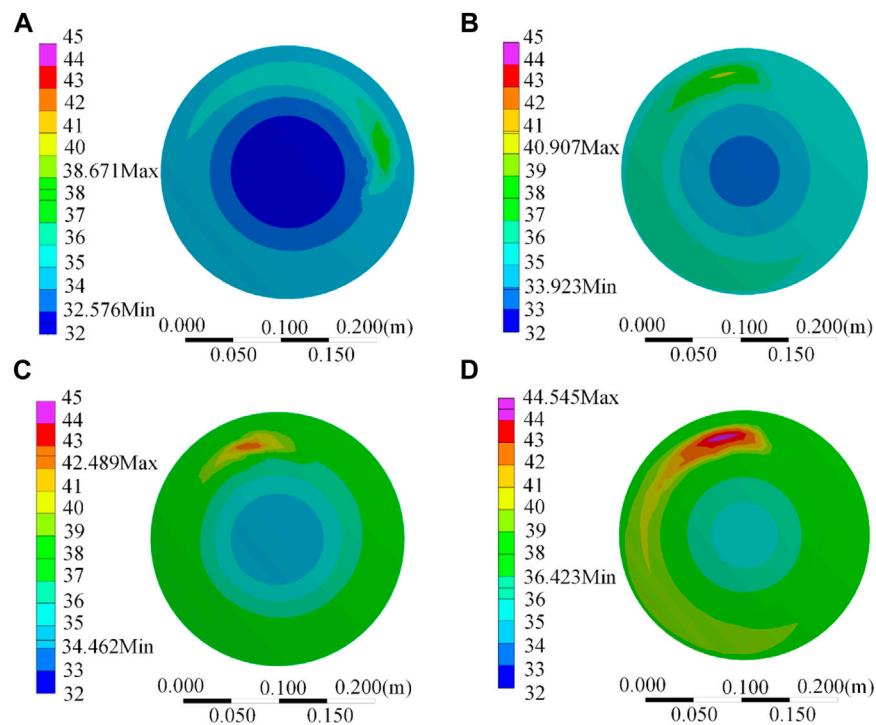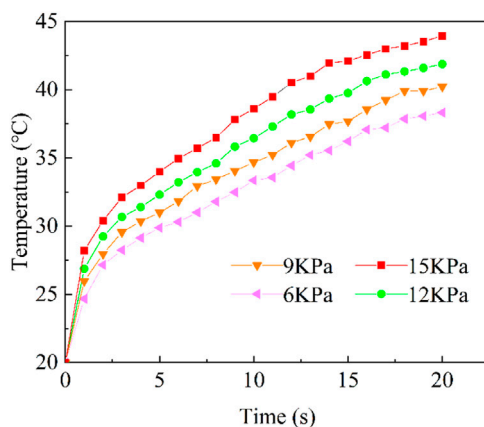

FIGURE 6 | The relationship between temperature and pressure.

on the hardness of the liquid metal, hence, affect the processing quality. The heat mainly comes from the mechanical friction between the workpiece and the lapping-polishing plate, and the temperature field on the surface of the lapping-polishing plate is mainly affected by various processing parameters, such as the lapping-polishing pressure and the rotation speed of the lapping-polishing plate. Thus, it is necessary to get an insight into the distribution of temperature field on the liquid metal lapping-polishing plate surface, such that the related numerical simulation has been first conducted in ANSYS to explore the underlying sciences, as detailed below.

To consider the experimental work that has been stated in **Section 4.1** where the single-side planetary lapping-polishing machine is used to carry out the experiments, and the associated model geometry in simulation is shown in **Figure 2**. The stainless steel is selected as the workpiece with a radius of 18 mm and thickness of 1.5 mm, and a Bismuth-based alloy with a melting point of 40°C is selected as the liquid metal that is used to model the lapping-polishing plate with a radius of 50 mm and thickness of 7.8 mm. Moreover, the major material properties used in the simulation are given in **Table 1** according to the corresponding experimental measurements, and the processing parameters considered in the simulation are as follows: four levels of the lapping-polishing pressure (P) at 6, 9, 12, 15 KPa are considered, four levels of rotation speed of the lapping-polishing plate (r_p) at 70, 100, 130, 160 r/min are selected, the rotation speed of workpiece (r_w) is set to be 130 r/min, and all the experiments are carried out at room temperature. Thus, by using a full factorial design 16 simulation test conditions can be considered for further analysis (Xie et al., 2021).

3.2 Results and Discussion
3.2.1 Overall Observation of the Temperature Field
Figure 3 presents the typical distribution of the temperature field on the liquid metal lapping-polishing plate with respect to the different processing times, t, at p = 12 kPa, r_p = 130 r/min, and r_w = 130 r/min. It can be seen from **Figure 3A** that the temperature increases quickly at the beginning of the lapping-polishing process and presents an obvious track on the surface of the lapping-polishing plate. With the further increase in the processing time the temperature shows a gradual increase due
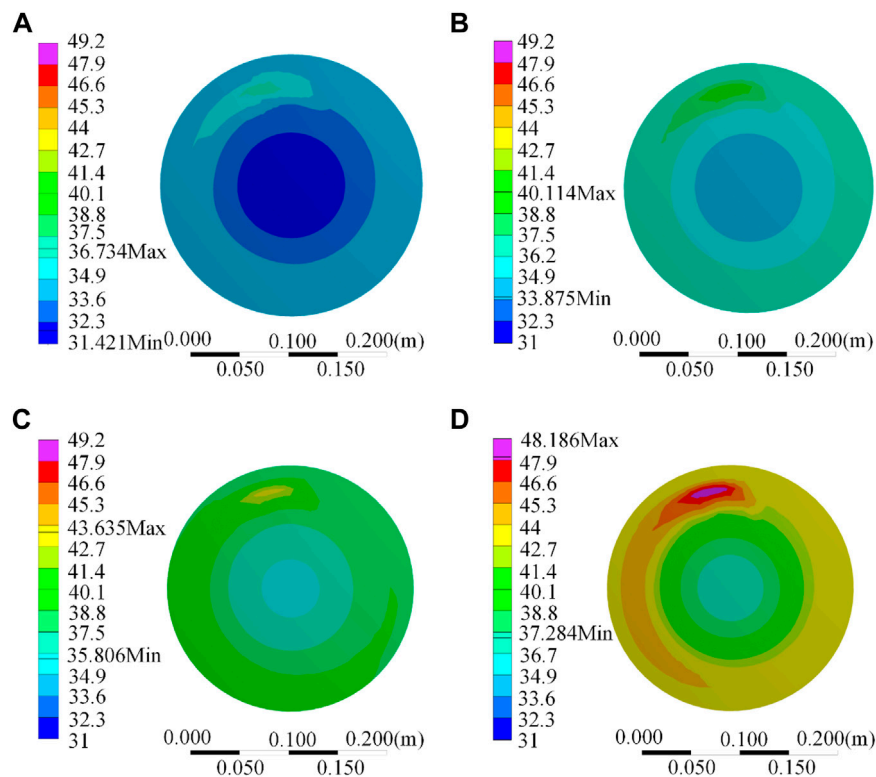
FIGURE 7 | Distribution of the temperature field on the liquid metal lapping-polishing plate with respect to the different rotation speeds in simulation. **(A)** rp=70 r/min, **(B)** rp=100 r/min, **(C)** rp=130 r/min, **(D)** rp=160 r/min.
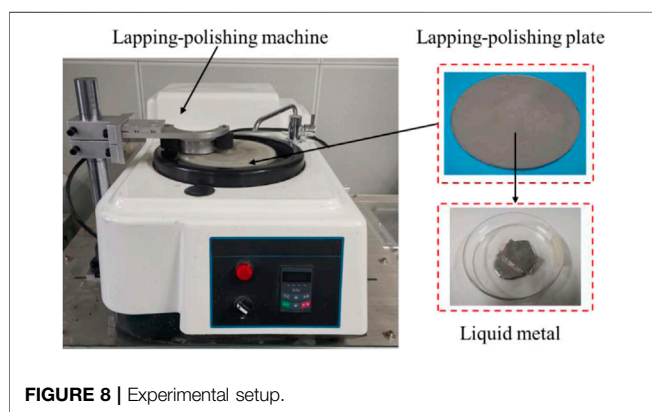

FIGURE 8 | Experimental setup.

to the frictional heat consumption in the air convection, heat conduction in the lapping-polishing plate, and the radiation to the outside environment (Lee et al., 2013; Totolin et al., 2016), as can be seen from **Figures 3B–D**. Additionally, it is also noticed from **Figure 3** that the distribution of the temperature on the lapping-polishing plate shows a ring shape, in which the temperature shows a gradually increasing trend from the center to the outer. It is attributed to the fact that the heat dissipation and transfer near the center of the lapping-polishing plate are faster, while in the outer area the temperature is higher because of the relatively higher linear speed.

A quantitative analysis of the variation of the temperature on the fixed-point A (see **Figure 3A**) on the lapping-polishing plate, which is the center of the workpiece, with respect to the processing time has been conducted. It can be seen from **Figure 4** that the mechanical friction occurs between the workpiece and the lapping-polishing plate in the early stage of the lapping-polishing process, which makes the heat continuously accumulated and to be transferred into the lapping-polishing plate, thus resulting in the fast increase of the temperature on the surface of the lapping-polishing plate. However, with the further increment of the processing time, the generation of the heat from the mechanical fraction and the consumption of the heat by the air convection, heat conduction in the lapping-polishing plate, and the radiation to the outside environment would achieve a dynamic balance, so that the variation of the temperature tends to be stable as shown in **Figure 4**.

3.2.2 The Effect of Processing Parameters on the Temperature Field

Since the lapping-polishing pressure would affect the contact force resultant fraction between the workpiece and the lapping-polishing plate which may induce the variation of the temperature in the lapping-polishing process, it is necessary to investigate the effect of pressure on the temperature field. **Figure 5** shows the distribution of the temperature field on the lapping-polishing plate with respect to different pressures

FIGURE 9 | Distribution of the temperature field on the liquid metal lapping-polishing plate with respect to the different pressures in the experiment. **(A)** P=6 KPa, **(B)** P=9 KPa, **(C)** P=12 KPa, **(D)** P=15 KPa.

FIGURE 10 | Distribution of the temperature field on the liquid metal lapping-polishing plate with respect to the different rotation speeds in the experiment. **(A)** rp=70 r/min, **(B)** rp=100 r/min, **(C)** rp=130 r/min, **(D)** rp=160 r/min.

at r_p = 130 r/min, r_w = 130 r/min, and t = 20 s. It can be seen from **Figure 5** that after the processing time of 20 s, the distribution of the temperature field on the lapping-polishing plate seems to be stable, and with the increase of pressure, the average temperature on the surface of the lapping-polishing plate gradually increases while along the radial direction of the lapping-polishing plate the temperature gradually decreases. It is also found from the simulation that the temperature in the region between the outer ring of the workpiece and the lapping-polishing plate is a little higher than in the other regions, which is attributed to the reason that there is more relative friction between the outer ring

and the workpiece in unit time as compared with the inner ring. However, the overall distribution of the temperature in the processing region is relatively uniform. **Figure 6** shows the quantitative analysis of the relation between the pressure and temperature on the lapping-polishing plate, and it is found that the highest temperature on the surface of the lapping-polishing plate reached about 38.671°C, 40.907°C, 42.489°C, and 44.545°C at the corresponding pressure of 6, 9, 12, 15 kPa, respectively.

Furthermore, the effect of the rotational speed of the lapping-polishing plate on the temperature has been also qualitatively and quantitatively analyzed according to the simulation results.
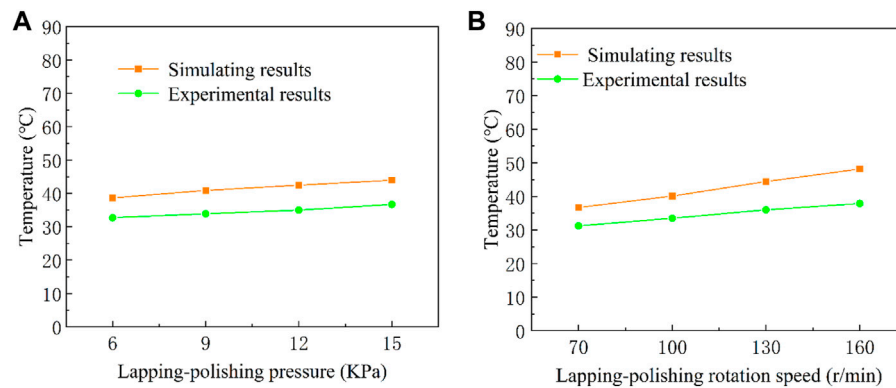
FIGURE 11 | Comparison of simulating and experimental results. **(A)** Under different lapping-polishing pressures, **(B)** Under different lapping-polishing rotation speed.

Original target surface

Surface morphology after liquid metal lapping-polishing.
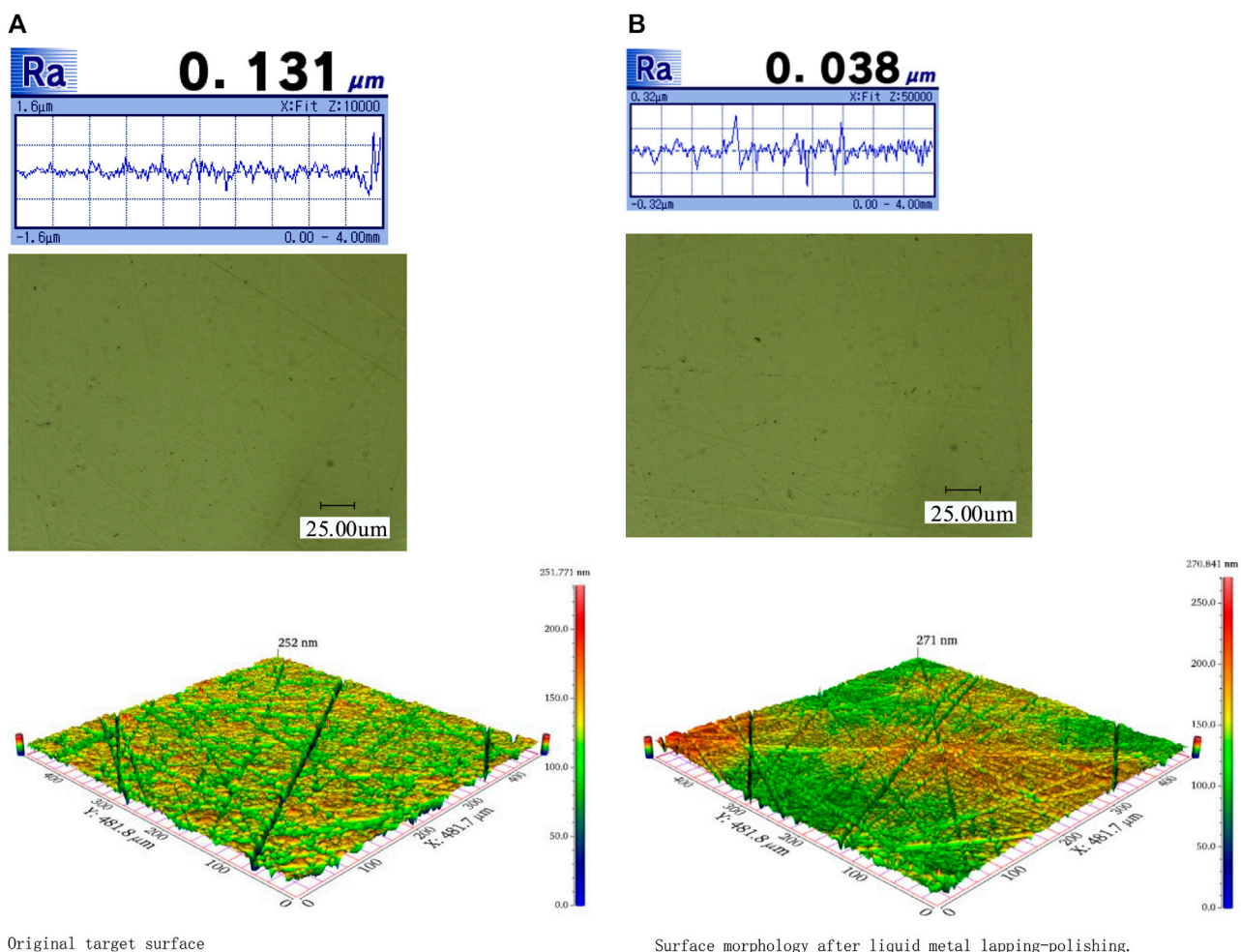
FIGURE 12 | Comparison of surface morphologies before and after liquid metal lapping-polishing. **(A)** Original target surface, **(B)** Surface morphology after liquid metal lapping-polishing.

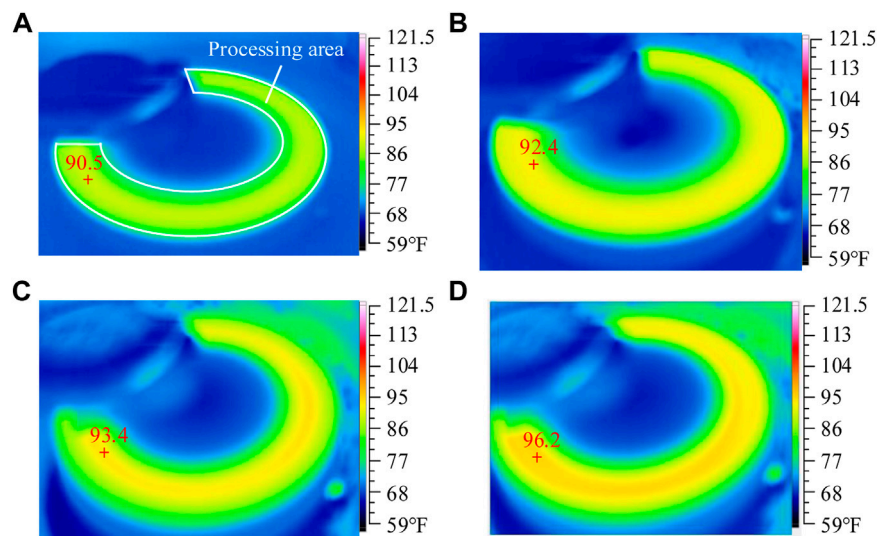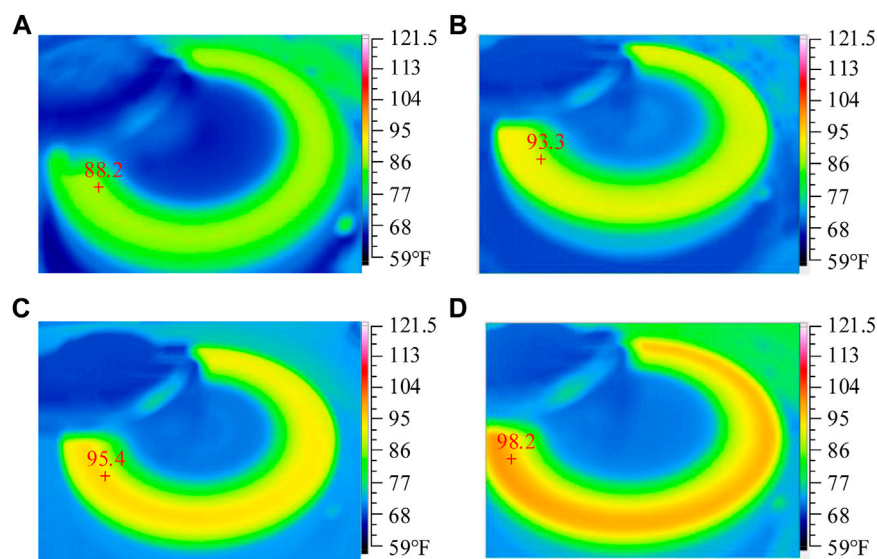**Figure 7** shows the distribution of the temperature field on the lapping-polishing plate with respect to different rotation speeds of the lapping-polishing plate at $p = 12$ kPa, $r_w = 130$ r/min, and

$t = 20$ s. It can be seen from this figure that in general the overall temperature on the surface of the lapping-polishing plate increases with an increment of the rotation speed of the

lapping-polishing plate, and it is due to the fact that increasing the rotation speed of the lapping-polishing plate the relative speed between the workpiece and the lapping-polishing plate increase as well, which results in the increase of the heat generation by the mechanical fraction. Similarity, it can be found from the quantitative analysis of the relation between the rotation speed of the lapping-polishing plate and temperature showing that the highest temperature on the surface of the lapping-polishing plate reached about 36.734°C, 40.114°C, 43.635°C, 48.186°C at the corresponding rotation speed of 70, 100, 130, 160 r/min, respectively.

4 EXPERIMENTAL STUDY

4.1 Experiments
The in-house developed liquid metal lapping-polishing plate which consists of the Bismuth-based alloy with the melting point of 40°C and SiC abrasive particles with a size of 3,000 mesh is fixed in the MP-1B lapping-polishing machine to realize the single-side planetary lapping-polishing of the stainless steel substrate, as shown in **Figure 8**, and the rotation speed of the lapping-polishing plate can be exactly controlled in the range of 50–1,000 r/min. Thus, the processing parameters considered in the experiment are similar to that in simulation, where four levels of P at 6, 9, 12, 15 KPa are selected, four levels of r_p at 70, 100, 130, 160 r/min are considered, r_w is set to be 130 r/min and all the experiments are carried out at room temperature. Again, a full factorial design is considered for P and r_p and it results in 16 tests in the experiment. In order to verify the numerical model and explore the processing performance, the temperature is real-time measured by using Fluke Tix640 Infrared Camera and the surface morphology is observed by using Keyence 3D Microscope VHX600.

4.2 Results and Discussion
Figure 9; **Figure 10** present the real-time measurement of temperature on the surface of the lapping-polishing plate with respect to different P and r_p at t = 20 s, and the highest temperature point on the surface is measured for each condition in units of ℉, so that the comparison between the simulating and experimental results can be obtained as shown in **Figure 11**. It can be seen from **Figures 9, 10** that with the increase of P and r_p, the temperature on the surface of the lapping-polishing plate increases as well, which indicates similar trends to the numerical results. It is also found from **Figure 9A** that the processing area shows a typical ring temperature and the temperature decreases to both sides of the processing area, which is also agreed with the numerical findings in **Section 3.2**. In addition, the quantitative comparison in **Figure 11** shows that the simulating trends of the temperature with respect to different P and r_p are similar to that in the experiment, and the model predictions have shown to be in good agreement with the corresponding experimental data for the highest temperature under specific conditions. Therefore, it may be deduced that the numerical model has been correctly developed for use to simulate the temperature field on the liquid metal lapping-polishing plate surface.

The processing performance has also been analyzed by using the developed liquid metal lapping-polishing plate in this study. The original surface morphology of the stainless steel substrate is shown in **Figure 12A** with a surface roughness of about 0.132 μm, and large scratches can be obviously observed on the target surface. After the lapping-polishing process at p = 12 kPa, r_p = 70 r/min, and t = 20 min, the surface morphology of the target surface is shown in **Figure 12B**, in which the surface roughness has been reduced to about 0.038 μm and the scale of the scratches on the target surface has been significantly reduced as well. Thus, the developed liquid metal lapping-polishing plate can be used to improve the abrasive lapping-polishing performance, and future work will be focused on the optimized design of the processing parameters during the liquid metal lapping-polishing process.

5 CONCLUSION

In this paper, the liquid metal lapping-polishing method has been proposed by using the lapping-polishing plate with the self-shaping function to realize the high quality and low surface damage in the processing of the metallic substrate. The underlying science of this method has been fundamentally explored and it is found that the temperature generated by the friction between the workpiece and plate plays an essential role in affecting the hardness of the liquid metal which could affect the distribution of abrasive particles on the surface of the plate and hence affecting the processing performance. Then, the effect of the processing parameters, including the lapping-polishing pressure and the rotation speed of the lapping-polishing plate, on the temperature field on the liquid metal lapping-polishing plate surface has been numerically carried out, and it is found from both qualitative and quantitative analysis that the temperature increases with the increment of the pressure and rotation speed of the lapping-polishing plate on the target surface. Finally, the in-house developed liquid metal lapping-polishing plate which consists of the Bismuth-based alloy with the melting point of 40°C and SiC abrasive particles with a size of 3,000 mesh is fixed in the MP-1B lapping-polishing machine to realize the single-side planetary lapping-polishing of the stainless steel substrate, and it is found from experiments that the experimental results have shown to be in good agreement with the corresponding experimental data for the highest temperature under specific conditions and the processing performance has been significantly improved as well. Therefore, the liquid metal lapping-polishing method proposed in this study could provide a reference for the development of the abrasive lapping-polishing process.

DATA AVAILABILITY STATEMENT

The raw data supporting the conclusion of this article will be made available by the authors, without undue reservation.

AUTHOR CONTRIBUTIONS

Conceptualization, LZ; Data curation, RJ; Formal analysis, YF; Investigation, LZ; Software, SL; Supervision, YL; Writing—original draft, RJ; Writing—review and editing, YL.

REFERENCES

Cheng, Z., Qin, S., and Fang, Z. (2022). Numerical Modeling and Experimental Study on the Material Removal Process Using Ultrasonic Vibration-Assisted Abrasive Water Jet. *Front. Mater. Accept. Publ.* 9, 895271. doi:10.3389/fmats.2022.895271

Choi, J. y., and Jeong, H. d. (2004). A Study on Polishing of Molds Using Hydrophilic Fixed Abrasive Pad. *Int. J. Mach. Tools Manuf.* 44, 1163–1169. doi:10.1016/j.ijmachtools.2004.04.006

Elashery, S. E. A., Attia, N. F., and Oh, H. (2022). Design and Fabrication of Novel Flexible Sensor Based on 2D Ni-MOF Nanosheets as a Preliminary Step toward Wearable Sensor for Onsite Ni (II) Ions Detection in Biological and Environmental Samples. *Anal. Chim. Acta* 1197, 339518. doi:10.1016/j.aca.2022.339518

Garner, S., Chowdhury, D., and Lewis, S. (2019). Ultrathin Glass Substrates for Thin, Lightweight, Flexible OLED Lighting. *Inf. Disp.* 35, 9–13. doi:10.1002/msid.1045

Goswami, P., and Gupta, G. (2022). Recent Progress of Flexible NO2 and NH3 Gas Sensors Based on Transition Metal Dichalcogenides for Room Temperature Sensing. *Mater. Today Chem.* 23, 100726. doi:10.1016/j.mtchem.2021.100726

Guan, X., Yu, Y., Hou, Z., Wu, K., Zhao, H., Liu, S., et al. (2022). A Flexible Humidity Sensor Based on Self-Supported Polymer Film. *Sensors Actuators B Chem.* 358, 131438. doi:10.1016/j.snb.2022.131438

Hu, W., Teng, Q., Hong, T., Saetang, V., and Qi, H. (2022). Stress Field Modeling of Single-Abrasive Scratching of BK7 Glass for Surface Integrity Evaluation. *Ceram. Int.* 48, 12819–12828. doi:10.1016/j.ceramint.2022.01.153

Jin, M., Wang, L., Ye, S., Qi, H., Kang, J., Hong, T., et al. (2020). A Novel Functionally Graded Lapping and Polishing Method for the Improvement of Material Removal Uniformity. *J. Manuf. Process.* 50, 102–110. doi:10.1016/j.jmapro.2019.12.039

Khalid, M. A. U., and Chang, S. H. (2022). Flexible Strain Sensors for Wearable Applications Fabricated Using Novel Functional Nanocomposites: A Review. *Compos. Struct.* 284, 115214. doi:10.1016/j.compstruct.2022.115214

Kim, H., Park, B., Lee, S., Jeong, H., and Dornfeld, D. A. (2004). Self-conditioning Fixed Abrasive Pad in CMP. *J. Electrochem. Soc.* 151, G858–G862. doi:10.1149/1.1813951

Lee, S. J., Chen, Y. H., Liu, C. P., and Fan, T. J. (2013). Electrochemical Mechanical Polishing of Flexible Stainless Steel Substrate for Thin-Film Solar Cells. *Int. J. Electrochem. Sci.* 8, 6878–6888.

Li, W., Zhang, X., Kou, H., Wang, R., and Fang, D. (2016). Theoretical Prediction of Temperature Dependent Yield Strength for Metallic Materials. *Int. J. Mech. Sci.* 105, 273–278. doi:10.1016/j.ijmecsci.2015.11.017

Li, H. N., Yang, Y., Zhao, Y. J., Zhang, Z., Zhu, W., Wang, W., et al. (2019). On the Periodicity of Fixed-Abrasive Planetary Lapping Based on a Generic Model. *J. Manuf. Process.* 44, 271–287. doi:10.1016/j.jmapro.2019.05.036

Li, Z., Shan, Y., Wang, X., Li, H., Yang, K., and Cui, Y. (2020). Self-healing Flexible Sensor Based on Metal-Ligand Coordination. *Chem. Eng. J.* 394, 124932. doi:10.1016/j.cej.2020.124932

Liu, M.-Y., Hang, C.-Z., Zhao, X.-F., Zhu, L.-Y., Ma, R.-G., Wang, J.-C., et al. (2021). Advance on Flexible Pressure Sensors Based on Metal and Carbonaceous Nanomaterial. *Nano Energy* 87, 106181. doi:10.1016/j.nanoen.2021.106181

Maciel, C. C., De Lima, L. F., Ferreira, A. L., De Araujo, W. R., and Ferreira, M.Q. Development of a Flexible and Disposable Electrochemical Sensor Based on Poly (Butylene Adipate-Co-Terephthalate) and Graphite for Hydroquinone Sensing. *Sensors Actuators Rep.* 4, 100091. doi:10.1016/j.snr.2022.100091

FUNDING

Qi, H., Qin, S., Cheng, Z., Teng, Q., Hong, T., and Xie, Y. (2021). Towards Understanding Performance Enhancing Mechanism of Micro-holes on K9 Glasses Using Ultrasonic Vibration-Assisted Abrasive Slurry Jet. *J. Manuf. Process.* 64, 585–593. doi:10.1016/j.jmapro.2021.01.048

Qi, H., Shi, L., Teng, Q., Hong, T., Tangwarodomnukun, V., Liu, G., et al. (2022). Subsurface Damage Evaluation in the Single Abrasive Scratching of BK7 Glass by Considering Coupling Effect of Strain Rate and Temperature. *Ceram. Int.* 48, 8661–8670. doi:10.1016/j.ceramint.2021.12.077

Ren, Y., Sun, X., and Liu, J. (2020). Advances in Liquid Metal-Enabled Flexible and Wearable Sensors. *Micromachines (Basel)* 11, 200. doi:10.3390/mi11020200

Sayginer, O., Iacob, E., Varas, S., Szczurek, A., Ferrari, M., Lukowiak, A., et al. (2021). Design, Fabrication and Assessment of an Optomechanical Sensor for Pressure and Vibration Detection Using Flexible Glass Multilayers. *Opt. Mater.* 115, 111023. doi:10.1016/j.optmat.2021.111023

Shrivastava, S. C., RamakantSrivastava, S., Srivastava, S., and Pandey, J. D. (2021). Computation of Thermophysical Properties of Liquid Metals and Alloys on the Basis of Generalized Version of Hole Theory. *Chem. Phys.* 549, 111284. doi:10.1016/j.chemphys.2021.111284

Totolin, V., Göcerler, H., Rodríguez Ripoll, M., and Jech, M. (2016). Tribo-electrochemical Study of Stainless Steel Surfaces during Chemical-Mechanical Polishing. *Lubr. Sci.* 28, 363–380. doi:10.1002/ls.1336

Wang, T., Kwok, T.-H., Zhou, C., and Vader, S. (2018). *In-situ* Droplet Inspection and Closed-Loop Control System Using Machine Learning for Liquid Metal Jet Printing. *J. Manuf. Syst.* 47, 83–92. doi:10.1016/j.jmsy.2018.04.003

Xie, Y., Gui, F. X., Wang, W. J., and Chien, C. F. (2021). A Two-Stage Multi-Population Genetic Algorithm with Heuristics for Workflow Scheduling in Heterogeneous Distributed Computing Environments. *IEEE Trans. Cloud Comput.*. doi:10.1109/tcc.2021.3137881

Zhang, L., Zheng, B., Xie, Y., Ji, R., Li, Y., and Mao, W. (2022). Control Mechanism of Particle Flow in the Weak Liquid Metal Flow Field on Non-uniform Curvature Surface Based on Lippmann Model. *Front. Mater. Accept. Publ.* 9, 895263. doi:10.3389/fmats.2022.895263

Zhao, P., Wang, Z., and Yuan, J. (2011). Analysis for Trap Effect Influence Factors of Semi-fixed Abrasive Plate. *China Mech. Eng.* 22, 2399–2403.

Zhao, J., Jiang, E., Qi, H., Ji, S., and Chen, Z. (2020). A Novel Polishing Method for Single-Crystal Silicon Using the Cavitation Rotary Abrasive Flow. *Precis. Eng.* 61, 72–81. doi:10.1016/j.precisioneng.2019.10.002

Optimization of Lapping and Polishing of Steel Samples for Nanoindentation Based on SVM-GA

Zhichao Cheng [1,2], Qianfeng Wei [1,2] and Donghui Wen [1,2]*

[1]College of Mechanical Engineering, Zhejiang University of Technology, Hangzhou, China, [2]Key Laboratory of Special Purpose Equipment and Advanced Processing Technology, Ministry of Education and Zhejiang Province, Zhejiang University of Technology, Hangzhou, China

The nanoindentation test is extensively used to obtain the mechanics performance of different kinds of materials. In this study, the general process in the lapping and polishing of Q235 steel samples for nanoindentation has been analyzed by considering the pressure (P), rotation speed of the lapping and polishing plate (r_p), flow rate of abrasive slurry (Q_a), and the processing time (t). It is found from the lapping experiments with a full factorial design that the optimized processing parameters are r_p of 200 r/min, P of 30 N, and t of 4 min considered in this study by considering the material removal rate and subsurface damage. The central composite design method has been used to design the polishing experiments, and the support vector machine (SVM) method has been used to deal with these experimental results, and it is found that the developed SVM model can accurately predict the surface roughness under different processing parameters. Then, based on the SVM model, the genetic algorithm (GA) method is used to obtain the optimized processing parameters in the polishing process, and it is found from the SVM-GA study that the optimized processing parameters in the lapping process are r_p of 108 r/min, P of 33 N, Q_a of 20 ml/min, and t of 3 min. Finally, a set of nanoindentation tests have been conducted to evaluate the lapping and polishing performance, and it is found that the surface integrity has been significantly improved after the optimization of the lapping and polishing parameters by using the SVM-GA method considered in this study.

Keywords: lapping and polishing process, processing parameter optimization, nanoindentation, SVM-GA, Q235 steel

INTRODUCTION

With the fast development in the fabrication of structures on the functional materials used in aerospace engineering, renewable energy engineering, and microelectronics engineering, the characterization of material properties at the microscale and nanoscale levels must be accurately obtained (Reggente et al., 2020; Hossain et al., 2022). Currently, nanoindentation is considered a powerful technique used to quantitatively characterize the mechanical properties of different kinds of materials (Das et al., 2022), and by fitting the appropriate models to the curve of force with respect to displacement obtained from the test, the major material properties, such as the elastic modulus, hardness, and fracture toughness can be measured at the microscale and nanoscale (Isik et al., 2022; Song et al., 2022). Since the indentation depths are in the order of nanometers, the surface quality of the sample has an essential effect on the nanoindentation test

FIGURE 1 | Automatic lapping and polishing machine.

FIGURE 2 | Schematic representation of the lapping and polishing of steel samples for nanoindentation.
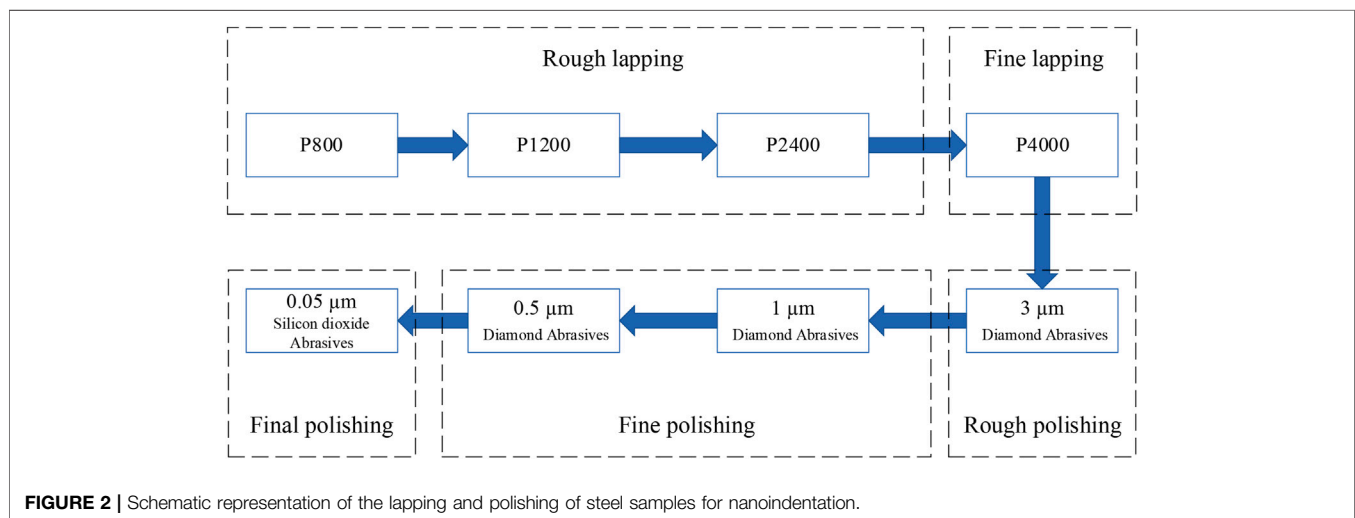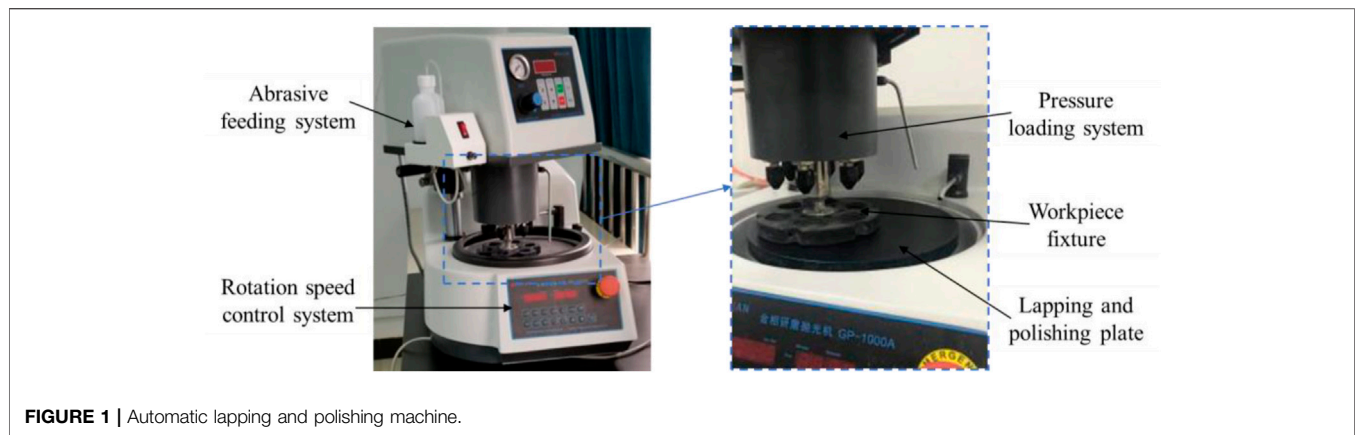
(Chen et al., 2014). Therefore, it is necessary to investigate the preparation of samples with good surface integrity.

Abrasive machining technology, as one of the non-traditional machining technologies, has been extensively used to produce complicated structures and smooth surfaces with high efficiency and accuracy (Ge J. et al., 2021; Cheng et al., 2022; Zhang et al., 2022), by which the material removal is made by the successive impacts of abrasive particles on the target surface (Hu et al., 2022; Qi et al., 2022). The abrasive lapping and polishing techniques are often used to realize the high surface finish of the flat target surface (Ge J. Q. et al., 2021; Ji et al., 2022). Li et al. conducted the investigation on the fixed-abrasive planetary lapping technology according to a generic model, and the lapping uniformity has been improved due to the uniform distribution of the particle trajectories moving on the target surface (Li et al., 2019). By analyzing the kinematics and trajectory in the fixed-abrasive planetary lapping process, Wen et al. explored the effect of the rotation speed ratio of the work piece to the lapping plate on the distribution of the particle trajectories in the machining of interdigitated micro-channels on bipolar plates, and it is found that the surface integrity has been enhanced (Wen et al., 2016). Chen et al. designed a novel driving system which was fixed on the

single-side planetary abrasive lapping machine to realize the irrational rotation speed ratio of the work piece to the lapping plate which can improve the surface quality in terms of the surface form uniformity (Chen et al., 2021). In addition, in the abrasive polishing process, the abrasive slurry is usually used to conduct the precision and ultra-precision polishing of the target surface with free abrasive particles. Strey and Scandian studied the effect of the abrasive polishing load on the surface roughness and material

TABLE 1 | Experimental results in the lapping process.

No.	r_P (r/min)	P (N)	SSD (μm)	MRR (mg/s)
1	100	20	1.28	0.060
2	100	30	1.10	0.088
3	100	40	1.54	0.095
4	150	20	1.35	0.099
5	150	30	1.12	0.145
6	150	40	1.80	0.153
7	200	20	1.43	0.100
8	200	30	1.39	0.167
9	200	40	1.92	0.200

TABLE 2 | Experimental results in the polishing process.

No.	r_p (r/min)	P (N)	Q_a (ml/min)	t (min)	R_a (nm)
1	150	30	15	2.0	1.741
2	200	40	20	1.5	3.518
3	200	20	10	2.5	3.264
4	150	30	25	2.0	1.664
5	100	20	10	1.5	3.845
6	200	40	10	2.5	2.744
7	200	40	20	2.5	2.738
8	150	30	15	2.0	1.590
9	200	40	10	1.5	2.515
10	100	20	20	1.5	3.113
11	200	20	20	1.5	1.798
12	150	30	15	2.0	1.645
13	100	40	20	2.5	1.574
14	100	20	10	2.5	3.565
15	150	30	15	2.0	1.528
16	150	30	5	2.0	2.199
17	150	30	15	3.0	1.808
18	150	30	15	2.0	1.776
19	200	20	10	1.5	2.102
20	50	30	15	2.0	2.846
21	100	20	20	2.5	1.903
22	150	50	15	2.0	2.412
23	100	40	10	2.5	1.859
24	150	10	15	2.0	3.495
25	150	30	15	1.0	2.140
26	250	30	15	2.0	3.564
27	150	30	15	2.0	1.528
28	150	30	15	2.0	1.517
29	100	40	10	1.5	1.974
30	200	20	20	2.5	1.916
31	100	40	20	1.5	2.105

TABLE 3 | Additional experimental results in the polishing process.

No.	r_p (r/min)	P (N)	Q_a (ml/min)	t (min)	R_a (nm)
1	100	40	20	1.5	2.91
2	100	30	20	1	3.00
3	150	20	10	1.5	2.45
4	150	40	20	2	1.70
5	200	30	15	3	2.57

removal rate of hard-brittle materials, and it is found that the related processing parameters have significant effects on the surface finish (Strey and Scandian, 2021). By designing the ice-bonded abrasive polishing tool, Nayak and Ramesh Babu investigated the influence of the tool and work piece interface temperature rise on the life of the polishing process, and this type of polishing plate could be used to improve the polishing life and the surface quality (Nayak and Ramesh Babu, 2020).

According to the aforementioned analysis, to improve the surface integrity in the lapping and polishing process, the novel designs of the lapping or polishing plate with different driving systems are generally used; however, limited research has been contributed to the optimization of the processing parameters involved in the lapping and polishing process for the improvement of the surface quality, which is the most convenient and effective way with the lowest cost as well. Thus, in this study, the optimization in the lapping and polishing of steel samples for nanoindentation will be investigated by using the support vector machine and genetic algorithm methods.

EXPERIMENTAL WORK

Experimental Setup

As shown in **Figure 1**, in the experiment, a GP-1000 A automatic lapping and polishing machine is used, including the abrasive slurry feeding system, rotation speed control system, lapping and polishing

plate, work piece fixture, and pressure loading system, in which the range of the pressure (P) is from 5 to 60 N, and the range of the rotation speed of the lapping and polishing plate (r_p) is from 0 to 1,000 r/min. In general, both the lapping and polishing processes are necessary for the preparation of samples for the nanoindentation tests with high surface integrity, and the lapping and polishing processes considered in this study are shown in **Figure 2**. In the lapping process, the sandpapers with relatively large sizes of abrasive particles are fixed on the lapping and polishing plates to achieve a high material removal rate from the target within a given processing time (t). In the polishing process, free abrasive particles with relatively small sizes are formed between the work piece and the lapping and polishing plates by using the abrasive slurry feeding system with a given flow rate (Q_a) to realize the high surface integrity on the target.

In this study, the Q235 steel is selected as the work piece, with dimensions of 15 mm × 15 mm×5 mm, whose density is 7.85 g/cm^3, elastic modulus is 210 GPa, and its original R_a and SSD are about 300–500 nm and 9–12 μm, respectively. Moreover, the PSA Silicon Carbide sandpapers with different sizes of P800 (average diameter of 22 μm), P1200 (average diameter of 15 μm), P2400 (average diameter of 10 μm), and P4000 (average diameter of 5 μm) are employed in the lapping process, while in the polishing process, the diamond and silicon dioxide abrasives with different sizes (see **Figure 2**) are used from the rough polishing process to the final polishing process. Since P, r_p, Q_a, and t are the major processing parameters that could affect the performance of the lapping and polishing processes, it is required to explore the optimized design of these processing parameters.

Experimental Design

In the lapping process, according to the previous studies, P and r_p are the essential factors that would affect the lapping performance in terms of the material removal rate (MRR) and subsurface damage (SSD), and it is found that when the processing time for each lapping process shown in **Figure 2** is more than 3 min, both of the MRR and SSD seems to be stable. Thus, in the lapping process, three levels of P at 20, 30, and 40 N and three levels of r_p at 100, 150, and 200 r/min are considered with a full factorial design under t = 4 min, which results in a total of nine tests (Xie et al., 2021).

In the polishing process, P, r_p, Q_a, and t are found to be the important factors affecting the polishing performance in terms of surface roughness (R_a) so that three levels of P at 20, 30, and 40 N, three levels of r_p at 100, 150, and 200 r/min, three levels of Q_a at 10, 15, and 20 ml/min, and three levels of t at 1.5, 2, and 2.5 min are used in this study. Because of the many processing parameters considered
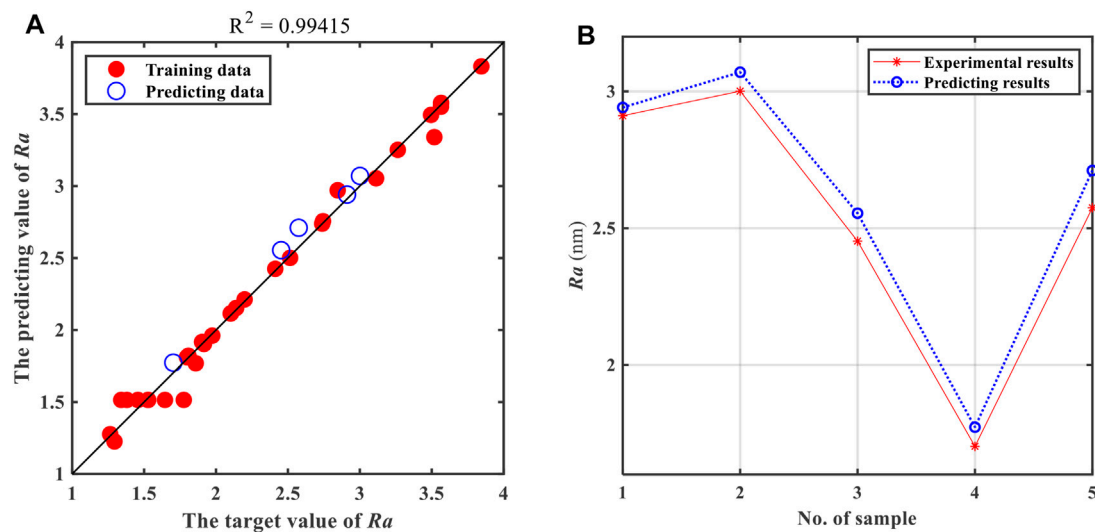
FIGURE 3 | (A) Evaluation of the predicting accuracy of the SVM and **(B)** quantitative comparison between the SVM predicting results and experimental results.
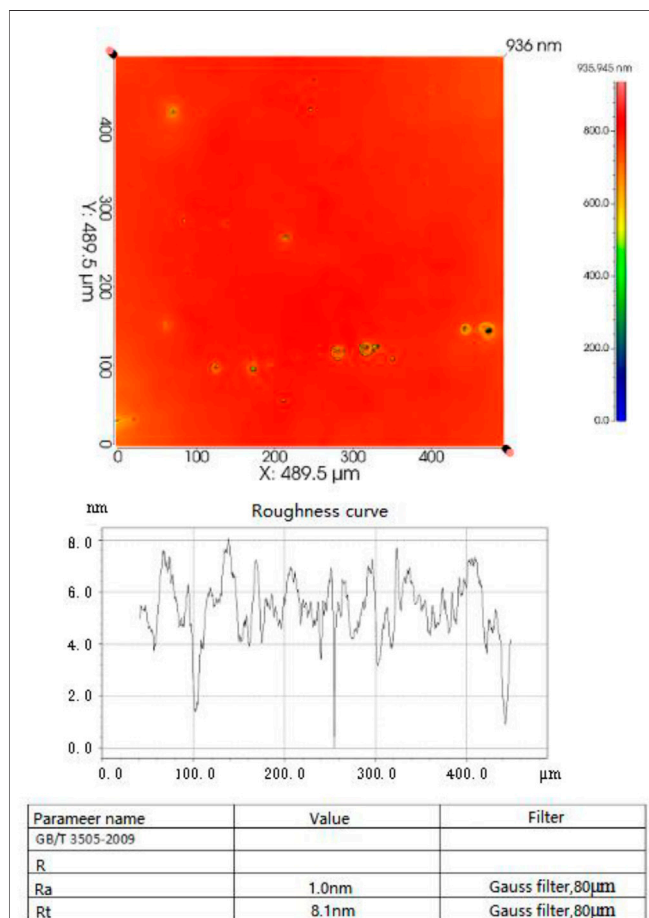

FIGURE 4 | Surface morphology of the Q235 steel sample after the lapping and polishing processes at r_p = 108 r/min, P = 33 N, Q_a = 20 ml/min, and t = 3 min.

previously, the traditional full factorial design would result in a large number of tests which is not suitable for this study. The central composite design (CCD) has been extensively used to optimize the experimental design with the least number of tests (Imanian and Biglari, 2022), which can not only evaluate the linear and interaction terms but can also estimate the high-order effects. Thus, the experimental design in the polishing process is determined by the CCD method which results in a total of 31 tests.

Experimental Measurement

The *MRR*, *SSD*, and R_a are the three essential factors that can be used to evaluate the lapping and polishing performance. The *MRR* can be calculated by measuring the mass of the work piece with an accuracy of 0.01 mg before and after the lapping process within the given processing time, whereas it is hard to obtain the *MRR* by measuring the mass loss before and after the polishing process because of the little material removal in this process. The *SSD* can be measured after the lapping process by using the Nano Indenter G200 with an accuracy of 0.01 nm and maximum depth of 500 μm, and again, this is hard to be obtained after the polishing process because the limited *SSD* can be observed. R_a can be measured after both the lapping and polishing processes with the assistance of the SuperView White Light Interferometer with an accuracy of 0.002 nm. Thus, these three significant factors are considered in this study to quantitatively evaluate the lapping and polishing performance.

RESULTS AND DISCUSSION

Optimization of Processing Parameters in the Lapping Process

The experimental results in the lapping process are shown in **Table 1**. When P is 30 N, the depth of the *SSD* is the smallest under the same r_p, and the depth of the *SSD* increases sharply
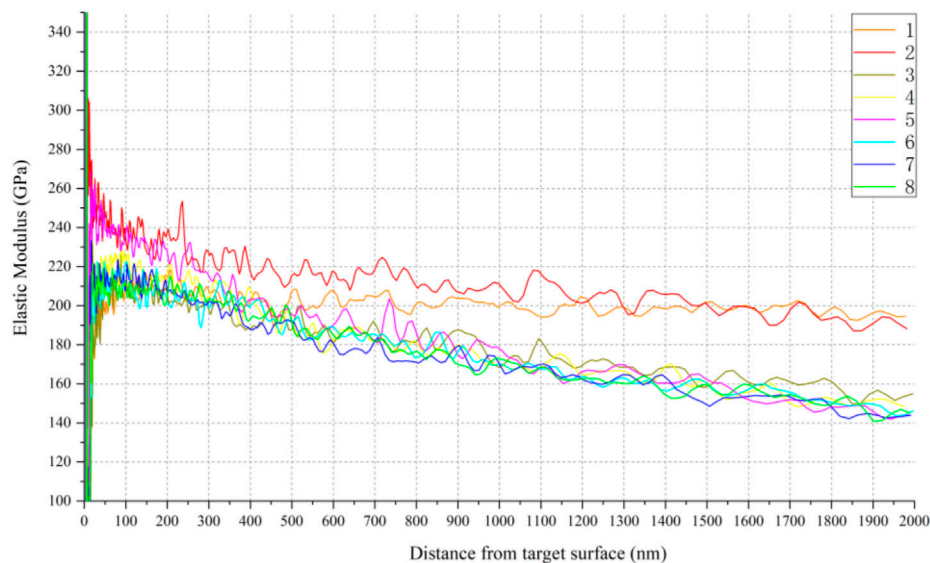
FIGURE 5 | Elastic modulus test results.

from 30 to 40 N, which agrees well with the existing research results. It is attributed to the reason that the variation of pressure in this range results in an increase in the thermal effect, thus causing large damage to the target. It is also found from **Table 1** that r_p is positively correlated with the depth of the *SSD*, which indicates that within the range of 100–200 r/min, the lower the rotation speed, the better the depth of the *SSD* will be. In addition, r_p and *P* are found to be positively correlated with the *MRR*, and the *MRR* is maximum when *P* is 40 N and r_p is 200 r/min. Since the results of the full factorial experiment can be directly compared from **Table 1**, the combination of the optimal levels of each factor is the optimized combination of processing parameters without considering the interactions. From the perspective of the *SSD* and *MRR*, the optimized processing parameters in the lapping process are found to be r_p of 200 r/min, *P* of 30 N, and *t* of 4 min considered in this study.

Optimization of Processing Parameters in the Polishing Process

According to the optimized processing parameters in the lapping process, the original samples of the Q235 steel have been first lapped with these optimized processing parameters, and then, they are polished under different conditions, as shown in **Table 2**, where the experimental results in the polishing process are given. Since many combinations of the processing parameters are considered by using the CCD method, in this study, a support vector machine (SVM) is proposed to deal with these experimental results. The SVM is a supervised machine learning model that uses classification algorithms for two-group classification problems. After giving an SVM model sets of labeled training data for each category, it can categorize new data (Fayed and Atiya, 2021; Liang et al., 2022). Thus, by using MATLAB software, 31 experimental data in terms of R_a are trained with the SVM method to obtain the fitness function, which

can be used to predict the R_a under different processing parameters. To evaluate the predicting capacity of the SVM method, additional five tests have been conducted, and the results are shown in **Table 3**.

Figure 3A shows the evaluation of the predicting accuracy of the SVM, where the red dots represent the training data based on the 31 experimental results, and the blue dots represent the predicting data according to the processing parameters given in **Table 3**, and it can be seen from this figure that the value of R^2 is 0.99415 which indicates that by using the developed SVM model, it can accurately predict R_a under different processing parameters considered in this study. It can be also seen from **Figure 3B** that the quantitative comparison between the SVM predicting results and experimental results show a good agreement.

Furthermore, according to the SVM fitness function, the genetic algorithm (GA) is used in this study to obtain the optimized processing parameters in the polishing process (Jeyaranjani and Devaraj, 2022), and it is found from the SVM-GA study that the optimized processing parameters in the lapping process are r_p of 108 r/min, *P* of 33 N, Q_a of 20 ml/min, and *t* of 3 min considered in this study, and the predicting value of R_a is 1.07 nm under this condition. The corresponding experiments have also been carried out to verify the accuracy of the SVM-GA method, and the surface morphology of the Q235 steel sample is shown in **Figure 4**, where the R_a is about 1 nm, so that it may be deduced that the SVM-GA method has been correctly developed for use to predict and optimize the polishing process.

Evaluation of the Lapping and Polishing Performance for Nanoindentation

To evaluate the lapping and polishing performance after the optimization of the processing parameters considered in this study, a set of nanoindentation tests have been conducted to
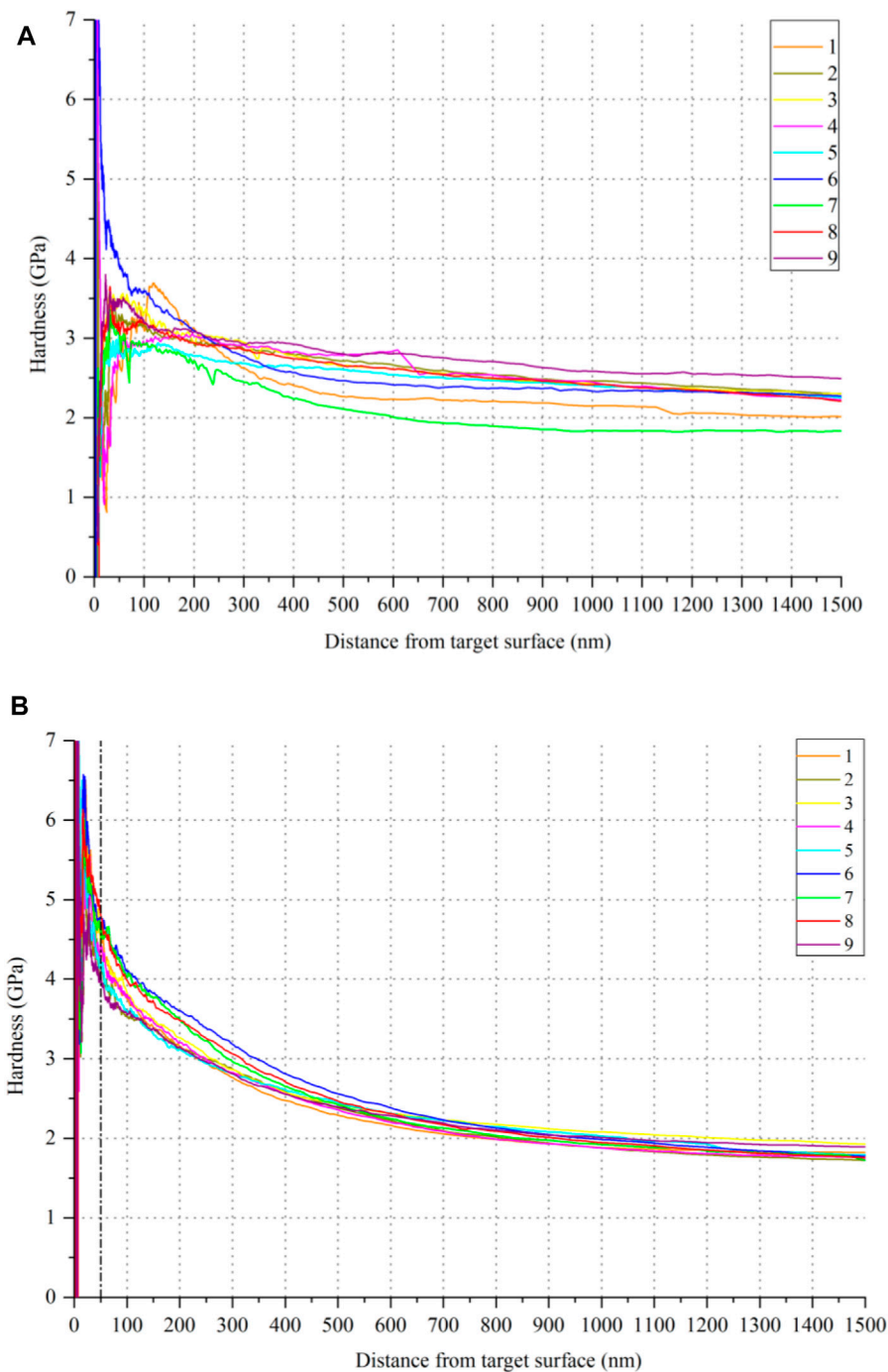
FIGURE 6 | (A) Hardness test results without optimization and **(B)** hardness test results after optimization.

measure the elastic modulus and hardness of the Q235 steel samples. The elastic modulus test results are shown in **Figure 5**. Indentation points 1 and 2 are taken from the Q235 steel sample without the optimization of the lapping and polishing parameters, and the remaining points are taken from the same work piece after the optimization of processing parameters. It can be seen from **Figure 5** that with the increase of depth from the

target surface, the elastic modulus gradually reduces to be stable. To be specific, the decreasing trend of the elastic modulus from points 1 and 2 is lower than other test points, and the overall values of the elastic modulus from points 1 and 2 are larger than other test points. It indicates that although the surface hardening phenomenon of the work piece could not be eliminated by the lapping and polishing processes, this surface hardening

phenomenon could be improved by the optimization of the processing parameters to control the surface integrity (Qi et al., 2018).

In addition, **Figure 6** shows the comparison of the hardness test results before and after the optimization of the lapping and polishing parameters. Nine different points are selected for each sample, and it can be seen from **Figure 6A** that the curves of hardness are relatively scattered without the optimization of the lapping and polishing parameters, which indicates that the differences in the nine curves of hardness are mainly caused by the non-uniform surface integrity. It is noticed from **Figure 6B** that the nine curves of hardness are similar after the optimization of the processing parameters, and the errors between each curve are small which demonstrates that the surface integrity has been significantly improved after the optimization of the lapping and polishing parameters by using the SVM-GA method considered in this study.

CONCLUSION

The nanoindentation test is extensively used to obtain the mechanics performance of different kinds of materials, and to accurately measure these values of mechanics, the sample is required to have good surface integrity in terms of surface roughness and subsurface damage. The abrasive lapping and polishing processes are often used to prepare the sample for nanoindentation with a good surface finish; however, many processing parameters are related to the lapping and polishing processes. It is necessary to optimize these parameters to perform good machining ability with high efficiency and accuracy. In this study, the general process in lapping and polishing of steel samples for nanoindentation has been analyzed, and an in-house developed automatic lapping and polishing machine has been used to conduct the lapping and polishing tests on Q235 steel samples by considering the major processing parameters, including the pressure, rotation speed of the lapping and polishing plate, flow rate of abrasive slurry, and processing time. It is found from the lapping experiments with a full

factorial design that the optimized processing parameters are r_p of 200 r/min, P of 30 N, and t of 4 min considered in this study by considering the MRR and SSD. The CCD method has been used to design the polishing experiments, and the SVM method has been used to deal with these experimental results, and it is found that the developed SVM model can accurately predict R_a under the different processing parameters considered in this study. Then, based on the SVM model, the GA method is used to obtain the optimized processing parameters in the polishing process, and it is found from the SVM-GA study that the optimized processing parameters in the lapping process are r_p of 108 r/min, P of 33 N, Q_a of 20 ml/min, and t of 3 min. Finally, a set of nanoindentation tests have been conducted to evaluate the lapping and polishing performance, and it is found that the surface integrity has been significantly improved after the optimization of the lapping and polishing parameters by using the SVM-GA method considered in this study.

DATA AVAILABILITY STATEMENT

The raw data supporting the conclusion of this article will be made available by the authors, without undue reservation.

AUTHOR CONTRIBUTIONS

Conceptualization, DW; data curation, QW; formal analysis, ZC; investigation, ZC; software, QW; supervision, DW; writing—original draft, ZC; writing—reviewing and editing, DW.

FUNDING

REFERENCES

Chen, Z., Wang, X., Giuliani, F., and Atkinson, A. (2014). Surface Quality Improvement of Porous Thin Films Suitable for Nanoindentation. *Ceramics Int.* 40, 3913–3923. doi:10.1016/j.ceramint.2013.08.035

Chen, Z., Wen, D., Lu, J., Yang, J., Hong, T., and Qi, H. (2021). Surface Quality Improvement by Using a Novel Driving System Design in Single-Side Planetary Abrasive Lapping. *Materials* 14, 1691. doi:10.3390/ma14071691

Cheng, Z., Qin, S., and Fang, Z. (2022). Numerical Modeling and Experimental Study on the Material Removal Process Using Ultrasonic Vibration-Assisted Abrasive Water Jet. *Front. Mater. Accepted Publ.* 9, 895271. doi:10.3389/fmats.2022.895271

Das, A., Altstadt, E., Kaden, C., Kapoor, G., Akhmadaliev, S., and Bergner, F. (2022). Nanoindentation Response of Ion-Irradiated Fe, Fe-Cr Alloys and Ferritic-Martensitic Steel Eurofer 97: The Effect of Ion Energy. *Front. Mater.* 8, 811851. doi:10.3389/fmats.2021.811851

Fayed, H. A., and Atiya, A. F. (2021). Decision Boundary Clustering for Efficient Local SVM. *Appl. Soft Comput.* 110, 107628. doi:10.1016/j.asoc.2021.107628

Ge, J. Q., Ren, Y. L., Xu, X. S., Li, C., Li, Z. A., and Xiang, W. F. (2021b). Numerical and Experimental Study on the Ultrasonic-Assisted Soft Abrasive Flow Polishing Characteristics. *Int. J. Adv. Manuf Technol.* 112, 3215–3233. doi:10.1007/s00170-021-06598-2

Ge, J., Hu, W., Xi, Y., Ren, Y., Xu, X., and Zhang, C. (2021a). Gas-liquid-solid Swirling Flow Polishing and Bubble Collapse Impact Characteristics. *Powder Tech.* 390, 315–329. doi:10.1016/j.powtec.2021.05.087

Hossain, M., Qin, B., Li, B., and Duan, X. (2022). Synthesis, Characterization, Properties and Applications of Two-Dimensional Magnetic Materials. *Nano Today* 42, 101338. doi:10.1016/j.nantod.2021.101338

Hu, W., Teng, Q., Hong, T., Saetang, V., and Qi, H. (2022). Stress Field Modeling of Single-Abrasive Scratching of BK7 Glass for Surface Integrity Evaluation. *Ceramics Int.* 48, 12819–12828. doi:10.1016/j.ceramint.2022.01.153

Imanian, M. E., and Biglari, F. R. (2022). Modeling and Prediction of Surface Roughness and Dimensional Accuracy in SLS 3D Printing of PVA/CB Composite Using the central Composite Design. *J. Manufacturing Process.* 75, 154–169. doi:10.1016/j.jmapro.2021.12.065

Isik, M., Gasanly, N. M., and Rustamov, F. A. (2022). Determination of Mechanical Properties of Bi12TiO20 Crystals by Nanoindentation. *Mater. Sci. Semiconductor Process.* 140, 106389. doi:10.1016/j.mssp.2021.106389

Jeyaranjani, J., and Devaraj, D. (2022). Improved Genetic Algorithm for Optimal Demand Response in Smart Grid. *Sust. Comput. Inform. Syst.* 35, 100710. doi:10.1016/j.suscom.2022.100710

Ji, R., Zhang, L., Zhang, L., Li, Y., Lu, S., and Fu, Y. (2022). Processing Method for Metallic Substrate Using the Liquid Metal Lapping-Polishing Plate. *Front. Mater. Submitted for publication* 9, 896346. doi:10.3389/fmats.2022. 896346

Li, H. N., Yang, Y., Zhao, Y. J., Zhang, Z., Zhu, W., Wang, W., et al. (2019). On the Periodicity of Fixed-Abrasive Planetary Lapping Based on a Generic Model. *J. Manufacturing Process.* 44, 271–287. doi:10.1016/j.jmapro.2019. 05.036

Liang, Y., Hu, S., Guo, W., and Tang, H. (2022). Abrasive Tool Wear Prediction Based on an Improved Hybrid Difference Grey Wolf Algorithm for Optimizing SVM. *Measurement* 187, 110247. doi:10.1016/ j.measurement.2021.110247

Nayak, B., and Ramesh Babu, N. (2020). Influence of Tool and Workpiece Interface Temperature Rise on the Life of Ice Bonded Abrasive Polishing Tool. *Wear* 462-463, 203511. doi:10.1016/j.wear.2020.203511

Qi, H., Cheng, Z., Cai, D., Yin, L., Wang, Z., and Wen, D. (2018). Experimental Study on the Improvement of Surface Integrity of Tungsten Steel Using Acoustic Levitation Polishing. *J. Mater. Process. Tech.* 259, 361–367. doi:10. 1016/j.jmatprotec.2018.04.043

Qi, H., Shi, L., Teng, Q., Hong, T., Tangwarodomnukun, V., Liu, G., et al. (2022). Subsurface Damage Evaluation in the Single Abrasive Scratching of BK7 Glass by Considering Coupling Effect of Strain Rate and Temperature. *Ceramics Int.* 48, 8661–8670. doi:10.1016/j.ceramint.2021.12.077

Reggente, M., Angeloni, L., Passeri, D., Chevallier, P., Turgeon, S., Mantovani, D., et al. (2020). Mechanical Characterization of Methanol Plasma Treated Fluorocarbon Ultrathin Films through Atomic Force Microscopy. *Front. Mater.* 6, 338. doi:10.3389/fmats.2019.00338

Song, Y., Pan, Z., Li, Y., Jin, W., Gao, Z., Wu, Z., et al. (2022). Nanoindentation Characterization on the Temperature-dependent Fracture Mechanism of

Chinese 316H Austenitic Stainless Steel under Creep-Fatigue Interaction. *Mater. Characterization* 186, 111806. doi:10.1016/j.matchar.2022.111806

Strey, N. F., and Scandian, C. (2021). Abrasive Polishing Load Effect on Surface Roughness and Material Removal Rate of Al2O3, ZTA and SiC. *Wear* 477, 203787. doi:10.1016/j.wear.2021.203787

Wen, D., Qi, H., Ma, L., Lu, C., and Li, G. (2016). Kinematics and Trajectory Analysis of the Fixed Abrasive Lapping Process in Machining of Interdigitated Micro-channels on Bipolar Plates. *Precision Eng.* 44, 192–202. doi:10.1016/j. precisioneng.2015.12.005

Xie, Y., Gui, F. X., Wang, W. J., and Chien, C. F. (2021). A Two-Stage Multi-Population Genetic Algorithm with Heuristics for Workflow Scheduling in Heterogeneous Distributed Computing Environments. *IEEE Trans. Cloud Comput.*, Accepted for publication. doi:10.1109/TCC.2021.3137881

Zhang, L., Zheng, B., Xie, Y., Ji, R., Li, Y., and Mao, W. (2022). Control Mechanism of Particle Flow in the Weak Liquid Metal Flow Field on Non-uniform Curvature Surface Based on Lippmann Model. *Front. Mater. Accepted Publ* 9, 895263. doi:10.3389/fmats.2022.895263

Roughness Prediction and Performance Analysis of Data-Driven Superalloy Belt Grinding

Youdong Zhang, Guijian Xiao*, Hui Gao, Bao Zhu, Yun Huang and Wei Li

College of Mechanical and Vehicle Engineering, Chongqing University, Chongqing, China

Abrasive belt grinding has unique advantages in avoiding machining defects and improving surface integrity while grinding hard materials such as superalloys. However, the random distribution of abrasive particles on the abrasive belt surface is uncontrollable, and chatter and machining errors accompany the machining process, leading to unclear mapping relationship between process parameters and surface roughness, which brings great challenges to the prediction of surface roughness of superalloy. Traditional empirical equations are highly dependent on empirical knowledge and the development of scientific theories and can only solve problems with relatively simple and clear mechanisms, but cannot effectively solve complex and mutually coupled problems. The method based on data-driven patterns has a better idea for mining the implicit mapping relationship and eliminating the uncertainty of complex problems. This study presents a data-driven roughness prediction method for GH4169 superalloy. First, a superalloy grinding platform is built. According to the grinding empirical equation, the mapping relationship between process parameters and surface roughness is analyzed, and a prediction model is established based on the error back propagation (BP) algorithm. Second, genetic algorithm (GA) and particle swarm optimization (PSO) algorithm are used to optimize the weights and thresholds of the neural network, and the global optimal solution is obtained. Finally, the prediction performance of different algorithms is compared. The results show that the non-uniform absolute errors of the BP algorithm, GA-BP algorithm, and PSO-BP algorithm are 0.12, 0.085, and 0.078, respectively. The results show that the roughness prediction algorithm based on PSO-BP is more suitable for GH4169 superalloy.

Keywords: belt grinding, GH4169 superalloy, roughness prediction, data driven, intelligent algorithm

INTRODUCTION

High-temperature alloys have been widely used in the aerospace field due to their high strength and good oxidation resistance. At present, the high-temperature alloy materials are mainly processed by die forging and precision milling, while this processing method inevitably has defects such as thermal stress concentration and large plastic deformation, which also leads to tool adhesion and chatter. In turn, it is easy for the large force to cause some surface defects such as burns, micro-cracks, and tensile stress on the surface of the workpiece, which makes it difficult to ensure the surface integrity of the parts (Zhu et al., 2020). Abrasive belt grinding can effectively improve the surface quality of superalloy materials with the advantages of low

temperature and strong vibration absorption performance, so it has been widely applied in aeronautic and astronautic fields (Huang et al., 2016; Xiao et al., 2021; Xiao et al., 2022; Zhou et al., 2022).

Since the surface integrity of components has an important impact on their fatigue life, it can improve the surface integrity and performance of the workpiece (Li et al., 2022; Gao et al., 2021). The surface topography after grinding has an important influence on the service performance (Cui et al., 2021). Among them, the surface roughness has an important influence on the surface properties of the workpiece after processing (Zhang et al., 2020). Obtaining surface roughness is the main unfavorable factor affecting the fatigue life of the workpiece. By analyzing the surface roughness, topography characteristics, and residual stress distribution of the workpiece, the influence of surface integrity characteristics on fatigue life is studied. At the same time, a method to improve fatigue life by optimizing process parameters is proposed (Wang et al., 2020). Considering the stress concentration on the surface of the external load and the residual stress of shot peening, the position of the dangerous section after processing was calculated, and experimental verification is also conducted. In the above research, it is found that better surface quality can improve the service life of the workpiece. The prediction of the surface integrity characteristics can ensure that the workpiece can be replaced in time, minimize the loss of resources, and achieve sustainability development.

However, due to the uneven distribution of abrasives, there is inherently weak rigidity, as well as the high degree of nonlinearity and coupling in the grinding process parameters and surface roughness, resulting in unstable surface characteristics after grinding. At present, there are two kinds of main predictions for the roughness of the ground surface.

The traditional surface roughness prediction method is to use online monitoring and surface inspection after grinding to analyze the grinding mechanism and then build a physical model of the surface roughness after grinding. A force-based temperature modeling method is proposed to predict the surface integrity of nickel-based alloy broaching (Klocke et al., 2014). Theoretical and experimental research studies are carried out on the polishing mechanism of complex curved parts, and the roughness prediction model is obtained (Slatineanu et al., 2010; Huang et al., 2020; Huang et al., 2018). A preliminary analysis of the weak stiffness characteristics of the system is carried out, and the vibration mechanism of the system is revealed from the perspective of dynamic analysis. On the basis of the theoretical model, the stable conditions and factors affecting the processing stability are put forward by analyzing the influence of important factors. According to the adjustment of the grinding parameters, the optimization of the surface roughness is realized. Using numerical simulation and advanced measurement methods to study the surface characteristics and formation process of the method of

micro-stiffener belt polishing (MSBP) titanium alloys has become a new method (Xiao and Huang, 2019). In addition, different surface characteristics can be obtained by adjusting the feed velocity and pressure. The surface contour line is obtained through the contour map, and the surface roughness distribution is obtained according to the contour line. The experimental results show that the surface characteristics, surface morphology, surface roughness, and residual stress all meet the given requirements. However, this method still has some limitations. The prediction accuracy, the generalization ability, and the transferability of the method are relatively low, so it is difficult to adapt to the complex grinding conditions.

With the development of artificial intelligence, many domestic and foreign researchers have applied the intelligent algorithms to the processing predictions. These intelligent algorithms have incomparable advantages in dealing with nonlinear, fuzzy, and unclear pattern features and high coupling problems. At the same time, these algorithms can also achieve accurate prediction of processing results. The input features of the algorithm are very important for predicting the results, and the selection of features can currently rely on sensor and machine data to build a multi-feature hybrid input model. Input features are selected by analyzing the correlation between input features and surface roughness, as well as hardware and time costs (Guo et al., 2021). A sequential deep learning framework long and short-term memory (LSTM) network was used to predict surface roughness. The convergence of the GA is relatively high, and the self-adaptive characteristics of the GA can be used to predict the surface roughness after processing (Cao et al., 2020). Experiments proved that this method could effectively improve grinding efficiency and obtain better surface roughness. By taking the grinding wheel velocity, workpiece velocity, cutting depth, and grinding wheel material as the research objects, production cost, production rate, and surface roughness are taken as the optimization goals. In the actual machining process, the influence of tool wear on the surface roughness is very important, and it has become the main trend to properly consider the real-time state of the tool in the algorithm (Xu et al., 2020). With the breakthrough of deep learning theory, the prediction method of grinding roughness based on the deep learning algorithm can effectively improve the prediction accuracy (Alavijeh and Amirabadi, 2019). In recent years, error back propagation (BP) has been used to predict tool life, and the radial basis function (RBF) network model are excellent in approximation ability, learning rate, and so on (Ding et al., 2010). At present, surface roughness prediction based on BP neural network algorithm is the key direction (Wu, 2007). Many experts at home and abroad have adopted the RBF network model to solve complex engineering problems. At the same time, other evolutionary algorithms are used to optimize the original model, and the model parameter values are dynamically optimized to improve the performance of the model (Gu et al., 2021; Zhang et al., 2012). The sensor is
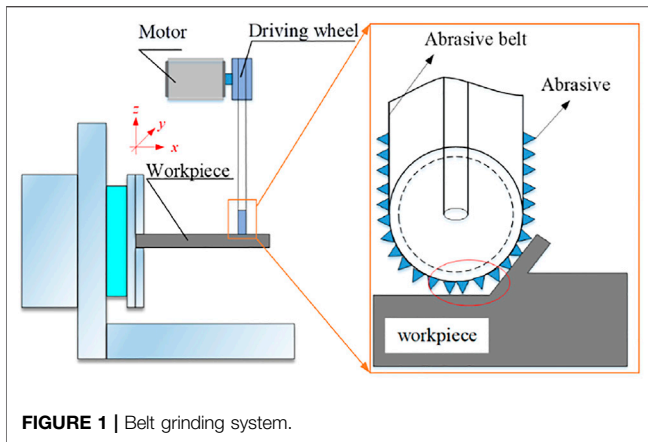
FIGURE 1 | Belt grinding system.

FIGURE 2 | Propagation process diagram of the neural network.

used to monitor the processing process in real time, process and analyze the detection signal, and propose the signal characteristics. The constructed roughness prediction model can further expand the application prospect (Pandiyan et al., 2018). Chang et al. used the experimental data as the training parameters of the SVM model by using bearings as materials for belt grinding experiments (Chang et al., 2019). This model could effectively shorten the grinding process optimization time and obtain the global optimal solution of the grinding surface integrity. However, the adjustment range of the radial basis center and other parameters was small during the correction process, and it was easy to fall into the local optimal solution, which restricted the generalization ability of RBF. The research shows that the improved particle swarm algorithm and the GA with excellent search performance are used to optimize the RBF parameters, search the optimal parameters in a wider range, and improve the prediction performance of the model (Golbabai and Mohebianfar, 2017).

GRINDING SYSTEM MODEL OF SUPERALLOY MATERIAL BELT

Belt Grinding System

The abrasive belt is a particular form of a coated belt, which is intensified by a tensioning mechanism and a driven wheel to make it move at a high velocity. It can achieve grinding by the workpiece's shape, processing requirements, the shape of the workpiece, and processing requirements. Besides, belt grinding is widely known as precision machining because of its high material removal precision (the highest accuracy can reach 0.1 μm), flexible machining, and other characteristics. It has significant advantages for the precision machining of some typical difficult-to-machine materials.

Figure 1 is the material removal model of belt grinding. The abrasive belt attached to the driving wheel moves with the rotation of the wheel. Abrasive particles perform micro-cutting and removal of material on the surface of the workpiece material. The results show that the grinding
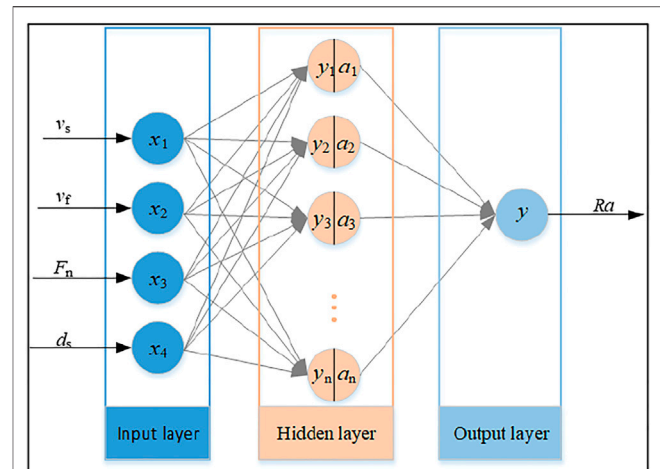
parameters such as belt linear velocity, feed velocity, grinding pressure, and grinding depth have great influence on the surface integrity of the workpiece.

Effect of Process Parameters on Roughness

The scholars in the previous research study have constructed the mathematical model of process parameters and surface roughness, as shown in **Eq. 1**:

$$\mathrm{Ra} = P_1 v_s^{(\mathrm{m})} v_f^{(\mathrm{n})} F_n^{(\mathrm{p})} d_s^{(\mathrm{q})} \tag{1}$$

where Ra is the surface roughness, v_s is the linear belt velocity, v_f is the feed velocity, F_n is the grinding pressure, d_s is the grinding depth, P_1 is the constant, and m, n, p, and q are relevant indexes. According to empirical **Eq. 1**, Ra is related to v_s, v_f, F_n, and d_s, and the four parameters are highly nonlinear and highly coupled.

BP ALGORITHM AND OPTIMIZATION METHOD

BP Neural Network Algorithm

Due to the characteristics of abrasive grains and the influence of processing, there are significant problems in constructing the mathematical model between process parameters and Ra. The prediction accuracy has always restricted the development of roughness prediction. However, the traditional back propagation (BP) algorithm causes some iterations to fall into the optimal local solution due to the influence of the characteristics of the algorithm. The PSO algorithm and GA are introduced to optimize the BP algorithm's initial weight and threshold to avoid the optimal local solution and obtain the optimal global solution. Simultaneously, the predicted results error after grinding is controlled within 5.00% to make the predicted
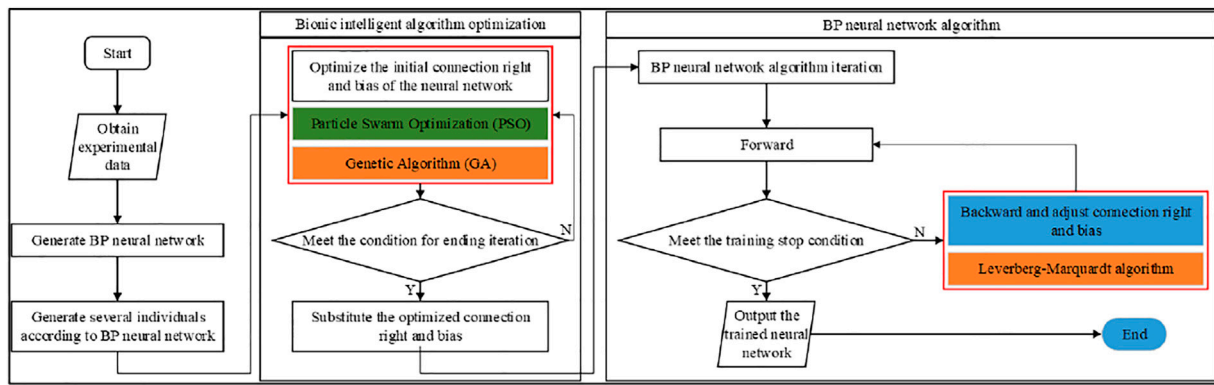
FIGURE 3 | Flow chart of BP neural network optimization algorithm.

value as accurate as possible. According to previous studies, linear belt velocity, feed velocity, grinding pressure, and grinding depth are the main factors that affect the surface roughness of the workpiece. The prediction model will give the surface roughness values obtained under the same grinding environment and grinding time for these four parameters. The grinding process parameters v_s, v_f, F_n, and d_s are taken as the input of the neural network, and the surface roughness was taken as the output.

Figure 2 shows the topology of the neural network. According to the principle of the neural network algorithm, the number of neurons in the hidden layer p is determined by the following empirical function:

$$p = |\sqrt{n}| + a \tag{2}$$

$$y = f(wx + b) \tag{3}$$

where p is the number of neurons in the hidden layer, n represents the number of input layers, and a represents a random value. For the convenience of calculation, the value is 10. According to the empirical **Eq. 2**, we choose 12 neurons in the hidden layer. x is the input vector, y is the output vector, w is the connection weight vector, b is the bias of the neural network, and $f(x)$ is the activation function. $f_1(x) = \tanh x$ and $f_2(x) = x$ are taken as activation functions of the hidden layer and the output layer, respectively.

Propagation of Neural Networks

For a given training set D = {(x_k, y_k): $x_k = [x_{k1}, x_{k2}, \cdots, x_{kn}]^T$, $y = [y_{k1}, y_{k2}, \cdots, y_{km}]^T$, $k = 1, 2, \cdots, N$}, and for a training sample (x_j, y_j)∈D. Neural network forward propagation method. Input layer: $x_j = [x_{j1}, x_{j2}, \cdots, x_{jn}]^T$. Hidden layer: input vector x as the input vector. The neuron in the kth hidden layer has the connection weight $w_{1k} = [w_{1k1}, w_{1k2}, \cdots, w_{1kp}]$ and the offset b_{2k}. The output h_k is given by **Eq. 4**:

$$h_{jk} = f_1(w_{1k}x_j + b_{1k}) \tag{4}$$

Use the output value of all neurons $h_j = [h_{j1}, h_{j2}, \cdots, h_{jp}]^T$ as the output vector of the entire network. The first k of output layer

neurons has the right to connect $w_{2k} = [w_{2k1}, w_{2k2}, \cdots, w_{2kp}]$ and offset b_{2k}, output $\hat{y}_k$ given by (5):

$$\hat{y} = f_2(w_{2k}h_j + b_{2k}) \tag{5}$$

For a training case, the prediction accuracy of the training cases is evaluated as an index of **Eq. 6**:

$$E_j = \frac{1}{2}\sum_{k=1}^{m}(y_{jk} - \hat{y}_{jk})^2 \tag{6}$$

E_j represents the loss function, $\hat{y}$ represents the predicted value, and y represents the actual value.

For the whole training example, the prediction accuracy is measured by the mean square error (MSE):

$$MSE = \frac{1}{N}\sum_{k=1}^{N}E_k \tag{7}$$

GA and PSO Optimization Methods

Before the neural network algorithm is trained, all the connection weights and thresholds are usually generated randomly by using the normal distribution. This makes the training effect of a simple BP neural network unstable. In order to improve the training effect of the algorithm, GA and PSO can be used to optimize the initial weight and threshold value of the neural network algorithm to the neural network, so that the iterative process is at a better starting point and many local optimal solutions can be avoided before the training iteration (**Figure 3**). The neural network iteration converges to a better local optimal solution or optimal global solution. Therefore, surface roughness can achieve higher accuracy and prediction accuracy based on the current data.

PSO algorithm is applied to construct a new vector because of BP algorithm connection weights and thresholds:

$$U = (\mu_1, \mu_2, \cdots, \mu_d)^T \tag{8}$$

where μ_i represents the moving speed of each particle, and U represents the set of moving speeds of all particles. According to
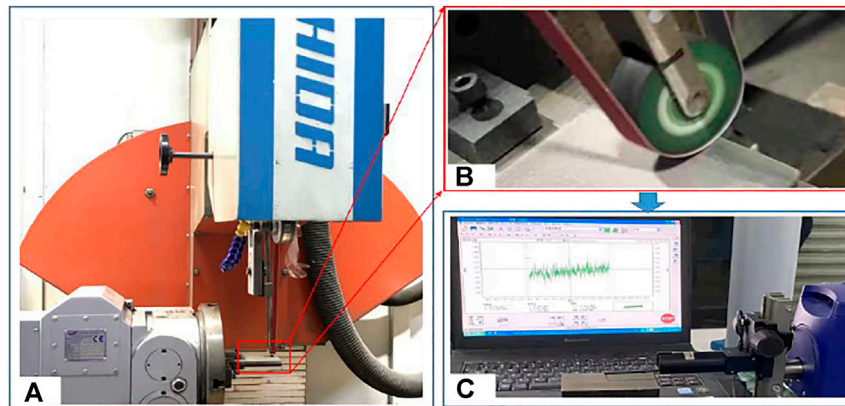
FIGURE 4 | Experimental equipment and testing equipment. **(A)** Seven-axis six-linkage CNC belt grinding machine. **(B)** Abrasive belt grinding process. **(C)** Roughness detection of superalloy.

the principle of the algorithm, the computer randomly generates the initial position and speed according to the normal distribution. In particle motion, it is assumed that the ith particle's proven optimal solution is p_i, and all particles' proven global optimal solution is G.

During the iteration of the algorithm, the velocity change of the ith particle is closely related to the particle's current position. Using the optimization method of the PSO algorithm, the optimal global solution of particles is obtained as follows:

$$U_i^{'} = wU_i + c_1\alpha_1 (P_i - U_i) + c_2\alpha_2 (G - U_i) \quad (9)$$

where w is the weight of the particle, c_1 is the individual learning factor, c_2 is the group learning factor, and a_1 *and* a_2 are random numbers. After the particle velocity vector is iteratively updated, the particle moves immediately. The new position of the particle is shown in **Eq. 10**:

$$X_i^{'} = X_i + U_i^{'} \quad (10)$$

After several iterations, all particles tend to move toward the optimal global solution. Simultaneously, the GA can be used for the optimization of complex systems and has better robustness. Compared with the traditional optimization method, it can directly take fitness as the search information, uses the search information of multiple points, and has implicit parallelism characteristics.

The GA optimizes the initial weights and thresholds. Using the characteristics of GA to optimize the initial parameters of BP algorithm can avoid the problem of local optimum caused by random parameters.

It comprises five parts: the input layers and the hidden layers, weight, threshold, and output layer. The difference between the predicted value and the expected value of the sample is selected as the error value, the obtained error value is formed into an error matrix, and the norm of the matrix is used as the objective function. The fitness function adopts the sorting of the appropriate allocation function. The selection operator simulates the "survival of the fittest," selects highly adaptable

individuals, increases relevant weights, and inherits these individuals to the next generation.

The basic steps of the GA algorithm are as follows:

1) In this study, the fitness function uses training data to train the BP neural network, and the prediction error of training data is regarded as the individual fitness value.
2) The selection operation uses roulette to select individuals with good fitness from the population to form a new population.
3) In crossover operation, two individuals are selected from the population and a new individual is obtained by crossing at a certain intersection.
4) Mutation operation selects an individual randomly from the population and obtains a new individual according to a certain probability of mutation.

On the contrary, particles with poor adaptability will be given a smaller weight and will not be inherited by the next generation during the training process. In this study, the roulette selection method is chosen. ΣF_i represents the sum of the population's fitness function, and f_i represents the fitness value of the ith chromosome of the people. The ratio of fitness to offspring is $f_i/\Sigma F_i$.

EXPERIMENTAL AND RESULT ANALYSIS

Experimental and Simulation

Figure 4 is the test equipment and surface roughness detection diagram. A seven-axis six-link abrasive belt grinder is used to grind the workpiece, and a roughness profiler is used to detect the workpiece. The grinding surface under different process parameters was detected by using a testing instrument, and the surface roughness of the workpiece was obtained, which is used as training data of the algorithm. The experimental material is a GH4169 superalloy sheet, and its size is $170 \times 100 \times 2$ mm. v_s, F_n, v_f, and d_s are selected as experimental variables and also as the input of the algorithm simulation. The experimental data obtained in the experiment is used as the input parameter of the algorithm. The
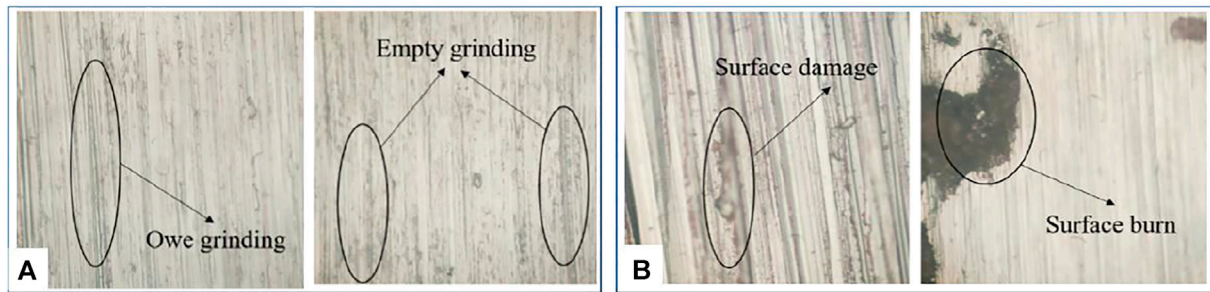
FIGURE 5 | Experimental equipment and testing equipment. **(A)** Machined surface with small grinding parameters. **(B)** Machined surface with grinding parameters.
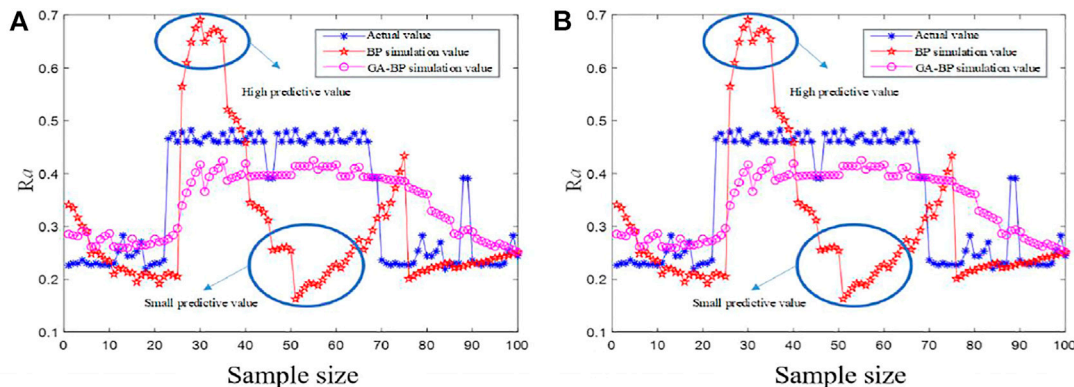

FIGURE 6 | Comparison of actual roughness and roughness predicted by different algorithms. **(A)** BP and GA-BP prediction results analysis. **(B)** BP and PSO-BP prediction results analysis.

600 sets of experimental data obtained are used as the data for the algorithm, 500 sets are used as the algorithm training data, and 100 sets are used as the data for the algorithm test.

In order to select the corresponding parameter range, exploratory experiments were carried out in the early stage of the experiment, and the corresponding smaller grinding parameters and larger grinding parameters were selected for the experiment. When the grinding parameters are too small, there are empty grinding and owe grinding on the grinding surface, as shown in **Figure 5A**. When the grinding parameters are too large, there are surface defects and surface burns on the machined surface, as shown in **Figure 5B**. In order to ensure the integrity of the processing surface and improve the accuracy of the algorithm application, the parameters of the experiment are specified. The linear belt velocity is 12–26 m/s, the feed velocity is distributed in the range of 0.01–0.05 m/min, the grinding pressure is distributed in the range of 10–30 N, and the grinding depth is distributed in the range of 0.2–1 mm.

Experimental Results and Analysis

The predicted surface roughness under different models is obtained by MATLAB simulation. The predicted value calculated by the algorithm is compared with the parameter value used in the experiment, and the error of the experiment is analyzed, as shown in **Figure 6**.

Comparing the prediction results of surface roughness by the BP algorithm, PSO-BP algorithm, and GA-BP algorithm, the results show that the predicted value of the BP algorithm is quite different from the actual value. The error value of the prediction effect is large, the precision is relatively low, and the local prediction value is different. The expected values of the GA-BP and PSO-BP algorithms are in good agreement with the actual values (**Figure 6**). The mean absolute error (MAE) is introduced to evaluate the algorithm's stability, and the mean error value of different algorithms is tested according to the absolute error theory (Manuela et al., 2021). The MAEs of the BP, GA-BP, and PSO-BP algorithms are 0.120, 0.085, and 0.079, respectively. It can be known from the above analysis that the MAE value of the PSO-BP algorithm is relatively small, and the algorithm has better prediction results and higher accuracy. By comparing the effects of different algorithms, the expected value and actual value of the expected result of the PSO-BP algorithm have a minor error and a great fit.

GA and PSO are both bionic intelligent algorithms and have good effects on local optimal solutions. The principle of the bionic algorithm is to search for high-performance parts in the solution space and assign better values to greater weights. The
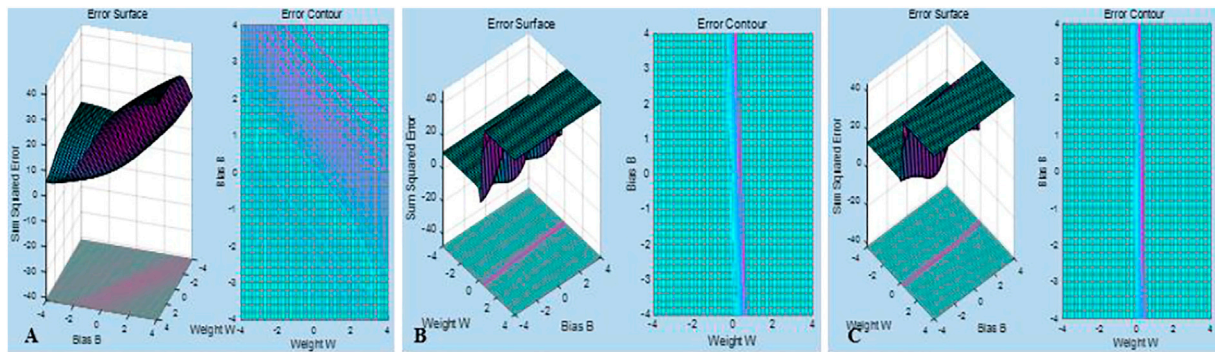
FIGURE 7 | Error surface diagram of different optimization methods' error. **(A)** Standard BP neural network error surface. **(B)** GA-BP neural network error surface. **(C)** PSO-BP neural network error surface.

optimization algorithm can effectively avoid local optimization, so the prediction effect is better than the BP algorithm. It can be known that all the particles generated in the PSO algorithm have better memory and can well inherit the training results. But the memory in the GA algorithm is not so good, because the related memory will be destroyed during the training process, and the genetic performance is relatively poor. Therefore, the theoretical prediction result of PSO-BP is better than that of GA-BP.

The error values of the BP algorithm, the GA-BP algorithm, and the PSO-BP algorithm are drawn into an error curve (**Figure 7**). The error generated by the BP algorithm is relatively large. Compared with the BP algorithm, the GA-BP and PSO-BP algorithms have smaller errors, which also proves that the bionic algorithm has optimized the BP algorithm to a certain extent. Error autocorrelation function and partial correlation function are introduced to measure the quality of the algorithm.

Figure 8A is the error autocorrelation graph and partial correlation graph predicted by the BP algorithm. In the autocorrelation graph, it can be known that the correlation coefficient value is located on the zero axes for a long time to have a monotonic trend and a normal distribution. It does not have a periodic change trend. It is a non-stationary sequence, indicating that the possibility of autocorrelation is very high. So in the prediction process, the error generated is random and uncontrollable. Simultaneously, the partial correlation graph of samples can know the tailing structure, and some error values exceed the confidence interval. The standard BP neural network algorithm is not so useful for the prediction of the multivariate input model.

Figure 8B is the error autocorrelation graph and partial correlation graph obtained by the GA-BP algorithm. It can be seen that the error autocorrelation graph of the optimized algorithm presents apparent sinusoidal fluctuations, and the autocorrelation coefficient is evenly distributed between positive and negative values. There is individual volatility, indicating that the error fluctuates around a specific value. It can be known that the error value is within a certain range and is controllable. Simultaneously, commemorating the partial correlation diagram of samples can know the tailing structure. All the values do not

exceed the confidence interval, indicating that the roughness prediction algorithm has a better prediction effect.

Figure 8C is the error autocorrelation and partial correlation diagram of the PSO-BP algorithm. It can be seen that the algorithm has apparent sinusoidal fluctuations. The autocorrelation value is relatively small (less than the value produced by GA-BP), and there is large volatility, indicating that the error is around a certain one. The value fluctuates, showing that the predicted error value fluctuates within a specific range. The amplitude of the fluctuation is relatively small. Simultaneously, we can know the tailing structure by observing the partial correlation diagram of the samples. All the values do not exceed the confidence interval, indicating that the PSO-BP prediction algorithm's prediction effect is better than the GA-BP prediction algorithm's.

The algorithm iteration process of the BP algorithm, GA-BP algorithm, and PSO-BP algorithm is shown (**Figure 9**). The green, red, and blue lines represent the iterative process graphs for the validation set, test set, and training set, respectively. The BP algorithm meets the requirements of the 32nd generation iteration and is within the error requirements, but after the iteration, the error between the three lines is still relatively large, and the convergence performance is poor. It can be explained that there is an overfitting phenomenon, and the prediction model is not stable. The training results of the GA-BP neural network algorithm meet the requirements of the 13th generation. In the subsequent 6 iterations, the gap is small and the prediction model is very stable, effectively avoiding the phenomenon of overfitting. The predictions work well. Iterative flowchart of the PSO-BP algorithm. The training value can meet the requirements before and after the 31st generation, and the experimental data can also achieve sufficient training, and the error value is relatively small in the subsequent 6 iterations. The mean square error is introduced to measure the stability of different algorithms. After calculation, the MSE values of BP, GA-BP, and PSO-BP algorithms are 0.0213, 0.099, and 0.098, respectively. Therefore, the dataset in the PSO-BP algorithm can be fully trained to avoid overfitting imagination and have better prediction results.
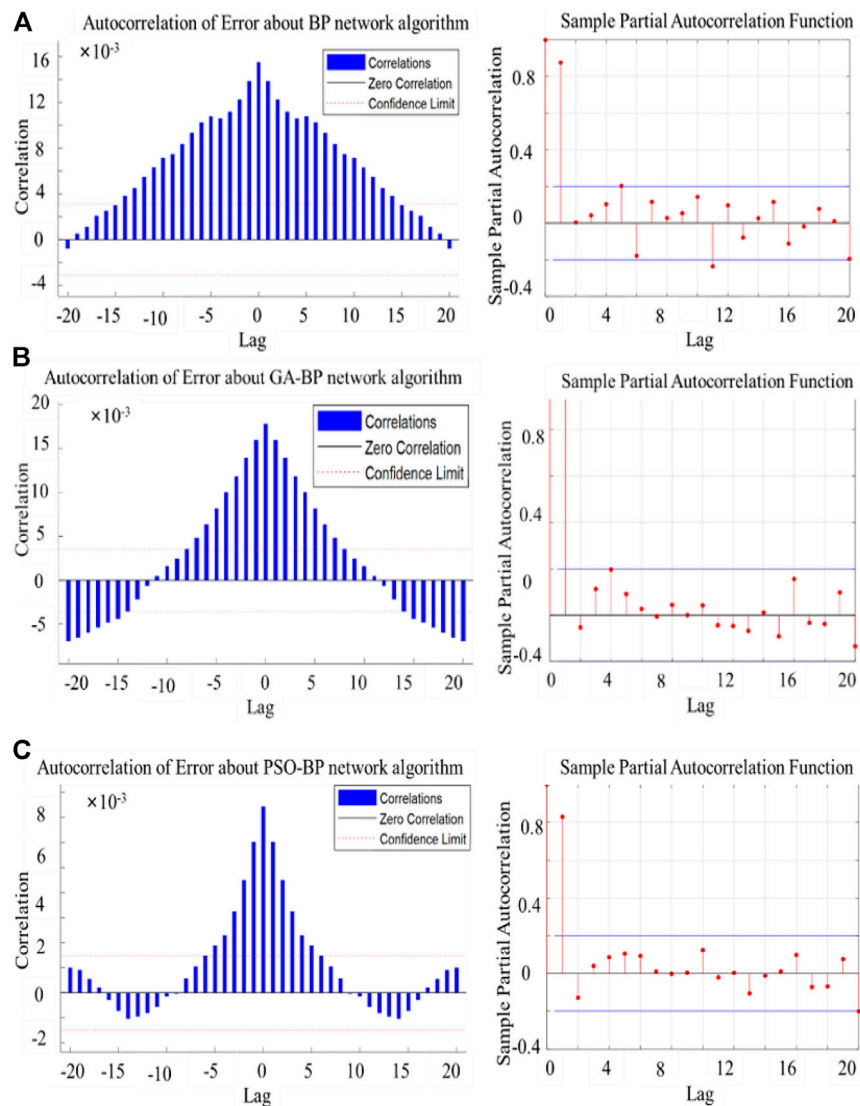
FIGURE 8 | Autocorrelation and partial correlation of prediction errors of different algorithms. **(A)** Autocorrelation and partial correlation of standard BP neural network. **(B)** Autocorrelation and partial correlation of GA-BP neural network. **(C)** Autocorrelation and partial correlation of PSO-BP neural network.
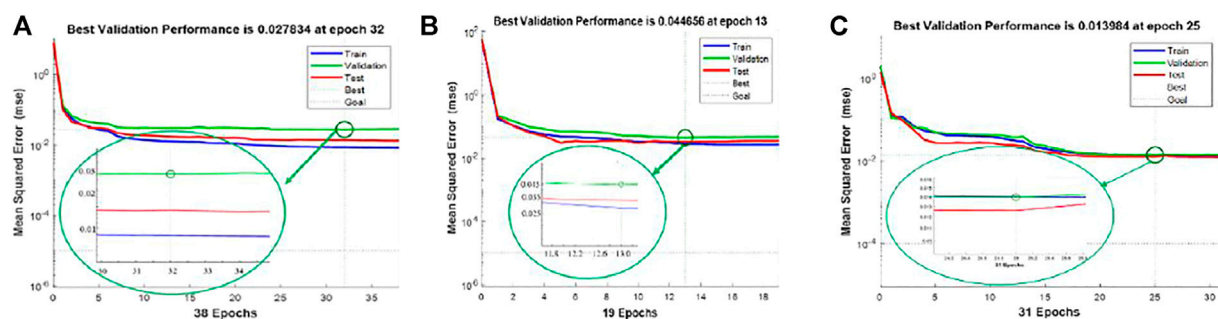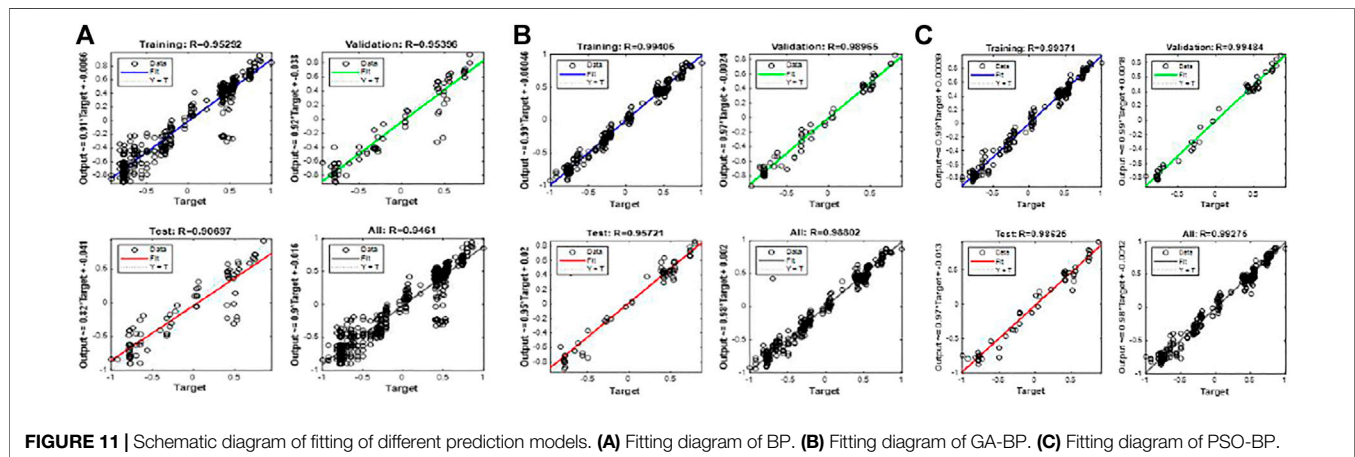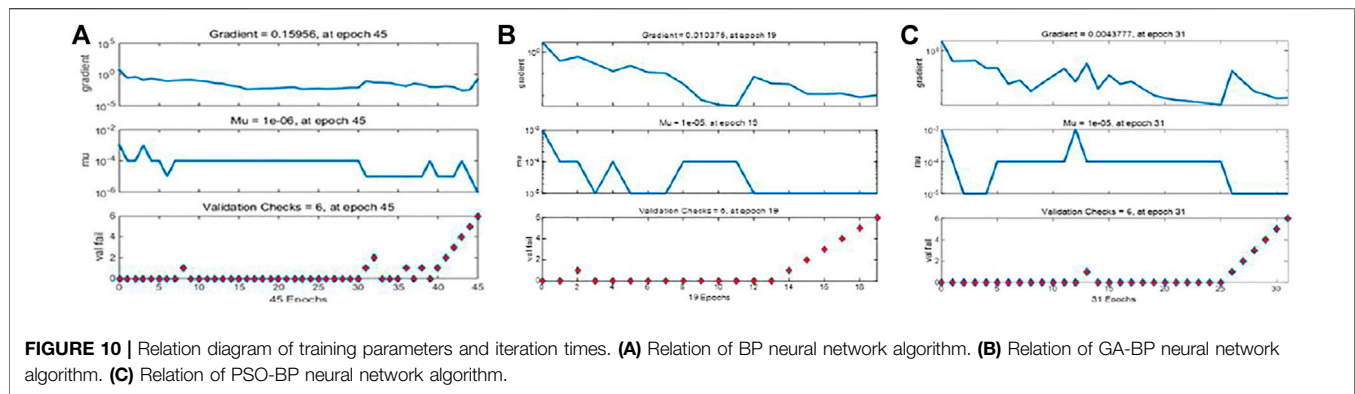

FIGURE 9 | Training results of different algorithms. **(A)** Training result of the BP neural network algorithm. **(B)** Training result of the GA-BP neural network algorithm. **(C)** Training result of the PSO-BP neural network algorithm.

FIGURE 10 | Relation diagram of training parameters and iteration times. **(A)** Relation of BP neural network algorithm. **(B)** Relation of GA-BP neural network algorithm. **(C)** Relation of PSO-BP neural network algorithm.

FIGURE 11 | Schematic diagram of fitting of different prediction models. **(A)** Fitting diagram of BP. **(B)** Fitting diagram of GA-BP. **(C)** Fitting diagram of PSO-BP.

To further evaluate the algorithm, the relationship between the training parameters and the number of iterations is plotted (**Figure 10**). It can be observed that the BP algorithm reaches a minimum value at the 26th iteration and does not change for 6 consecutive iterations. The GA-BP algorithm shows that the optimal solution can be reached when the number of iterations is 13, but a local optimal solution will appear during the training process. The PSO-BP algorithm shows that the optimal solution is obtained after 31 iterations, and there are also some optimal solutions.

A simple regression analysis was used to evaluate the network training. The closer the R value was to 1 in the regression analysis, the better the effect of the algorithm. The regression analysis of the BP algorithm, the GA-BP algorithm, and the PSO-BP algorithm was carried out (**Figure 11**). During the training process of the standard BP neural network, the overall fitting value R was 0.946, the overall fitting degree of the GA-BP algorithm was 0.990, and the GA- The overall fitting degree of the BP algorithm is 0.994, and the results show that the PSO-BP algorithm has a good fitting effect.

CONCLUSION

In this study, a data-driven surface roughness prediction model is proposed. The mapping relationship between

processing parameters and surface roughness is established, which avoids the shortcomings of traditional models such as large interference and weak generalization ability and has a broader application prospect. The main conclusions of the article are as follows:

First, based on the BP algorithm model, GA and PSO algorithms are used to optimize the weights and thresholds of the network topology. A surface roughness prediction model for the belt grinding of the GH4169 superalloy is constructed.

Second, the simulation and comparison of BP, GA-BP, and PSO-BP algorithms are conducted by using experimental data as input. The expected values of the different algorithms are compared, which are 0.120, 0.085, and 0.079, respectively. The analysis shows that the prediction accuracy of the PSO-BP algorithm is higher, and it is more suitable for surface roughness prediction in belt grinding of GH4169 superalloy.

Finally, the pros and cons of the proposed algorithm are further analyzed, the error surface graphs of different algorithms are established, and the prediction errors are analyzed. The training process of the algorithm before and after optimization is also analyzed, and the PSO-BP algorithm can fully train the experimental parameters. In addition, the fitting degree of different algorithms is also analyzed in-depth, and the fitting degree of the PSO-BP algorithm can reach 0.993. It

shows that the proposed algorithm is more applicable to the grinding of GH4169 superalloy.

However, the exploration of the algorithm principle in this study is relatively simple, and the improvement of the accuracy of the algorithm needs to be further improved. The amount of data in this study is still relatively small, and the training of the model needs to be further improved. For future research, a predictive model for multi-information fusion of multi-sensor inputs can be constructed.

DATA AVAILABILITY STATEMENT

The original contributions presented in the study are included in the article/Supplementary Material; further inquiries can be directed to the corresponding author.

REFERENCES

Alavijeh, M. S., and Amirabadi, H. (2019). Investigation and Optimization of the Internal Cylindrical Surface Lapping Process of 440c Steel. *J. Mech. Sci. Technol.* 33 (8), 3933–3941. doi:10.1007/s12206-019-0738-7

Cao, H., Zhou, J., Jiang, P., Hon, K. K. B., Yi, H., and Dong, C. (2020). An Integrated Processing Energy Modeling and Optimization of Automated Robotic Polishing System. *Robotics and Computer-Integrated Manufacturing* 65, 101973. doi:10.1016/j.rcim.2020.101973

Chang, Z., Jia, Q., Xing, Y., and Chen, Y-L. (2019). Optimization of Grinding Efficiency Considering Surface Integrity of Bearing Raceway. *SN Appl. Sci.* 1 (9-12), 4243–4252. doi:10.1007/s42452-019-0697-8

Cui, B., Sun, F., Ding, Q., Wang, H., Lin, Y., Shen, Y., et al. (2021). Preparation and Characterization of Sodium Aluminum Silicate-Polymer Composites and Effects of Surface Roughness and Scratch Directions on Their Flexural Strengths. *Front. Mater.* 8, 655156. doi:10.3389/fmats.2021.655156

Ding, Y., He, W-P., Zhang, W., Wang, W., Li, Y-J., and Dong, R. (2010). Tool Life Prediction Model Based on BP Neural Network. *Aeronaut. Manuf. Technol.* 6 (8), 93–96. doi:10.3969/j.issn.1671-833X.2010.08.019

Galati, M., Rizza, G., Defanti, S., and Denti, L. (2021). Surface Roughness Prediction Model for Electron Beam Melting (EBM) Processing Ti6Al4V. *Precision Eng.* 69 (2), 19–28. doi:10.1016/j.precisioneng.2021.01.002

Golbabai, A., and Mohebianfar, E. (2017). A New Method for Evaluating Options Based on Multiquadric RBF-FD Method. *Appl. Mathematics Comput.* 308, 130–141. doi:10.1016/j.amc.2017.03.019

Gao, H., Yang, Y., Xu, Q.-H., Wang, J.-L., and Wang, Y. (2021). Experimental Study on High Efficiency Grinding Process of 5G Copper Clad Laminate Composites. *Diam. Abrasives. Eng.* 41, 82–88. doi:10.13394/j.cnki.jgszz.2021.3.0012

Gu, Q., Deng, Z., Lv, L., Liu, T., Teng, H., Wang, D., et al. (2021). Prediction Research for Surface Topography of Internal Grinding Based on Mechanism and Data Model. *Int. J. Adv. Manuf Technol.* 113 (3), 821–836. doi:10.1007/s00170-021-06604-7

Guo, W., Wu, C., Ding, Z., and Zhou, Q. (2021). Prediction of Surface Roughness Based on A Hybrid Feature Selection Method and Long Short-Term Memory Network in Grinding. *Int. J. Adv. Manuf Technol.* 112 (9), 2853–2871. doi:10.1007/s00170-020-06523-z

Huang, Y., He, S., Xiao, G., Li, W., Jiahua, S., and Wang, W. (2020). Effects Research on Theoretical-Modelling Based Suppression of the Contact Flutter in Blisk Belt Grinding. *J. Manufacturing Process.* 54, 309–317. doi:10.1016/j.jmapro.2020.03.021

Huang, Y., Xiao, G-J., and Zou, L. (2016). Current Situation and Development Trend of Polishing Technology for Blisk. *Chin. J. Aeronaut.* 37 (7), 2045–2064. doi:10.7527/S1000-6893.2016.0055

Huang, Y., Xiao, G., Zhao, H., Zou, L., Zhao, L., Liu, Y., et al. (2018). Residual Stress of Belt Polishing for the Micro-stiffener Surface on the Titanium Alloys. *Proced. CIRP* 71, 11–15. doi:10.1016/j.procir.2018.05.007

AUTHOR CONTRIBUTIONS

GX, YH, and WL conceived and designed the study. YZ, HG, and BZ performed the experiments. WL and YZ wrote the manuscript. GX and YH reviewed and edited the manuscript. All authors read and approved the manuscript.

FUNDING

Klocke, F., Gierlings, S., Brockmann, M., and Veselovac, D. (2014). Force-Based Temperature Modeling for Surface Integrity Prediction in Broaching Nickel-Based Alloys. *Proced. CIRP* 13, 314–319. doi:10.1016/j.procir.2014.04.053

Li, C., Piao, Y., Meng, B., Hu, Y., Li, L., and Zhang, F. (2022). Phase Transition and Plastic Deformation Mechanisms Induced by Self-Rotating Grinding of GaN Single Crystals. *Int. J. Mach. Tools Manuf.* 172, 103827. doi:10.1016/j.ijmachtools.2021.103827

Pandiyan, V., Caesarendra, W., Tjahjowidodo, T., and Tan, H. H. (2018). In-Process Tool Condition Monitoring in Compliant Abrasive Belt Grinding Process Using Support Vector Machine and Genetic Algorithm. *J. Manufacturing Process.* 31, 199–213. doi:10.1016/j.jmapro.2017.11.014

Slătineanu, L., Coteață, M., Dodun, O., Iosub, A., and Sîrbu, V. (2010). Some Considerations Regarding Finishing by Abrasive Flap Wheels. *Int. J. Mater. Form.* 3 (2), 123–134. doi:10.1007/s12289-009-0665-8

Wang, X., Xu, C-L., Li, Z-X., Pei, C-H., and Tang, Z-H. (2020). Effect of Shot Peening Intensity and Surface Coverage on Room-Temperature Fatigue Property of TC4 Titanium Alloy. *Cailiao. Gongcheng.* 48 (9), 138–143. doi:10.11868/j.issn.1001-4381.2019.000142

Wu, D-H. (2007). A Prediction Model for Surface Roughness in Milling Based on Least Square Support Vector Machine. *Chin. J. Mech. Eng-en.* 18 (07), 838–841. doi:10.3321/j.issn:1004-132X.2007.07.020

Xiao, G., Chen, B., Li, S., and Zhuo, X. (2022). Fatigue Life Analysis of Aero-Engine Blades for Abrasive Belt Grinding Considering Residual Stress. *Eng. Fail. Anal.* 131, 105846–105846. doi:10.1016/j.engfailanal.2021.105846

Xiao, G., and Huang, Y. (2019). Micro-Stiffener Surface Characteristics with Belt Polishing Processing for Titanium Alloys. *Int. J. Adv. Manuf Technol.* 100 (1-4), 349–359. doi:10.1007/s00170-018-2727-x

Xiao, G., Zhang, Y-D., Huang, Y., Zhang, Y., Huang, Y., Song, S., et al. (2021). Grinding Mechanism of Titanium alloy: Research Status and prospect. *J. Adv. Manuf. Sci. Tech.* 1 (1), 2020001–2020012. doi:10.51393/j.jamst.2020001

Xu, L., Huang, C., Li, C., Wang, J., Liu, H., and Wang, X. (2020). An Improved Case Based Reasoning Method and its Application in Estimation of Surface Quality toward Intelligent Machining. *J. Intell. Manuf.* 32 (1), 313–327. doi:10.1007/s10845-020-01573-2

Zhang, M-J., Wang, C., and Chen, H. (2012). The Application Research on the Combination of IMF Energy and RBF Neural Network in Rolling Bearing Fault Diagnosis. *Machinery* 39 (06), 63–66+70. doi:10.3969/j.issn.1006-0316.2012.06.017

Zhang, S., Yang, Z., Jiang, R., Jin, Q., Zhang, Q., and Wang, W. (2021). Effect of Creep Feed Grinding on Surface Integrity and Fatigue Life of Ni3al Based Superalloy IC10. *Chin. J. Aeronautics* 34 (1), 438–448. doi:10.1016/j.cja.2020.02.025

Zhou, K., Xu, J., Xiao, G., and Huang, Y. (2022). A Novel Low-Damage and Low-Abrasive Wear Processing Method of Cf/Sic Ceramic Matrix Composites: Laser-Induced Ablation-Assisted Grinding. *J. Mater. Process. Technology* 302, 117503. doi:10.1016/j.jmatprotec.2022.117503

Zhu, D., Feng, X., Xu, X., Yang, Z., Li, W., Yan, S., et al. (2020). Robotic Grinding of Complex Components: A Step towards Efficient and Intelligent Machining - Challenges, Solutions, and Applications. *Robotics and Computer-Integrated Manufacturing* 65, 101908. doi:10.1016/j.rcim.2019.101908

Conflict of Interest: The authors declare that the research was conducted in the absence of any commercial or financial relationships that could be construed as a potential conflict of interest.

The reviewer LW declared a shared affiliation with the author GX to the handling editor at the time of review.

APPENDIX TABLE: PART OF THE ORIGINAL EXPERIMENTAL DATA.

F_n (N)	v_f (m/min)	v_s (m/s)	d_s (mm)	Ra (µm)									Mean value
				Point 1	Point 2	Point 3	Point 4	Point 5	Point 6	Point 7	Point 8	Point 9	
20	0.05	12	0.6	0.226	0.226	0.227	0.269	0.234	0.229	0.217	0.216	0.227	0.230
20	0.05	12	0.8	0.227	0.216	0.234	0.229	0.217	0.264	0.245	0.226	0.269	0.236
20	0.05	12	1	0.269	0.234	0.229	0.217	0.216	0.209	0.218	0.245	0.234	0.230
20	0.05	14	0.2	0.234	0.236	0.238	0.209	0.218	0.216	0.234	0.229	0.229	0.227
20	0.05	14	0.4	0.229	0.218	0.226	0.226	0.227	0.269	0.234	0.229	0.217	0.231
20	0.05	14	0.6	0.217	0.226	0.227	0.216	0.234	0.229	0.217	0.264	0.216	0.227
20	0.05	14	0.8	0.216	0.245	0.269	0.234	0.229	0.217	0.216	0.209	0.218	0.228
20	0.05	14	1	0.234	0.234	0.229	0.217	0.229	0.217	0.216	0.238	0.226	0.227
20	0.05	16	0.2	0.269	0.234	0.229	0.217	0.216	0.209	0.218	0.245	0.234	0.230
20	0.05	16	0.4	0.234	0.236	0.238	0.209	0.218	0.216	0.234	0.229	0.229	0.227
20	0.05	16	0.6	0.229	0.218	0.226	0.226	0.227	0.269	0.234	0.229	0.217	0.231
20	0.05	16	0.8	0.217	0.226	0.227	0.216	0.234	0.229	0.217	0.264	0.216	0.227
20	0.05	16	1	0.216	0.245	0.269	0.234	0.229	0.217	0.216	0.209	0.218	0.228
20	0.05	18	0.2	0.209	0.226	0.227	0.269	0.234	0.229	0.217	0.224	0.227	0.229
20	0.05	18	0.4	0.218	0.227	0.216	0.234	0.229	0.217	0.264	0.216	0.234	0.228
20	0.05	18	0.6	0.198	0.194	0.201	0.178	0.198	0.186	0.188	0.206	0.247	0.200
20	0.05	18	0.8	0.229	0.218	0.226	0.226	0.227	0.269	0.234	0.229	0.217	0.231
20	0.05	18	1	0.217	0.226	0.227	0.216	0.234	0.229	0.217	0.264	0.216	0.227
20	0.05	20	0.2	0.216	0.245	0.269	0.234	0.229	0.217	0.216	0.209	0.218	0.228
20	0.05	20	0.4	0.209	0.226	0.227	0.269	0.234	0.229	0.217	0.224	0.227	0.229
20	0.05	20	0.6	0.218	0.227	0.216	0.234	0.229	0.217	0.264	0.216	0.234	0.228
20	0.05	20	0.8	0.198	0.194	0.201	0.178	0.198	0.186	0.188	0.206	0.247	0.200
20	0.05	20	1	0.184	0.188	0.186	0.186	0.184	0.184	0.183	0.182	0.185	0.185
25	0.01	12	0.2	0.483	0.512	0.468	0.457	0.448	0.463	0.465	0.457	0.448	0.467
25	0.01	12	0.4	0.468	0.457	0.469	0.458	0.461	0.458	0.461	0.465	0.457	0.462

Numerical and Experimental Study on Reasonable Coverage of Shot Peening on ZGMn13 High Manganese Steel

Haiyang Yuan[1,2], Zhangping You[1,2]*, Yaobin Zhuo[1,2], Xiaoping Ye[1,2], Liangliang Zhu[3] and Weibo Yang[3]

[1]Lishui University, Lishui, China, [2]Key Laboratory of Digital Design and Intelligent Manufacture in Culture and Creativity Product of Zhejiang Province, Lishui University, Lishui, China, [3]Zhejiang Guanlin Machinery Inc., Anji, China

Shot peening technology is usually employed to improve the ability of mechanical parts to resist failure due to fatigue and wear. It is often used to strengthen the surface of a target, but the induced residual stress and its distribution with respect to the coverage can affect the performance of the shot peening process. In this study, a comprehensive numerical and experimental study was conducted to overcome these issues. Using numerical simulation we found that both the surface and subsurface residual stress increases with the increase of the coverage before stabilizing. Quantitative analysis using the Entropy Method indicates that under the shot peening parameters considered in the simulation coverage of 200% is best for the shot peening of ZGMn13 High Manganese Steel. The following experimental study agreed with the corresponding numerical data for the residual stresses at varied depths from surface to subsurface with errors of less than 25%. Thus, the related research outcomes can guide the shot peening process to obtain the optimized surface strengthening of the target.

Keywords: shot peening, residual stress, reasonable coverage, entropy method, ZGMn13

INTRODUCTION

Advanced manufacturing technologies, including traditional and non-traditional machining technologies (Ji et al., 2022; Zhang et al., 2022), have been extensively employed to fabricate structures on the different kinds of functional materials used in aerospace engineering, information engineering, and microelectronics engineering (Cheng et al., 2022; Hu et al., 2022; Qi et al., 2022). High Manganese Steel possessing excellent wear-resistant performance has been widely used in the industry, but fatigue may occur in the main load-bearing structures under alternating loads during service (Prysyazhnyuk et al., 2022). As such, it is particularly important to improve the fatigue performance of High Manganese Steel by surface strengthening treatment (Syed et al., 2021).

Shot peening technology is a surface strengthening technology that can effectively enhance the ability of mechanical parts to resist fatigue failure and wear failure. It has been widely used in the aerospace automobile industries as well as other fields (Balbaa et al., 2022; Unal et al., 2022; Zhao et al., 2022). Menezes et al. found that the wear resistance of AISI316L steel after shot peening was improved due to the formation of a certain thickness hardening layer on its surface (Menezes et al., 2017). Li et al. found that the shot peening technique can significantly improve the fatigue strength of gear made of 20CrMnMo, thereby increasing its service life (Li and Liu, 2018). Moreover, the shot peening treatment of 17CrNiMo6 steel can introduce higher residual compressive stress and refine the target surface grain, which could improve the target fatigue life.
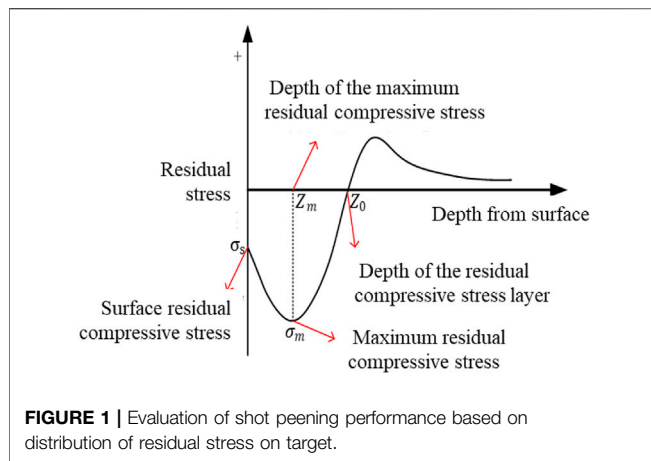
FIGURE 1 | Evaluation of shot peening performance based on distribution of residual stress on target.

TABLE 1 | J-C model parameters of ZGMn13 High Manganese Steel (Teng, 2011).

A/MPa	B/MPa	N	C	m
634	897	0.913	0.04	1

It has also been found that secondary shot peening can further improve the residual compressive stress field, microstructure and surface morphology on the basis of the first shot peening process, to further improve its fatigue life (Sun et al., 2016). Yan et al. found that a certain thickness of the nanocrystalline layer was formed on the surface of ZGMn13 steel after the shot peening treatment, and the grain was refined and the surface was strengthened. After a certain period of shot peening, the wear resistance of ZGMn13 steel is significantly improved. However, if the shot peening time was too long, the wear resistance can decrease due to the formation of microcracks (Yan et al., 2007). According to the above analysis, the fundaments of the shot peening technology are properly investigated.
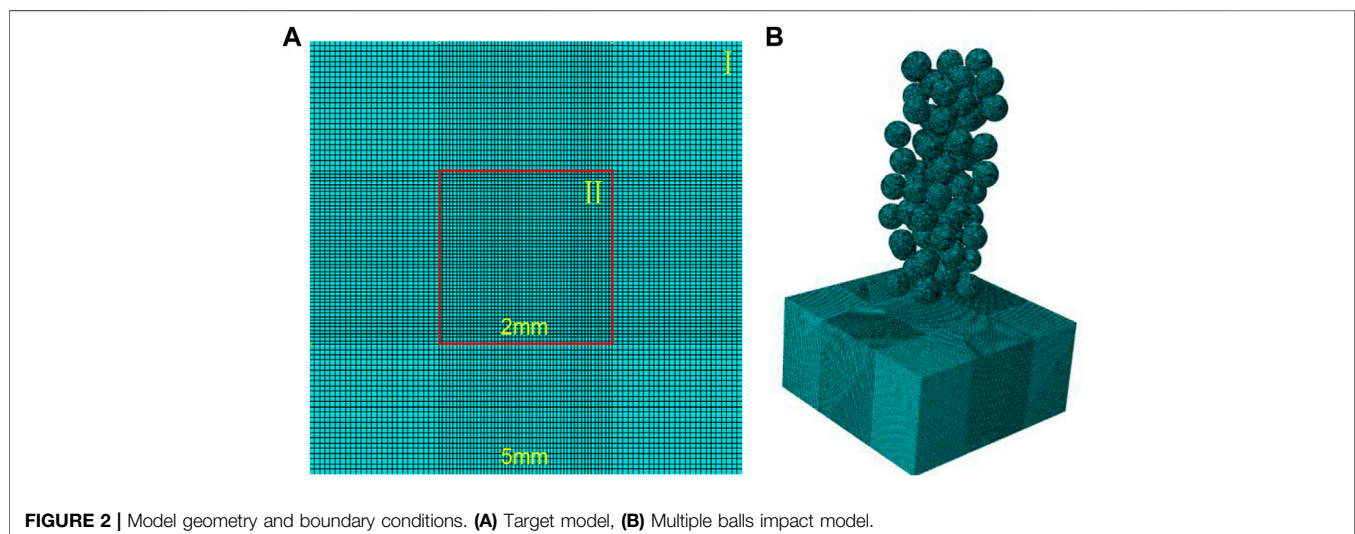
Shot peening coverage is another important factor affecting the effect of shot peening. Insufficient shot peening coverage cannot achieve the strengthening effect of the workpiece, while excessive shot peening coverage causes burrs on the surface of the workpiece and microcracks (Maleki and Unal, 2018). Furthermore, the influence of shot peening coverage on the evolution of residual stress and surface morphology is not fully clear (Wu et al., 2020; Qin et al., 2022). It is therefore necessary to conduct in-depth research on reasonable shot peening coverage, and to further understanding of the relation between induced residual stress by shot peening and the failure of the target materials. Generally, the surface residual compressive stress (σ_s), the maximum residual compressive stress (σ_m), the depth of maximum residual compressive stress (Z_m). and the depth of residual compressive stress layer (Z_0), as shown in **Figure 1**, are the four essential factors that affect the performance of the shot peening process. However, further exploration of the best way to comprehensively consider the coupling effects of these values on the shot peening performance with respect to its coverage is needed.

In this paper numerical and experimental studies were performed to explore the reasonable coverage of shot peening on ZGMn13 High Manganese Steel. Firstly, a numerical model was developed in ABAQUS to consider the random shot peening process and observe the residual stress both on the surface and subsurface. Then the Entropy Method was employed to evaluate the shot peening performance based on these numerical results. Finally, corresponding experiments were carried out to verify the numerical results and explore the reasonable coverage of shot peening on ZGMn13 High Manganese Steel.

NUMERICAL STUDY

Model Development

This study used ABAQUS Software to conduct the numerical study. The geometry of the target is modelled as shown in **Figure 2A** with the dimensions 5 mm × 5 mm × 2.4 mm. Zone I is the coarsening mesh and Zone II is the refined mesh
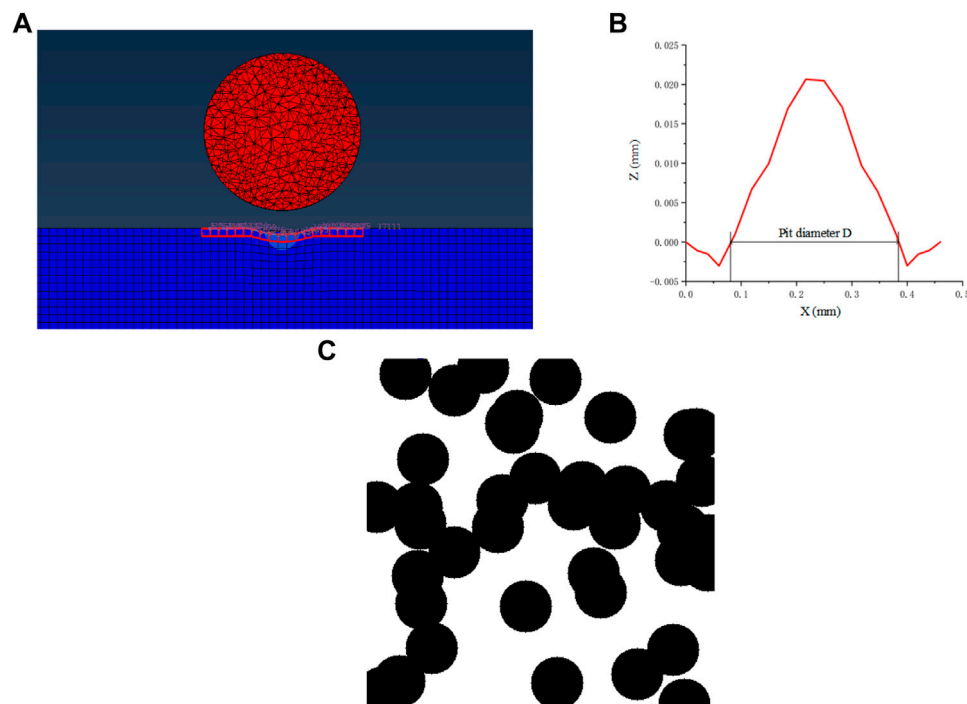

FIGURE 2 | Model geometry and boundary conditions. **(A)** Target model, **(B)** Multiple balls impact model.

FIGURE 3 | Calculation of the pit diameter of the shot peening ball on the target. **(A)** Simulation of single ball impacts, **(B)** Measurement of pit diameter, **(C)** Calculation of coverage with respect to the number of balls.
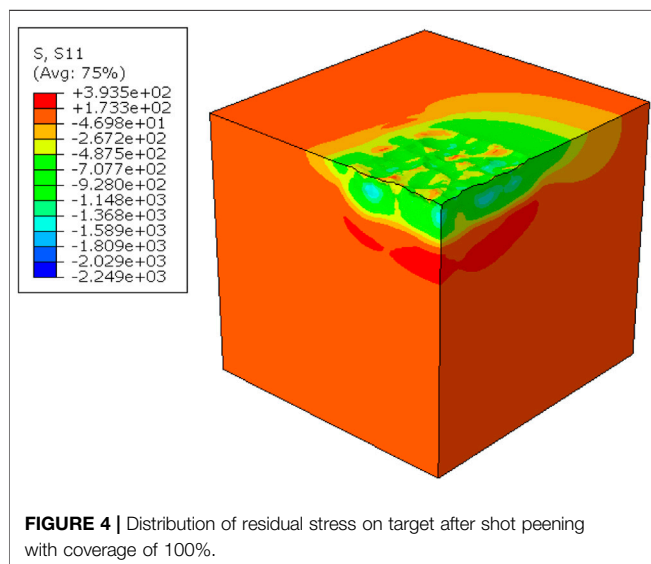

FIGURE 4 | Distribution of residual stress on target after shot peening with coverage of 100%.

TABLE 2 | The relation between the number of balls and coverage.

No.	Coverage (%)	Number of balls
1	23	10
2	40	20
3	64	40
4	87	80
5	100	160
6	150	240
7	200	320
8	250	400

The balls used for the shot peening in the simulation can be randomly generated up Zone II by defining the related functions in ABAQUS. The constitutive model for the target, ZGMn13 High Manganese Steel, is Johnson-Cook model and its parameters are shown in **Table 1**. In the simulation, the ZGMn13 high manganese steel was considered as the target material, whose density is 7.98×10^{-6} kg/mm^3, Elastic Modulus is 210 GPa and Poisson ratio is 0.3, and the Steel Cut Wire Shot, with density of 7.8×10^{-6} kg/mm^3, Elastic Modulus of 210 GPa and Poisson ratio of 0.3, was used to model the shot peening ball. The boundary conditions are as follows: the top face of the target is set free, which is impacted by the shot peening balls, while the other five exterior faces of the target are set at zero freedom in both translational and angular velocities. This paper used a shot peening ball size of 0.6 mm, and the its impact speed and angle were 80 m/s and 90°, respectively.

used for the shot peening. The mesh independence test was conducted in the Zone II with mesh sizes of 0.04, 0.03 and, 0.02 mm, respectively. We found that the difference of numerical results between adjacent mesh densities is less than 3.2%. A mesh size of 0.04 mm in Zone II with dimensions of 2 mm × 2 mm × 2.4 mm was selected for the model to achieve an accurate solution and reduce the computation time.
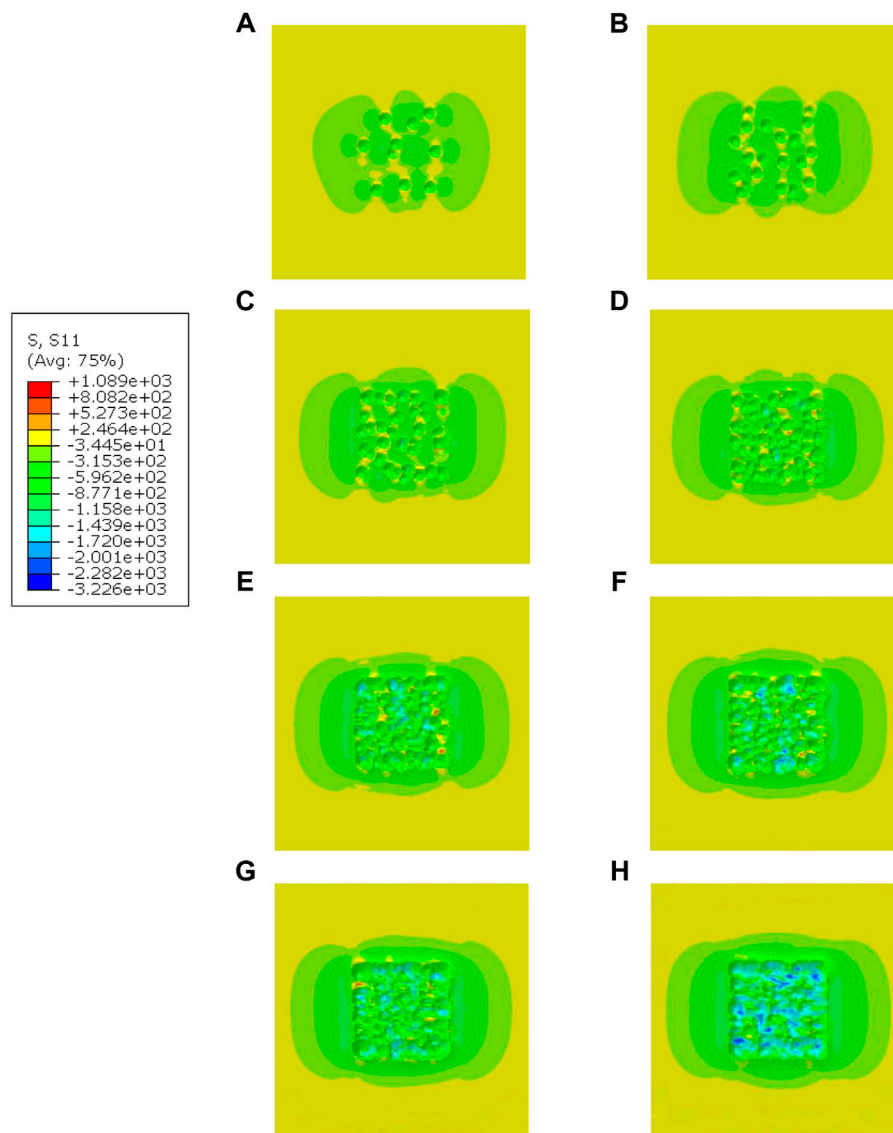
FIGURE 5 | Distributions of the surface residual stress for coverage from 23 to 250%. **(A)** 23%, **(B)** 40%, **(C)** 64%, **(D)** 87%, **(E)** 100%, **(F)** 150%, **(G)** 200%, **(H)** 250%.

The coverage of shot peening was defined as the ratio of the total area of the impacting ball on the target to the whole area of the target. According to previous studies, the ratio needs to be changed often by using different numbers of shot peening balls, but it is hard to quantitatively obtain the relation between the number of balls and coverage. In this study this relationship was quantitatively given as follows: firstly, the pit diameter of the shot peening ball on the target was calculated by modeling the single ball impact on the target with the above-mentioned parameters, as shown in **Figure 3A**. This value can be measured as 0.3 mm, seen in **Figure 3B**. Then, inside the impact area with dimensions of 1.6 mm × 1.6 mm, the random circles with a diameter of 0.3 mm were generated by responding to the number of balls, as shown in **Figure 3C**, and the coverage was also taken. Finally, by

repeating this calculation more than 1,000 times, the relation between the number of balls and the coverage was calculated, as shown in **Table 2**. The numerical work was carried out according to the parameters in **Table 2**, and the effect of the coverage on the target residual stress was analyzed to explore the reasonable coverage of shot peening of ZGMn13 High Manganese Steel.

Results and Discussion

A typical distribution of residual stress on target is shown in **Figure 4** under the coverage of 100%. It can be seen from this figure that the shot peening process mainly induces the residual compressive stress on the target, and a layer of residual compressive stress may be formed due to the impact of many balls, where the maximum residual compressive stress can be
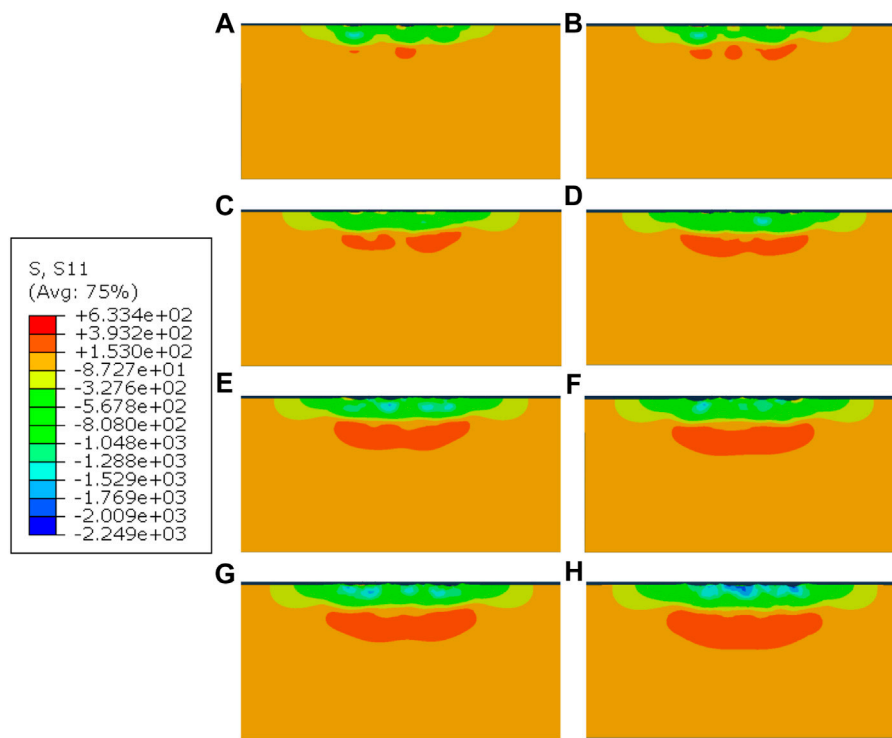
FIGURE 6 | Distribution of subsurface residual stress with respect to coverage from 23 to 250%. **(A)** 23%, **(B)** 40%, **(C)** 64%, **(D)** 87%, **(E)** 100%, **(F)** 150%, **(G)** 200%, **(H)** 250%
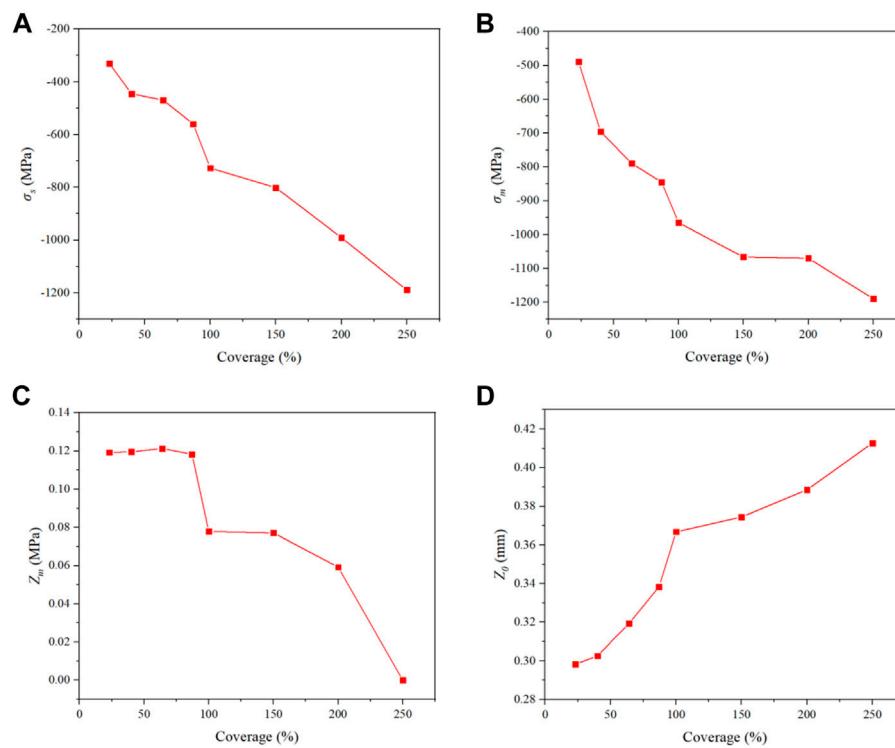
FIGURE 7 | Effects of the shot peening coverage on the **(A)** σ_s, **(B)** σ_m, **(C)** Z_m, and **(D)** Z_0.

TABLE 3 | Original simulation results.

No.	Coverage (%)	Parameters			
		σ_s (MPa)	σ_m (MPa)	Z_m (mm)	Z_0 (mm)
1	23	−329.736	−488.709	0.119	0.298
2	40	−444.871	−695.29	0.120	0.303
3	64	−469.309	−789.06	0.121	0.319
4	87	−559.818	−845.101	0.118	0.338
5	100	−726.799	−964.628	0.078	0.367
6	150	−801.443	−1065.89	0.077	0.374
7	200	−990.732	−1069.94	0.059	0.389
8	250	−1189.05	−1189.05	0	0.413

TABLE 4 | Dimensionless values.

No.	Coverage (%)	Parameters			
		σ_s	σ_m	Z_m	Z_0
1	23	0.4786	0.5501	1.3757	0.8511
2	40	0.6457	0.7826	1.3873	0.8654
3	64	0.6812	0.8881	1.3988	0.9111
4	87	0.8125	0.9512	1.3642	0.9654
5	100	1.0549	1.0857	0.9017	1.0482
6	150	1.1632	1.1997	0.8902	1.0682
7	200	1.4380	1.2043	0.6821	1.1110
8	250	1.7258	1.3383	0.0000	1.1796

TABLE 5 | Scores from entropy method.

No.	Coverage (%)	Score
1	23	0.8139
2	40	0.9202
3	64	0.9698
4	87	1.0233
5	100	1.0226
6	150	1.0803
7	200	1.1088
8	250	1.0609
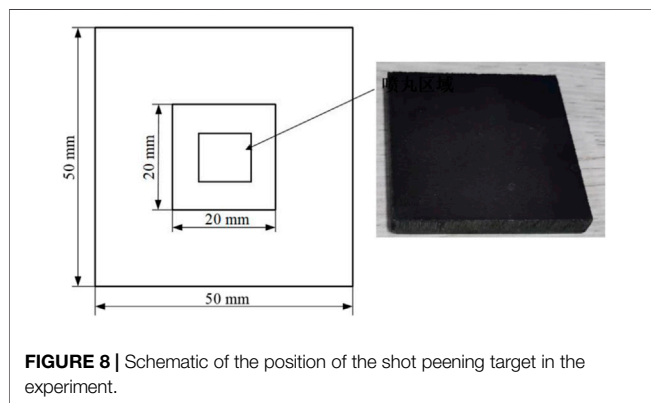
FIGURE 8 | Schematic of the position of the shot peening target in the experiment.

found in the subsurface of the target. It is also interesting to notice from the target surface that the residual tensile stress is observed due to the interaction of shot peening balls, and in the target

TABLE 6 | Material properties of ZGMn13 High Manganese Steel (by mass%) (Teng, 2011).

Contents	C	Si	Mn	P	S
Percentages	0.98	0.41	12.80	0.020	0.001

subsurface, the residual tensile stress was also found to achieve a balance.

Figure 5 shows the different distributions of the surface residual stress for coverage from 23 to 250%. We found that the surface residual stress increases with the increase of the coverage from 23 to 100%. When the coverage is more than 100% there is almost no variation of surface residual stress, which indicates that this value was stable. Moreover, it is noteworthy that the surface residual tensile stress had a coverage of 100%, and can be reduced by further increasing the coverage.

Figure 6 shows the different distributions of subsurface residual stress concerning coverage from 23 to 250%. In general, a layer of residual compressive stress was generated under the impact zone. To be specific, the subsurface residual compressive stress increases with the increase of coverage from 23 to 100%, while when the coverage is more than 100% there is almost no variation of subsurface residual compressive stress that demonstrates that this value was stable. The subsurface residual tensile stress increases with an increase of the coverage up to 100%, but this trend stabilizes when the coverage is more than 100%. Furthermore, by comparing **Figures 6A–H** it is interesting to note that all the maximum residual compressive stress occurs in the subsurface of the target, except the condition with coverage of 250%, where its maximum residual compressive stress is found to be at the target surface. This indicates that further increasing the coverage could result in the failure of the target material, which is not expected in shot peening.

The surface residual compressive stress (σ_s), the maximum residual compressive stress (σ_m), the depth of the maximum residual compressive stress (Z_m), and the depth of the residual compressive stress layer (Z_0) are the four essential factors that affect the performance of the shot peening process. As mentioned in the introduction, their relations concerning coverage can be numerically summarized, as shown in **Figure 7**. This figure shows that the surface residual compressive stress, the maximum residual compressive stress, and the depth of the residual compressive stress layer all increase by increasing the coverage. To be specific, the variation of the maximum residual compressive stress and the depth of the residual compressive stress layer is larger when the coverage is less than 100%. While the depth of the maximum residual compressive stress gradually increases from 0.119 to 0.121 mm concerning the coverage from 23 to 100%. It then gradually reduces to 0 when the coverage is 250%. This demonstrates that with an increase in coverage, the position of the maximum residual compressive stress could move to the target surface gently and that further increasing coverage may induce the surface damage and result in the failure of the target.

To assess the performance of the shot peening process considered in this study, further quantitative analysis is conducted based on the distribution of the residual

FIGURE 9 | Experimental machine and procedure.

TABLE 7 | Experimental processing parameters.

Parameters	Values
Shot peening ball diameter	0.6 mm (Steel: 55–62 HRC)
Pressure	0.52 MPa
Flow rate	3–5 kg/min
Number of shot peening gun	1
Distance between gun and target surface	160 mm
Coverage	100, 150, 200, 250%
Pieces of target	8 (Each group 4)

compressive stress concerning the corresponding coverage. The original simulation results of the σ_s, σ_m, Z_m, and Z_0 can be obtained as shown in **Table 3**. These data are then treated as dimensionless values (see **Table 4**), which are convenient for the following comparisons. The Entropy Method is a commonly used weighting method that measures value dispersion in decision-making. The greater the degree of dispersion, the greater the degree of differentiation, meaning more information can be derived. Meanwhile, higher weight should be given to the index, and vice versa (Zhu et al., 2020). Thus, it is employed to process these dimensionless values to evaluate the weight of the residual compressive stress for different corresponding coverages (Li et al., 2022), the scores are given in **Table 5**. According to the rule of the Entropy Method the higher the score the better the performance. Under the shot peening parameters considered in the simulation, the coverage of 200% is found to be best for the shot peening of ZGMn13 High Manganese Steel.

EXPERIMENTAL STUDY

Experiment Work

ZGMn13 High Manganese Steel with dimensions of 5 mm × 5 mm × 6 mm is selected as the target, that is, fixed in the central
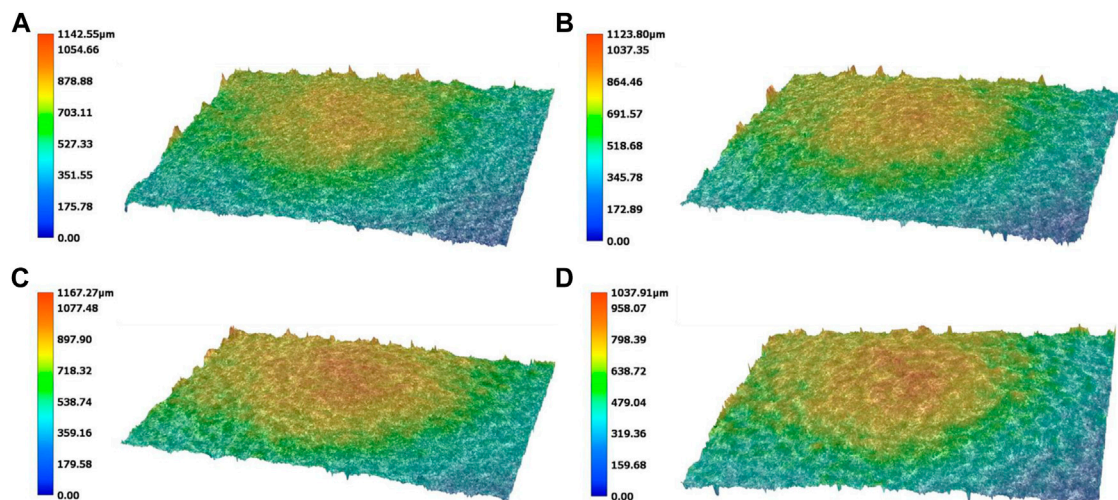

FIGURE 10 | The overall observations of target surface morphologies under different coverages. **(A)** 100%, **(B)** 150%, **(C)** 200%, **(D)** 250%.

TABLE 8 | Comparison of experimental results and numerical data.

	Coverage (%)	0 μM (MPa)	30 μM (MPa)	60 μM (MPa)	90 μM (MPa)	120 μM (MPa)	240 μM (MPa)	360 μM (MPa)
Exp	100	−950	−1,209	−1,118	−792	−716	−484	−20
Num		−727	−889	−945	−950	−920	−620	−10
Err. (%)		23	26	15	20	29	28	50
Exp	150	−1,069	−1,303	−1,410	−943	−856	−508	−98
Num		−810	−930	−1,053	−1,042	−989	−630	−56
Err. (%)		24	29	25	10	16	24	43
Exp	200	−1,105	−1,366	−1,436	−1,120	−912	−91	−203
Num		−991	−1,038	−1,075	−1,055	−1,009	−637	−117
Err. (%)		10	24	25	6	11	600	42
Exp	250	−1,139	−1,480	−1,287	−1,095	−882	−653	−280
Num		−1,189	−1,181	−1,170	−1,115	−1,025	−632	−210
Err. (%)		4	20	9	2	16	3	25
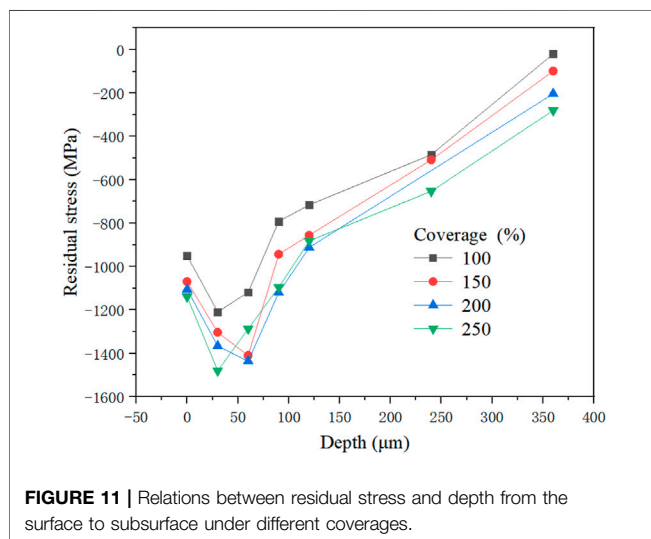
FIGURE 11 | Relations between residual stress and depth from the surface to subsurface under different coverages.

impact zone (20 mm × 20 mm) as shown in **Figure 8**, and the major material properties of the target are given in **Table 6**. In the experiment, all tests were carried out on a pneumatic shot peening machine (SP1200-V20/1/2X) with the procedure shown in **Figure 9**. In terms of the performance of this shot peening machine, the processing parameter settings considered in the experiment are given in **Table 7**, which corresponds to the numerical study in this paper.

After each test, the surface and subsurface residual stress were measured using X-ray diffraction (XRD), which is one of the most extensively used techniques for the evaluation of residual stress due to its accurate, effective, and non-destructive measurement (Alhumaidan et al., 2015). In this study, the GNR EDGE Residual Stress-Retained Austenite XRD was used to measure the residual stress. However, the penetrability of this machine into the ZGMn13 High Manganese Steel is limited, and the surface residual stress alone cannot reflect the distribution of the

residual stress for the thickness. Electrolytic polishing etching was needed to treat the target surface layer by layer since this process does not induce the mechanical force, which means it does not induce new residual stress and that it cannot affect the measurement results. Therefore, under different coverages, i.e., 100, 150, 200, and 250%, the residual stresses were measured at 0, 30, 60, 90, 120, 240, and 360 μM from surface to the subsurface, respectively.

Results and Discussion

The overall observations of the target surface morphologies after the shot peening process are shown in **Figure 10**. When the coverage is 100%, the distribution of the pits caused by the impacts seems to be uniform without obvious uplift and depression. With an increase in coverage, the uplift and depression become more obvious, which induces larger plastic deformations. A comparison between **Figures 10C,D** indicates that when the coverage reaches approximately 200% the surface morphology seems to be stable even by further increasing the coverage as per the numerical results.

A quantitative comparison was then carried out. **Table 8** shows that the experimental results are in general in agreement with corresponding numerical data for the residual stresses at varied depths from surface to subsurface with errors of less than 25%. It is also interesting to notice that some errors are larger than 100%. These were mainly caused by the experimental measurements and these results have not been considered in further analysis. As can be seen from **Figure 11**, for each coverage the overall residual compressive stress increases with an increase of the depth from the surface until reaching the maximum value, and then it gradually reduces. The surface residual compressive stress and the maximum residual compressive stress show an increasing trend with the increase of the coverage. It can therefore be deduced that the depth of the residual compressive stress layer should have a similar trend. Moreover, the depth of the maximum residual compressive stress first increases in terms of coverage to 150% before then reducing gradually. These findings show the overall

trend with corresponding numerical results. **Figure 11** also indicates 11 that when the coverage is 100% the overall value of the residual compressive stress from the surface to the subsurface is larger than that with other coverages, which indicates that in this situation further increasing the coverage can increase the shot peening performance. However, when the coverage is more than 150% the overall values of the residual compressive stress from the surface to the subsurface are similar, which demonstrates that in this situation further increasing the coverage may not improve the shot peening performance but induce the failure of the target. Therefore, considering the processing parameters in this study and its effect on the distribution of the residual compressive stress, it can be that reasonable coverage in the shot peening of ZGMn13 High Manganese Steel is between 150 and 200%, which agrees with the numerical study.

CONCLUSION

Shot peening technology is a surface strengthening technology that can effectively enhance the ability of mechanical parts to resist fatigue failure and wear failure, but the influence of shot peening coverage on the evolution of residual stress and surface morphology is not fully clear. In this study, a comprehensive numerical and experimental study were conducted to explore the reasonable coverage of shot peening on ZGMn13 High Manganese Steel. The quantitative relation between the number of balls and the coverage were obtained in simulation and from the numerical study, indicating that both the surface and subsurface residual stress increases with the increase of the coverage before stabilizing. By using the Entropy Method the quantitative analysis has been conducted to explore the effects of the surface residual compressive stress, the maximum residual compressive stress, the depth of the maximum residual compressive stress, and the depth

of the residual compressive stress layer on the performance of the shot peening process, which indicates that under the shot peening parameters considered in simulation the coverage of 200% is found to be best for the shot peening of ZGMn13 High Manganese Steel. Finally, a corresponding experimental study was carried out to verify the numerical results, and the results agreed well with the corresponding numerical data for the residual stresses at varied depths from the surface to the subsurface with errors of less than 25%. These research outcomes provide guidance on the shot peening process in obtaining the optimized surface strengthening of the target.

DATA AVAILABILITY STATEMENT

The raw data supporting the conclusions of this article will be made available by the authors, without undue reservation.

AUTHOR CONTRIBUTIONS

Conceptualization, HY; Data curation, YZ; Formal analysis, XY; Investigation, LZ; Software, LZ; Supervision, HY; Writing-original draft, ZY; Writing—review and editing, ZY.

FUNDING

REFERENCES

Alhumaidan, F. S., Hauser, A., Rana, M. S., Lababidi, H. M. S., and Behbehani, M. (2015). Changes in Asphaltene Structure during Thermal Cracking of Residual Oils: XRD Study. *Fuel* 150, 558–564. doi:10.1016/j.fuel.2015.02.076

Balbaa, M., Ghasemi, A., Fereiduni, E., Al-Rubaie, K., and Elbestawi, M. (2022). Improvement of Fatigue Performance of Laser Powder Bed Fusion Fabricated IN625 and IN718 Superalloys via Shot Peening. *J. Mater. Process. Technol.* 304, 117571. doi:10.1016/j.jmatprotec.2022.117571

Cheng, Z., Qin, S., and Fang, Z. (2022). Numerical Modeling and Experimental Study on the Material Removal Process Using Ultrasonic Vibration-Assisted Abrasive Water Jet. *Front. Mater.* 9, 895271. Accepted for Publication. doi:10.3389/fmats.2022.895271

Hu, W., Teng, Q., Hong, T., Saetang, V., and Qi, H. (2022). Stress Field Modeling of Single-Abrasive Scratching of BK7 Glass for Surface Integrity Evaluation. *Ceram. Int.* 48, 12819–12828. doi:10.1016/j.ceramint.2022.01.153

Ji, R., Zhang, L., Zhang, L., Li, Y., Lu, S., and Fu, Y. (2022). Processing Method for Metallic Substrate Using the Liquid Metal Lapping-Polishing Plate. *Front. Mater.* 9, 896346. doi:10.3389/fmats.2022.896346

Li, G., Wang, Y. X., Zeng, Y., and He, W. X. (2022). A New Maximum Entropy Method for Estimation of Multimodal Probability Density Function. *Appl. Math. Model.* 102, 137–152. doi:10.1016/j.apm.2021.09.029

Li, W., and Liu, B. (2018). Experimental Investigation on the Effect of Shot Peening on Contact Fatigue Strength for Carburized and Quenched Gears. *Int. J. Fatigue* 106, 103–113. doi:10.1016/j.ijfatigue.2017.09.015

Maleki, E., and Unal, O. (2018). Roles of Surface Coverage Increase and Re-peening on Properties of AISI 1045 Carbon Steel in Conventional and Severe Shot Peening Processes. *Surfaces Interfaces* 11, 82–90. doi:10.1016/j.surfin.2018.03.003

Menezes, M. R., Godoy, C., Buono, V. T. L., Schvartzman, M. M. M., and Avelar-Batista Wilson, J. C. (2017). Effect of Shot Peening and Treatment Temperature on Wear and Corrosion Resistance of Sequentially Plasma Treated AISI 316L Steel. *Surf. Coatings Technol.* 309, 651–662. doi:10.1016/j.surfcoat.2016.12.037

Prysyazhnyuk, P., Ivanov, O., Matvienkiv, O., Marynenko, S., Korol, O., and Koval, I. (2022). Impact and Abrasion Wear Resistance of the Hardfacings Based on High-Manganese Steel Reinforced with Multicomponent Carbides of Ti-Nb-Mo-V-C System. *Procedia Struct. Integr.* 36, 130–136. doi:10.1016/j.prostr.2022.01.014

Qi, H., Shi, L., Teng, Q., Hong, T., Tangwarodomnukun, V., Liu, G., et al. (2022). Subsurface Damage Evaluation in the Single Abrasive Scratching of BK7 Glass by Considering Coupling Effect of Strain Rate and Temperature. *Ceram. Int.* 48, 8661–8670. doi:10.1016/j.ceramint.2021.12.077

Qin, Z., Li, B., Zhang, H., Youani Andre Wilfried, T., Gao, T., and Xue, H. (2022). Effects of Shot Peening with Different Coverage on Surface Integrity and Fatigue Crack Growth Properties of 7B50-T7751 Aluminum Alloy. *Eng. Fail. Anal.* 133, 106010. doi:10.1016/j.engfailanal.2021.106010

Sun, H. X., Zhu, Y. L., Hou, S., Wang, Y. L., and Wang, W. (2016). Effects of Fatigue Load on Residual Stress and Microstructure of 17CrNiMo6 Shot Peening Strengthened Laye. *China Surf. Eng.* 29, 43–48. doi:10.11933/j.issn.1007-9289.2016.04.006

Syed, B., Maurya, P., Lenka, S., Padmanabham, G., and Shariff, S. (2021). Analysis of High Strength Composite Structure Developed for Low-Carbon-Low-Manganese Steel Sheet by Laser Surface Treatment. *Opt. Laser Technol.* 143, 107285. doi:10.1016/j.optlastec.2021.107285

Teng, T. (2011). *Simulation Research of ZGMn13 Drilling Force and Temperature Based on ABAQUS*. Master. Dalian, China: Dalian Jiaotong University.

Unal, O., Maleki, E., Karademir, I., Husem, F., Efe, Y., and Das, T. (2022). Effects of Conventional Shot Peening, Severe Shot Peening, Re-shot Peening and Precised Grinding Operations on Fatigue Performance of AISI 1050 Railway Axle Steel. *Int. J. Fatigue* 155, 106613. doi:10.1016/j.ijfatigue.2021.106613

Wu, J., Liu, H., Wei, P., Zhu, C., and Lin, Q. (2020). Effect of Shot Peening Coverage on Hardness, Residual Stress and Surface Morphology of Carburized Rollers. *Surf. Coatings Technol.* 384, 125273. doi:10.1016/j.surfcoat.2019.125273

Yan, W., Fang, L., Sun, K., and Xu, Y. (2007). Effect of Surface Nanocrystallization on Abrasive Wear Properties in Hadfield Steel. *J. Xi'an Jiaot. Univ.* 41, 611–615. doi:10.3321/j.issn:0253-987X.2007.05.024

Zhang, L., Zheng, B., Xie, Y., Ji, R., Li, Y., and Mao, W. (2022). Control Mechanism of Particle Flow in the Weak Liquid Metal Flow Field on Non-uniform Curvature Surface Based on Lippmann Model. *Front. Mater.* 9, 895263. Accepted for publication. doi:10.3389/fmats.2022.895263

Zhao, J., Tang, J., Zhou, W., Jiang, T., Liu, H., and Xing, B. (2022). Numerical Modeling and Experimental Verification of Residual Stress Distribution Evolution of 12Cr2Ni4A Steel Generated by Shot Peening. *Surf. Coatings Technol.* 430, 127993. doi:10.1016/j.surfcoat.2021.127993

Zhu, Y. X., Tian, D. Z., and Yan, F. (2020). Effectiveness of Entropy Weight Method in Decision-Making. *Math. Problems Eng.* 2020, 1–5. doi:10.1155/2020/3564835

Advantages of publishing in Frontiers

OPEN ACCESS
Articles are free to read for greatest visibility and readership

FAST PUBLICATION
Around 90 days from submission to decision

HIGH QUALITY PEER-REVIEW
Rigorous, collaborative, and constructive peer-review

TRANSPARENT PEER-REVIEW
Editors and reviewers acknowledged by name on published articles

REPRODUCIBILITY OF RESEARCH
Support open data and methods to enhance research reproducibility

DIGITAL PUBLISHING
Articles designed for optimal readership across devices

FOLLOW US
@frontiersin

IMPACT METRICS
Advanced article metrics track visibility across digital media

EXTENSIVE PROMOTION
Marketing and promotion of impactful research

LOOP RESEARCH NETWORK
Our network increases your article's readership